UNIVERSITÀ
DEGLI STUDI
FIRENZE
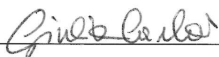
PhD in
Physics and Astronomy

CYCLE XXXV

COORDINATOR Prof. D'Alessandro Raffaello

Tip-tilt anisoplanatism in multiconjugate adaptive optics systems
and its impact on astrometric observations with next-generation telescopes
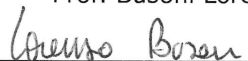
Academic Discipline (SSD) FIS/05
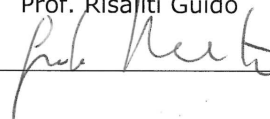
Doctoral Candidate
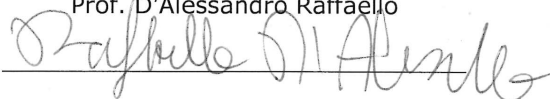Dr. Carlà Giulia

Supervisor
Prof. Busoni Lorenzo

Prof. Risaliti Guido

Coordinator
Prof. D'Alessandro Raffaello

Years 2019/2022

Table of contents

List of acronyms

AO	Adaptive Optics
CPSD	Cross Power Spectral Density
DM	Deformable Mirror
ELT	Extremely Large Telescope
FoV	Field of View
FWHM	Full Width at Half Maximum
GS	Guide Star
LBT	Large Binocular Telescope
LGS	Laser Guide Star
LSE	Least Square Estimator
MAD	Multiconjugate Adaptive Optics Demonstrator
MAVIS	Mcao Assisted Visible Imager and Spectrograph
MCAO	MultiConjugate Adaptive Optics
MICADO	Multi-AO Imaging CamerA for Deep Observations
MMSE	Minimum Mean Square Estimator
MORFEO	Multiconjugate adaptive Optics Relay For ELT Observations
NFIRAOS	Narrow-Field InfraRed Adaptive Optics System
NGS	Natural Guide Star
NTF	Noise Transfer Function
OLTF	Open-Loop Transfer Function
PFDM	Post-Focal Deformable Mirror
PFRO	Post-Focal Relay Optics
POLC	Pseudo-Open Loop Control
PSD	Power Spectral Density
PSF	Point Spread Function
RTC	Real Time Computer
RTF	Rejection Transfer Function

SCAO	Single-Conjugated Adaptive Optics
SH	Shack Hartmann
SNR	Signal to Noise Ratio
SOUL	Single conjugated adaptive Optics Upgrade for LBT
SVD	Singular Value Decomposition
TMT	Thirty Meter Telescope
TSVD	Truncated Singular Value Decomposition
VLT	Very Large Telescope
WFS	WaveFront Sensor

Introduction

The new class of 25-40 m extremely large telescopes will provide unprecedented resolutions to astronomical observations from the ground. The use of adaptive optics (AO) is mandatory to overcome the effects of atmospheric turbulence on the images and to fully exploit the capabilities of these telescopes by restoring their diffraction limit. In particular, the use of multiconjugate adaptive optics (MCAO) is foreseen for near-infrared observations at the Extremely Large Telescope (ELT) with the Multiconjugate adaptive Optics Relay For ELT Observations (MORFEO) and at the Thirty Meter Telescope with the Narrow Field InfraRed Adaptive Optics System (NFIRAOS). MCAO will also assist observations in the visible at the Very Large Telescope with the MCAO Assisted Visible Imager and Spectrograph (MAVIS). The high angular resolution, the uniformity of the correction over wide areas, the large number of reference sources with high image quality provided and the control of the field distortions through the DMs conjugated in altitude are characteristics that make MCAO a good candidate for astrometric observations. High-precision differential astrometry is, indeed, among the main science drivers of the future instruments equipped with MCAO. Among them, the near-infrared Multi-AO Imaging CamerA for Deep Observations (MICADO) assisted by MORFEO is required to achieve 50 μas (goal of 10 μas) of precision on the differential astrometry. Such challenging requirements ask for accurate analyses of the astrometric error budget, that must include an estimation of the impact of the MCAO control on astrometric measurements as well.

In this context, the aim of the present PhD project is to investigate the contribution to the astrometric error of the residuals of atmospheric tip-tilt from an MCAO loop and to include the results in the framework of the MORFEO project. The work is divided in different steps that are below described.

First, an analytical formulation has been derived to estimate temporal cross power spectral densities (CPSDs) of the turbulent phase: considering a general framework with two different apertures each looking at a different object, the spatiotemporal correlation between the two observed wavefronts has been computed. Analytical expressions have been derived either considering the whole (piston-filtered) phase, either assuming the

phase as decomposed into Zernike modes. The general framework allows to study different aspects of actual and future AO systems. For our case study in particular, the configuration with one aperture and two sources can help analyze the spatiotemporal statistics between the multiple beams involved in MCAO-assisted observations.

Temporal CPSDs have then been used for the estimation of the residual phase from an AO loop. The calculations have been performed first for the simpler SCAO case: the residual phase in the direction of a scientific target on axis considering an off-axis guide star has been derived and the AO control has been included. From the residual phase, estimated in the temporal domain, the temporal PSD, as well as the variance of the residuals, have been extracted. The formulation takes into account temporal and noise errors, as well as the effect of anisoplanatism on the residuals.

The work on SCAO residuals has then been extended to the MCAO case: an analytical formulation to estimate the residual phase from an MCAO loop in any direction of the scientific field of view has been carried out. In this context, temporal transfer functions to describe the MCAO control have been derived. The formulas are general and allows to analyze specific frameworks depending on the telescope aperture, the turbulence profile, the guide stars constellation, the number and conjugation heights of the deformable mirrors and the modes of distortion, both sensed and corrected. Results have been provided also considering different tomographic reconstruction algorithms.

The analytical derivation for the MCAO case has represented a basis for the analysis of tip-tilt anisoplanatism in MCAO observations. Different aspects of MCAO tip-tilt residuals have been analyzed: the dependence on the asterism of guide stars, on the position of the target with respect to the asterism, as well as on the integration time of the scientific exposure.

Thus, the impact of tip-tilt residuals on MCAO-assisted astrometric observations has been investigated: analytical expressions for the computation of differential tilt jitter in MCAO observations has been derived and an estimation of the centroiding error due to tip-tilt residuals has been provided. The results have been applied to the MORFEO case, to estimate the contribution of tip-tilt residuals within the astrometric error budget of the system. The analysis has been carried out for MAVIS as well.

All the analytical derivations have been implemented into Python codes, that have been included in the libraries of the AO group of INAF - Arcetri Astrophysical Observatory (https://github.com/ArcetriAdaptiveOptics/arte) and that are going to be available for the MORFEO project.

Finally, a proposal of observation of Jupiter's light bending by means of differential astrometry with the Single conjugated adaptive Optics Upgrade for LBT (SOUL) at the Large

Binocular Telescope has been submitted; the aim is to test the astrometric capabilities of actual AO systems for a better comprehension of potential issues with future facilities like MORFEO.

Chapter 1

General overview

The quality of astronomical observations through ground-based telescopes can be strongly affected by atmospheric turbulence. The spatial and temporal variations in the refractive index induce fluctuations of the wavefront phase that can lead to blurry images of the astronomical target. In 1953, Babcock [1] proposed an idea to compensate for the turbulence-induced wavefront distortions, giving birth to the concept of adaptive optics (AO). The basic principle foresees the measurement of the wavefront aberrations through a wavefront sensor (WFS), the compensation for these aberrations by means of a deformable mirror (DM) and a feedback control to update the shape of the DM depending on the turbulence evolution. After about 40 years, technological advances allowed to finally develop the first astronomical AO system [2], marking a new era of ground-based astronomical observations. Several flavors of AO have been developed over the years, giving the possibility to exploit the capability of bigger and bigger telescopes. The actual class of telescopes of 8-10 m is going to be joined by a new generation of 25-40 m that will increase the angular resolution of the astronomical images by a factor of ≈ 5 at the most at same wavelengths, allowing astronomers to look deeper and sharper at the Universe than ever. Among the branches of astrophysical research, astrometry represents one of the main science drivers of the future instruments. This is the case of the Multi-AO Imaging CamerA for Deep Observations (MICADO) [3] at the Extremely Large Telescope (ELT) [4] that will be equipped with the Multi-conjugate adaptive Optics Relay For ELT Observations (MORFEO, formerly known as MAORY) [5].

In this chapter, we introduce the basic principles of AO and of astrometric observations from ground-based telescopes equipped with AO systems: in Section 1.1, we review the theory of statistics of turbulence-induced wavefront distortions; in Section 1.2, we summarize the basics of AO; in Section 1.3, we introduce the concept of multiconjugate adaptive optics and we briefly describe MORFEO system; and in Section 1.4, we introduce

the main sources of astrometric error in ground-based observations, focusing on the effects of tip-tilt residuals from AO correction.

1.1 Statistics of turbulence-induced aberrations

The modeling of optical turbulence represents an important step within the design of an AO system. In the following, referring to [6–8], we will summarize the main elements for a statistical description of turbulence and we will introduce the parameters that are commonly used to characterize it.

1.1.1 Wavefront distortions

The optical effects of atmospheric turbulence are due to local temperature variations that produce fluctuations in the air refractive index. These fluctuations are responsible for the distortions induced on a flat wavefront passing through the Earth's atmosphere.

To model the behavior of wavefront aberrations, we start from a statistical description of the air refractive index fluctuations, by means of the difference between its value $n(\boldsymbol{r})$ at a point $\boldsymbol{r}$ and its value $n(\boldsymbol{r} + \boldsymbol{\rho})$ at a point with distance $\rho = |\boldsymbol{\rho}|$. We introduce, from Tatarski [6], the variance of the difference between the two values

$$D_n(\rho) = \left\langle |n(\boldsymbol{r}) - n(\boldsymbol{r} + \boldsymbol{\rho})|^2 \right\rangle = C_n^2 \rho^{2/3}, \tag{1.1}$$

where $D_n(\rho)$ is called the index structure function and $\langle \rangle$ represents an ensemble average. C_n^2 is called the index structure coefficient and gives a measure of the local amount of inhomogeneities, showing a dependence on the atmospheric altitude (Fig. 1.1). To a first approximation, the process is homogeneous (it depends only on the separation ρ but not on the position $\boldsymbol{r}$) and isotropic (it depends on the modulus of the vector $\boldsymbol{\rho}$).

Let us now consider a monochromatic plane wave propagating through the atmosphere. The wavefront phase at position $\boldsymbol{r}$ on a surface that is perpendicular to the propagation direction z can be described by the following expression:

$$\varphi(\boldsymbol{r}) = k \int n(\boldsymbol{r}, z)\mathrm{d}z, \tag{1.2}$$

where k is the wave number ($k = 2\pi/\lambda$, with λ the wavelength). However, we are not interested in an absolute value of the wavefront phase, but rather in the difference of it between a point $\boldsymbol{x}$ on a telescope entrance aperture and a nearby point a distance $\xi = |\boldsymbol{\xi}|$ apart. The variance of the difference is called the structure function of the phase and it
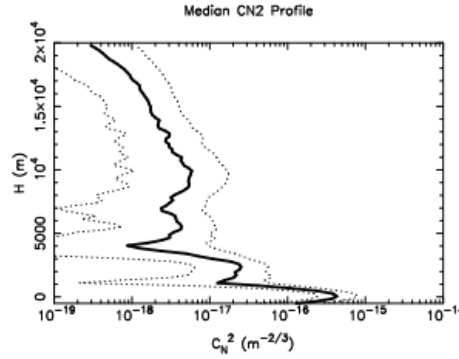
Fig. 1.1 Example of median C_n^2 profile from Masciadri *et al.* [9]. Its behavior with the atmospheric altitude is plotted, showing a major strength of the turbulence at the ground layer.

can be demonstrated that is given by

$$D_\varphi(\xi) = \left\langle |\varphi(\boldsymbol{x}) - \varphi(\boldsymbol{x} + \boldsymbol{\xi})|^2 \right\rangle \approx 2.91 k^2 \int C_n^2(z) \mathrm{d}z \, \xi^{5/3} . \tag{1.3}$$

As the atmosphere is generally considered to be stratified in plane parallel layers, C_n^2 depends only on the height h above the ground and Eq. (1.3) can be rewritten as

$$D_\varphi(\xi) \approx 2.91 k^2 (\cos\gamma)^{-1} \int C_n^2(h) \mathrm{d}h \, \xi^{5/3} , \tag{1.4}$$

where γ is the angular distance of the source from zenith and the quantity $(\cos\gamma)^{-1}$ is called the air mass. The structure function of the phase can also be described through the Fried parameter r_0:

$$D_\varphi(\xi) \approx 6.88 \, (\xi/r_0)^{5/3} , \tag{1.5}$$

where

$$r_0 \approx \left[0.423 k^2 (\cos\gamma)^{-1} \int C_n^2(h) \mathrm{d}h \right]^{-3/5} . \tag{1.6}$$

The Fried parameter defines a typical coherence length of the wavefront. Larger the wavelength, larger r_0 ($r_0 \propto \lambda^{6/5}$); smaller the air mass, larger r_0 ($r_0 \propto \cos\gamma^{3/5}$). From r_0, a definition of seeing can be found as

$$\epsilon \approx \frac{\lambda}{r_0} , \tag{1.7}$$

that leads to the dependence on the wavelength as $\epsilon \propto \lambda^{-1/5}$ and on the air mass as $\epsilon \propto \cos\gamma^{-3/5}$. A seeing of 1" corresponds to $r_0 \approx 10$ cm in V band ($\lambda = 0.5 \, \mu$m).

Two other parameters used to characterize turbulence, that are related to r_0, are the isoplanatic angle θ_0

$$\theta_0 \approx 0.057\,\lambda^{6/5}\,\cos\gamma^{8/5}\left(\int_0^\infty h^{5/3}\,C_n^2(h)\,\mathrm{d}h\right)^{-3/5},\qquad(1.8)$$

that represents the angular equivalent of r_0, and the coherence time τ_0

$$\tau_0 \approx 0.057\,\lambda^{6/5}\,\cos\gamma^{3/5}\left(\int_0^\infty |v(h)|^{5/3}\,C_n^2(h)\,\mathrm{d}h\right)^{-3/5},\qquad(1.9)$$

that quantifies temporal correlation of turbulence-induced wavefront phase distortions, where $v(h)$ is the wind speed at height h. Equation (1.9) can also be written as

$$\tau_0 \approx 0.31\frac{r_0}{v_m},\qquad(1.10)$$

with v_m the mean wind speed defined as

$$v_m = \left[\frac{\int C_n^2(h)\,v(h)^{5/3}\mathrm{d}h}{\int C_n^2(h)\mathrm{d}h}\right]^{3/5}.\qquad(1.11)$$

It is worth noting that the parameter r_0 weights equally the turbulence at all heights in the atmosphere, while θ_0 and τ_0 take into account the variations of turbulence and wind speed with height as well.

Typical values are few arcseconds for θ_0 and few milliseconds for τ_0 in V band.

The mechanical structure of turbulence was investigated by Kolmogorov [10], whose model assumes that energy is added to the system in the form of large-scale disturbances, the outer scale, which then break down into smaller and smaller structures at which the turbulent motion is finally dissipated by the viscosity of air. Kolmogorov theory predicted a power spectral density (PSD) of the air refractive index fluctuations and derived the following expression:

$$\Phi_n(\kappa) \approx 0.033 C_n^2 \kappa^{-11/3},\qquad(1.12)$$

where Φ_n is the PSD of air refractive index fluctuations, κ is the spatial wavenumber defined as $\kappa = 2\pi/l$, with l the scale size of turbulence. This spectrum holds within the inertial range, that is, for $l_0 < l < L_0$, with L_0 the outer scale and l_0 the inner scale of turbulence. For $l < l_0$ ($\kappa > \kappa_m$, with $\kappa_m = 2\pi/l_0$), the dissipation of energy due to viscous forces results in a rapid drop in $\Phi_n(\kappa)$ that was included by Tatarski [6] in the following

expression:

$$\Phi_n(\kappa) \approx 0.033 C_n^2 \kappa^{-11/3} e^{-\kappa^2/\kappa_m^2}, \tag{1.13}$$

where $\kappa_m = 2\pi/l_0$. Equations (1.12)-(1.13) can not be used to model the spectrum of the index of refraction fluctuations for $\kappa \to 0$ because of the non-integrable pole at $\kappa = 0$. To overcome this problem, an alternate form known as the Von Karman spectrum is often used:

$$\Phi_n(\kappa) \approx \frac{0.033 C_n^2}{(\kappa^2 + \kappa_0^2)^{11/6}} e^{-\kappa^2/\kappa_m^2}, \tag{1.14}$$

where $\kappa_0 = 2\pi/L_0$. In Fig. 1.2, both Kolmogorov and Von Karman PSD are shown.
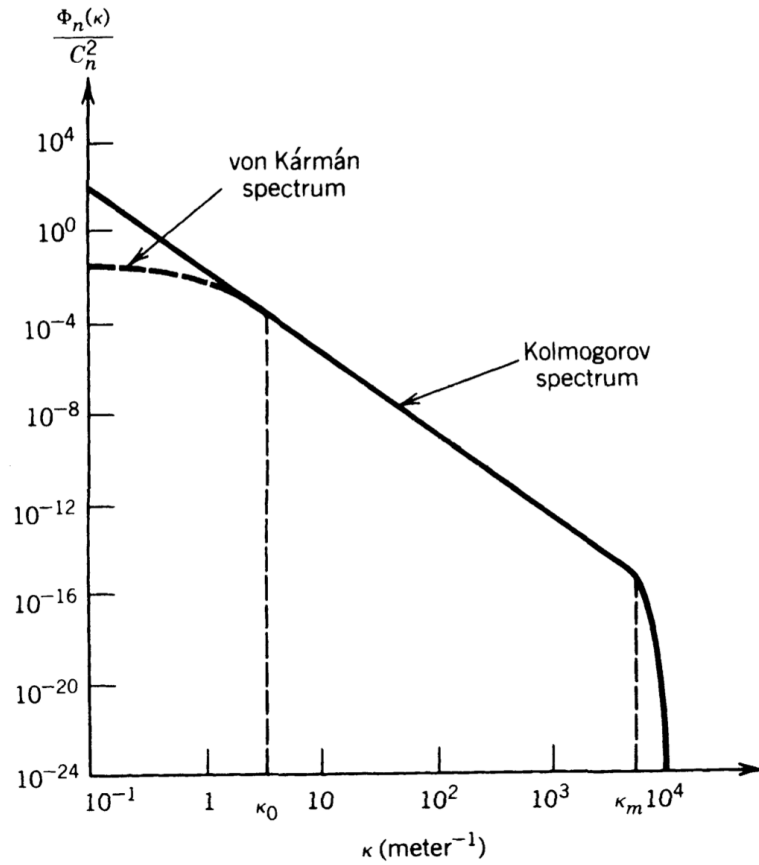
Fig. 1.2 PSD of the air refractive index fluctuations from Goodman [11]. Both Kolmogorov (solid line) and Von Karman (dashed line) spectra are shown.

Through proper conversion factors, from Eq. (1.12) an expression of the PSD of wavefront phase distortions under Kolmogorov model can be derived:

$$\Phi_\phi(f) \approx 0.00969 \left(\frac{2\pi}{\lambda}\right)^2 C_n^2 f^{-11/3}, \tag{1.15}$$

where the spatial frequency $f = \kappa/2\pi$ has been considered. The equation can be modified to derive the PSD of wavefront phase distortions under Von Karman model as well:

$$\Phi_\phi(f) \approx 0.00969 \left(\frac{2\pi}{\lambda}\right)^2 C_n^2 (f^2 + f_0^2)^{-11/6}, \tag{1.16}$$

where $f_0 = \kappa_0/2\pi$.

1.1.2 Modal expansion of wavefront distortions through Zernike polynomials

Wavefront turbulence-induced distortions are usually modeled through their expansion in a series of orthogonal functions. Zernike polynomials are commonly used to describe the wavefront aberrations on a telescope pupil, as they represent an orthogonal basis on a circular aperture, which is the most common aperture shape in optical systems. For a circular aperture without obstruction, using polar coordinates (r, θ), the Zernike modes are defined by

$$Z_j = \begin{cases} \sqrt{n+1}\, R_n^m(r)\, \sqrt{2}\, \cos(m\theta), & \text{even } j,\, m \neq 0 \\ \sqrt{n+1}\, R_n^m(r)\, \sqrt{2}\, \sin(m\theta), & \text{odd } j,\, m \neq 0 \\ \sqrt{n+1}\, R_n^0(r), & m = 0, \end{cases} \tag{1.17}$$

where we referred to the notation in Noll's paper [12]. The radial part $R_n^m(r)$ is given by

$$R_n^m(r) = \sum_{s=0}^{(n-m)/2} \frac{(-1)^s (n-s)!}{s![(n+m)/2 - s]![(n-m)/2 - s]!}\, r^{n-2s}. \tag{1.18}$$

Each Zernike polynomial is characterized by three indices: j is a mode ordering number and is a function of n and m, that are the radial and azimuthal degree, respectively. The values of n and m are always integral and satisfy the relationships $m \leq n$, $n - |m| = $ even. In Fig. 1.3, Noll's ordering of Zernike modes is shown.

The definition in Eq. (1.17) allows to write the modal orthogonality relation:

$$\int_0^1 \int_0^{2\pi} W(r)\, Z_j(r,\theta)\, Z_{j'}(r,\theta)\, r \mathrm{d}r \mathrm{d}\theta = \delta_{jj'}, \tag{1.19}$$

where $W(r)$ is a weight function defined as

$$W(r) = \begin{cases} 1/\pi, & r \leq 1 \\ 0, & r > 1. \end{cases} \tag{1.20}$$

n	$m \rightarrow$ 0	1	2	3	4
0	$Z_1 = 1$ Piston				
1		$Z_2 = 2r\cos\theta$ $Z_3 = 2r\sin\theta$ Tip/tilt			
2	$Z_4 = \sqrt{3}(2r^2 - 1)$ Defocus		$Z_5 = \sqrt{6}r^2\sin 2\theta$ $Z_6 = \sqrt{6}r^2\cos 2\theta$ Astigmatism (3rd order)		
3		$Z_7 = \sqrt{8}(3r^3 - 2r)\sin\theta$ $Z_8 = \sqrt{8}(3r^3 - 2r)\cos\theta$ Coma		$Z_9 = \sqrt{8}r^3\sin 3\theta$ $Z_{10} = \sqrt{8}r^3\cos 3\theta$ Trefoil	
4	$Z_{11} = \sqrt{5}(6r^4 - 6r^2 + 1)$ Spherical		$Z_{12} = \sqrt{10}(10r^4 - 3r^2)\cos 2\theta$ $Z_{13} = \sqrt{10}(10r^4 - 3r^2)\sin 2\theta$ Astigmatism (5th order)		$Z_{14} = \sqrt{10}r^4\cos 4\theta$ $Z_{15} = \sqrt{10}r^4\sin 4\theta$ Ashtray

Fig. 1.3 Noll's ordering of Zernike polynomials: even j corresponds to the symmetric modes defined by $\cos(m\theta)$, while odd j corresponds to the antisymmetric modes given by $\sin(m\theta)$. For a given n, modes with a lower value of m are ordered first.

The Fourier transform of Zernike polynomials can be defined as well. Given $Q_j(f, \phi)$ the Fourier transform of $Z_j(r, \theta)$ so that

$$W(r)Z_j(r, \theta) = \int d\boldsymbol{f}\, Q_j(f, \phi)e^{-2\pi i \boldsymbol{f}\cdot\boldsymbol{r}}, \tag{1.21}$$

the transform can be written from Eq. (1.17) as

$$Q_j(f, \phi) = \sqrt{n+1}\frac{J_{n+1}(2\pi f)}{\pi f}\begin{cases} (-1)^{(n-m)/2}i^m\sqrt{2}\cos(m\theta), & \text{even } j,\, m \neq 0 \\ (-1)^{(n-m)/2}i^m\sqrt{2}\sin(m\theta), & \text{odd } j,\, m \neq 0 \\ (-1)^{n/2}, & m = 0, \end{cases} \tag{1.22}$$

where $J_l(x)$ is the lth order Bessel function of the first kind.

A decomposition of an arbitrary wavefront over a circular aperture of arbitrary radius R can be performed by means of Zernike polynomials. If $\phi(r, \theta)$ is some arbitrary function representing a wavefront phase, its polynomial expansion over a circle of radius R is given by

$$\phi(R\rho, \theta) = \sum_j a_j Z_j(\rho, \theta), \tag{1.23}$$

with $\rho = r/R$ and where the expansion coefficients a_j are defined as

$$a_j = \int d\boldsymbol{\rho}\, W(\rho)\, \phi(R\rho, \theta)\, Z_j(\rho, \theta). \tag{1.24}$$

Since we are dealing with random wavefront aberrations, we are interested in their statistical properties. The covariance of Zernike coefficients can be computed as

$$\left\langle a_j^* a_{j'} \right\rangle = \int \mathrm{d}\boldsymbol{\rho} \int \mathrm{d}\boldsymbol{\rho}' W(\rho) W(\rho') Z_j(\rho,\theta) Z_{j'}(\rho',\theta') \left\langle \phi(R\rho)\phi(R\rho') \right\rangle, \tag{1.25}$$

where the coefficients a_j have been considered to be Gaussian random variables with zero mean. Equation (1.25) can be written in Fourier space as

$$\left\langle a_j^* a_{j'} \right\rangle = \frac{1}{R^2} \int \int \mathrm{d}\boldsymbol{f} \mathrm{d}\boldsymbol{f}' Q_j^*(f) \Phi(f/R, f'/R) Q_{j'}(f') \delta(f - f'), \tag{1.26}$$

where $\Phi(f)$ is derived from Eq. (1.15). Substituting Eq. (1.22) into Eq. (1.26), after some calculations, the covariance of Zernike coefficients on a pupil of diameter D can be written as

$$\left\langle a_j^* a_{j'} \right\rangle = c_{jj'} \left(\frac{D}{r_0}\right)^{5/3}, \tag{1.27}$$

where the analytic expression for the coefficients $c_{jj'}$ was derived by Noll [12] as

$$c_{jj'} \approx \frac{0.046}{2^{5/3}\pi} \sqrt{(n+1)(n'+1)} (-1)^{(n+n'-2n)/2} \delta_{mm'} \int \mathrm{d}f f^{-8/3} \frac{J_{n+1}(2\pi k) J_{n'+1}(2\pi k)}{k^2}, \tag{1.28}$$

where the integral is tabulated:

$$\int \mathrm{d}f f^{-8/3} \frac{J_{n+1}(2\pi k) J_{n'+1}(2\pi k)}{k^2}$$
$$= \frac{\Gamma(14/3)\Gamma[(n+n'-14/3+3)/2]}{2^{14/3}\Gamma[(-n+n'+14/3+1)/2]\Gamma[(n-n'+14/3+1)/2]\Gamma[(n+n'+14/3+3)/2]}, \tag{1.29}$$

for $n, n' \neq 0$, where $\Gamma(x)$ is Euler's Gamma function. For $n = n' = 0$, the integral diverges, showing that the variance of the piston terms is infinite (under the assumption of an infinite outer scale). From Eq. (1.27) and Eq. (1.28), it is shown that only Zernike terms with the same azimuthal degree are correlated. In Fig. 1.4, the variance of Zernike coefficients as a function of the Zernike index j is shown. It is worth noting that low-order modes contribute for most of the error and, in particular, global tilt accounts for 87% of the variance.

From the variance of Zernike coefficients the mean square wavefront phase fluctuation can be derived as

$$\sigma^2 = \left\langle \int W(r)\phi^2(r,\theta)\mathrm{d}\boldsymbol{r} \right\rangle = \sum_{j=2} \left\langle a_j^2 \right\rangle, \tag{1.30}$$

where the sum does not take into account the piston term since we are interested in the deviation from the mean surface; moreover, considering the piston term would give an
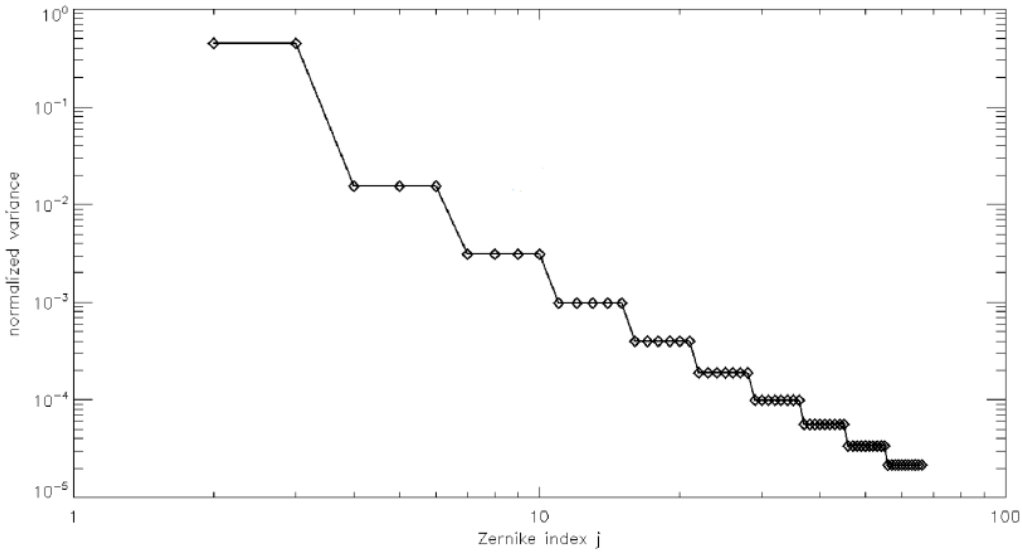
Fig. 1.4 Variance of Zernike coefficients as a function of the index j, assuming Kolmogorov model of wavefront phase distortions. The variance is normalized to $(D/r_0)^{5/3}$.

infinite value. If we consider a system compensating for the first J modes, the corrected phase can be written as

$$\phi_C = \sum_{j=1}^{J} a_j Z_j \tag{1.31}$$

and the mean square residual error becomes

$$\Delta_J = \int \mathrm{d}\rho\, W(\rho) \left\langle \left[\phi(R\rho) - \phi_C(R\rho)\right]^2 \right\rangle = \left\langle \phi^2 \right\rangle - \sum_{j=1}^{J} \left\langle |a_j|^2 \right\rangle = \sum_{j=J+1} \left\langle a_j^2 \right\rangle. \tag{1.32}$$

where $\langle a_j \rangle = 0$ was considered. In Fig. 1.5, a table with the values of the mean square residual error for the first 21 modes is shown.

1.1.3 Temporal spectrum of wavefront aberrations

A complete characterization of turbulence-induced wavefront distortions has to consider the temporal evolution of atmospheric turbulence. For the derivation of temporal power spectra of wavefront distortions, we refer to the work of Conan [13], who determined the temporal PSD of phase-related quantities (e.g. Zernike coefficients).

The case of a plane wave and a single turbulent layer following Kolmogorov's model is considered. To derive the basic equations to compute the PSD of a phase-related quantity $G(\boldsymbol{r}, t)$, with $\boldsymbol{r}$ the spatial coordinate vector (x, y) and t the time, we start from

$$\Delta_1 = 1.0299 \ (D/r_0)^{5/3} \qquad\qquad \Delta_{12} = 0.0352 \ (D/r_0)^{5/3}$$

$$\Delta_2 = 0.582 \ (D/r_0)^{5/3} \qquad\qquad \Delta_{13} = 0.0328 \ (D/r_0)^{5/3}$$

$$\Delta_3 = 0.134 \ (D/r_0)^{5/3} \qquad\qquad \Delta_{14} = 0.0304 \ (D/r_0)^{5/3}$$

$$\Delta_4 = 0.111 \ (D/r_0)^{5/3} \qquad\qquad \Delta_{15} = 0.0279 \ (D/r_0)^{5/3}$$

$$\Delta_5 = 0.0880 \ (D/r_0)^{5/3} \qquad\qquad \Delta_{16} = 0.0267 \ (D/r_0)^{5/3}$$

$$\Delta_6 = 0.0648 \ (D/r_0)^{5/3} \qquad\qquad \Delta_{17} = 0.0255 \ (D/r_0)^{5/3}$$

$$\Delta_7 = 0.0587 \ (D/r_0)^{5/3} \qquad\qquad \Delta_{18} = 0.0243 \ (D/r_0)^{5/3}$$

$$\Delta_8 = 0.0525 \ (D/r_0)^{5/3} \qquad\qquad \Delta_{19} = 0.0232 \ (D/r_0)^{5/3}$$

$$\Delta_9 = 0.0463 \ (D/r_0)^{5/3} \qquad\qquad \Delta_{20} = 0.0220 \ (D/r_0)^{5/3}$$

$$\Delta_{10} = 0.0401 \ (D/r_0)^{5/3} \qquad\qquad \Delta_{21} = 0.0208 \ (D/r_0)^{5/3}$$

$$\Delta_{11} = 0.0377 \ (D/r_0)^{5/3}$$

$$\Delta_J \sim 0.2944 \, J^{-\sqrt{3}/2} \ (D/r_0)^{5/3} \quad \text{(For large } J\text{)}$$

Fig. 1.5 Mean square residual error when J modes ($J = 1, ..., 21$) are corrected. From Noll [12].

the expression for its spatial covariance

$$B_G(\boldsymbol{\rho}) = \left\langle G(\boldsymbol{r}, t) G(\boldsymbol{r} + \boldsymbol{\rho}, t) \right\rangle, \tag{1.33}$$

that leads, by means of Parseval's theorem, to its spatial power spectrum W_G

$$W_G(\boldsymbol{f}) = \int B_G(\boldsymbol{\rho}) e^{2i\pi \boldsymbol{f} \cdot \boldsymbol{\rho}} \mathrm{d}\boldsymbol{\rho}, \tag{1.34}$$

where $\boldsymbol{f}$ is the spatial frequency vector (f_x, f_y). If we consider that a phase-related quantity can be expressed as the convolution of the phase ϕ with a spatial function $M_G(\boldsymbol{r})$

$$G(\boldsymbol{r}, t) = \int M_G(\boldsymbol{r} - \boldsymbol{\rho}) \phi(\boldsymbol{\rho}, t) \mathrm{d}\boldsymbol{\rho} = M_G(\boldsymbol{\rho}) * \phi(\boldsymbol{r}, t), \tag{1.35}$$

the spatial power spectrum W_G can be derived as

$$W_G(\boldsymbol{f}) = |\tilde{M}_G(\boldsymbol{f})|^2 W_\phi(\boldsymbol{f}), \tag{1.36}$$

where $\tilde{M}_G(\boldsymbol{f})$ is the Fourier transform of M_G and $W_\phi(\boldsymbol{f})$ is the spatial power spectrum of wavefront phase distortions given by Eq. (1.15). The spatial PSD $W_G(\boldsymbol{f})$ can be related to the one-dimensional temporal PSD $w_G(v)$, where v is the temporal frequency:

$$w_G(v) = \frac{1}{v} \int_{-\infty}^{+\infty} W_G\left(\frac{v}{v}, f_y\right) \mathrm{d}f_y, \tag{1.37}$$

where a wind v along the x axis has been considered and the Taylor's frozen flow hypothesis, stating that the whole phase screen is translated at the wind velocity $\boldsymbol{v}$ without changing shape, has been assumed. By substituting Eq. (1.36) into Eq. (1.37), the temporal PSD becomes

$$
\begin{aligned}
w_G(v) &= \frac{1}{v} \int_{-\infty}^{+\infty} \left| \tilde{M}_G \left(\frac{v}{v}, f_y \right) \right|^2 W_\phi \left(\frac{v}{v}, f_y \right) \mathrm{d}f_y \\
&= 0.00969 \left(\frac{2\pi}{\lambda} \right)^2 \frac{C_n^2 dh}{v} \int_{-\infty}^{+\infty} \left| \tilde{M}_G \left(\frac{v}{v}, f_y \right) \right|^2 \left[\left(\frac{v}{v} \right)^2 + f_y^2 \right]^{-11/6} \mathrm{d}f_y ,
\end{aligned}
\tag{1.38}
$$

where we replaced W_ϕ with its expression in Eq. (1.15). As applications, we summarize the results on the temporal PSD of the wavefront phase and of the Zernike modes as well.

Wavefront phase

The function G is in this case the direct measure of the phase:

$$
G(\boldsymbol{r}) = \phi(\boldsymbol{r}) .
\tag{1.39}
$$

Then, from the integration of Eq. (1.38), the temporal phase PSD can be obtained as

$$
w_\phi(v) \propto C_n^2 \frac{\mathrm{d}h}{v} \left(\frac{v}{v} \right)^{-8/3} ,
\tag{1.40}
$$

where a -8/3 power law has been found for the dependence on temporal frequency.

Zernike modes

To derive the temporal PSD of Zernike modes, we have to consider

$$
G(\boldsymbol{r}) = Z_j(\boldsymbol{r}) * \phi(\boldsymbol{r}, t) .
\tag{1.41}
$$

$\tilde{M}_G$ is in this case the Fourier transform of the Zernike polynomial, as defined in Eq. (1.22). Through proper substitutions, we can retrieve the expression of the temporal PSD of Zernike modes that was given in Roddier *et al.* [14]:

$$
w_\phi(v) \propto \frac{1}{v} \int \mathrm{d}f_y (v^2 v^2 + f_y^2)^{-17/6} \left| J_{n+1} \left[2\pi \left(\frac{v^2}{v^2} + f_y^2 \right)^{1/2} \right] \right|^2 \times
\begin{cases}
\cos^2(m\theta), & \text{even } j, \, m \neq 0 \\
\sin^2(m\theta), & \text{odd } j, \, m \neq 0 \\
1, & m = 0 .
\end{cases}
\tag{1.42}
$$

Interesting properties of Zernike temporal PSD are:

- the spectra are characterized by a cutoff frequency that depends on the radial
  degree of the polynomial and on the ratio between the wind speed and the aperture
  diameter

$$\nu_c \approx 0.3(n+1)\frac{v}{D}\,; \tag{1.43}$$

- at high temporal frequencies, all the spectra follow a $v^{-17/3}$ law;

- the behavior at low frequencies depends on the Zernike polynomial: both tip and
  tilt follow a $v^{-2/3}$ law, radially symmetric polynomials follow v^0, the seventh and
  eighth mode (two comas) follow a v^0 and v^2 law respectively. The other modes have
  a 0, 4/3 and 2 power laws;

- radially symmetric polynomial spectra do not depend on the wind direction. For
  other polynomials, the behavior at low frequencies is affected by wind changes.

In Fig. 1.6, the behavior of the temporal spectrum of Zernike modes with $n = 1, 3, 9$ is
shown.
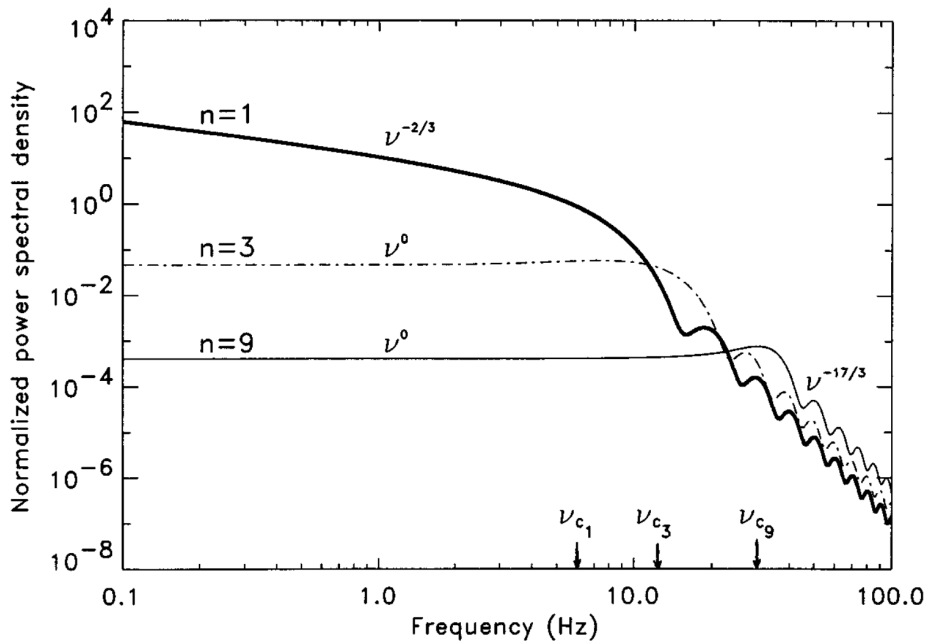
Fig. 1.6 Mean temporal power spectrum of Zernike polynomials with $n = 1, 3, 9$, from Conan *et al.*
[13]. The ratio v/D is 10 Hz. The power laws and the cutoff frequencies are indicated.

1.2   Principles of adaptive optics

A simplified scheme of the functioning of an AO system is shown in Fig. 1.7. The basic principle foresees the measurements of the turbulence-induced wavefront distortions by a WFS, the analysis of the signals from the WFS by a real-time computer (RTC) which calculates an appropriate correction and sends the commands to a DM that properly changes its shape in order to flatten the wavefront. This feedback loop typically works at ~ 1 kHz, in order to follow the temporal evolution of turbulence-induced aberrations that is represented by τ_0. The reference target, whose wavefront is analyzed by the WFS, must be
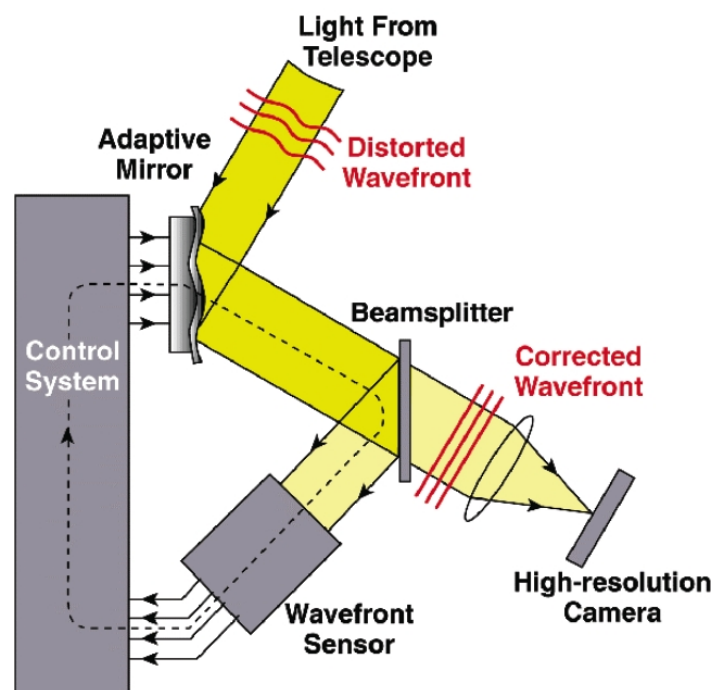
Fig. 1.7 Simplified working scheme of AO. The light incoming to the telescope is sent to the DM that reflects it to a beamsplitter. The flux is then split between the WFS and the scientific camera. The WFS measures the wavefront aberrations from a reference source and the RTC analyzes the signals, computes the correction and sends the commands to the DM. The DM changes its shape in order to flatten the wavefront that is again observed by the scientific camera as a diffraction-limited image.

a bright and point-like source in order to minimize the error on the WFS measurements. In many cases, such a natural guide star (NGS) is not available near the astronomical object and the use of a laser guide star (LGS) is foreseen, that is, an artificial guide star produced by scattering of laser radiation by atmospheric particles. LGSs can be generated through resonance scattering by atmospheric sodium that involves the use of a laser at 589 nm to excite atoms in the atmospheric sodium layer at ~ 90 km, or through Rayleigh scattering

from air molecules sending light back to the telescope from altitudes up to ~ 15 km. A strong limitation of LGSs is tilt indetermination, though: LGSs are not able to provide a useful signal for tilt correction, since the upward wandering of the laser beam is generally unknown [15]. In the simple case of using the same telescope to project and sense the laser beacon, the light encounters the same tilt in upward and downward directions and the LGS will appear motionless. Then, tip-tilt measurement still requires the use of NGS but, in this case, fainter magnitudes are allowed.

1.2.1   Wavefront sensors

The objective of a WFS is to measure wavefront aberrations. The basic functioning foresees the conversion of either the phase or, most commonly, the spatial derivative of the phase into an intensity variation that can be sensed by a detector. Without entering into detail, as it is beyond the interest of this work, we will briefly review the most used WFSs in actual AO systems: Shack-Hartmann (SH) [16] and Pyramid WFSs [17, 18].

Shack-Hartmann WFS

The principle of the SH WFS is to use an array of lenslets placed in a conjugate pupil plane in order to sample the incoming wavefront. If the wavefront is flat, each lenslet forms an image of the source at its focus; if the wavefront is aberrated, each lenslet receives a tilted wavefront and forms an off-axis image in its focal plane (Fig. 1.8). The angle of arrival of the wavefront over each lenslet can then be estimated from the measurement of the position of the image formed by the lenslet. A common technique to measure the positions of the SH images is to use a 2×2 detector (quad-cell) for each subaperture. Referring to Fig. 1.9, each quad-cell measures a signal

$$
\begin{aligned}
S_x &= \frac{I_2 + I_4 - I_1 + I_3}{\sum_i I_i} \\
S_y &= \frac{I_1 + I_2 - I_3 + I_4}{\sum_i I_i},
\end{aligned}
\tag{1.44}
$$

where I_i is the intensity on the ith pixel. It can be demonstrated that the signals depend on the spatial derivative of the wavefront along x and y according to the relation

$$
\begin{aligned}
S_x &= \frac{2}{\theta} \frac{\partial W}{\partial x} \\
S_y &= \frac{2}{\theta} \frac{\partial W}{\partial y},
\end{aligned}
\tag{1.45}
$$
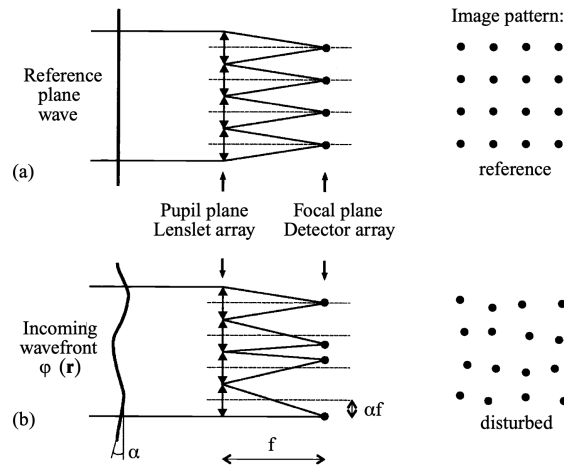
Fig. 1.8 Basic scheme of the SH WFS. If the wavefront is flat, each lenslet forms an image of the source in its focal plane along the lens axis (top); if the wavefront is locally tilted by an angle α, the lenslet forms an image of the source at a distance αf from the focus, with f the focal length (bottom).

where θ is the size of the spot on the quad-cell.
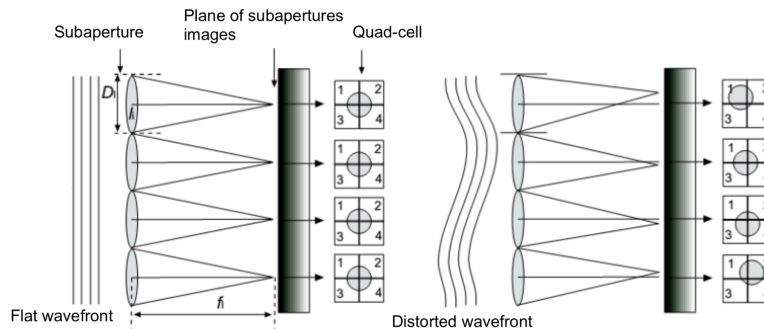
Fig. 1.9 Scheme of a SH WFS with a quad-cell detector.

Pyramid WFS

The Pyramid WFS uses a pyramidal prism placed in the image plane to create four sub-beams that are then optically related to a detector (Fig. 1.10). If the wavefront is flat, the beam is split into four identical images of the pupil; if the wavefront is distorted, the beam is split into four images of the pupil with different flux. Any point of the pupil is imaged on each of the four pupil images, so on four pixels of the detector. It can be demonstrated that a signal proportional to the wavefront gradient is obtained if combining the intensity of the four pixels in the same way as for quad-cell detectors.

Since the mentioned functioning provides information about the sign of the wavefront inclination only, the Pyramid WFS usually uses the *tilt modulation*: a flat oscillating mirror is positioned in a pupil-conjugated plane in order to steer the image in the focal plane and to let the image perform a circular trajectory centered around the pyramid vertex with a period equal to the detector integration time. It can be demonstrated that the measured signal, whose computation takes the same form as Eq. (1.44), provides information about the local inclination of the wavefront through the following expressions:

$$
\begin{aligned}
S_x &= \frac{2}{\pi}\left[\operatorname{asin}\left(\frac{2}{\theta_M}\frac{\partial W}{\partial x}\right)\right] \\
S_y &= \frac{2}{\pi}\left[\operatorname{asin}\left(\frac{2}{\theta_M}\frac{\partial W}{\partial y}\right)\right],
\end{aligned}
\tag{1.46}
$$

with θ_M the modulation angle.
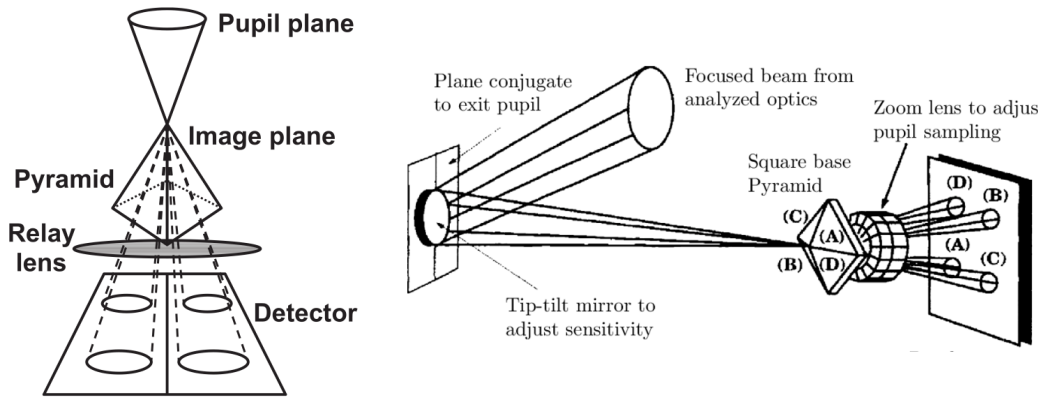
Fig. 1.10 Basic scheme of the Pyramid WFS (left). A scheme with the tilt modulation is also shown (right; from Esposito *et al.* [18]).

1.2.2   Deformable mirrors

The objective of DMs is to compensate for the wavefront aberrations introduced by atmospheric turbulence. They usually consist of an array of actuators that are connected to a thin optical surface that deforms under the expansion of the actuators. General requirements for a DM concern spacing, stroke, response time and number of actuators. Spacing, as projected onto the telescope aperture, and response time should agree with the requirements set by r_0 and τ_0, whereas stroke and number of actuators depend on aperture diameter. Without entering into detail, some of the most common technologies are, for instance, piezo-stack DMs, voice-coil actuator DMs, MEMS [19].

1.2.3   Feedback control loop

An AO system can be defined as a servo-loop system with the goal of compensating for the incoming wavefront distorted by atmospheric turbulence. In its basic configuration, it is made of a sensor, the WFS, a control device, the RTC, and a corrector, the DM. The input and output of such a control loop are, respectively, the distorted wavefront phase and the residual phase after compensation. The aim is the minimization of the residual phase.

The temporal behavior of an AO control loop is typically described by means of a temporal transfer function representation [20]. Figure 1.11 gives a schematic view of an AO control loop through a block diagram representation: ϕ_{turb} is the input turbulent phase, ϕ_a is the compensating phase actuated by the DM, which is based on the correction phase ϕ_{corr} that is computed from the residual phase ϕ_{res}. The phase is here intended as the $\mathscr{L}$- or Z-transform of the phase defined in the time domain, depending on whether a continuous or discrete domain is considered.
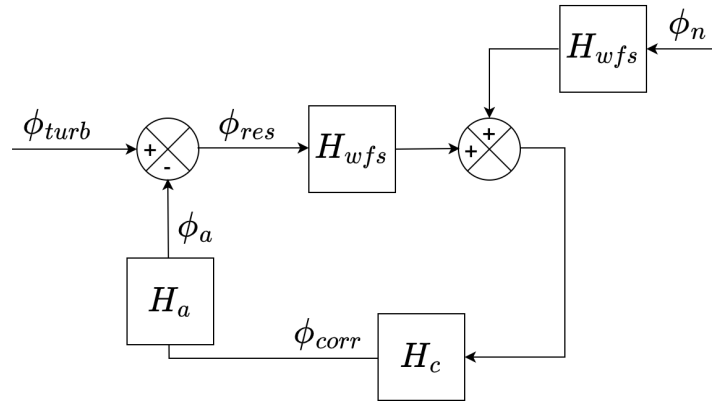
Fig. 1.11 Block diagram representation of a basic AO control loop.

Basic expressions describing the above quantities are:

$$\phi_{res}(v) = \phi_{turb}(v) - \phi_a(v) \tag{1.47}$$

$$\phi_a(v) = H_{wfs}(v)\big(\phi_{res}(v) + \phi_n(v)\big)H_c(v)H_a(v)\,, \tag{1.48}$$

where the noise ϕ_n is assumed to be injected in the loop at the level of the WFS integration only (i.e. photon noise is considered). v is the temporal frequency and H_x is the temporal transfer function of the block x, where $x = wfs$ represents the WFS, $x = c$ the control by the RTC and $x = a$ the actuation by the DM. Assuming the linearity of the system, its open-loop transfer function (OLTF) can be computed from the product of all the temporal

transfer functions just defined:

$$H_{ol}(\nu) = H_{wfs}(\nu)H_c(\nu)H_a(\nu).\tag{1.49}$$

An explicit expression of the OLTF can be derived, in the case of a simple pure integrator, as [20]

$$H_{ol}(s) = \frac{1 - e^{-sT}}{sT}e^{-sT_d}\frac{g}{sT},\tag{1.50}$$

where $s = 2\pi i\nu$ is the Laplace variable, g is the integrator gain, T is the WFS integration time that defines the frequency frame rate of the loop ($\nu_{loop} = 1/T$), T_d is a delay (e.g. readout time) and where the transfer functions have been defined as $H_{wfs}(\nu) = (1 - e^{-sT})/sT$, $H_c(\nu) = e^{-sT_d}g/sT$ and $H_a(\nu) = 1$.

Both the rejection transfer function (RTF) and noise transfer function (NTF) of the loop can be derived by combining Eqs. (1.47), (1.48) and (1.49):

$$\begin{aligned}
\phi_{res}(\nu) &= \phi_{turb}(\nu) - \phi_a(\nu)\\
&= \phi_{turb}(\nu) - H_{wfs}(\nu)\big(\phi_{res}(\nu) + \phi_n(\nu)\big)H_c(\nu)H_a(\nu)\\
&= \phi_{turb}(\nu) - H_{ol}(\nu)\big(\phi_{res}(\nu) + \phi_n(\nu)\big),
\end{aligned}\tag{1.51}$$

and grouping the terms related to ϕ_{res}

$$\big(1 + H_{ol}(\nu)\big)\phi_{res}(\nu) = \phi_{turb}(\nu) - H_{ol}(\nu)\phi_n(\nu).\tag{1.52}$$

An alternative expression for ϕ_{res} can then be obtained

$$\begin{aligned}
\phi_{res}(\nu) &= \frac{1}{1 + H_{ol}(\nu)}\phi_{turb}(\nu) - \frac{H_{ol}(\nu)}{1 + H_{ol}(\nu)}\phi_n(\nu)\\
&= H_r(\nu)\phi_{turb}(\nu) - H_n(\nu)\phi_n(\nu),
\end{aligned}\tag{1.53}$$

that leads to the following expressions for the RTF and the NTF:

$$H_r(\nu) = \frac{1}{1 + H_{ol}(\nu)}\tag{1.54}$$

$$H_n(\nu) = \frac{H_{ol}(\nu)}{1 + H_{ol}(\nu)}.\tag{1.55}$$

The RTF is defined as the transfer function between the residual and turbulent phase and represents the ability of the AO control to compensate for phase perturbations as a function of frequency; the NTF is defined as the ratio between the residual phase due to noise propagation and the measurement noise and characterizes the effect of noise

on the residual phase. From Eq. (1.54) and Eq. (1.55), it can be seen that the following relationship between RTF and NTF holds:

$$H_r(\nu) + H_n(\nu) = 1 \,. \tag{1.56}$$

In Fig. 1.12, RTF and NTF are shown for three different values of the loop frequency.
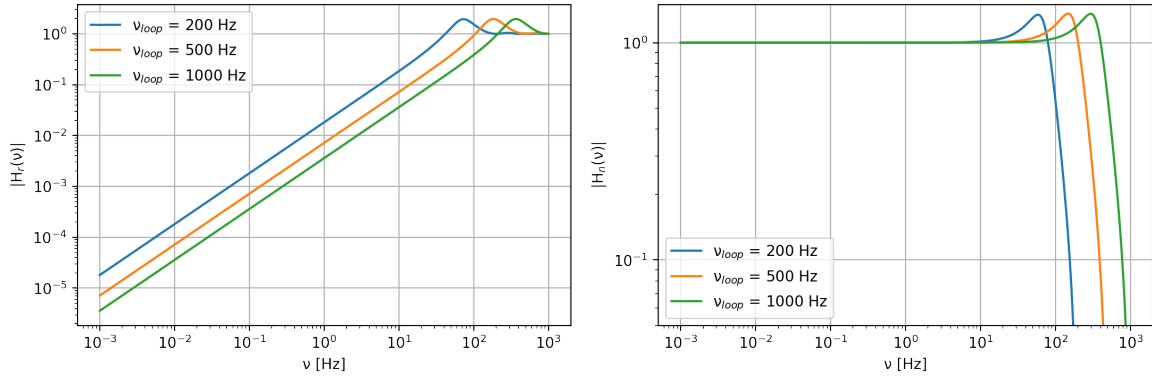
Fig. 1.12 RTF (left) and NTF (right) as a function of temporal frequencies. Three values of the loop frequency are shown, corresponding to WFS integration time of 5 ms (blue), 2 ms (orange) and 1 ms (green). Delay from the WFS integration only is considered.

From Eq. (1.53), the temporal power spectrum of the residual wavefront on the guide star can be obtained as

$$S_{res}(\nu) = |H_r(\nu)|^2 S_{turb}(\nu) + |H_n(\nu)|^2 S_n(\nu) \,, \tag{1.57}$$

where S_{turb} and S_n are temporal spectra of, respectively, turbulence and noise and where turbulence and noise are assumed to be uncorrelated.

1.2.4   Wavefront reconstruction

The reconstruction problem concerns the derivation of the commands to be applied to the DM starting from the knowledge of the wavefront slopes in two directions x, y (SH and Pyramid WFS produce, as seen in Section 1.2.1, signals proportional to the wavefront slopes). The unknown quantity, a vector $\boldsymbol{a}$ of N commands must be calculated from the data, that is, a measurement vector $\boldsymbol{s}$ of M elements of slopes. This translates into the

solution of a set of linear equations

$$
\begin{aligned}
s_1 &= a_1 D_{11} + a_2 D_{12} + ... a_N D_{1N} \\
s_2 &= a_1 D_{21} + a_2 D_{22} + ... a_N D_{2N} \\
&\vdots \\
s_M &= a_1 D_{M1} + a_2 D_{M2} + ... a_N D_{MN},
\end{aligned}
\tag{1.58}
$$

that can be written in matrix representation as

$$
\boldsymbol{s} = \boldsymbol{D} \boldsymbol{a}, \tag{1.59}
$$

where the vectors are defined as

$$
\boldsymbol{s} = \begin{pmatrix} s_1 \\ s_2 \\ \vdots \\ s_M \end{pmatrix}, \; \boldsymbol{a} = \begin{pmatrix} a_1 \\ a_2 \\ \vdots \\ a_N \end{pmatrix} \tag{1.60}
$$

and the interaction matrix $\boldsymbol{D}$, that relates the DM commands and the WFS measurements, is defined as

$$
D = \begin{pmatrix}
D_{11} & D_{12} & ... & D_{1N} \\
D_{21} & D_{22} & ... & D_{2N} \\
D_{31} & D_{32} & ... & D_{3N} \\
\vdots & & \vdots & \\
D_{M1} & D_{M2} & ... & D_{MN}
\end{pmatrix}. \tag{1.61}
$$

The required solution is then an inversion of Eq. (1.59): when $M < N$, the system is undetermined and cannot be solved uniquely; when $M = N$, the matrix $\boldsymbol{D}$ is square and it can be directly inverted to solve the equation ($\boldsymbol{a} = \boldsymbol{D}^{-1} \boldsymbol{s}$), as long as it is not singular; when $M > N$, the system is overdetermined and the problem reduces to the calculation of the unknowns quantities such that the error between the measured parameters and the actual values is small. The latter represents the most common case in AO control systems. The least-squares estimator (LSE) approach can be used to solve overdetermined systems; the method finds the minimum of

$$
\chi^2 = \sum_{i=1}^{M} \left[s_i - \sum_{k=1}^{N} a_k D_{ik} \right]^2 \tag{1.62}
$$

and, by setting $\partial \chi^2 / \partial a = 0$, computes the solution for the vector $\boldsymbol{a}$ as

$$\boldsymbol{a} = (\boldsymbol{D}^T \boldsymbol{D})^{-1} \boldsymbol{D}^T \boldsymbol{s}, \tag{1.63}$$

where $\boldsymbol{D}^T$ is the transpose of the matrix $\boldsymbol{D}$ and $(\boldsymbol{D}^T \boldsymbol{D})^{-1} \boldsymbol{D}^T$ is the pseudo-inverse of $\boldsymbol{D}$, that we denote as $\boldsymbol{D}^+$. In many cases, the inversion of the matrix $(\boldsymbol{D}^T \boldsymbol{D})^{-1}$ is not possible, since the matrix is either singular or close to singular, and singular value decomposition (SVD) is used: the $M \times N$ matrix $\boldsymbol{D}$ can be broken into the product of three matrices

$$\boldsymbol{D} = \boldsymbol{U} \boldsymbol{\Sigma} \boldsymbol{V}^T, \tag{1.64}$$

where $\boldsymbol{U}$ is an $M \times N$ matrix, $\boldsymbol{V}^T$ is an $N \times N$ square matrix and $\boldsymbol{\Sigma}$ is an $N \times N$ diagonal matrix. The diagonal elements of $\boldsymbol{\Sigma}$, σ_i, are called *singular values* of $\boldsymbol{D}$. The columns of $\boldsymbol{U}$ and the columns of $\boldsymbol{V}$ are called left-singular vectors and right-singular vectors of $\boldsymbol{D}$ respectively and form two sets of orthonormal bases, in this case, of signals and commands respectively. From Eq. (1.64), the inverse can be computed as

$$\boldsymbol{D}^+ = \boldsymbol{V} \boldsymbol{\Sigma}^{-1} \boldsymbol{U}^T, \tag{1.65}$$

where $\boldsymbol{\Sigma}^{-1}$ is a diagonal matrix with elements $1/\sigma_i$. Equation (1.65) allows to derive the command vector as

$$\begin{aligned} \boldsymbol{a} &= \boldsymbol{D}^+ \boldsymbol{s} \\ \boldsymbol{a} &= \boldsymbol{W} \boldsymbol{s}, \end{aligned} \tag{1.66}$$

where $\boldsymbol{W} = \boldsymbol{D}^+$ is the reconstructor. The singular values σ_i represent the ability of the WFS to measure the wavefront. An element a_i that is related to a singular value $\sigma_i = 0$ (or close to zero) produces a signal $s_i = 0$, that is, it is not seen by the WFS. The unseen ($\sigma_i = 0$), or badly seen (σ_i close to zero) modes are typically discarded during the pseudo-inverse operation, by setting the related value $1/\sigma_i$ equal to zero. A threshold of $\sim 1/100$ of the maximum σ_i is typically used. This method is commonly known as truncated SVD (TSVD).

1.2.5   Limitations of classical adaptive optics

We list here the major sources of error in AO systems.

- **Fitting error**: the spatial scale of turbulence goes down to the order of millimeters. For apertures of a few meters, a perfect correction would mean DMs with hundreds of thousands of actuators. Moreover, as seen in Section 1.1.1, the spatial power

spectrum of the input phase fluctuation goes down with increasing spatial frequency, meaning that there is small interest in correcting higher and higher frequencies. The residual phase due to spatial frequencies that are not corrected leads to the fitting error:

$$\sigma^2_{fitting} = \int_{f_c}^{\infty} \Phi(f)\mathrm{d}f, \tag{1.67}$$

where f_c is the cutoff frequency of the DM, that is, the maximum frequency that the DM can compensate for ($f_c = 1/2d_{DM}$, with d_{DM} the inter-actuator pitch projected onto the pupil). It can be demonstrated that, for correction of Kolmogorov turbulence, Eq. (1.67) becomes

$$\sigma^2_{fitting} = a_F \left(\frac{d}{r_0}\right)^{5/3}, \tag{1.68}$$

where d is the subaperture size, r_0 the Fried parameter (Eq. (1.6)) and a_F is a coefficient that depends on the geometry of the corrector.

- **Temporal error**: as seen in Section 1.2.3, an AO control loop is inevitably characterized by a delay between the WFS measurements and the application of the correction by the DM, given at least by the integration time of the WFS. By the time the correction is applied, the input perturbation will have changed and this will result in an imperfect correction. This is called temporal (or servo-lag) error and can be computed as

$$\sigma^2_{temporal} = K \left(\frac{T}{\tau_0}\right)^{5/3}, \tag{1.69}$$

where τ_0 is the coherence time defined in Eq. (1.9), T is the loop sampling time (i.e. WFS integration time) and K depends on the characteristics of the loop and control law.

- **WFS measurement error**: the measurement noise of the WFS introduces an error that reduces wavefront reconstruction accuracy. It can be demonstrated that the variance depends on the inverse of SNR^2 (where SNR is the signal-to-noise ratio).

- **Aliasing error**: in the case of wavefront measurements, there exist spatial frequencies in the wavefront that are greater than the Nyquist frequency of the WFS ($f_{Nyq} = 1/2f_{samp}$, with f_{samp} the sampling frequency; e.g. for a SH WFS, it is determined by the lenslet spacing). These frequencies are not seen by the WFS, but can appear in the measurement as low spatial frequencies and cause large errors in the estimation of the wavefront.

- **Anisoplanatic error**: if the scientific target is not a valid reference source for AO, another reference must be used in the proximity of the scientific object. However, in this case the cylinder of atmosphere seen and measured by the WFS does not match perfectly the cylinder of atmosphere through which the science target beam propagates (Fig. 1.13). The residual due to the uncorrected turbulence is commonly
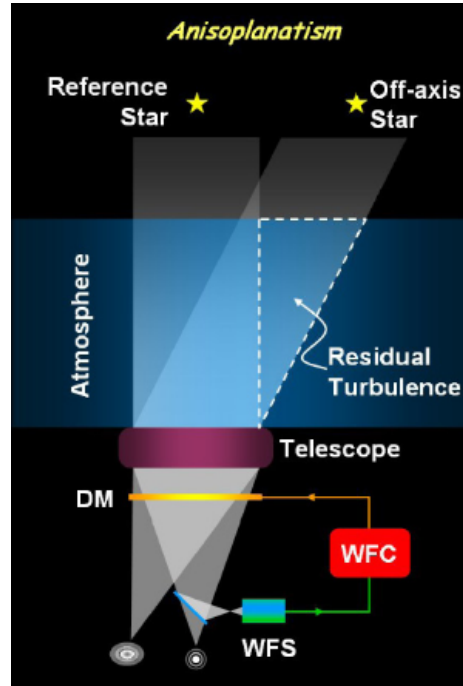
Fig. 1.13 Scheme of classical AO with on-axis reference source and off-axis scientific target. The turbulence sampled by the WFS is different from that in the imaging path, leading to a residual turbulence that degrades the AO correction.

known as angular anisoplanatic error. Considering the scientific object and the AO reference source separated by an angular distance θ, the error can be derived from the equation for the structure function in Eq. (1.4):

$$\sigma^2_{aniso} \approx 2.91 k^2 (\cos\gamma)^{-1} \int C_n^2(h) \mathrm{d}h \left[\theta h (\cos\gamma)^{-1}\right]^{5/3}, \tag{1.70}$$

where the linear separation ξ in Eq. (1.4) has been replaced by θz, with $z = h(\cos\gamma)^{-1}$. Remembering the definition of θ_0 in Eq. (1.8), Eq. (1.70) becomes

$$\sigma^2_{aniso} = \left(\frac{\theta}{\theta_0}\right)^{5/3}, \tag{1.71}$$

showing the increasing of the anisoplanatic error with the target-reference separation θ.

Considering typical values of θ_0, the anisoplanatic error strongly limits the AO correction to few arcseconds of field of view in V band, or tens of arcseconds in K band.

1.2.6   Tip-tilt anisoplanatism in classical adaptive optics

The anisoplanatic error introduced in the previous section includes the effect of all the turbulent phase. In this section, we report the results presented in Sandler *et al.* [21] on the anisoplanatic error as limited to the contribution of tip and tilt modes only.

We consider the AO guide star (GS) at an angular separation θ from the scientific target. The determination of tip-tilt correction through an off-axis GS introduces an error that can be evaluated as

$$\sigma_{TT}^2 = \left\langle (\phi_{GS} - \phi_t)(\phi_{GS} - \phi_t)^\dagger \right\rangle, \tag{1.72}$$

where σ_{TT}^2 is the mean-square error of tip-tilt, † denotes the conjugate-transpose and ϕ_{GS} and ϕ_t are the phases from the GS and the target respectively. These can be decomposed into Zernike modes as

$$\begin{aligned}
\phi_{GS} &= \sum_{j=2,3} a_j Z_j(\boldsymbol{r}) \\
\phi_t &= \sum_{j=2,3} b_j Z_j(\boldsymbol{r}),
\end{aligned} \tag{1.73}$$

where a_j is the jth Zernike coefficient related to the measured phase, b_j is the jth Zernike coefficient related to the scientific phase, Z_j is the jth Zernike modes and where we limited the contribution to tip and tilt, considering the sum of j=2 and j=3 only. Equation (1.72) can then be written as

$$\sigma_{TT}^2 = \sum_{j=2,3} 2(1 - \Gamma_j)\langle a_j^2 \rangle, \tag{1.74}$$

where $\langle a_j^2 \rangle$ is the variance of the a_j coefficient and Γ_j is the normalized correlation defined as $\Gamma_j = \langle a_j b_j \rangle / \langle a_j^2 \rangle$. The calculations presented in Sandler *et al.* [21] allow to derive, from Eq. (1.74), the following expressions for the anisoplanatic error related to tip and tilt:

$$\frac{\sigma_\parallel^2}{(\lambda/D)^2} \approx 0.0472 \left(\frac{\theta}{\theta_0}\right)^2 \left(\frac{D}{r_0}\right)^{-1/3} - 0.0107 \left(\frac{\theta}{\theta_0}\right)^4 \left(\frac{D}{r_0}\right)^{-7/3}, \tag{1.75}$$

$$\frac{\sigma_\perp^2}{(\lambda/D)^2} \approx 0.0157 \left(\frac{\theta}{\theta_0}\right)^2 \left(\frac{D}{r_0}\right)^{-1/3} - 0.00214 \left(\frac{\theta}{\theta_0}\right)^4 \left(\frac{D}{r_0}\right)^{-7/3}, \tag{1.76}$$

where $\sigma_\parallel^2$ is defined as longitudinal tilt error (i.e. along the axis joining the science object and the GS) and $\sigma_\perp^2$ as the lateral tilt error (i.e. along the axis perpendicular to the target-GS direction). The formulas, valid in the case of Kolmogorov turbulence, show a dependence on the turbulence parameters r_0 and θ_0, on the telescope diameter D and on the angular separation θ. In particular, the quadratic terms in θ are valid out to field angles $\theta \leq 0.5(D/r_0)\theta_0$, while the sum of the quadratic and the fourth-order terms is accurate out to $\theta \leq (D/r_0)\theta_0$. Another aspect, emerging from Eqs. (1.75)-(1.76) and shown in Fig. 1.14, is that the longitudinal error is larger than the lateral one, due to a faster decorrelation of tip than tilt (shown in Fig. 1.15). Moreover, the equations show that the errors do not depend on the wavelength.
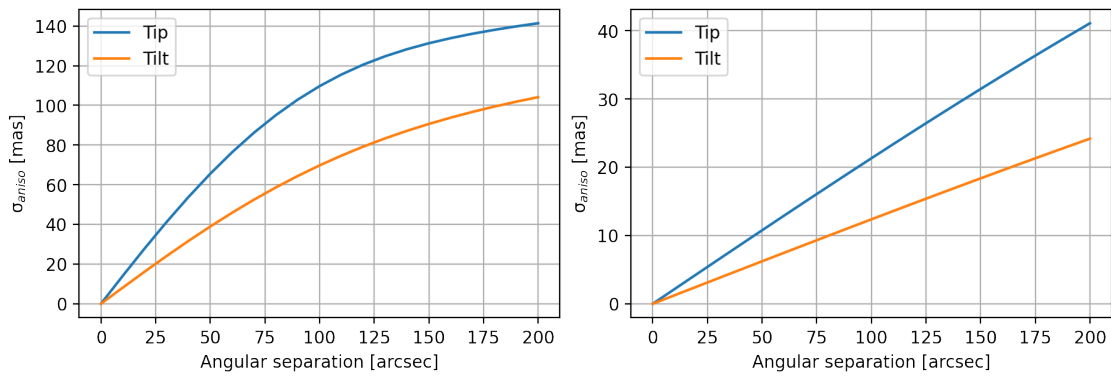
Fig. 1.14 Anisoplanatic error for tip (blue line) and tilt (orange line) as a function of the angular separation between the scientific object and the AO reference source. Two aperture diameters are considered, $D = 8$ m (left) and $D = 40$ m (right). A single-layer turbulence profile has been used, with $r_0 = 16$ cm, $\theta_0 = 1$ arcsec, infinite outer scale, wind speed of 10 m/s and altitude of 10 km.

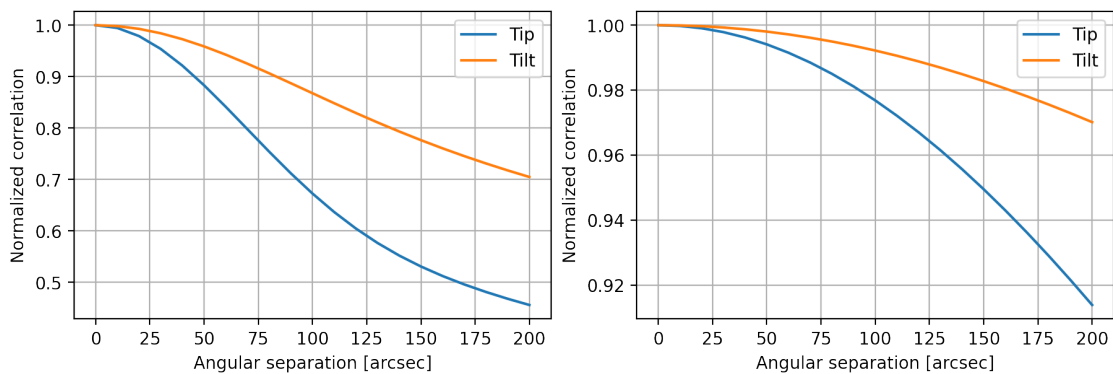**Fig. 1.15** Normalized correlation parameter as a function of the angular separation between the scientific object and the AO reference source. Both tip (blue line) and tilt (orange line) correlation parameters are shown. The turbulence profile is the same as the one used in Fig. 1.14. The error is shown for $D = 8$ m (left) and $D = 40$ m (right).

1.3   Multiconjugate adaptive optics

We have reviewed the basic principles of classical AO systems so far. These systems, characterized by a single WFS and a single DM are known as single-conjugated adaptive optics (SCAO). As seen in the previous paragraph, SCAO systems are strongly affected by anisoplanatism that limits the good quality of the AO correction to small fields of view. To overcome this problem, in 1988 Beckers proposed the concept of multiconjugate adaptive optics (MCAO) [22]. The basic idea, represented in Fig. 1.16, foresees the use of multiple GSs to perform a 3D measurement of the turbulent volume and of multiple DMs conjugated to different altitudes to compensate for different layers of the atmosphere. Indeed, it was
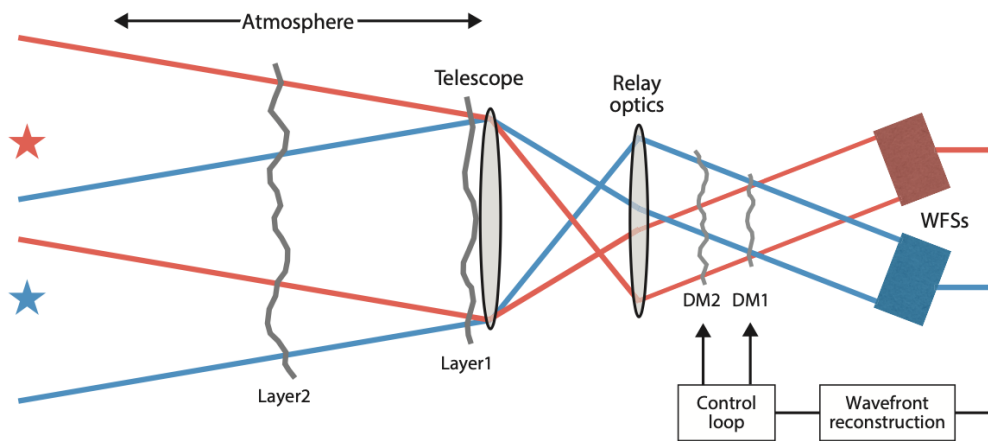
Fig. 1.16 Scheme of MCAO (from Rigaut *et al.* [23]). The volume of atmospheric turbulence is probed by multiple WFSs (two in the figure), each looking at a different GS. The measurements are processed through tomographic techniques and the correction phase is projected onto multiple DMs (two in the figure), optically conjugated at various atmospheric layers above the telescope.

demonstrated [24] that the conjugation of N DMs to N layers of atmospheric turbulence can increase the isoplanatic patch identified by θ_0. In particular, the anisoplanatic error becomes

$$\sigma^2_{aniso} = \left(\frac{\theta}{2\theta_0 N}\right)^{5/3}, \tag{1.77}$$

the formula showing that the isoplanatic angle is reduced by a factor $2N$ with respect to the case of a single DM conjugated to the ground.

   The compensation for various layers of atmospheric turbulence clearly requires the measurement of the turbulent layers conjugated at each DM, that is obtained through the tomography approach. Several methods have been proposed for the tomographic reconstruction through the use of multiple GSs, considering either a zonal approach [25],

or a modal approach [26]. These works involved the use of LGSs only, thus overcoming the AO problem of limited sky coverage. However, the tip-tilt indetermination problem that characterizes LGS-based wavefront sensing has driven the use of NGSs as well. In particular, typical configurations foresee the use of NGSs for tip-tilt measurements and of LGSs to sense higher orders of distortion; such configurations do not reintroduce the sky coverage problem, since a fainter NGS limiting magnitude is allowed by the small number of modes that have to be measured by the NGS WFSs.

To date, the Gemini Multi-conjugated adaptive optics System (GeMS) [27, 28] at the Gemini South Telescope is the only MCAO system operating on sky and new systems are currently under design and realization. Some examples are the MCAO Assisted Visible Imager and Spectrograph (MAVIS) [29] for the Very Large Telescope (VLT), the Narrow-Field InfraRed Adaptive Optics System (NFIRAOS) [30] for the Thirty Meter Telescope (TMT) and the Multiconjugate adaptive Optics Relay For ELT Observations (MORFEO) [31] for the Extremely Large Telescope (ELT). A brief description of the latter will be provided in Section 1.3.3.

1.3.1 Tomographic reconstruction

We review the basics to retrieve the 3D distribution of atmospheric turbulence from a set of wavefront measurements in different directions. In particular, we report the modal approach presented in Ragazzoni *et al.* [26] that shows that the deformations of several DMs can be controlled by measuring a certain number of Zernike modes on LGSs (the analysis can be applied to NGSs as well).

We consider that the wavefronts from M GSs are sensed through the telescope entrance pupil of diameter D by M different WFSs. The incoming wavefront is assumed to be perturbed by N layers located at different altitudes. The geometry is shown in Fig. 1.17. Figure 1.18 shows the geometry of the footprints projected on a single layer j and defines the metapupil, that is, the circular region encompassing all of the GSs beams. Assuming that θ is the radius of the technical field of view (FoV) (i.e. the FoV identified by the GSs asterism), the size of the metapupil on a layer j is $D + 2\theta H_j$, with H_j the height of the layer. The beam footprint diameter is equal to D if NGSs are considered, smaller than D in the case of LGSs and varies depending on the altitude of the layer.
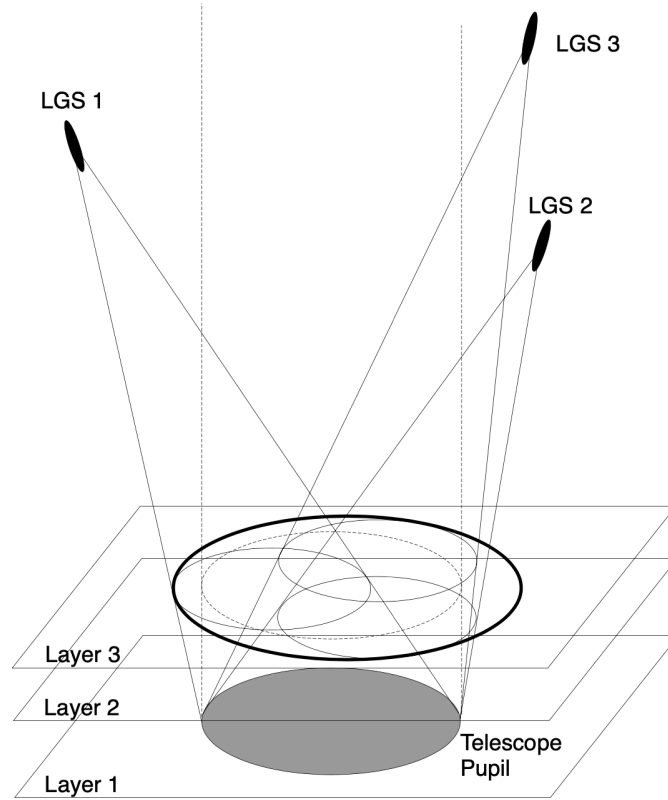
Fig. 1.17 Geometry of the configuration (from Ragazzoni *et al.* [26]). The wavefronts from three GSs (LGSs in the figure) pass the layers (three in the figure) of atmospheric turbulence before arriving to the entrance pupil.

The wavefront for the ith GS can be expanded into a sum of n Zernike polynomials as

$$\varphi_{GS_i} = \begin{pmatrix} a_2 \\ a_3 \\ \vdots \\ a_n, \end{pmatrix} \tag{1.78}$$

where the piston term has been omitted since it is not accessible and where, differently from Ragazzoni *et al.* [26], we have included tip and tilt modes in order to extend the analysis to the case of NGSs as well. φ_{GS_i} is the modal expansion of the wavefront coming from the ith GS, integrated over the layers, i.e.:

$$\varphi_{GS_i} = \sum_{j=1}^{N} \varphi_{GS_{ij}}, \tag{1.79}$$
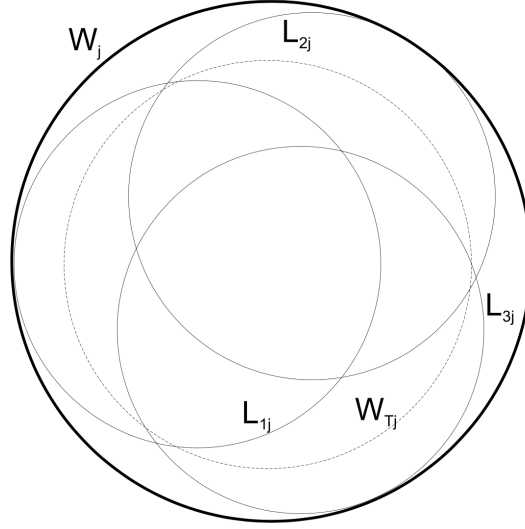
Fig. 1.18 Geometry of the beams footprints on a layer j (from Ragazzoni *et al.* [26]). L_{ij}, with i=1, 2, 3, represents the beam from the ith GS (defined as $\varphi_{GS_{ij}}$ in the text); W_j is the metapupil (φ_{DM_j} in the text); W_{Tj} is the footprint from the scientific object that is assumed on axis (φ_{O_j} in the text).

where $\varphi_{GS_{ij}}$ is the expansion of the wavefront from the ith GS on a single layer j and can be related to the wavefront defined on the metapupil:

$$\varphi_{GS_{ij}} = \left(P^{GS}_{DM}\right)_{ij} \varphi_{DM_j}, \tag{1.80}$$

where $\left(P^{GS}_{DM}\right)_{ij}$ is a matrix of size $n \times n$ that contains information about the geometry between the metapupil and the footprint and φ_{DM_j} is the expansion of the wavefront on the metapupil. We considered to have a DM conjugated to each layer and to reconstruct on each layer the same number of modes measured by each WFS. Combining Eq. (1.79) and Eq. (1.80) leads to:

$$\varphi_{GS_i} = \sum_{j=1}^{N} \left(P^{GS}_{DM}\right)_{ij} \varphi_{DM_j}. \tag{1.81}$$

This equation, for all GSs, can be combined in a single matrix equation including all the N layers and all the M GSs in the same relationship

$$\begin{pmatrix} \varphi_{GS_1} \\ \varphi_{GS_2} \\ \varphi_{GS_3} \\ \vdots \\ \varphi_{GS_M} \end{pmatrix} = \begin{pmatrix} P_{11} & P_{12} & \dots & P_{1N} \\ P_{21} & P_{22} & \dots & P_{2N} \\ P_{31} & P_{32} & \dots & P_{3N} \\ \vdots & & \vdots & \\ P_{M1} & P_{M2} & \dots & P_{MN} \end{pmatrix} \begin{pmatrix} \varphi_{DM_1} \\ \varphi_{DM_2} \\ \varphi_{DM_3} \\ \vdots \\ \varphi_{DM_N} \end{pmatrix}, \tag{1.82}$$

that can be written in compact form as

$$\varphi_{GS} = P_{DM}^{GS} \varphi_{DM}. \tag{1.83}$$

The equation takes the same form as Eq. (1.59), indeed it represents the relationship between the wavefronts arriving on the WFSs and the wavefronts to be applied on the DMs through the interaction matrix P_{DM}^{GS}. However, differently from classical AO, the interaction matrix contains information, for each layer, on the reaction of all WFSs to a given Zernike mode on a metapupil in altitude.

In the same way, the wavefront expansion φ_{DM_j} from the metapupil can be projected onto the smaller on-axis footprint of the scientific object on the jth layer:

$$\varphi_{O_j} = \left(P_{DM}^{O}\right)_j \varphi_{DM_j}, \tag{1.84}$$

that leads to the compact form

$$\varphi_{O} = P_{DM}^{O} \varphi_{DM}. \tag{1.85}$$

It follows that the dimension of P_{DM}^{GS} is $(M \cdot n) \times (N \cdot n)$ and of P_{DM}^{O} is $n \times (N \cdot n)$. These matrices contain coefficients that depend on the geometry of the problem. In Appendix B.1, we report as an example the analytical computation of these coefficients that was derived in Negro [32].

As seen in Section 1.2.4, as long as $M \geq N$, the interaction matrix P_{DM}^{GS} can be inverted to derive the tomographic reconstructor:

$$W_{tomo} = \left[\left(P_{DM}^{GS}\right)^T P_{DM}^{GS}\right]^{-1} \left(P_{DM}^{GS}\right)^T. \tag{1.86}$$

Unseen modes and Minimum Mean Square Estimator approach

The geometry of the GSs asterism can introduce a fundamental limitation to the tomographic process, that is, the problem of *unseen modes*. A geometric scheme describing the problem is shown in Fig. 1.19: the wavefront distortions are measured by two WFSs looking at two different directions and a third direction (on axis) is observed. In this configuration, the sum of the phase perturbations induced by the turbulent layers is exactly zero in the GSs directions. Therefore, the WFSs provide a piston measurement only and no information on the phase deformation is available; these aberrations are not estimated in the reconstruction process. Clearly, in the GSs directions these modes are not important, but they lead to wavefront distortions in other directions, limiting the goal of MCAO to provide a good correction across the entire FoV.
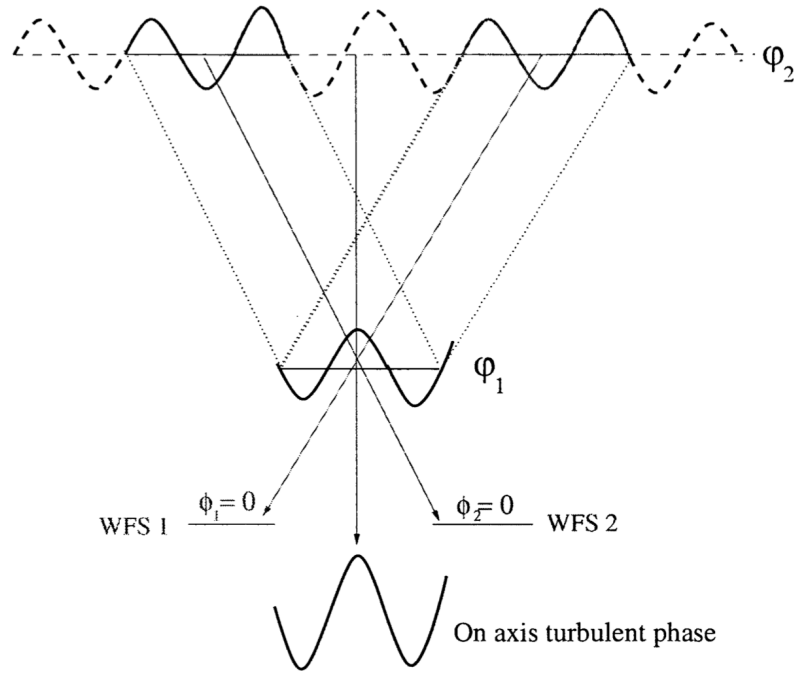
Fig. 1.19 Geometric scheme to represent the unseen modes problem (from Fusco *et al.* [33]). Two WFSs measure turbulence-induced distortions from two different GSs. The sum of the phase perturbations on the two layers is zero in the GSs directions, thus provides zero signal on the WFSs. On the other hand, the wavefront deformations do not cancel out in the on-axis direction. Thus, the modes unseen by the WFSs can still degrade the correction in other directions.

Unseen frequencies represent a strong limitation for the pure LSE reconstructor. Indeed, the interaction matrix coefficients go to zero for these frequencies and the noise is overamplified within the inversion operation. The *badly-seen* frequencies impact the LSE reconstruction as well: for these frequencies, measurement is close to zero and falls within the noise of the WFSs; thus, the same problem as for the unseen frequencies applies. One method to overcome the noise amplification is to use the truncated LSE (TLSE) reconstructor (also identified as TSVD in Section 1.2.4), but at the price of uncorrected frequencies. Moreover, the truncation is selected through a trial and error approach and this choice can be not easy for real systems.

In this context, a solution was proposed that foresees a reconstruction through the Minimum Mean Square Estimator (MMSE) approach [34]. The MMSE estimator minimizes the residual phase variance in each reconstructed layer between actual and estimated phases:

$$\sigma^2_{res} = \left\langle \left| \varphi_{turb} - W_{tomo} \left(P_L^{GS} \varphi_{turb} + \varphi_n \right) \right|^2 \right\rangle , \tag{1.87}$$

where φ_{turb} is the turbulent phase and P_L^{GS} is the interaction matrix that projects the turbulent layers seen in the GSs directions in the pupil plane ($P_L^{GS} = P_{DM}^{GS}$ if considering to have a DM conjugated at each layer). Differently from Eq.(15) of Neichel *et al.* [34], we assumed a direct measurement of the phase by setting $M = 1$, with M the matrix that models the wavefront sensing operation. The minimization process leads to the following expression for the MMSE reconstructor:

$$W_{MMSE} = \left[\left(P_L^{GS}\right)^T \left(C_{\varphi_n}\right)^{-1} P_L^{GS} + \left(C_{\varphi_t}\right)^{-1}\right]^{-1} \left(P_L^{GS}\right)^T \left(C_{\varphi_n}\right)^{-1}, \quad (1.88)$$

where C_{φ_t} is the covariance of the turbulent phase and C_{φ_n} is the covariance of the noise. This reconstructor includes prior knowledge of the phase statistics and noise power spectrum by means of C_{φ_t} and C_{φ_n}. The noise term can be factorized under the assumption of same noise σ_n^2 for all GSs and x and y directions and Eq. (1.88) can be rewritten as

$$W_{MMSE} = \left[\left(P_L^{GS}\right)^T P_L^{GS} + \sigma_n^2 \left(C_{\varphi_t}\right)^{-1}\right]^{-1} \left(P_L^{GS}\right)^T, \quad (1.89)$$

showing the inverse of the SNR, i.e. $\sigma_n^2 \left(C_{\varphi_t}\right)^{-1}$.

In contrast to the TLSE reconstructor, the MMSE reconstructor does not require any truncation. Through the regularization term $\sigma_n^2 \left(C_{\varphi_t}\right)^{-1}$, the MMSE reconstructor weights the noise propagation and is able to optimize the reconstruction depending on the SNR: for frequencies with good SNR, MMSE and TLSE are equivalent; for frequencies with small SNR, the inverse of the interaction matrix is weighted by the regularization term, avoiding noise amplification.

One issue of the MMSE tomographic reconstruction is that it makes use of a priori information on the turbulent phase statistics but it has to deal with closed-loop configurations where the WFSs are after the DMs, hence only see the residual turbulence that does not obey the same statistics. To overcome this problem, the concept of pseudo open-loop control (POLC) was introduced [35]: the idea is to reconstruct the virtual open loop measurements from a combination of the closed-loop measurements and the shape of the DMs.

1.3.2 Limitations of multiconjugate adaptive optics

We summarize the main MCAO-specific error sources, without entering into detail on the limitations due to the use of LGSs as it is beyond the interest of this work.

- **Generalized fitting error**: in Section 1.3.1, we assumed to have a DM conjugated at each turbulent layer. In real cases, this is not the case and only a limited number of

DMs is available to compensate for the turbulent volume. The residual wavefront
due to the uncorrected layers leads to the generalized fitting error.

- **Tomographic error**: the use of multiple GSs does not ensure a complete covering of
  the turbulent volume. Some part of the turbulence above the telescope will always
  be probed by one GS only and this will limit the tomography as it can not determine
  at which altitude the perturbation is located in this part of the beam. Another
  limitation of tomography comes from unseen modes that have been described in
  Section 1.3.1.

- **Generalized aliasing error**: turbulent layers above and below the altitude control
  domain of the MCAO system are seen and wrongly interpreted as layers inside the
  control domain and this causes an error that is commonly called generalized aliasing
  error. Unlike classical spatial aliasing (see Section 1.2.5), that is due to the WFS, the
  generalized aliasing is caused by the tomographic process.

1.3.3   MORFEO at the Extremely Large Telescope

MORFEO [5, 31, 36, 37] is the MCAO system of the 39-m ELT [38, 39] that will provide
large diffraction-limited correction to the near-infrared Multi-AO Imaging Camera for
Deep Observations (MICADO) [3] and to a second instrument still to be defined. The
primary observing mode of MICADO is astrometric imaging with either a large FoV of
50×50 arcsec, or a small FoV of 18×18 arcsec, with wavelength coverage from 0.8 μm to
2.4 μm [40]. Jointly with the MICADO consortium, MORFEO will provide a SCAO system
as well.

From the opto-mechanical point of view, MORFEO consists of an optical relay that
re-images the telescope focal plane for the science instruments (Fig. 1.20). The relay is
supported by an optical bench mounted on the telescope Nasmyth platform in gravity
invariant configuration (Fig. 1.21) and consists of six mirrors and a dichroic beam-splitter
separating the light for the science path from the light for the LGS WFSs. MORFEO will
provide two DMs in the optical relay (DM1 = M9 conjugated at 6-12 km, DM2 = M10
conjugated at 17-20 km) that will work together with the adaptive (M4)[41] and tip-tilt
(M5) mirrors of the ELT.

The tomographic reconstruction relies on the measurements from three NGS WFSs
and six LGS WFSs. The former are 2×2 SH WFSs, working in H band and measuring five
modes (tip, tilt, focus and the two astigmatisms) at a frame rate of 100-1000 Hz on stars
with magnitude in H band up to 21; the latter are 68×68 SH WFSs and sense the higher
orders of distortion at a frame rate of 500 Hz. An asterism of up to three NGSs can be
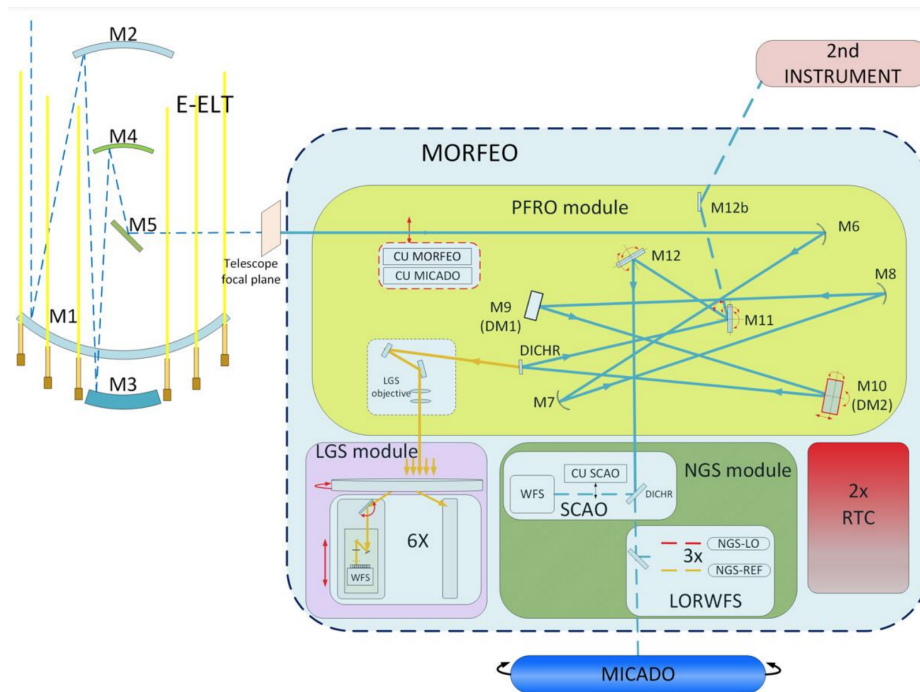
Fig. 1.20 Functional overview of MORFEO in relation to ELT and MICADO (from Ciliegi *et al.* [5]). MORFEO is divided in the figure into the post-focal relay optics (PFRO), the LGS and NGS modules. The PFRO contains the two post-focal DMs (PFDMs) conjugated in altitude (6-12 km and 17-20 km) and a dichroic feeding the six LGS WFSs in the LGS module. The light coming out of the PFRO module is sent to the NGS module, where is split between the NGS WFSs (LORWFS in the scheme) and the MICADO instrument. The measurements from LGS WFSs and NGS WFSs are collected by MORFEO RTC which drives the DMs (M4/M5 and the two PFDMs).

selected in a technical FoV with a diameter of 160 arcsec; the LGS asterism radius is kept fixed at 45 arcsec for any telescope elevation.

The adaptive correction is given by ELT's M4 and by the two MORFEO's DMs, these DMs providing more than 5000 modes controlled.

1.4   Ground-based astrometric observations

To date, astrometry is one of the main science drivers of actual and future instruments either observing from the ground or from space. Indeed, astrometric measurements represent the starting point for a wide variety of topics in astrophysical research: the detection of intermediate-mass black holes (IMBHs) in cluster centers, the analysis of Galactic globular clusters (spatial distribution, cluster proper motions and orbits around the Milky Way, internal kinematics, ...) and more accurate studies of our Galactic center, as well as the one of nearby galaxies, are just few examples. The Gaia satellite [42] has
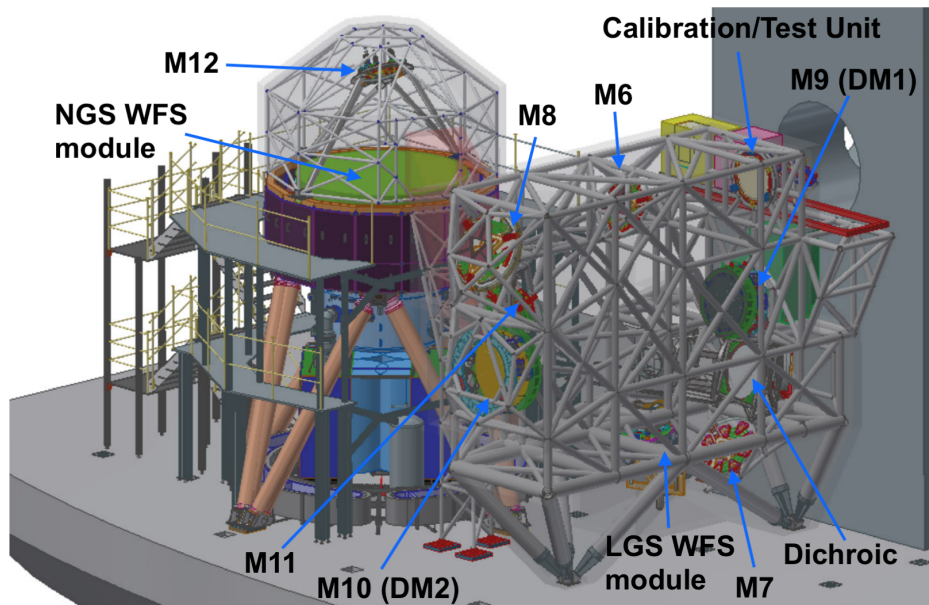
Fig. 1.21 General overview of MORFEO as installed on the ELT's Nasmyth platform.

provided astrometry of single stellar sources out to large distances with exceptional accuracy. The limited telescope diameter strongly affects the measurements in crowded fields, though. Thanks to the implementation of AO systems, ground-based telescopes are now valid competitors to space-based ones and most of the future AO-assisted instruments are designed with high-precision astrometry among their requirements. In this context, it is worth pointing out that ground-based observations aim at providing high precision on *differential* astrometry, that is, on the measurement of the distance of different science objects in the field relative to each other (or relative to other objects in the scientific field). *Absolute* astrometry, as it is intended for space-based observations, is not feasible from the ground since it would require to observe sources with large separations (~ 1 rad) in order to control the uncertainties. Requirements for ground-based instruments on absolute astrometry do exist, but they actually refer to the estimation of a science object position in the sky coordinate system, where the position measurement is again intended as obtained through differential measurements with respect to reference sources with known coordinates (e.g. from Hipparcos or Gaia catalogs) that are in the science field.

MCAO is a good candidate for astrometric observations with ground-based telescopes. Indeed, as seen in Section 1.3, it aims at providing uniform correction over wide areas reducing the high spatial variability of the point spread function (PSF) in the field that limits the accuracy of the data reduction. Moreover, thanks to the DMs conjugated in altitude, MCAO is able to compensate for the field distortions induced by atmospheric turbulence. In addition, it provides a large number of reference sources in the science field

that have good image quality (in classical AO, reference sources are likely outside the small corrected FoV). These characteristics help understand why GeMS and the Multiconjugate Adaptive Optics Demonstrator (MAD [43]; temporarily installed at the VLT in 2007), though not optimized for astrometric observations, led to several publications on astrometry topics (e.g. [44, 45]) and why future instruments equipped with MCAO modules have high precision astrometry as one of the main science drivers. In particular, the following requirements of precision have been set on the differential astrometry: 50 μas for MORFEO (goal of 10 μas)[46], 150 μas for MAVIS (goal of 50 μas)[47] and 50 μas for NFIRAOS (goal of 10 μas)[48]. These systems will be fully relevant to complement astrometric observations with space-based systems like Gaia. Indeed, one of the main observational limits of such system is its "blindness" in very crowded regions, in particular down to faint magnitudes. The high spatial resolution of ground-based observations, for instance with MORFEO at the ELT, will allow to access these regions with high-precision astrometry. This will bring advantage to scientific cases requiring astrometric measurements in the very center of globular clusters, for example (e.g. to unveil the presence of IMBHs).

1.4.1 Sources of astrometric error

In order to exploit the astrometric capabilities of future ground-based instruments, a great effort has been made to understand and model all possible sources of error that can affect astrometric measurements from the ground [49–51]. In the following, referring to Trippe *et al.* [51], we summarize the main sources of error that have been identified in the literature.

- **Sampling and pixel scales**: in order to have a good measurement of the detector position of a point source, the PSF must be sufficiently sampled. If the pixel scale of the detector (i.e. the angular field sampled by a single pixel) is too large, any displacement of the source within the pixel does not involve a flux variation in the adjacent pixels and position information is lost. The choice of the pixel scale plays an important role during the instrument design.

- **Instrumental distortion**: any real optical system suffers from geometric distortions that can be linear and non-linear. The former include terms like shifts, rotations, scaling and can be caused by telescope instabilities that change the plate scale, or by rotator instabilities that can introduce systematic frame-to-frame rotation; the latter can be caused by gravitational flexure of the telescope, by misalignment of the optics, etc.

- **Differential atmospheric refraction**: any ground-based position measurement is affected by atmospheric refraction. Differential astrometry is affected by differential refraction that is due to the slight difference in zenith angles of the two sources that leads to different deviation between physical and observed zenith angle for the sources. Therefore, the observed distance between the two objects deviates from the physical one.

- **Guide star measurement errors**: in MCAO systems, the use of multiple NGSs for the low-order correction makes use of the guide star positions and the knowledge of the relative positions is required. The measurements of guide stars positions will suffer from uncertainties due to atmospheric fluctuations that will introduce time-variable distortion into the AO corrected FoV.

- **Differential tilt jitter**: as introduced in Section 1.2.6, the fact that the light from a science target and the light from the GS travel through different columns of atmospheric turbulence leads to a non-perfect correction on the target. Considering the correction of tip-tilt, the result is a fluctuation of the target position. Considering the measurement of the distance between two targets, the effect translates into random, achromatic and anisotropic fluctuations of the measured distance [49].

- **Anisoplanatism**: the anisoplanatic error introduced in Section 1.2.5 causes the PSF shape to vary in the FoV, depending on the position of the target with respect to the AO reference. Tip-tilt modes determines, in classical AO systems, typical PSF elongation effects that increase with the target-GS angular separation.

- **Calibration of projected pixel scale**: among the steps of a typical astrometric data reduction, one needs to calibrate the pixel scale as projected on sky in order to convert measured positions from pixel to angular units. Astrometric references in the FoV are required to compute the scaling factors and errors on the reference positions propagate into the positions calculated from the data.

On top of these error sources, a statistical limit to astrometric precision is set by photon noise that introduces an intrinsic uncertainty in the position measurement. This error, identified as *centroiding error*, was modeled for a circular diffraction-limited telescope of diameter D as [52]

$$\sigma = \frac{1}{\pi} \frac{\lambda}{D} \frac{1}{\sqrt{N}} \tag{1.90}$$

where λ is the observation wavelength and N is the number of photons collected from the object.

Among the error sources listed, the focus of the present thesis is on differential tilt jitter and tip-tilt anisoplanatism, that is, in general, on the impact of tip-tilt atmospheric residuals on astrometric precision. In the following, we give a more detailed description of the effect of tip-tilt on differential astrometry.

1.4.2 Effect of tip-tilt on astrometric precision

Tip-tilt residuals can affect astrometric precision as they introduce fluctuations of the position of a source with respect to its nominal position on the detector. On the one hand, the amount of fluctuations integrated during an individual exposure can determine an increasing of the size and a change in shape of the PSF, with typical PSF elongation effect; on the other hand, if the fluctuations are not totally integrated within the exposure time of the image, a jitter of the source position can also be observed between successive frames (Fig. 1.22). Differential astrometry can be affected by both effects: the former contributes to the centroiding error, while the latter leads to the differential tilt jitter error.
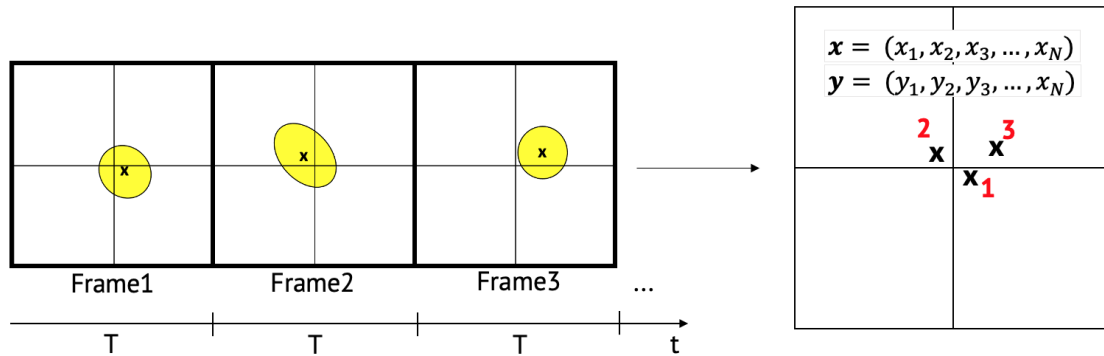
Fig. 1.22 Schematic representation of the effects of tip-tilt residuals on exposures of integration time T. The fluctuations integrated during an exposure can result in an elongation of the PSF (yellow spots); the fluctuations that are not integrated can determine a variation of the PSF position between successive frames (black crosses).

Clearly, the knowledge of the spatial and temporal dependence of tip-tilt residuals is needed to characterize the behavior of the related astrometric errors. For SCAO systems, tip-tilt anisoplanatism is well known and has been thoroughly modeled: as shown in Section 1.2.6, the measurement of tip-tilt through a GS that is separated by the scientific object by an angle θ leads to tip-tilt residuals that, at first order, linearly depend on the separation ($\sigma \propto \theta$). Moreover, the error along the axis joining the science object and the GS is larger than the error along the perpendicular direction. These characteristics explain the behavior of the PSF elongation effect, as well as of the differential tilt jitter, observed

in SCAO-assisted observations (examples are shown in Fig. 1.23). For MCAO systems the characterization is more elaborate, since the geometry with multiple GSs and multiple DMs needs to be taken into account and can lead to complex behaviors that may not be easily parameterized. As pointed out in Trippe *et al.* [51], tip-tilt anisoplanatism is not well understood for this flavour of AO.

In Carlà *et al.* [53, 54], we proposed our analysis of tip-tilt anisoplanatism in MCAO systems and its impact on astrometric precision, that we report in Chapters 3, 4, 5. The study is based on the derivation of analytical expressions to estimate the residual phase, hence the PSD, from an MCAO system in any direction of the scientific field of view. These formulas can provide a fast evaluation of the residuals without the need for time-consuming simulations, by assuming a statistics of turbulence-induced distortions and considering the temporal filtering from the MCAO loop. In this context, in Plantet *et al.* [55], we first derived general expressions to model spatiotemporal statistics of the turbulent phase that allow to take into account spatiotemporal cross-correlations between all directions involved in an MCAO configuration. We present these first results in the next chapter.
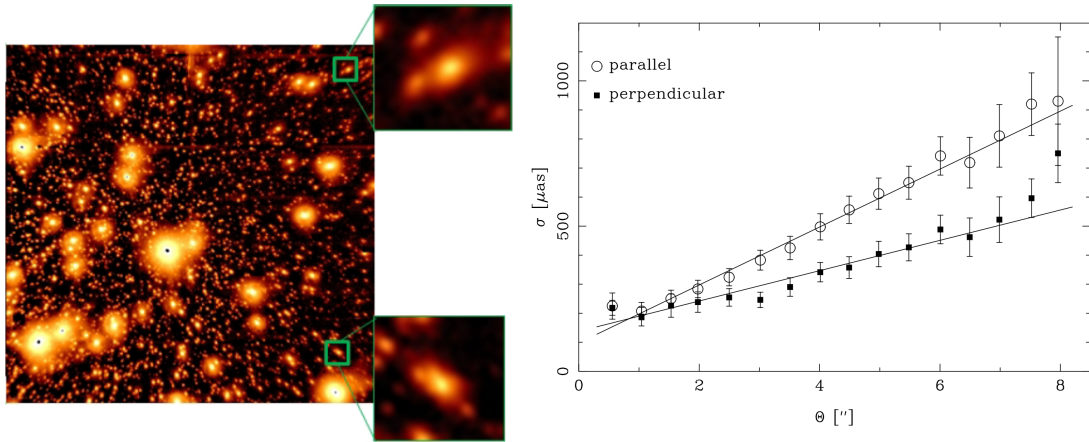

Fig. 1.23 PSF elongation observed from FLAO [56] data at the Large Binocular Telescope (LBT; left). Differential tilt jitter observed from NACO data at the Very Large Telescope (right; from Trippe *et al.* [51]).

Chapter 2

Spatiotemporal statistics of the turbulent phase

In the context of AO for astronomy, one can rely on the statistics of the turbulent phase to assess and optimize a part of the system's performance. Many studies of the turbulence statistics have been done considering a wavefront decomposition on the Zernike modes [12–14, 32, 57–65]. These studies mostly focus on the temporal statistics of the turbulence seen from one source to one aperture [13, 14, 66] or the spatial covariance from one or two sources to one or two apertures [12, 13, 57, 58, 64, 65]. Though, the knowledge of both temporal and spatial statistics in a general framework can be useful for the development of new analytical expressions to estimate the adaptive optics performance. These tools can help in the analysis of existing SCAO or Wide-Field AO (WFAO) systems [67–70] and future systems that are going to equip the next generation of telescopes [71–76]. Indeed, the classical approach for the analysis of the performance of an AO system is to decompose the overall residual in several sources of errors (temporal, anisoplanatism, noise, aliasing, fitting...), considering them uncorrelated [20, 21, 34, 77–79]. In that case, most of the error computations do not take into account the temporal filtering of the AO loop, while alternative approaches [80–83] apply the AO control in the whole performance analysis, highlighting for example the correlation between the temporal and the anisoplanatism errors. These methods to evaluate the AO performance often rely on an analysis in the spatial frequency domain [34, 77–81].

In this chapter, we present the analytical formulation that we proposed in Plantet *et al.* [55] to derive temporal Cross Power Spectral Densities (CPSDs) of the turbulent phase for two different sources and two different apertures. We first considered the whole (piston-filtered) phase and then its decomposition into Zernike modes. To our knowledge, this framework is the only one that offers the possibility to directly take into account the

following aspects altogether in a single formula, while allowing the application of a time filtering: distinct apertures of different size, distinct sources at finite or infinite distance, direction of the wind. We then present a case study that makes use of the CPSDs to derive the anisoplanatism error for a SCAO system and for an interferometer such as the Large Binocular Telescope Interferometer (LBTI) [84]. We show that a simple computation from covariances would overestimate the anisoplanatism error with respect to a more precise computation that takes into account the temporal filtering of the AO loop. Finally, we make use of CPSDs to provide a first analysis of tip-tilt anisoplanatism in SCAO systems, that will be then extended to MCAO in the next chapter.

In Section 2.1, we present the aperture-source geometry used throughout the analytical derivation. In Section 2.2, we give the expression of the inter-aperture spatial covariance of the piston-removed phase, that we then use to compute the corresponding spatiotemporal CPSDs in Section 2.3. In Section 2.4, we use the formalism introduced in Section 2.3 to derive the expression of Zernike coefficients CPSDs. In Section 2.5, we present an application of CPSDs to analyze anisoplanatism as filtered by a SCAO loop on either a single-aperture or a two-aperture interferometric telescope. Finally, in Section 2.6, we use CPSDs to model and analyze atmospheric tip-tilt residuals in SCAO systems.

2.1 Geometry

The aperture-source geometry we consider here is the one introduced in Whiteley *et al.* [65], that is reproduced in Fig. 2.1. We have two apertures of radii R_1 and R_2 (located by the vectors $\mathbf{r}_{a1}$ and $\mathbf{r}_{a2}$) observing two different sources (located by the vectors $\mathbf{r}_{s1}$ and $\mathbf{r}_{s2}$) through a turbulent layer at altitude $\mathbf{z}_l$. A ray coming from the first (respectively the second) source and arriving at a point located by the vector $R_1\boldsymbol{\rho}_1$ (resp. $R_2\boldsymbol{\rho}_2$) with respect to the first (resp. the second) aperture center will pass by the point located by $\mathbf{q}_{1l}$ (resp. $\mathbf{q}_{2l}$) in the aperture footprint in the turbulent layer. The projected vectors $\mathbf{q}_{1l}$ and $\mathbf{q}_{2l}$ are expressed as

$$\mathbf{q}_{1l} = (1 - A_{1l})R_1\boldsymbol{\rho}_1\,, \tag{2.1}$$

$$\mathbf{q}_{2l} = (1 - A_{2l})R_2\boldsymbol{\rho}_2\,, \tag{2.2}$$

where A_{1l} and A_{2l} are the layer scaling factors

$$A_{1l} = \frac{z_l - \mathbf{r}_{a1} \cdot \hat{z}}{(\mathbf{r}_{s1} - \mathbf{r}_{a1}) \cdot \hat{z}}\,, \tag{2.3}$$

$$A_{2l} = \frac{z_l - \mathbf{r}_{a2} \cdot \hat{z}}{(\mathbf{r}_{s2} - \mathbf{r}_{a2}) \cdot \hat{z}}\,. \tag{2.4}$$

If $\mathbf{r}_{a1} = \mathbf{r}_{a2} = \mathbf{0}$, then Eq. (2.3) and Eq. (2.4) simplify into:

$$A_{1l} = \frac{z_l}{z_1} \tag{2.5}$$

$$A_{2l} = \frac{z_l}{z_2}, \tag{2.6}$$

with z_1 and z_2 the altitudes of the sources.
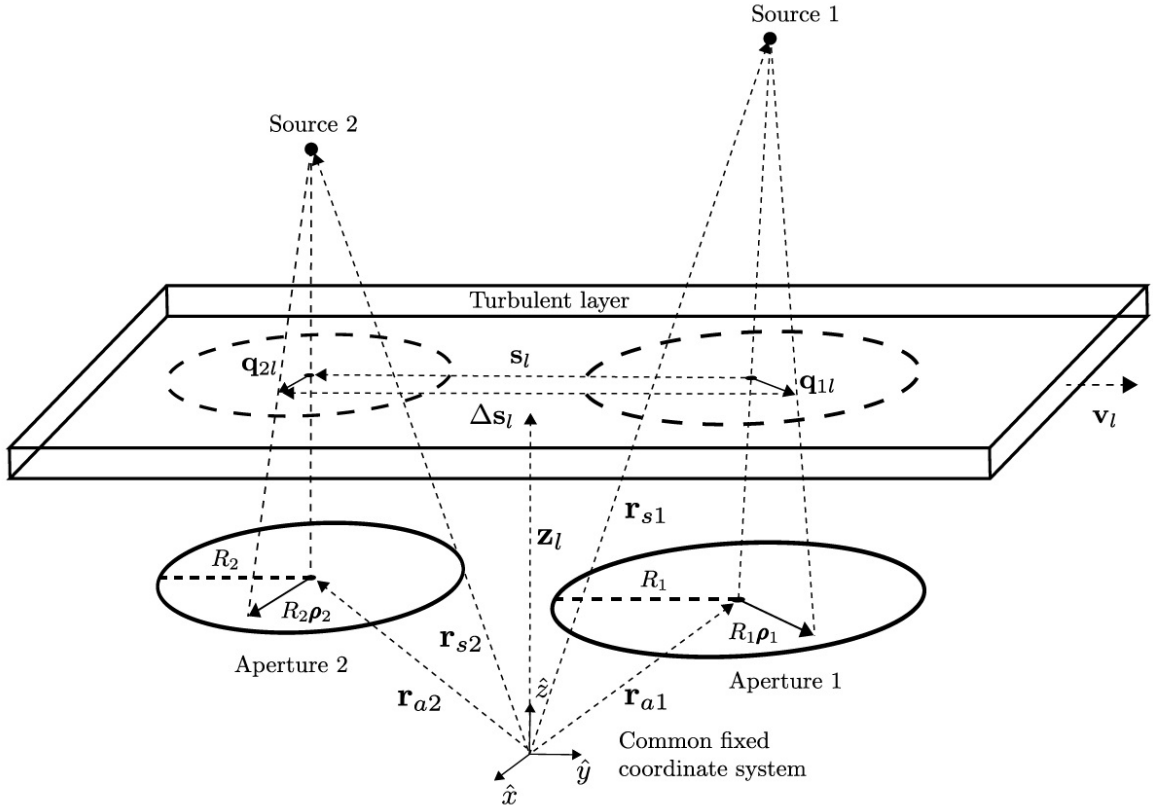
Fig. 2.1 Geometry used to compute the spatiotemporal CPSDs.

In the following, we will need to express the vector joining two points of the apertures footprints in the turbulent layer

$$\Delta \mathbf{s}_l = \mathbf{q}_{2l} - \mathbf{q}_{1l} + \mathbf{s}_l, \tag{2.7}$$

with $\mathbf{s}_l$ the vector joining the centers of the footprints

$$\mathbf{s}_l = \mathbf{r}_{a2} - \mathbf{r}_{a1} + \frac{z_l - \mathbf{r}_{a2} \cdot \hat{z}}{\mathbf{r}'_{s2} \cdot \hat{z}} \mathbf{r}'_{s2} - \frac{z_l - \mathbf{r}_{a1} \cdot \hat{z}}{\mathbf{r}'_{s1} \cdot \hat{z}} \mathbf{r}'_{s1}, \tag{2.8}$$

with $\mathbf{r}'_{s1} = \frac{\mathbf{r}_{s1} - \mathbf{r}_{a1}}{|\mathbf{r}_{s1} - \mathbf{r}_{a1}|}$ (resp. $\mathbf{r}'_{s2} = \frac{\mathbf{r}_{s2} - \mathbf{r}_{a2}}{|\mathbf{r}_{s2} - \mathbf{r}_{a2}|}$) the unitary vector from the center of aperture 1 (resp. 2) to source 1 (resp. 2). This formula allows to take into account the case of sources either at finite or infinite distance. In the following, we derive the covariance of the piston-removed phase, in order to then find the temporal CPSD of this same quantity.

2.2   Inter-aperture covariance of the piston-removed phase

In this section, we consider the whole phases ϕ_1 and ϕ_2 in the respective apertures 1 and 2, without any decomposition on wavefront modes. We define their piston-filtered covariance as

$$
\begin{aligned}
C_{\phi_1,\phi_2} = \mathrm{E}\Bigg\{ &\int \mathrm{d}\boldsymbol{\rho} \left(\phi_1(R_1\boldsymbol{\rho}) - \int \mathrm{d}\boldsymbol{\rho}' \phi_1(R_1\boldsymbol{\rho}') P(\boldsymbol{\rho}') \right) \\
&\times \left(\phi_2(R_2\boldsymbol{\rho}) - \int \mathrm{d}\boldsymbol{\rho}'' \phi_2(R_2\boldsymbol{\rho}'') P(\boldsymbol{\rho}'') \right) P(\boldsymbol{\rho}) \Bigg\},
\end{aligned}
\tag{2.9}
$$

where $\boldsymbol{\rho} = \boldsymbol{\rho}_1 = \boldsymbol{\rho}_2$ if one refers to Fig. 2.1. $\mathrm{E}\{\}$ is the mathematical expectation and $P(\boldsymbol{\rho})$ is the aperture weighting function:

$$
P(\boldsymbol{\rho}) = \begin{cases} \dfrac{1}{\pi} & \text{if } |\boldsymbol{\rho}| \le 1 \\[2mm] 0 & \text{otherwise}. \end{cases}
\tag{2.10}
$$

We develop Eq. (2.9):

$$
\begin{aligned}
C_{\phi_1,\phi_2} = &\int \mathrm{d}\boldsymbol{\rho}\, \mathrm{E}\left\{ \phi_1(R_1\boldsymbol{\rho})\phi_2(R_2\boldsymbol{\rho}) \right\} P(\boldsymbol{\rho}) \\
&- \int \mathrm{d}\boldsymbol{\rho} \int \mathrm{d}\boldsymbol{\rho}'\, \mathrm{E}\left\{ \phi_1(R_1\boldsymbol{\rho}')\phi_2(R_2\boldsymbol{\rho}) \right\} P(\boldsymbol{\rho}') P(\boldsymbol{\rho}) \\
&- \int \mathrm{d}\boldsymbol{\rho} \int \mathrm{d}\boldsymbol{\rho}''\, \mathrm{E}\left\{ \phi_1(R_1\boldsymbol{\rho})\phi_2(R_2\boldsymbol{\rho}'') \right\} P(\boldsymbol{\rho}'') P(\boldsymbol{\rho}) \\
&+ \int \mathrm{d}\boldsymbol{\rho}\, P(\boldsymbol{\rho}) \int \mathrm{d}\boldsymbol{\rho}' \int \mathrm{d}\boldsymbol{\rho}''\, \mathrm{E}\left\{ \phi_1(R_1\boldsymbol{\rho}')\phi_2(R_2\boldsymbol{\rho}'') \right\} \\
&\times P(\boldsymbol{\rho}') P(\boldsymbol{\rho}'').
\end{aligned}
\tag{2.11}
$$

We notice that the second, the third and the last integral are equivalent, given that $\int \mathrm{d}\boldsymbol{\rho}\, P(\boldsymbol{\rho}) = 1$. Besides, C_{ϕ_1,ϕ_2} depends on the phase cross-correlation that, when considering independent turbulent layers, can be expressed as

$$
\mathrm{E}\left\{ \phi_1(R_1\boldsymbol{\rho}_1)\phi_2(R_2\boldsymbol{\rho}_2) \right\} = \sum_l B_{\phi_l}(\mathbf{q}_{1l}, \mathbf{q}_{2l}),
\tag{2.12}
$$

with $\mathbf{q}_{1l}$ and $\mathbf{q}_{2l}$ as defined by Eq. (2.1) and Eq. (2.2). Assuming that the turbulent phase is spatially stationary, the cross-correlation $B_{\phi_l}(\mathbf{q}_{1l}, \mathbf{q}_{2l})$ only depends on the vector separating the two considered points:

$$B_{\phi_l}(\mathbf{q}_{1l}, \mathbf{q}_{2l}) = B_{\phi_l}(\Delta\mathbf{s}_l) = B_{\phi_l}(\mathbf{q}_{2l} - \mathbf{q}_{1l} + \mathbf{s}_l). \tag{2.13}$$

We then have:

$$\begin{aligned}
C_{\phi_1,\phi_2} = \sum_l C_{\phi_1,\phi_2,l} = \sum_l &\left[\frac{1}{R_1(1 - A_{1l})} \int d\mathbf{q}_{1l} \right. \\
&\times B_{\phi_l}(\mathbf{q}_{2l} - \mathbf{q}_{1l} + \mathbf{s}_l) P\left(\frac{\mathbf{q}_{1l}}{R_1(1 - A_{1l})} \right) \\
&- \frac{1}{R_1 R_2(1 - A_{1l})(1 - A_{2l})} \int d\mathbf{q}_{1l} \int d\mathbf{q}'_{2l} \\
&\times B_{\phi_l}(\mathbf{q}'_{2l} - \mathbf{q}_{1l} + \mathbf{s}_l) P\left(\frac{\mathbf{q}'_{2l}}{R_2(1 - A_{2l})} \right) \\
&\left. \times P\left(\frac{\mathbf{q}_{1l}}{R_1(1 - A_{1l})} \right) \right],
\end{aligned} \tag{2.14}$$

with $\mathbf{q}'_{2l} = (1 - A_{2l})R_2\boldsymbol{\rho}''$. Since $\boldsymbol{\rho} = \boldsymbol{\rho}_1 = \boldsymbol{\rho}_2$, we must have:

$$\mathbf{q}_{2l} = (1 - A_{2l})R_2\boldsymbol{\rho} = \frac{(1 - A_{2l})R_2}{(1 - A_{1l})R_1} \mathbf{q}_{1l} = K\mathbf{q}_{1l}. \tag{2.15}$$

We evaluate the first integral using the variable change $\mathbf{q} = (K - 1)\mathbf{q}_{1l}$:

$$\begin{aligned}
T_1 &= \frac{1}{R_1(1 - A_{1l})} \int d\mathbf{q}_{1l} B_{\phi_l}(\mathbf{q}_{2l} - \mathbf{q}_{1l} + \mathbf{s}_l) P\left(\frac{\mathbf{q}_{1l}}{R_1(1 - A_{1l})} \right) \\
&= \frac{1}{R_1(1 - A_{1l})(K - 1)} \int d\mathbf{q} B_{\phi_l}(\mathbf{q} + \mathbf{s}_l) \\
&\times P\left(\frac{\mathbf{q}}{R_1(1 - A_{1l})(K - 1)} \right).
\end{aligned} \tag{2.16}$$

Using Parseval's theorem, we can write T_1 as

$$\begin{aligned}
T_1 = &\frac{1}{R_1(1 - A_{1l})(K - 1)} \int d\mathbf{f} \, \mathrm{FT}\{B_{\phi_l}(\mathbf{q} + \mathbf{s}_l)\}^* \\
&\times \mathrm{FT}\left\{ P\left(\frac{\mathbf{q}}{R_1(1 - A_{1l})(K - 1)} \right) \right\},
\end{aligned} \tag{2.17}$$

where FT{ } is the Fourier transform (from $\mathbf{q}$ to $\mathbf{f}$ in this case). The Fourier transform of the phase correlation is given by Wiener-Khinchin's theorem

$$\text{FT}\left\{B_{\phi_l}(\mathbf{q} + \mathbf{s}_l)\right\} = W_{\phi_l}(\mathbf{f}) \exp[2i\pi\mathbf{f}\cdot\mathbf{s}_l], \tag{2.18}$$

where W_{ϕ_l} is the spatial power spectrum of the turbulent phase in the layer l, often assumed to follow Von Karman model [58]

$$W_{\phi_l}(f) = \left[\frac{24}{5}\Gamma\left(\frac{6}{5}\right)\right]^{\frac{5}{6}} \frac{\Gamma\left(\frac{11}{6}\right)^2}{2\pi^{\frac{11}{3}}} r_{0_l}^{-\frac{5}{3}} \left(f^2 + \frac{1}{L_0^2}\right)^{-\frac{11}{6}}, \tag{2.19}$$

with $\Gamma(\ )$ the gamma function, r_{0_l} the Fried parameter for the layer l and L_0 the outer scale. Hence, we finally have

$$T_1 = \int d\mathbf{f}\, W_{\phi_l}(\mathbf{f}) \exp[-2i\pi\mathbf{f}\cdot\mathbf{s}_l] \frac{J_1\left(2\pi R_1(1 - A_{1l})(K - 1)f\right)}{\pi R_1(1 - A_{1l})(K - 1)f}, \tag{2.20}$$

with J_1 the Bessel function of the first kind and order 1. The second integral to evaluate is

$$\begin{aligned}
T_2 = \frac{1}{R_1 R_2(1 - A_{1l})(1 - A_{2l})} \int d\mathbf{q}_{1l} \int d\mathbf{q}'_{2l} B_{\phi_l}(\mathbf{q}'_{2l} - \mathbf{q}_{1l} + \mathbf{s}_l) \\
\times P\left(\frac{\mathbf{q}'_{2l}}{R_2(1 - A_{2l})}\right) P\left(\frac{\mathbf{q}_{1l}}{R_1(1 - A_{1l})}\right).
\end{aligned} \tag{2.21}$$

Again, using Parseval's and Wiener-Khinchin's theorems with a Fourier transform on $\mathbf{q}'_{2l}$, we find

$$\begin{aligned}
T_2 = \frac{1}{R_1(1 - A_{1l})} \int d\mathbf{q}_{1l} \int d\mathbf{f}\, W_{\phi_l}(\mathbf{f}) \exp[2i\pi\mathbf{f}\cdot(\mathbf{q}_{1l} - \mathbf{s}_l)] \\
\times \frac{J_1\left(2\pi R_2(1 - A_{2l})f\right)}{\pi R_2(1 - A_{2l})f} P\left(\frac{\mathbf{q}_{1l}}{R_1(1 - A_{1l})}\right).
\end{aligned} \tag{2.22}$$

When re-ordering the integrals, one finds a Fourier transform in $\mathbf{q}_{1l}$, leading to

$$\begin{aligned}
T_2 = \int d\mathbf{f}\, W_{\phi_l}(\mathbf{f}) \exp[-2i\pi\mathbf{f}\cdot\mathbf{s}_l] \frac{J_1\left(2\pi R_1(1 - A_{1l})f\right)}{\pi R_1(1 - A_{1l})f} \\
\times \frac{J_1\left(2\pi R_2(1 - A_{2l})f\right)}{\pi R_2(1 - A_{2l})f}.
\end{aligned} \tag{2.23}$$

The piston-filtered covariance for the layer l is then

$$
\begin{aligned}
C_{\phi_1,\phi_2,l} = T_1 - T_2 = \int \mathrm{d}\mathbf{f}\, W_{\phi_l}(\mathbf{f}) \exp[-2i\pi\mathbf{f}\cdot\mathbf{s}_l] \\
\times \left[\frac{J_1\left(2\pi R_1(1-A_{1l})(K-1)f\right)}{\pi R_1(1-A_{1l})(K-1)f} \right. \\
\left. - \frac{J_1\left(2\pi R_1(1-A_{1l})f\right)}{\pi R_1(1-A_{1l})f} \frac{J_1\left(2\pi R_2(1-A_{2l})f\right)}{\pi R_2(1-A_{2l})f} \right].
\end{aligned}
\tag{2.24}
$$

For a single aperture and sources at infinity, the last term of the integral becomes the classical filter function for piston removal $1 - \left[\frac{J_1(2\pi Rf)}{\pi Rf}\right]^2$ [57] (we remind that $\frac{J_1(0)}{0} = 1$). When integrating over the angle, we find

$$
\begin{aligned}
C_{\phi_1,\phi_2,l} = 2\pi \int_0^\infty f \mathrm{d}f\, W_{\phi_l}(f) J_0\left(2\pi f s_l\right) \\
\times \left[\frac{J_1\left(2\pi R_1(1-A_{1l})(K-1)f\right)}{\pi R_1(1-A_{1l})(K-1)f} \right. \\
\left. - \frac{J_1\left(2\pi R_1(1-A_{1l})f\right)}{\pi R_1(1-A_{1l})f} \frac{J_1\left(2\pi R_2(1-A_{2l})f\right)}{\pi R_2(1-A_{2l})f} \right].
\end{aligned}
\tag{2.25}
$$

2.3   Spatiotemporal cross power spectrum of the piston-removed phase

We now consider that we observe the first source at a time $t = 0$ and the second source at $t = \tau$. Here, we assume a motion of the turbulent layer following Taylor's frozen flow hypothesis along the wind vector $\mathbf{v}_l$ (Fig. 2.1), while the sources and apertures remain fixed. We can then define the effective footprint separation as a function of τ in the layer l:

$$
\mathbf{s}'_l(\tau) = \mathbf{s}_l - \mathbf{v}_l \tau.
\tag{2.26}
$$

The spatiotemporal cross-correlation is then (from Eq. (2.24))

$$
\begin{aligned}
R_{\phi_1,\phi_2,l}(\tau) = \int \mathrm{d}\mathbf{f}\, W_{\phi_l}(\mathbf{f}) \exp[-2i\pi\mathbf{f}\cdot\mathbf{s}'_l(\tau)] \\
\times \left[\frac{J_1\left(2\pi R_1(1-A_{1l})(K-1)f\right)}{\pi R_1(1-A_{1l})(K-1)f} \right. \\
\left. - \frac{J_1\left(2\pi R_1(1-A_{1l})f\right)}{\pi R_1(1-A_{1l})f} \frac{J_1\left(2\pi R_2(1-A_{2l})f\right)}{\pi R_2(1-A_{2l})f} \right].
\end{aligned}
\tag{2.27}
$$

If $\tau = 0$, one retrieves $C_{\phi_1, \phi_2, l}$. The spatiotemporal CPSD of the piston-removed phase is the Fourier transform of its cross-correlation:

$$S_{\phi_1, \phi_2, l}(\nu) = \int \mathrm{d}\tau \, R_{\phi_1, \phi_2, l}(\tau) \exp[2i\pi\nu\tau], \qquad (2.28)$$

$$
\begin{aligned}
S_{\phi_1, \phi_2, l}(\nu) = \int \mathrm{d}\tau \int \mathrm{d}\mathbf{f} \, W_{\phi_l}(\mathbf{f}) \exp[-2i\pi\mathbf{f}\cdot\mathbf{s}'_l(\tau)] \\
\times \left[\frac{J_1\left(2\pi R_1(1 - A_{1l})(K-1)f\right)}{\pi R_1(1 - A_{1l})(K-1)f} \right. \\
\left. - \frac{J_1\left(2\pi R_1(1 - A_{1l})f\right)}{\pi R_1(1 - A_{1l})f} \frac{J_1\left(2\pi R_2(1 - A_{2l})f\right)}{\pi R_2(1 - A_{2l})f} \right] \\
\times \exp[2i\pi\nu\tau],
\end{aligned}
\qquad (2.29)
$$

where ν is the temporal frequency. We replace $\mathbf{s}'_l(\tau)$ with $\mathbf{s}_l - \mathbf{v}_l\tau$:

$$
\begin{aligned}
S_{\phi_1, \phi_2, l}(\nu) = \int \mathrm{d}\mathbf{f} \, W_{\phi_l}(\mathbf{f}) \exp[-2i\pi\mathbf{f}\cdot\mathbf{s}_l] \\
\times \left[\frac{J_1\left(2\pi R_1(1 - A_{1l})(K-1)f\right)}{\pi R_1(1 - A_{1l})(K-1)f} \right. \\
\left. - \frac{J_1\left(2\pi R_1(1 - A_{1l})f\right)}{\pi R_1(1 - A_{1l})f} \frac{J_1\left(2\pi R_2(1 - A_{2l})f\right)}{\pi R_2(1 - A_{2l})f} \right] \\
\times \int \mathrm{d}\tau \, \exp\left[2i\pi(\nu + \mathbf{f}\cdot\mathbf{v}_l)\tau\right].
\end{aligned}
\qquad (2.30)
$$

We now consider the components of $\mathbf{f}$, $\mathbf{f}_\perp$ and $\mathbf{f}_\parallel$, so that $\mathbf{f}_\perp$ is orthogonal to $\mathbf{v}_l$ and $\mathbf{f}_\parallel$ is parallel to $\mathbf{v}_l$ (see Fig. 2.2). We also define the unitary vector along the wind direction $\hat{u} = \frac{\mathbf{v}_l}{v_l}$. Equation (2.30) can be written as

$$
\begin{aligned}
S_{\phi_1, \phi_2, l}(\nu) = \int \mathrm{d}\mathbf{f}_\perp \int \mathrm{d}\mathbf{f}_\parallel \, W_{\phi_l}(\mathbf{f}_\parallel, \mathbf{f}_\perp) \exp[-2i\pi\mathbf{f}\cdot\mathbf{s}_l] \\
\times \left[\frac{J_1\left(2\pi R_1(1 - A_{1l})(K-1)f\right)}{\pi R_1(1 - A_{1l})(K-1)f} \right. \\
\left. - \frac{J_1\left(2\pi R_1(1 - A_{1l})f\right)}{\pi R_1(1 - A_{1l})f} \frac{J_1\left(2\pi R_2(1 - A_{2l})f\right)}{\pi R_2(1 - A_{2l})f} \right] \\
\times \int \mathrm{d}\tau \, \exp\left[2i\pi\left(\frac{\nu}{v_l} + \mathbf{f}_\parallel \cdot \hat{u}\right)v_l\tau\right].
\end{aligned}
\qquad (2.31)
$$

The last integral is a Dirac function. If we consider that $f_\parallel$ is positive when $\mathbf{f}_\parallel$ is pointing
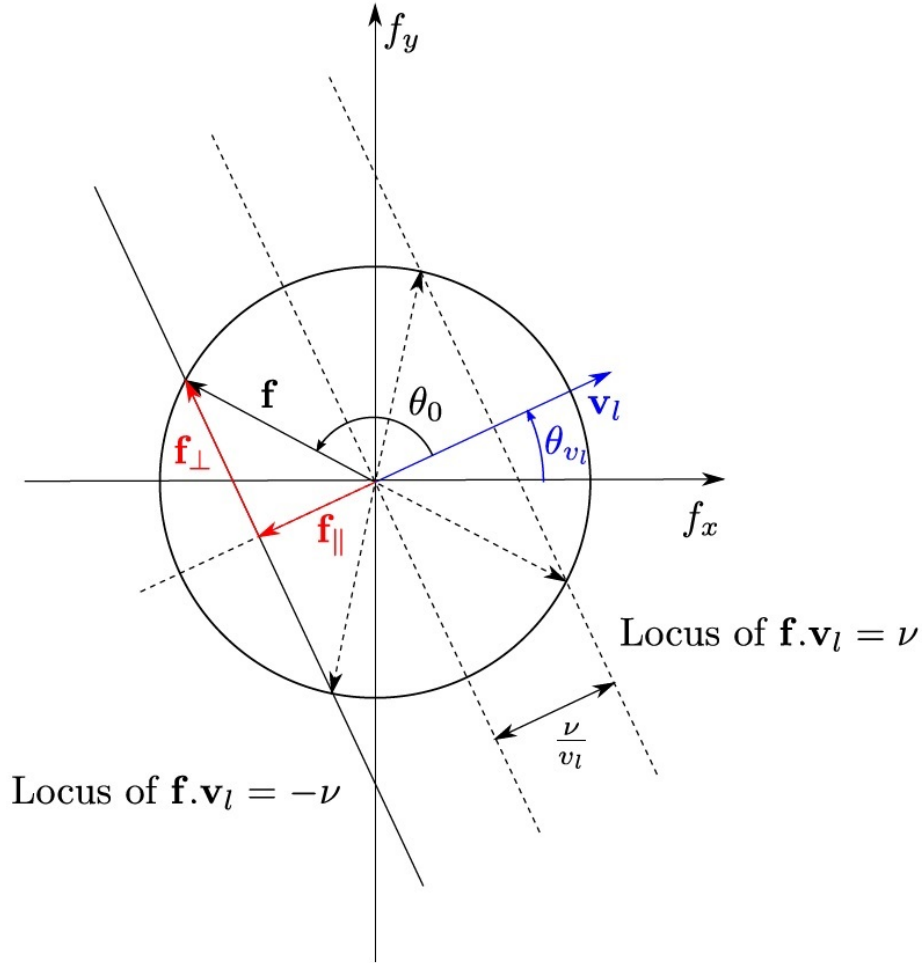
Fig. 2.2 Vectors and angles defined in the CPSD computation. Two lines represent the loci of $\mathbf{f} \cdot \mathbf{v}_l = \nu$ (dashed line on right-hand side) and $\mathbf{f} \cdot \mathbf{v}_l = -\nu$ (solid line), considering a positive ν. For a given frequency, the Dirac defined in Eq. (2.32) reduces the CPSD expression to the sum of 2 points, either on the left or the right side of the figure, that are indicated by $\mathbf{f}$ and the dashed vectors. In this figure, we have $\mathbf{f} = \mathbf{f}_1$ (see Eq. (2.33)).

towards the same direction as $\mathbf{v}_l$ and negative otherwise, then:

$$
\int \mathrm{d}\tau \, \exp\left[2i\pi\left(\frac{\nu}{\nu_l} + \mathbf{f}_\parallel \cdot \hat{u}\right)\nu_l\tau\right] = \frac{1}{\nu_l}\int \mathrm{d}t \, \exp\left[2i\pi\left(\frac{\nu}{\nu_l} + f_\parallel\right)t\right]
$$
$$
= \frac{1}{\nu_l}\delta\left(f_\parallel + \frac{\nu}{\nu_l}\right),
$$

(2.32)

where we made the variable change $t = \nu_l \tau$. We also define the sign of $f_\perp$: it is positive when the cross product $\mathbf{v}_l \times \mathbf{f}_\perp$ points towards the reader, and negative otherwise. Hence, replacing $f_\parallel$ with $-\frac{\nu}{\nu_l}$ and considering both signs for $f_\perp$, we find two frequency vectors that

satisfy the Dirac condition, $\mathbf{f_1}$ and $\mathbf{f_2}$, with a norm $f = f_1 = f_2 = \sqrt{f_\perp^2 + \left(\frac{v}{v_l}\right)^2}$ and respective angles $\theta_1 = \theta_0 + \theta_{v_l}$ and $\theta_2 = -\theta_0 + \theta_{v_l}$, with $\theta_0 = \mathrm{acos}\left(\frac{f_\parallel}{f}\right) = \mathrm{acos}\left(-\frac{v}{f v_l}\right)$ and θ_{v_l} the angle between $\mathbf{v}_l$ and the X axis. Equation (2.31) then becomes

$$
\begin{aligned}
S_{\phi_1,\phi_2,l}(v) =& \frac{1}{v_l} \int_0^\infty \mathrm{d}f_\perp \left[\frac{J_1\left(2\pi R_1(1-A_{1l})(K-1)f\right)}{\pi R_1(1-A_{1l})(K-1)f} \right. \\
& \left. - \frac{J_1\left(2\pi R_1(1-A_{1l})f\right)}{\pi R_1(1-A_{1l})f} \frac{J_1\left(2\pi R_2(1-A_{2l})f\right)}{\pi R_2(1-A_{2l})f} \right] \\
& \times \left\{ W_{\phi_l}\left(-\frac{v}{v_l}, f_\perp\right) \exp[-2i\pi \mathbf{f_1} \cdot \mathbf{s}_l] \right. \\
& \left. + W_{\phi_l}\left(-\frac{v}{v_l}, -f_\perp\right) \exp[-2i\pi \mathbf{f_2} \cdot \mathbf{s}_l] \right\}.
\end{aligned}
\tag{2.33}
$$

By definition, W_{ϕ_l} is a radial quantity, so $W_{\phi_l}\left(-\frac{v}{v_l}, f_\perp\right) = W_{\phi_l}\left(-\frac{v}{v_l}, -f_\perp\right) = W_{\phi_l}(f)$. We can thus write the final expression of the piston-removed phase CPSD as

$$
\begin{aligned}
S_{\phi_1,\phi_2,l}(v) =& \frac{1}{v_l} \int_0^\infty \mathrm{d}f_\perp \, W_{\phi_l}(f) \left[\frac{J_1\left(2\pi R_1(1-A_{1l})(K-1)f\right)}{\pi R_1(1-A_{1l})(K-1)f} \right. \\
& \left. - \frac{J_1\left(2\pi R_1(1-A_{1l})f\right)}{\pi R_1(1-A_{1l})f} \frac{J_1\left(2\pi R_2(1-A_{2l})f\right)}{\pi R_2(1-A_{2l})f} \right] \\
& \times \left\{ \exp\left[-2i\pi f s_l \cos(\theta_1 - \theta_{s_l})\right] \right. \\
& \left. + \exp\left[-2i\pi f s_l \cos(\theta_2 - \theta_{s_l})\right] \right\},
\end{aligned}
\tag{2.34}
$$

with θ_{s_l} the angle between $\mathbf{s}_l$ and the X axis. We can also write the CPSD value at the corresponding negative frequency:

$$
\begin{aligned}
S_{\phi_1,\phi_2,l}(-v) =& \frac{1}{v_l} \int_0^\infty \mathrm{d}f_\perp \, W_{\phi_l}(f) \left[\frac{J_1\left(2\pi R_1(1-A_{1l})(K-1)f\right)}{\pi R_1(1-A_{1l})(K-1)f} \right. \\
& \left. - \frac{J_1\left(2\pi R_1(1-A_{1l})f\right)}{\pi R_1(1-A_{1l})f} \frac{J_1\left(2\pi R_2(1-A_{2l})f\right)}{\pi R_2(1-A_{2l})f} \right] \\
& \times \left\{ \exp\left[-2i\pi f s_l \cos(\theta_3 - \theta_{s_l})\right] \right. \\
& \left. + \exp\left[-2i\pi f s_l \cos(\theta_4 - \theta_{s_l})\right] \right\},
\end{aligned}
\tag{2.35}
$$

with $\theta_3 = \pi + \theta_1 = \pi + \theta_0 + \theta_{v_l}$ and $\theta_4 = \pi + \theta_2 = \pi - \theta_0 + \theta_{v_l}$.

One can easily show that $S_{\phi_1,\phi_2,l}(-v)$ is the conjugate of $S_{\phi_1,\phi_2,l}(v)$. We then have $\int_{-\infty}^\infty \mathrm{d}v S_{\phi_1,\phi_2,l}(v) = \int_0^\infty \mathrm{d}v S'_{\phi_1,\phi_2,l}(v) = C_{\phi_1,\phi_2,l}$, with $S'_{\phi_1,\phi_2,l}(v) = 2\,\mathrm{Re}\left[S_{\phi_1,\phi_2,l}(v)\right]$, where

Re[ ] is the real part, that is:

$$
\begin{aligned}
S'_{\phi_1,\phi_2,l}(\nu) = \frac{2}{\nu_l} \int_0^\infty \mathrm{d}f_\perp \; W_{\phi_l}(f) &\left[\frac{J_1\left(2\pi R_1(1-A_{1l})(K-1)f\right)}{\pi R_1(1-A_{1l})(K-1)f} \right. \\
&\left. - \frac{J_1\left(2\pi R_1(1-A_{1l})f\right)}{\pi R_1(1-A_{1l})f} \frac{J_1\left(2\pi R_2(1-A_{2l})f\right)}{\pi R_2(1-A_{2l})f} \right] \\
&\times \left\{ \cos\left[2\pi f s_l \cos(\theta_1 - \theta_{s_l})\right] \right. \\
&\left. + \cos\left[2\pi f s_l \cos(\theta_2 - \theta_{s_l})\right] \right\}.
\end{aligned}
\tag{2.36}
$$

Using the classical trigonometry formulas for the combination of sinusoids, we can write Eq. (2.36) as

$$
\begin{aligned}
S'_{\phi_1,\phi_2,l}(\nu) = \frac{4}{\nu_l} \int_0^\infty \mathrm{d}f_\perp \; W_{\phi_l}(f) &\left[\frac{J_1\left(2\pi R_1(1-A_{1l})(K-1)f\right)}{\pi R_1(1-A_{1l})(K-1)f} \right. \\
&\left. - \frac{J_1\left(2\pi R_1(1-A_{1l})f\right)}{\pi R_1(1-A_{1l})f} \frac{J_1\left(2\pi R_2(1-A_{2l})f\right)}{\pi R_2(1-A_{2l})f} \right] \\
&\times \cos\left[2\pi f s_l \cos(\theta_{\nu_l} - \theta_{s_l}) \cos(\theta_0)\right] \\
&\times \cos\left[2\pi f s_l \sin(\theta_{\nu_l} - \theta_{s_l}) \sin(\theta_0)\right],
\end{aligned}
\tag{2.37}
$$

or equivalently:

$$
\begin{aligned}
S'_{\phi_1,\phi_2,l}(\nu) = \frac{4}{\nu_l} \cos\left[2\pi\nu\frac{s_l}{\nu_l}\cos(\Delta\theta)\right] \int_0^\infty \mathrm{d}f_\perp \; W_{\phi_l}(f) \\
\times \left[\frac{J_1\left(2\pi R_1(1-A_{1l})(K-1)f\right)}{\pi R_1(1-A_{1l})(K-1)f} \right. \\
\left. - \frac{J_1\left(2\pi R_1(1-A_{1l})f\right)}{\pi R_1(1-A_{1l})f} \frac{J_1\left(2\pi R_2(1-A_{2l})f\right)}{\pi R_2(1-A_{2l})f} \right] \\
\times \cos\left[2\pi f_\perp s_l \sin(\Delta\theta)\right],
\end{aligned}
\tag{2.38}
$$

with $\Delta\theta = \theta_{\nu_l} - \theta_{s_l}$.

In Fig. 2.3, we show the CPSD of the piston-removed phase as derived from Eq. (2.38). We considered a single-layer turbulent profile with $r_0 = 16$ cm, $L_0 = \infty$, $z_l = 10$ km, $\nu_l = 10$ m/s, $\theta_{\nu_l} = 0°$ and both a single 8-m aperture and two 8-m apertures looking at one source at infinity. We retrieve the $\nu^{-8/3}$ power law at high frequencies, as shown in Section 1.1.3 for the full turbulent phase (the piston contribution is negligible at high frequencies). At low temporal frequencies, we get a $\nu^{-2/3}$ power law that reflects the major contribution of tip-tilt due to the piston filtering. We also note that the frequencies ν_0, representing the transition from correlation to anti-correlation (and vice versa), show a dependence on the

apertures separation. From the formula, we also find a dependence on the wind velocity and $\Delta\theta$. The complete expression is: $\nu_0 = \dfrac{1}{4}\dfrac{\nu_l}{s_l}\dfrac{1}{\cos(\Delta\theta)}(1+2k)$, for any integer k.

In Appendix A.1, we verify our results through a comparison with end-to-end simulations.
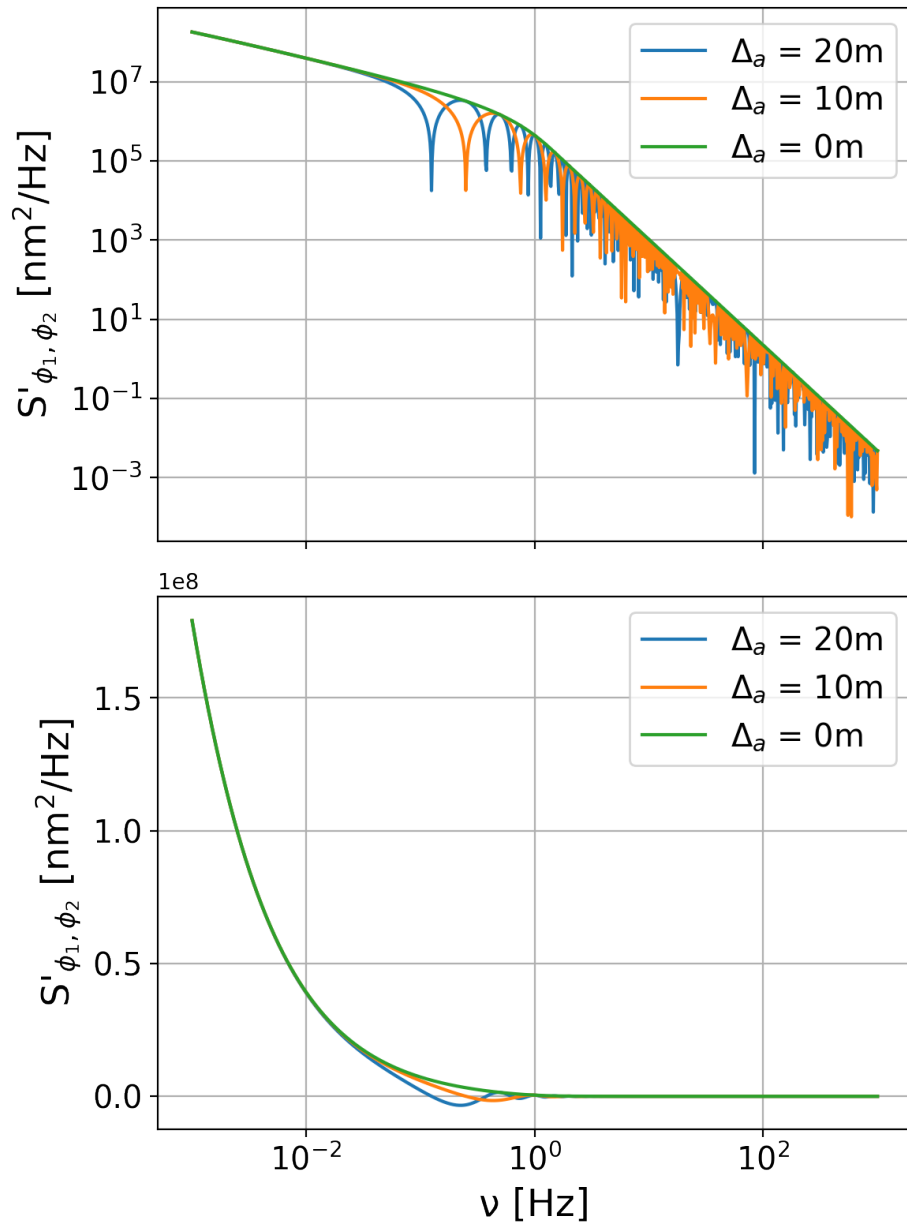

Fig. 2.3 CPSD of the piston-removed phase plotted in logarithmic (top) and linear (bottom) scales, for one aperture (green) and two apertures with a separation of 10 m (orange) and 20 m (blue) along the x-axis. The source is at (0", 0°, ∞) in cylindrical coordinates.

2.4 Spatiotemporal cross power spectrum of Zernike coefficients

We now use the geometry introduced in Fig. 2.2 to develop Whiteley *et al.*'s [65] equation describing the spatiotemporal CPSD of the Zernike coefficients:

$$
\begin{aligned}
S_{a_{1j},a_{2k},l}(\nu) = \int d\tau \int d\mathbf{f}\, W_{\phi_l}(\mathbf{f}) \exp[-2i\pi\mathbf{f}\cdot\mathbf{s}'_l(\tau)] \\
\times Q_j\,(R_1(1-A_{1l})\mathbf{f})\, Q_k^*\,(R_2(1-A_{2l})\mathbf{f}) \exp[2i\pi\nu\tau]\,,
\end{aligned}
\tag{2.39}
$$

where a_{1j} and a_{2k} are the coefficients representing, respectively, the phases ϕ_1 and ϕ_2 in the apertures 1 and 2:

$$
a_{1j} = \int d\boldsymbol{\rho}_1 \phi_1(R_1\boldsymbol{\rho}_1) Z_j(\boldsymbol{\rho}_1) P(\boldsymbol{\rho}_1)\,,
\tag{2.40}
$$

$$
a_{2k} = \int d\boldsymbol{\rho}_2 \phi_2(R_2\boldsymbol{\rho}_2) Z_k(\boldsymbol{\rho}_2) P(\boldsymbol{\rho}_2)\,,
\tag{2.41}
$$

and $Q_j(\mathbf{f})$ is the Fourier transform of $Z_j(\boldsymbol{\rho})P(\boldsymbol{\rho})$:

$$
\begin{aligned}
Q_j(f,\theta) = i^{m_j}\sqrt{n_j+1}(-1)^{(n_j-m_j)/2}\sqrt{2}^{\,1-\delta_{m_j 0}} \\
\times \frac{J_{n_j+1}(2\pi f)}{\pi f}\cos\left\{m_j\theta + \frac{\pi}{4}(1-\delta_{m_j 0})[(-1)^j - 1]\right\}\,,
\end{aligned}
\tag{2.42}
$$

with n_j and m_j the radial and azimuthal orders of Z_j and $\delta_{m_j 0}$ the Kronecker delta ($= 1$ if $m_j = 0$, $= 0$ otherwise).

Following the reasoning in Section 2.3, we find:

$$
\begin{aligned}
S_{a_{1j},a_{2k},l}(\nu) = \frac{1}{v_l}\int_0^\infty df_\perp\, W_{\phi_l}(f)\Big[\exp[-2i\pi\mathbf{f_1}\cdot\mathbf{s}_l] \\
\times Q_j\,(R_1(1-A_{1l})\mathbf{f_1})\, Q_k^*\,(R_2(1-A_{2l})\mathbf{f_1}) \\
+ \exp[-2i\pi\mathbf{f_2}\cdot\mathbf{s}_l] Q_j\,(R_1(1-A_{1l})\mathbf{f_2}) \\
\times Q_k^*\,(R_2(1-A_{2l})\mathbf{f_2})\Big]\,.
\end{aligned}
\tag{2.43}
$$

We now replace the expressions of Q_j and Q_k^* from Eq. (2.42), in order to find the final

formula of Zernike coefficients CPSD. We obtain:

$$
\begin{aligned}
S_{a_{1j},a_{2k},l}(\nu) = {} & (-1)^{m_k} i^{n_j+n_k} \sqrt{(n_j+1)(n_k+1)} 2^{1-(\delta_{m_j0}+\delta_{m_k0})/2} \\
& \times \left[\nu_l \pi^2 R_1 R_2 (1-A_{1l})(1-A_{2l}) \right]^{-1} \int_0^\infty \frac{\mathrm{d}f_\perp}{f^2} \\
& \times W_{\phi_l}(f) J_{n_j+1}\left(2\pi R_1(1-A_{1l})f\right) J_{n_k+1}\left(2\pi R_2(1-A_{2l})f\right) \\
& \times \Bigg[\exp[-2i\pi f s_l \cos(\theta_1 - \theta_{s_l})] \\
& \times \cos\left\{ m_j \theta_1 + \frac{\pi}{4}(1-\delta_{m_j0})[(-1)^j - 1] \right\} \\
& \times \cos\left\{ m_k \theta_1 + \frac{\pi}{4}(1-\delta_{m_k0})[(-1)^k - 1] \right\} \\
& + \exp[-2i\pi f s_l \cos(\theta_2 - \theta_{s_l})] \\
& \times \cos\left\{ m_j \theta_2 + \frac{\pi}{4}(1-\delta_{m_j0})[(-1)^j - 1] \right\} \\
& \times \cos\left\{ m_k \theta_2 + \frac{\pi}{4}(1-\delta_{m_k0})[(-1)^k - 1] \right\} \Bigg].
\end{aligned}
\tag{2.44}
$$

In the specific case of one aperture of radius R, one source only at infinity, $j = k$ and a wind along the X axis, we have:

$$
\begin{aligned}
S_{a_j,a_j,l}(\nu) = {} & (n_j+1)\frac{2^{2-\delta_{m_j0}}}{\nu_l \pi^2 R^2} \int_0^\infty \frac{\mathrm{d}f_\perp}{f^2} W_{\phi_l}(f) J_{n_j+1}\left(2\pi R f\right)^2 \\
& \times \cos^2\left\{ m_j \theta_0 + \frac{\pi}{4}(1-\delta_{m_j0})[(-1)^j - 1] \right\},
\end{aligned}
\tag{2.45}
$$

that is equivalent to the combination of Eqs.(8) and (27) in Conan *et al.* [13], with $f_\perp = f_y$.

Keeping the same assumptions, we also derive the PSD of the differential piston between two apertures of same radius. Assuming a homogeneous and isotropic turbulence, one can demonstrate that this PSD is equal to (with $j = k = 1$ for the piston)

$$
\begin{aligned}
S_{dpist,l}(\nu) &= S_{a_{11},a_{11},l}(\nu) - S_{a_{11},a_{21},l}(\nu) - S_{a_{21},a_{11},l}(\nu) + S_{a_{21},a_{21},l}(\nu) \\
&= 2\left\{ S_{a_{11},a_{11},l}(\nu) - \mathrm{Re}\left[S_{a_{11},a_{21},l}(\nu) \right] \right\},
\end{aligned}
\tag{2.46}
$$

that is

$$
S_{dpist,l}(\nu) = \frac{4}{\nu_l \pi^2 R^2} \int_0^\infty \frac{\mathrm{d}f_\perp}{f^2} W_{\phi_l}(f) J_1\left(2\pi R f\right)^2 [1 - \cos(2\pi f s_l)],
\tag{2.47}
$$

hence

$$
S_{dpist,l}(\nu) = \frac{8}{\nu_l \pi^2 R^2} \int_0^\infty \frac{\mathrm{d}f_\perp}{f^2} W_{\phi_l}(f) J_1\left(2\pi R f\right)^2 \sin\left(\pi\nu \frac{s_l}{\nu_l}\right)^2,
\tag{2.48}
$$

which is equivalent to Eq. (19) in Conan *et al.* [13] with $s_l = B$.

As in section 2.3, we also compute $S'_{a_{1j},a_{2k},l}$, defined in the same way as $S'_{\phi_1,\phi_2,l}$. Indeed, in this case as well, one can verify that $S_{a_{1j},a_{2k},l}(-\nu) = S_{a_{1j},a_{2k},l}(\nu)^*$. The expression of $S'_{a_{1j},a_{2k},l}$ depends on the parity of $n_j + n_k$:

- if $n_j + n_k$ is even:

$$
\begin{aligned}
S'_{a_{1j},a_{2k},l}(\nu) =& (-1)^{m_k} i^{n_j+n_k} \sqrt{(n_j+1)(n_k+1)} 2^{2-(\delta_{m_j 0}+\delta_{m_k 0})/2} \\
&\times \left[\nu_l \pi^2 R_1 R_2 (1-A_{1l})(1-A_{2l}) \right]^{-1} \\
&\times \int_0^\infty \frac{\mathrm{d}f_\perp}{f^2} W_{\phi_l}(f) J_{n_j+1}\left(2\pi R_1(1-A_{1l})f\right) \\
&\times J_{n_k+1}\left(2\pi R_2(1-A_{2l})f\right) \\
&\times \Big[\cos[2\pi f s_l \cos(\theta_1 - \theta_{s_l})] \\
&\times \cos\left\{ m_j\theta_1 + \frac{\pi}{4}(1-\delta_{m_j 0})[(-1)^j - 1] \right\} \\
&\times \cos\left\{ m_k\theta_1 + \frac{\pi}{4}(1-\delta_{m_k 0})[(-1)^k - 1] \right\} \\
&+ \cos[2\pi f s_l \cos(\theta_2 - \theta_{s_l})] \\
&\times \cos\left\{ m_j\theta_2 + \frac{\pi}{4}(1-\delta_{m_j 0})[(-1)^j - 1] \right\} \\
&\times \cos\left\{ m_k\theta_2 + \frac{\pi}{4}(1-\delta_{m_k 0})[(-1)^k - 1] \right\} \Big];
\end{aligned}
\tag{2.49}
$$

- if $n_j + n_k$ is odd:

$$
\begin{aligned}
S'_{a_{1j},a_{2k},l}(\nu) =& (-1)^{m_k} i^{n_j+n_k-1} \sqrt{(n_j+1)(n_k+1)} 2^{2-(\delta_{m_j 0}+\delta_{m_k 0})/2} \\
&\times \left[\nu_l \pi^2 R_1 R_2 (1-A_{1l})(1-A_{2l}) \right]^{-1} \\
&\times \int_0^\infty \frac{\mathrm{d}f_\perp}{f^2} W_{\phi_l}(f) J_{n_j+1}\left(2\pi R_1(1-A_{1l})f\right) \\
&\times J_{n_k+1}\left(2\pi R_2(1-A_{2l})f\right) \\
&\times \Big[\sin[2\pi f s_l \cos(\theta_1 - \theta_{s_l})] \\
&\times \cos\left\{ m_j\theta_1 + \frac{\pi}{4}(1-\delta_{m_j 0})[(-1)^j - 1] \right\} \\
&\times \cos\left\{ m_k\theta_1 + \frac{\pi}{4}(1-\delta_{m_k 0})[(-1)^k - 1] \right\} \\
&+ \sin[2\pi f s_l \cos(\theta_2 - \theta_{s_l})] \\
&\times \cos\left\{ m_j\theta_2 + \frac{\pi}{4}(1-\delta_{m_j 0})[(-1)^j - 1] \right\} \\
&\times \cos\left\{ m_k\theta_2 + \frac{\pi}{4}(1-\delta_{m_k 0})[(-1)^k - 1] \right\} \Big].
\end{aligned}
\tag{2.50}
$$

We derive the general formula:

$$
\begin{aligned}
S'_{a_{1j},a_{2k},l}(\nu) =& (-1)^{m_k} i^{n_j+n_k+\left[(-1)^{n_j+n_k}-1\right]/2} \sqrt{(n_j+1)(n_k+1)}\, 2^{2-(\delta_{m_j0}+\delta_{m_k0})/2} \\
& \times \left[\nu_l \pi^2 R_1 R_2 (1-A_{1l})(1-A_{2l}) \right]^{-1} \\
& \times \int_0^\infty \frac{\mathrm{d}f_\perp}{f^2}\, W_{\phi_l}(f) J_{n_j+1}\left(2\pi R_1(1-A_{1l})f \right) \\
& \times J_{n_k+1}\left(2\pi R_2(1-A_{2l})f \right) \\
& \times \left[\cos\left\{ 2\pi f s_l \cos(\theta_1-\theta_{s_l}) + \frac{\pi}{4}[(-1)^{n_j+n_k}-1] \right\} \right. \\
& \times \cos\left\{ m_j\theta_1 + \frac{\pi}{4}(1-\delta_{m_j0})[(-1)^j-1] \right\} \\
& \times \cos\left\{ m_k\theta_1 + \frac{\pi}{4}(1-\delta_{m_k0})[(-1)^k-1] \right\} \\
& + \cos\left\{ 2\pi f s_l \cos(\theta_2-\theta_{s_l}) + \frac{\pi}{4}[(-1)^{n_j+n_k}-1] \right\} \\
& \times \cos\left\{ m_j\theta_2 + \frac{\pi}{4}(1-\delta_{m_j0})[(-1)^j-1] \right\} \\
& \left. \times \cos\left\{ m_k\theta_2 + \frac{\pi}{4}(1-\delta_{m_k0})[(-1)^k-1] \right\} \right].
\end{aligned}
\tag{2.51}
$$

In Fig. 2.4, we show the CPSDs of tip-tip ($j = 2$, $k = 2$) and tip-defocus ($j = 2$, $k = 4$).

In Fig. 2.5, we show the CPSDs of coma-coma ($j = 8$, $k = 8$) and coma-tip ($j = 8$, $k = 2$). We used the same parameters as in Fig. 2.3. The curves behavior is in agreement with Conan *et al.* [13], indeed we retrieve the following power-laws: $\nu^{-17/3}$ at the high frequencies for both $S'_{2,2}$ and $S'_{8,8}$ and, at the low frequencies, $\nu^{-2/3}$ for $S'_{2,2}$ and ν^{+2} for $S'_{8,8}$. The CPSDs zeros are at $\nu_0 = \frac{1}{2}\frac{\nu_l}{s_l}\left\{ \frac{1}{2} - \frac{1}{4}\left[(-1)^{n_j+n_k}-1\right] + k \right\}$, for any integer k. This expression holds only for $\Delta\theta = 0$, as we were unable to derive a general expression for $\Delta\theta \neq 0$. It is also worth noting that the cutoff frequency of Zernike temporal PSD derived in Conan *et al.* and reported in Eq. (1.43) is still valid for CPSDs.

In Appendix A.1, we verify our results through a comparison with end-to-end simulations.

2.5 A first application of CPSDs: time-filtered anisoplanatism in a SCAO loop

In this section, we propose an analytical method that requires the CPSDs to estimate the wavefront residuals that are left by a SCAO system sensing the turbulence-induced distortions from an off-axis reference star. The approach allows to estimate residuals that
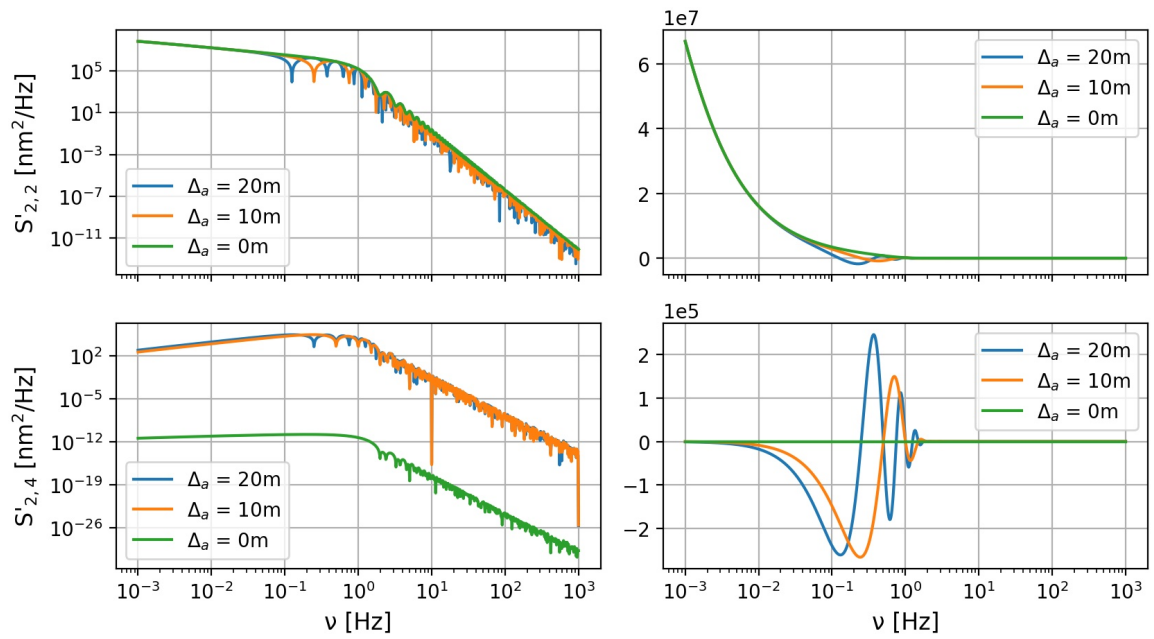
Fig. 2.4 CPSD of tip-tip (top) and tip-defocus (bottom), plotted in logarithmic (left) and linear (right) scales. The aperture-source configuration and the turbulence profile are the same as Fig. 2.3.

Fig. 2.5 CPSD of coma-coma (top) and coma-tip (bottom), plotted in logarithmic (left) and linear (right) scales. The aperture-source configuration and the turbulence profile are the same as Fig. 2.3.
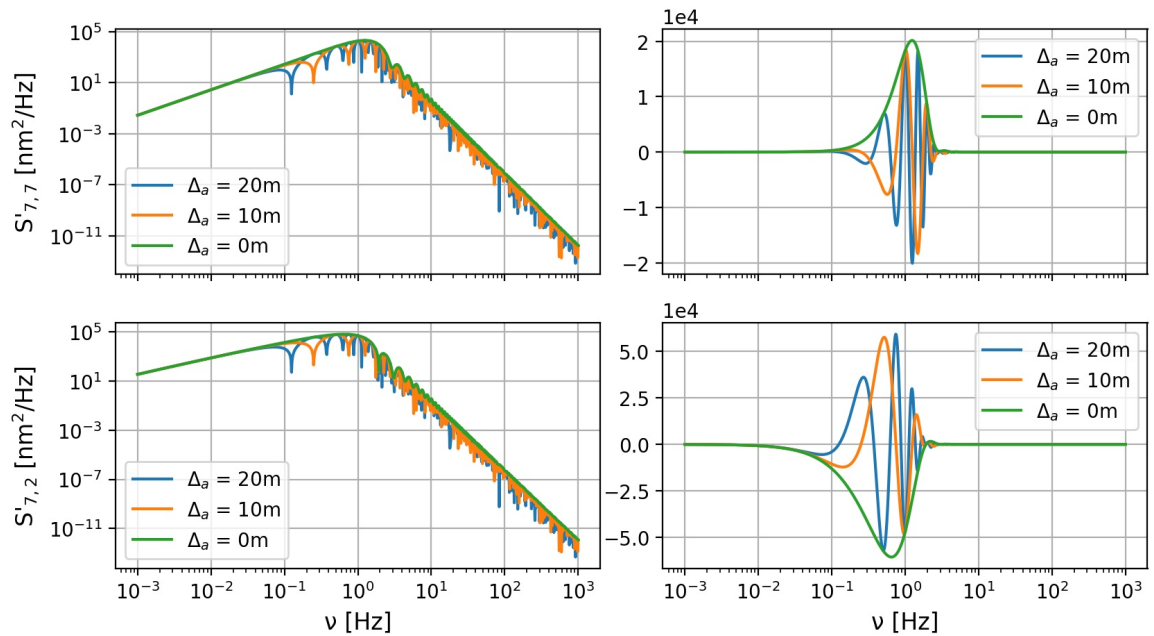
are due to anisoplanatism, to temporal filtering of the AO control and to WFS noise. We neglect other sources of error (fitting error, aliasing error, ...), as they are beyond the scope of our application.

Though some approaches consider the correlation between anisoplanatism and temporal errors [80–83], these two terms are often studied separately [20, 21, 34, 77–79]. The former is usually evaluated from the covariances of the turbulent phase [21, 77, 85]. The latter is determined from the AO control filtering of the temporal Power Spectral Density (PSD) of the turbulence (Eq. (6.36) in Madec [20]) and it represents the error left on the guide star. Through the CPSDs though, we are able to study the temporal and the spatial errors together and estimate anisoplanatism as affected by the temporal filtering of the adaptive optics correction.

In the following, we develop these computations and we show the difference between the anisoplanatism error as computed through the covariances or using the CPSDs. We consider either a single-aperture or a two-aperture interferometric telescope.

2.5.1 Time-filtered anisoplanatism for a single-aperture telescope

We consider an aperture observing a target on axis and sensing the phase aberrations from an off-axis NGS.

The residual phase on target is given by the difference between the turbulent phase on target and the correction phase estimated from the NGS:

$$\phi_{res}^{\alpha}(v) = \phi_{turb}^{\alpha}(v) - \phi_{corr}(v), \tag{2.52}$$

where α identifies the direction of the target. The correction phase can be derived as

$$\begin{aligned}\phi_a(v) &= \phi_{turb}^{\theta}(v) - \phi_{res}^{\theta}(v) \\ &= \phi_{turb}^{\theta}(v) - H_r(v)\phi_{turb}^{\theta}(v) + H_n(v)\phi_n(v) \\ &= H_n(v)\left(\phi_{turb}^{\theta}(v) + \phi_n(v)\right).\end{aligned} \tag{2.53}$$

where ϕ_{turb}^{θ} is the turbulent phase in the direction of the NGS, ϕ_n is the WFS noise, H_n is the NTF and where we used Eq. (1.53) to express ϕ_{res}^{θ}. Substituting Eq. (2.53) in Eq. (2.52) leads to:

$$\begin{aligned}\phi_{res}^{\alpha}(v) &= \phi_{turb}^{\alpha}(v) - H_n(v)\left(\phi_{turb}^{\theta}(v) + \phi_n(v)\right) \\ &= (H_r(v) + H_n(v))\,\phi_{turb}^{\alpha}(v) - H_n(v)\phi_{turb}^{\theta}(v) - H_n(v)\phi_n(v) \\ &= H_r(v)\phi_{turb}^{\alpha}(v) + H_n(v)\left(\phi_{turb}^{\alpha}(v) - \phi_{turb}^{\theta}(v) - \phi_n(v)\right),\end{aligned} \tag{2.54}$$

where ϕ^{α}_{turb} is the turbulent phase in the direction of the target and where we used the relationship for the transfer functions defined in Eq. (1.56). It is worth noting that anisoplanatism, described in the equation by the difference between ϕ^{α}_{turb} and ϕ^{θ}_{turb}, is filtered as a noise by the AO loop.

From Eq. (2.54), we can compute the temporal PSD of the phase residuals on target as

$$
\begin{aligned}
S^{\alpha}_{res}(\nu) &= \left\langle \phi^{\alpha}_{res}(\nu)\, \phi^{\alpha}_{res}(\nu)^{\dagger} \right\rangle \\
&= |H_r(\nu)|^2 S_{turb}(\nu) + |H_n(\nu)|^2 S_n(\nu) + 2\operatorname{Re}\left[H_n(\nu)\left(S_{turb}(\nu) - S^{\theta,\alpha}_{turb}(\nu)\right)\right],
\end{aligned}
\tag{2.55}
$$

where $\langle \cdot \rangle$ is the mean, S_{turb} is the PSD of the turbulence, $S^{\alpha,\theta}_{turb}$ is the CPSD between the phase on the NGS and the phase on target and where we assumed no correlation between noise and turbulent phase. By assuming homogeneous and isotropic atmospheric turbulence, we considered $S^{\alpha,\alpha}_{turb} = S^{\theta,\theta}_{turb} = S_{turb}$ and $S^{\alpha,\theta}_{turb} = S^{\theta,\alpha}_{turb}$. The formula has been verified through a comparison with end-to-end simulations (see Appendix A.2). The first two terms of the equation represent the residual PSD left in the direction of the NGS (see Eq. (1.57)):

$$
S_{temp}(\nu) = |H_r(\nu)|^2 S_{turb}(\nu) + |H_n(\nu)|^2 S_n(\nu),
\tag{2.56}
$$

where S_{temp} denotes the residual PSD due to the temporal error. The last two terms represent the residual PSD due to anisoplanatism as filtered by the AO control:

$$
S_{aniso}(\nu) = 2\operatorname{Re}\left[H_n(\nu)\left(S_{turb}(\nu) - S^{\theta,\alpha}_{turb}(\nu)\right)\right],
\tag{2.57}
$$

where S_{aniso} denotes the residual PSD due to anisoplanatism. If the latter is integrated with respect to the temporal frequencies, it provides the anisoplanatism error

$$
\sigma^2_{aniso} = \int \mathrm{d}\nu\, 2\operatorname{Re}\left[H_n(\nu)\left(S_{turb}(\nu) - S^{\theta,\alpha}_{turb}(\nu)\right)\right],
\tag{2.58}
$$

that is generally computed through the spatial covariances of the phase as [21, 77, 85]

$$
\sigma^2_{aniso} = 2\left[(\sigma_{turb})^2 - \left(\sigma^{\theta,\alpha}_{turb}\right)^2\right].
\tag{2.59}
$$

In Fig. 2.6, we investigate the difference between the anisoplanatism error computed through the CPSDs (Eq. (2.58)) or through the covariances (Eq. (2.59)). We show the results for the phase and we use Eq. (2.38) to compute the CPSDs, in order to limit the integration to the temporal frequency range [0,∞) and thus gain computation time. As a case study, we considered the LBT [86] observing with one of the two 8.2-m pupils and compensating

the turbulence-induced distortions through a SCAO correction, where the control is a pure integrator with $\nu_{loop} = 500$ Hz, $g = 0.2$ and $d = 2$ (d is the delay in frames). The turbulence profile we used to compute the CPSDs is a four-layer profile taken from Agapito *et al.* [87]. The parameters are shown in Table 2.1. We computed every CPSD as sum of the

Height [m]	103	725	2637	11068
C_N^2 *fraction*	0.70	0.06	0.14	0.10
Wind speed [m/s]	2	4	6	25
Seeing [arcsec]	0.66			
Zenith angle [°]	40			

Table 2.1 Parameters of the atmospheric turbulence profile. The seeing and layer altitudes are given at zenith and are scaled with respect to the airmass in the simulation.

single-layer CPSDs, assuming that the phase perturbations at each layer are not correlated. As expected, the anisoplanatism error computed through the CPSD method is smaller than the one computed through the covariances, as it includes the temporal filtering by the AO control. We note that this behavior is valid within the whole range of L_0, which is between limit values of 1 m and ∞. For the typical values (10 m - 50 m), measuring the anisoplanatism error through the covariances leads to an overestimation of ≈ 40 nm at $\approx$ 2" off axis.

2.5.2 Time-filtered anisoplanatism for an interferometric telescope

We now consider a two-aperture interferometric telescope. The off-axis NGS is needed to sense the differential phase between the two sides of the telescope, that is the signal to be minimized in interferometric observations.

In this case, we have to determine the residual PSD from the difference between the residual phases on the two sides of the interferometer. Thus, we define the temporal PSD in the direction of the target as

$$
\begin{aligned}
S_{res}^{\alpha}(\nu) &= \left\langle \left(\phi_{res}^{\alpha_1}(\nu) - \phi_{res}^{\alpha_2}(\nu) \right) \left(\phi_{res}^{\alpha_1}(\nu) - \phi_{res}^{\alpha_2}(\nu) \right)^{\dagger} \right\rangle \\
&= 2 \Bigg\{ |H_r(\nu)|^2 \left(S_{turb}(\nu) - S_{turb}^{\theta_1,\theta_2}(\nu) \right) \\
&\quad + 2\,\mathrm{Re}\left[H_n(\nu) \left(S_{turb}^{\theta_1,\alpha_1}(\nu) - S_{turb}(\nu) \right) \right] \\
&\quad + \mathrm{Re}\left[H_n(\nu) \left(2 S_{turb}^{\theta_1,\theta_2}(\nu) - S_{turb}^{\theta_1,\alpha_2}(\nu) - S_{turb}^{\theta_2,\alpha_1}(\nu) \right) \right] \Bigg\},
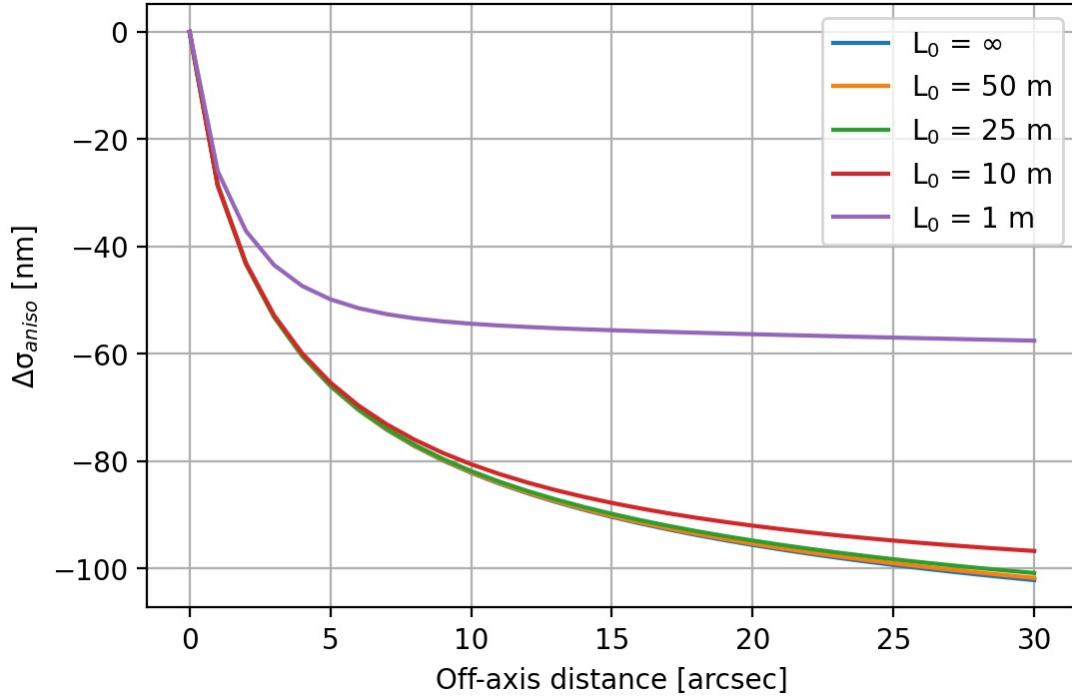\end{aligned}
\tag{2.60}
$$

Fig. 2.6 Difference between the anisoplanatism error computed through the CPSD or with the covariance method, as a function of the angular off-axis distance of the NGS and for several values of the turbulence outer scale. The assumed telescope is the LBT.

where $\phi_{res}^{\alpha_1}$ and $\phi_{res}^{\alpha_2}$ are the residual phases on the first and the second aperture of the interferometer, both given by Eq. (2.54), S_{turb} is the PSD of the turbulent phase in a given line of sight seen by a single aperture and $S_{turb}^{x_i,y_j}$ is the CPSD between the turbulent phases seen from two directions (x, y) by two apertures (i, j). Here, x and y can either be θ for the NGS or α for the target. By assuming homogeneous and isotropic atmospheric turbulence, we used the following relationships for the CPSDs: $S_{turb}^{\alpha_1,\alpha_1} = S_{turb}^{\alpha_2,\alpha_2} = S_{turb}^{\theta_1,\theta_1} = S_{turb}^{\theta_2,\theta_2} = S_{turb}$, $S_{turb}^{\alpha_1,\theta_1} = S_{turb}^{\alpha_2,\theta_2}$, $S_{turb}^{\alpha_1,\alpha_2} = S_{turb}^{\alpha_2,\alpha_1} = S_{turb}^{\theta_1,\theta_2} = S_{turb}^{\theta_2,\theta_1}$, $S_{turb}^{\alpha_1,\theta_2} = S_{turb}^{\theta_2,\alpha_1}$. The two AO systems equipping each side of the interferometer work independently from one another, but as they see the same atmospheric conditions and the same star, we assumed that they have the same control law (e. g. the same integrator gain and delay), hence they are characterized by the same RTF and NTF. As in the single-aperture case, we note that the first two terms represent the residual PSD left in the direction of the NGS, while the last five terms, if integrated on the temporal frequencies, represent the anisoplanatism error as filtered by the AO loops. This last source of error is usually computed through the spatial covariances of the phase, as we find in Esposito *et al.* [88]. The formula, presented

for the differential piston errors but still valid for the differential phase in general, is

$$\sigma^2_{aniso} = 2 \left[2 \left(\sigma_{turb} \right)^2 - 2 \left(\sigma^{\alpha_1, \theta_1}_{turb} \right)^2 - 2 \left(\sigma^{\theta_1, \theta_2}_{turb} \right)^2 + \left(\sigma^{\alpha_1, \theta_2}_{turb} \right)^2 + \left(\sigma^{\alpha_2, \theta_1}_{turb} \right)^2 \right]. \quad (2.61)$$

In Fig. 2.7, we show the difference between the anisoplanatism error computed through the CPSDs or through the covariances. As an interferometric telescope, we considered the LBTI, that is characterized by two 8.2-m pupils and a center-to-center distance of 14.4 m. We used the same parameters as in the previous paragraph for the AO loop and the turbulence profile. As in the single-aperture case, we note that the AO temporal filtering has a significant effect in reducing the contribution of anisoplanatism, with a difference greater than 200 nm at 10" off axis for typical L_0 values. This applica-
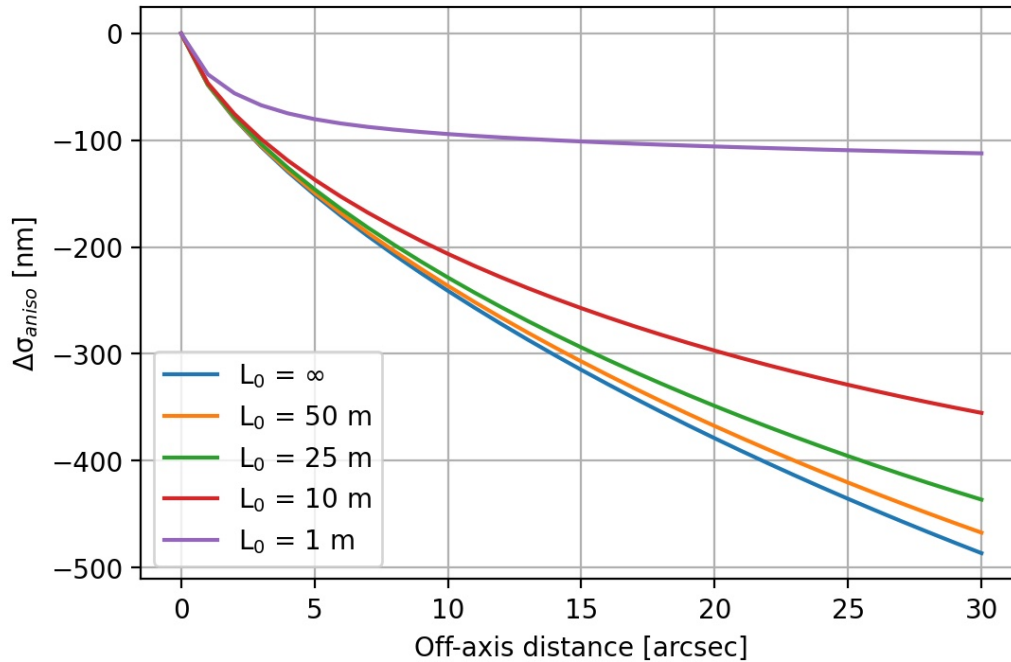

Fig. 2.7 Difference between the anisoplanatism error computed through the CPSD or with the covariance method, as a function of the angular off-axis distance of the NGS and for several values of the turbulence outer scale. The assumed interferometric telescope is the LBTI.

tion shows that the two beams of a small-baseline interferometer are likely to be highly correlated. This correlation between adjacent beams can be of interest for the study of segmented telescopes. For example, the Giant Magellan Telescope (GMT) [74], that has a primary composed of 7 segments and a deformable secondary segmented in the same way, could be considered as a 7-aperture interferometer, since each pair primary segment - secondary segment is equivalent to one side of the LBT.

2.6   Residual tip-tilt in SCAO-assisted astrometric observations

The analysis carried out in Section 2.5.1 on the piston-filtered phase anisoplanatism can be applied to tip-tilt as well. Indeed, considering the CPSDs of Zernike modes derived in Section 2.4, Eq. (2.55) can be specialized to tip and tilt and provide tip-tilt residual PSD in a direction α of the field of view in case of an off-axis NGS at position θ. The residual variance can be evaluated as well, through the integration of Eq. (2.55) over temporal frequencies:

$$\left(\sigma_{res}^{\alpha}\right)^2 = \int d\nu \left\{ |H_r(\nu)|^2 S_{turb}(\nu) + |H_n(\nu)|^2 S_n(\nu) + 2\operatorname{Re}\left[H_n(\nu)\left(S_{turb}(\nu) - S_{turb}^{\theta,\alpha}(\nu) \right) \right] \right\}.$$
(2.62)

In the following, we analyze tip-tilt residuals from a SCAO loop on a single-aperture telescope.

2.6.1   Characterization of tip-tilt PSDs

PSD of turbulent tip-tilt

The CPSDs (and PSDs) of Zernike modes derived in Section 2.4 allow to consider either Kolmogorov or Von Karman profiles of turbulence, as well as either single-layer or multi-layer profiles with generic wind direction. The temporal PSDs computed in Conan *et al.* [13], and reported in Section 1.1.3, are instead limited to the case of Kolmogorov model of turbulence and, in the analysis of a single-layer profile, to a wind direction along the x axis. Under these assumptions, tip-tilt temporal PSDs have been demonstrated to follow a $\nu^{-2/3}$ law at low temporal frequencies.

In Fig. 2.8, we show tip-tilt temporal PSDs derived for a single-layer Von Karman turbulence profile, with wind direction either along the x axis or along the y axis. The plots show a different behavior at low temporal frequencies with respect to the Kolmogorov assumption, the behavior of each mode depending on the wind direction.

In real cases, multi-layer Von Karman turbulence profiles have to be taken into account and the dependence on the wind direction is almost canceled out. Indeed, the effect due to different wind directions of the layers averages out, unless there is a particularly dominant layer. This is shown in Fig. 2.9, where tip-tilt temporal PSDs are derived for the 35-layers ELT median profile reported in Sarazin *et al.* [89]. Both tip and tilt curves show a flat behavior at low temporal frequencies. Moreover, it is worth noting that in this case the
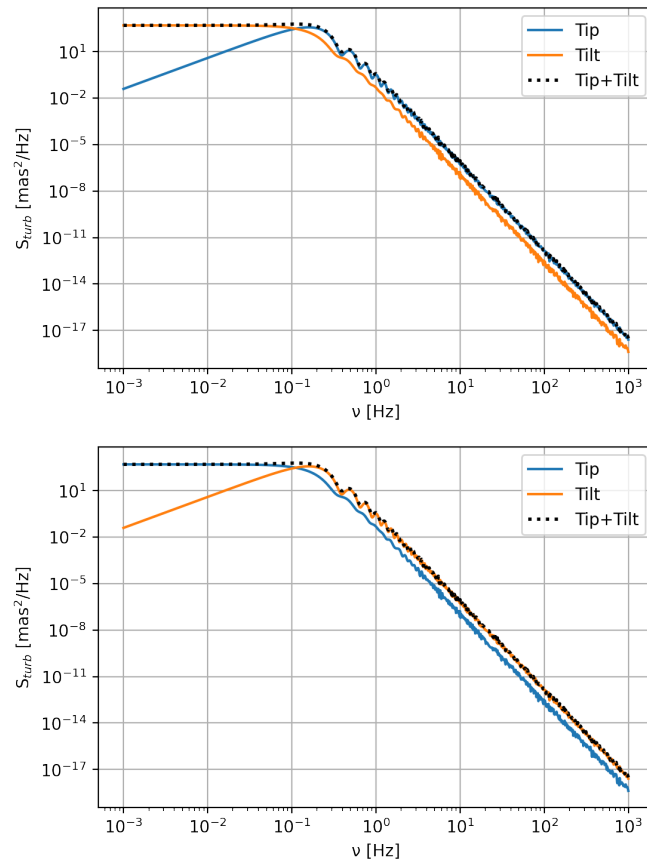
Fig. 2.8 Temporal PSDs of tip (solid blue line), tilt (solid orange line) and the sum of tip and tilt (dotted black line) for a single-layer profile with wind direction of 0° (top) and 90° (bottom), wind speed of 10 m/s, $r_0 = 16$ cm, $L_0 = 25$ m, zenith angle of 0°. The aperture diameter is 40 m.
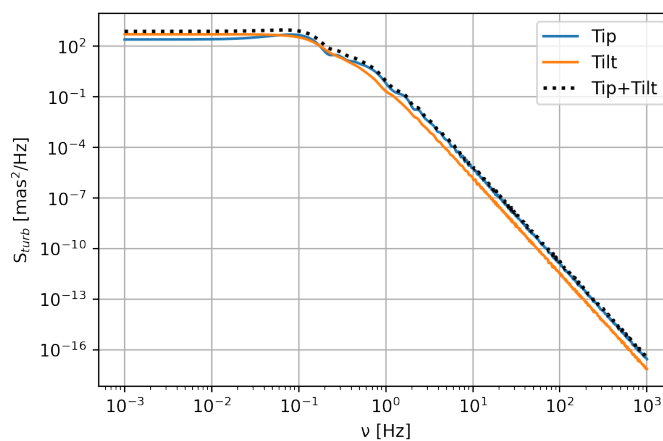

Fig. 2.9 Temporal PSDs of tip (solid blue line), tilt (solid orange line) and the sum of tip and tilt (dotted black line) for the multi-layer profile of Sarazin *et al.* [89], with mean wind speed of 9.2 m/s, $r_0 = 16$ cm, $L_0 = 25$ m, zenith angle of 0°. The aperture diameter is 40 m.

cutoff frequency of tip-tilt temporal PSDs can be approximately still evaluated as

$$\nu_c \approx 0.6 \nu_m / D, \tag{2.63}$$

where, considering Eq. (1.43), the mean wind speed ν_m (given in Eq. (1.11)) has replaced the single-layer wind speed and where we considered $n = 1$ for tip and tilt.

PSD of residual tip-tilt

We now specialize to multi-layer turbulence profile and we analyze tip-tilt residual PSDs from Eq. (2.55), and the contribution of temporal and anisoplanatic errors from, respectively, Eq. (2.56) and Eq. (2.57). We do not consider noise.

In Fig. 2.10, we show the total residual PSD, as well as the ones due to temporal and anisoplanatic errors, for three different angular separations between the GS and the science object. The plots show, as expected, the contribution of only the temporal error to the residual PSD when the target corresponds to the GS (d = 0"). In this case, the flat behavior of the input PSD is filtered by the RTF and the amount of filtered power depends on the AO control (e.g. loop frequency frame rate). For larger separations, an increasing contribution of the anisoplanatic error is observed. In particular, it is worth noting that the flat behavior at low frequencies is conserved. This derives from the fact that, as shown in Eq. (2.57), anisoplanatism is filtered by the NTF, which acts as a low-pass filter.

This characterization will help explain tip-tilt residuals dependence on the integration time of the scientific exposure, that will be analyzed in Section 4.4.

2.6.2   Tip-tilt residuals and differential tilt jitter

In the context of AO-assisted astrometric observations, in Section 1.4.1 we showed that tip-tilt residuals can affect astrometric precision on distance measurements through tip-tilt anisoplanatic error and differential tilt jitter error. Here we present our first understanding to model the two effects, that will be applied in the next chapters to MCAO as well.

Tip-tilt anisoplanatic error is directly given by tip-tilt residual phase in Eq. (2.52), thus represents the difference between the turbulent phase on the target and the correction phase estimated from the GS. It depends on the AO control; if the AO control is ideal (i.e. $H_r = 0$, $H_n = 1$, no noise), as assumed in Sandler *et al.*'s [21] formulation presented in Section 1.2.6, the correction phase is exactly the turbulent phase in the direction of the GS and the residual phase becomes the difference between the turbulent phases in the two directions. On the other hand, differential tilt jitter represents the difference between the residual phases for any pair of astrometric targets in the FoV; since, in the
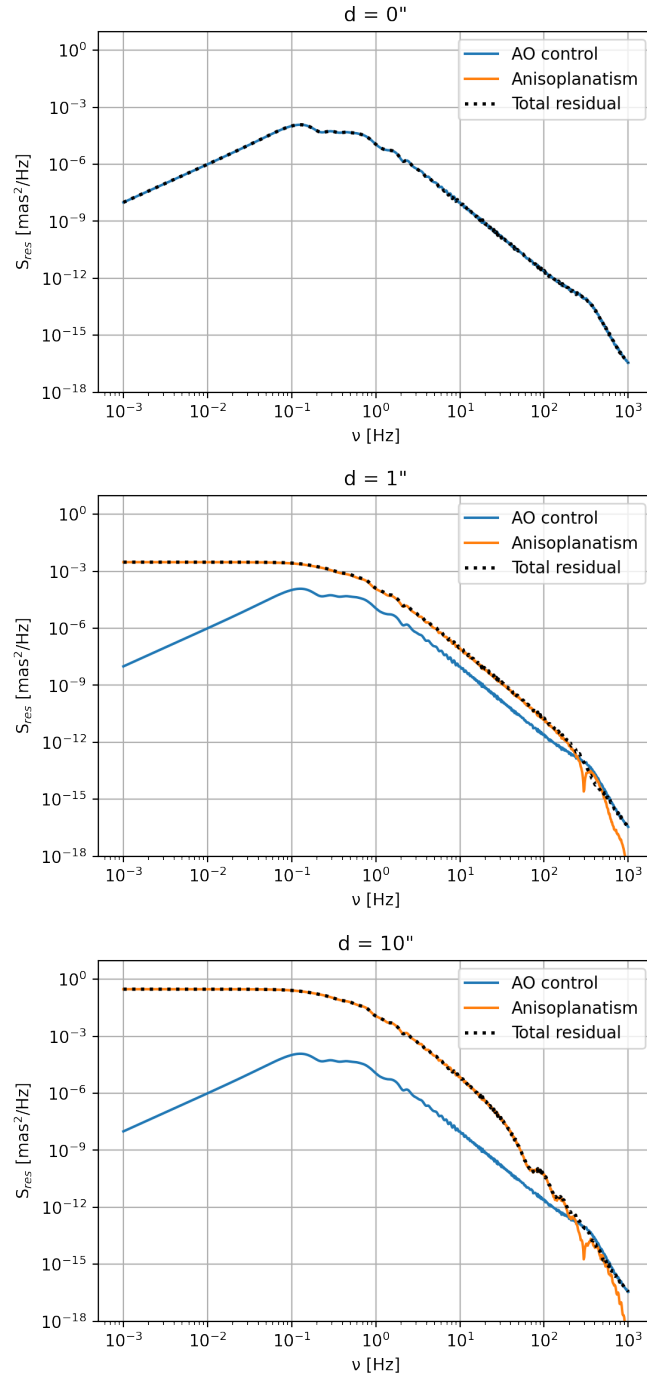
Fig. 2.10 Temporal PSDs of tip-tilt residuals (dotted black line) and of the only contribution of temporal error (solid blue line) and anisoplatic error (solid orange line). The sum of tip and tilt is considered. The curves are obtained with three values of the target-GS angular separation: d = 0" (top), 1" (center), 10" (bottom). The spectra are computed with the multi-layer profile of Sarazin *et al.* [89], with mean wind speed of 9.2 m/s, r_0 = 16 cm, L_0 = 25 m, zenith angle of 0°. The aperture diameter is 40 m.

SCAO case, the correction phase is common to all directions of the FoV, the difference between residual phases becomes the difference between turbulent phases. Thus, for two targets at positions α and β, the differential tilt jitter phase is

$$
\begin{aligned}
\phi_{DTJ}^{\alpha,\beta}(\nu) &= \phi_{res}^{\alpha}(\nu) - \phi_{res}^{\beta}(\nu) \\
&= \left(\phi_{turb}^{\alpha}(\nu) - \phi_{corr}(\nu) \right) - \left(\phi_{turb}^{\beta}(\nu) - \phi_{corr}(\nu) \right) \\
&= \phi_{turb}^{\alpha}(\nu) - \phi_{turb}^{\beta}(\nu) \, .
\end{aligned}
\tag{2.64}
$$

For the sake of completeness, we also derive the differential tilt jitter PSD:

$$
\begin{aligned}
S_{DTJ}^{\alpha,\beta}(\nu) &= \left\langle \phi_{DTJ}^{\alpha,\beta}(\nu) \, \phi_{DTJ}^{\alpha,\beta}(\nu)^{\dagger} \right\rangle \\
&= \left\langle \left(\phi_{turb}^{\alpha}(\nu) - \phi_{turb}^{\beta}(\nu) \right) \left(\phi_{turb}^{\alpha}(\nu) - \phi_{turb}^{\beta}(\nu) \right)^{\dagger} \right\rangle \\
&= 2 \left(S_{turb}(\nu) - S_{turb}^{\alpha,\beta}(\nu) \right) ,
\end{aligned}
\tag{2.65}
$$

where, assuming homogeneous and isotropic turbulence, we considered $S_{turb}^{\alpha,\alpha} = S_{turb}^{\beta,\beta} = S_{turb}$. The differential tilt jitter variance is then

$$
\left(\sigma_{DTJ}^{\alpha,\beta} \right)^2 = 2 \int \mathrm{d}\nu \left(S_{turb}(\nu) - S_{turb}^{\alpha,\beta}(\nu) \right) .
\tag{2.66}
$$

Thus, in SCAO configurations, residual tip-tilt and differential tilt jitter are equivalent in case an "ideal" AO control is considered, as we find in the literature (e.g. Sandler's *et al.* [21]). In case a real AO control is taken into account, the contribution of the AO temporal error is also included and it will be dominant at small angular target-NGS separations where anisoplanatism is not relevant. This behavior is shown in Fig. 2.11, where we consider two values of the loop frequency frame rate, 100 Hz and 1000 Hz. In the "slow" loop case, it can be seen the contribution of the AO temporal error at small angular distances where anisoplanatism is not the dominant factor. The errors derived from Sandler *et al.*'s equations are shown for comparison.

In Fig. 2.12, we show another comparison between Sandler's formula and Eq. (2.62), where we consider Von Karman turbulence profile. We assume two values of the outer scale, $L_0 = 25$ m and 50 m. The curves show larger values of tip-tilt residuals obtained from Sandler's equations, as they are limited to Kolmogorov spectrum of turbulence, that is, to infinite outer scale that brings a larger amount of power into tip-tilt components. Smaller the outer scale, larger the difference.
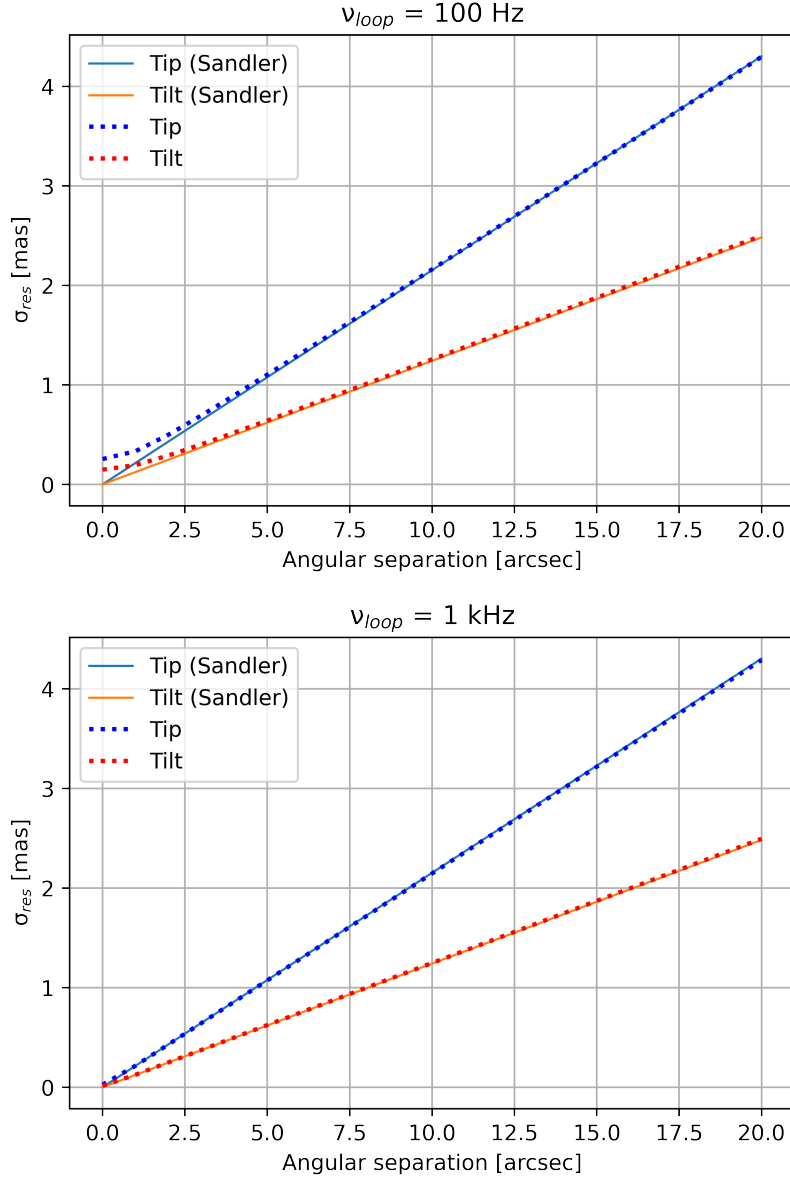
Fig. 2.11 Tip (blue)-tilt (red) residual from SCAO correction, as a function of the angular separation between the NGS and the science target. Solid lines are obtained from Sandler *et al.*'s equations (reported in Eq. (1.74)) and dotted lines are obtained from Eq. (2.62) applied to tip and tilt modes. For the latter case, two values of the loop frequency frame rate are considered: 100 Hz (top) and 1 kHz (bottom). The NGS-target separation is considered along the x-axis, so as Sandler's longitudinal and lateral errors correspond to, respectively, tip and tilt errors. A telescope with aperture of D = 40 m is considered. A single-layer Kolmogorov turbulence profile is used, with r_0 = 16 cm, θ_0 = 1 arcsec, wind speed of 10 m/s and altitude of 10 km.
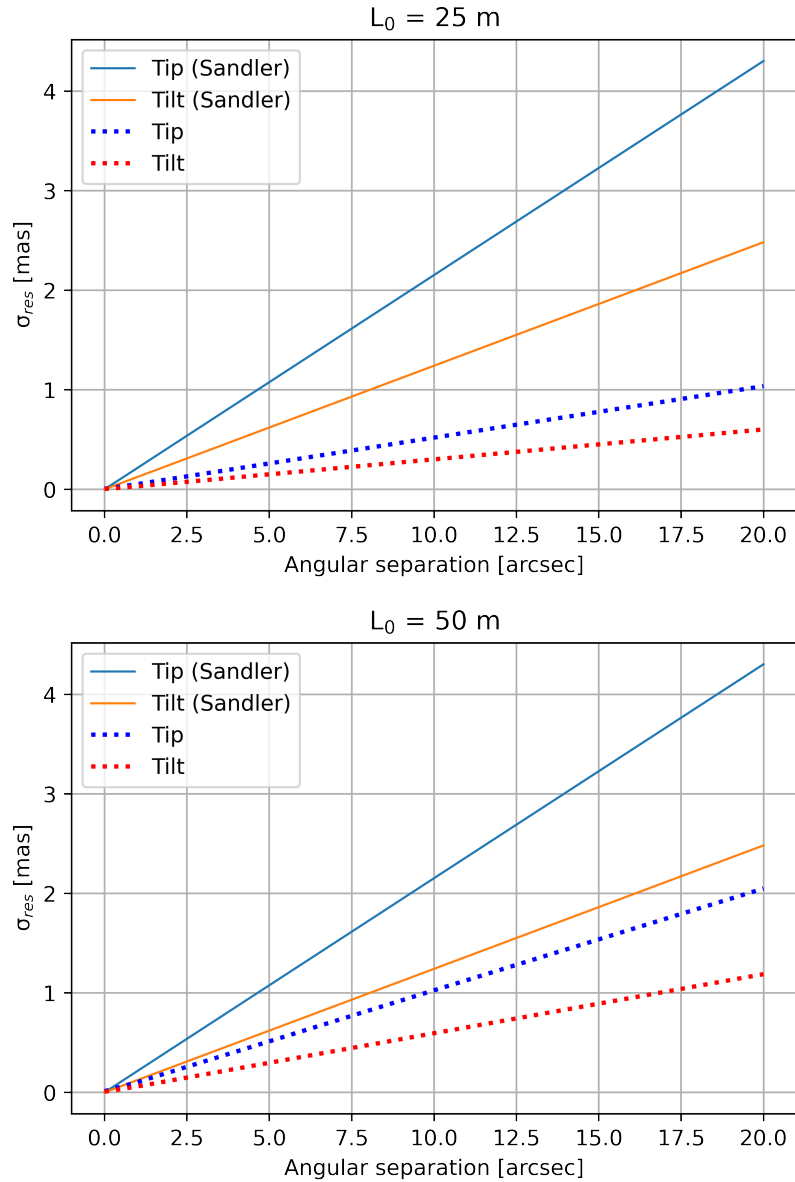
Fig. 2.12 Tip (blue)-tilt (red) residual from SCAO correction, as a function of the angular separation between the NGS and the science target. Solid lines are obtained from Sandler's equations (reported in Eq. (1.74)) and dotted lines are obtained from Eq. (2.62) applied to tip and tilt modes. For the latter case, Von Karman atmospheric profile has been considered, with outer scale $L_0 = 25$ m (top) and 50 m (bottom). The other atmospheric parameters, as well as telescope and sources configuration, are the same as Fig. 2.11. The loop frequency frame rate is 1 kHz.

Chapter 3

Temporal power spectral density of MCAO residuals

In this chapter, we present an analytical formulation to derive the temporal PSD of the residual phase from an MCAO correction in a generic direction of the scientific field of view. This has been object of publication in Carlà *et al.* [53]. The method is based on the approach presented in Section 2.5 to compute wavefront residuals in a SCAO configuration and is extended to the MCAO case. The formulas allow to estimate tomographic, noise and temporal errors.

In the following, we consider the configuration in Fig. 3.1: the target is at position α and the guide stars are at positions $\boldsymbol{\theta} = [\theta_1, \theta_2, ..., \theta_N]$ with respect to the axis of the telescope. The light from the sources passes through N_l layers of atmospheric turbulence before arriving at the pupil of the telescope. We assume the turbulent layers to follow Taylor's frozen flow hypothesis. We consider the turbulence-induced distortions as decomposed on to wavefront modes (e.g. Zernike modes) and measured by N wavefront sensors, each sensing n modes, and corrected by M deformable mirrors, optically conjugated at altitudes $h_{j=1}^M$ and compensating for a total of $m = \sum_{k=1}^M m_k$ modes. We will denote the turbulent and residual phase in the direction of the target as ϕ_{turb}^{α} and ϕ_{res}^{α} respectively, the turbulent and residual phase in the direction of the guide stars as $\phi_{turb}^{\boldsymbol{\theta}}$ and $\phi_{res}^{\boldsymbol{\theta}}$ respectively and the phase applied on the deformable mirrors as ϕ_{DM}. It follows that ϕ_{turb}^{α} and ϕ_{res}^{α} are vectors of n elements, $\phi_{turb}^{\boldsymbol{\theta}}$ and $\phi_{res}^{\boldsymbol{\theta}}$ are vectors of $(n \cdot N)$ elements and ϕ_{DM} is a vector of m elements.
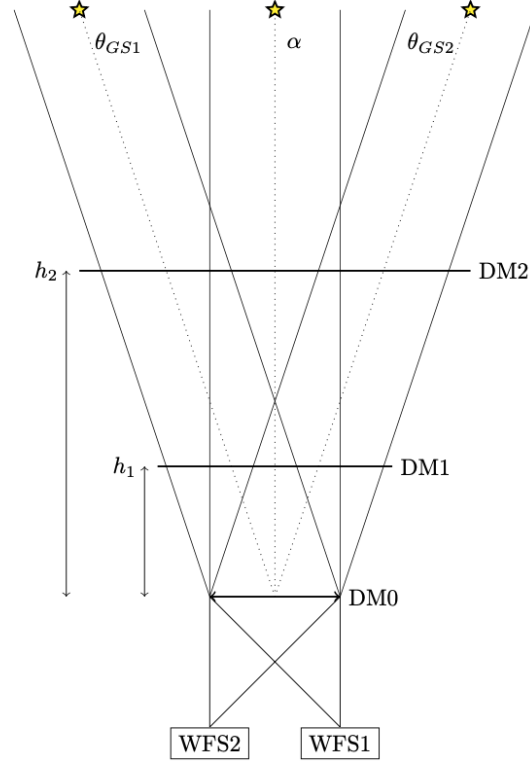
Fig. 3.1 Scheme of the system geometry. In the example, there are two DMs conjugated at h_1 (DM1) and h_2 (DM2) and one at the ground layer (DM0), two guide stars at coordinates θ_{GS1} and θ_{GS2} and the scientific target at α. The wavefront distortion is measured by WFS1 and WFS2 looking at GS1 and GS2, respectively.

3.1 Temporal transfer functions of an MCAO loop

We write the residual phase along $\boldsymbol{\theta}$ as

$$\begin{aligned}
\phi^{\boldsymbol{\theta}}_{res}(\nu) &= \phi^{\boldsymbol{\theta}}_{turb}(\nu) - \phi^{\boldsymbol{\theta}}_{corr}(\nu) \\
&= \phi^{\boldsymbol{\theta}}_{turb}(\nu) - P^{\boldsymbol{\theta}}_{DM}\phi_{DM}(\nu),
\end{aligned} \tag{3.1}$$

where ν is the temporal frequency and $P^{\boldsymbol{\theta}}_{DM}$ is a matrix of size $(n \cdot N) \times m$ that projects onto the pupil the modes on the DMs as seen in the directions $\boldsymbol{\theta}$.

We define ϕ_{DM} as

$$\phi_{DM}(\nu) = H_{ol}(\nu) W \left(\phi^{\boldsymbol{\theta}}_{res}(\nu) + \phi_n(\nu) \right), \tag{3.2}$$

where H_{ol} is the open-loop transfer function of the AO feedback loop, W is the reconstruction matrix, with dimension $m \times (n \cdot N)$, relating the modes measured by the WFSs and the ones to be applied by the DMs and $\phi_n(v)$ is the WFSs measurement noise on the modes. We assumed ideal WFSs, meaning that they perform a direct measurement of the phase.

We replace Eq. (3.2) in Eq. (3.1):

$$\phi_{res}^{\boldsymbol{\theta}}(v) = \phi_{turb}^{\boldsymbol{\theta}}(v) - P_{DM}^{\boldsymbol{\theta}} H_{ol}(v) W \left(\phi_{res}^{\boldsymbol{\theta}}(v) + \phi_n(v) \right), \tag{3.3}$$

we group the terms related to $\phi_{res}^{\boldsymbol{\theta}}$:

$$\left(Id + P_{DM}^{\boldsymbol{\theta}} H_{ol}(v) W \right) \phi_{res}^{\boldsymbol{\theta}}(v) = \phi_{turb}^{\boldsymbol{\theta}}(v) - P_{DM}^{\boldsymbol{\theta}} H_{ol}(v) W \phi_n(v), \tag{3.4}$$

where Id is an $(n \cdot N) \times (n \cdot N)$ identity matrix, and we obtain an expression of the residual phase on the guide stars:

$$\begin{aligned}
\phi_{res}^{\boldsymbol{\theta}}(v) &= \left(Id + P_{DM}^{\boldsymbol{\theta}} H_{ol}(v) W \right)^{-1} \phi_{turb}^{\boldsymbol{\theta}}(v) \\
&\quad - \left(Id + P_{DM}^{\boldsymbol{\theta}} H_{ol}(v) W \right)^{-1} P_{DM}^{\boldsymbol{\theta}} H_{ol}(v) W \phi_n(v) \\
&= H_r(v) \phi_{turb}^{\boldsymbol{\theta}}(v) - H_n(v) \phi_n(v),
\end{aligned} \tag{3.5}$$

where we have defined

$$H_r(v) = \left(Id + P_{DM}^{\boldsymbol{\theta}} H_{ol}(v) W \right)^{-1} \tag{3.6}$$

as the RTF and

$$H_n(v) = \left(Id + P_{DM}^{\boldsymbol{\theta}} H_{ol}(v) W \right)^{-1} P_{DM}^{\boldsymbol{\theta}} H_{ol}(v) W \tag{3.7}$$

as the NTF of the MCAO loop. Both are matrices of dimension $(n \cdot N) \times (n \cdot N)$. The extended form of Eq. (3.5) is

$$\begin{aligned}
\begin{pmatrix} \phi_{res}^{\theta_1} \\ \phi_{res}^{\theta_2} \\ \vdots \\ \phi_{res}^{\theta_N} \end{pmatrix} &= \begin{pmatrix} (H_r)_{11} & (H_r)_{12} & \dots & (H_r)_{1(n \cdot N)} \\ (H_r)_{21} & (H_r)_{22} & \dots & (H_r)_{2(n \cdot N)} \\ \vdots & & \vdots & \\ (H_r)_{(n \cdot N)1} & (H_r)_{(n \cdot N)2} & \dots & (H_r)_{(n \cdot N)(n \cdot N)} \end{pmatrix} \begin{pmatrix} \phi_{turb}^{\theta_1} \\ \phi_{turb}^{\theta_2} \\ \vdots \\ \phi_{turb}^{\theta_N} \end{pmatrix} \\
&\quad - \begin{pmatrix} (H_n)_{11} & (H_n)_{12} & \dots & (H_n)_{1(n \cdot N)} \\ (H_n)_{21} & (H_n)_{22} & \dots & (H_n)_{2(n \cdot N)} \\ \vdots & & \vdots & \\ (H_n)_{(n \cdot N)1} & (H_n)_{(n \cdot N)2} & \dots & (H_n)_{(n \cdot N)(n \cdot N)} \end{pmatrix} \begin{pmatrix} \phi_n^{\theta_1} \\ \phi_n^{\theta_2} \\ \vdots \\ \phi_n^{\theta_N} \end{pmatrix},
\end{aligned} \tag{3.8}$$

where $\phi_{res}^{\theta_i}$, $\phi_{turb}^{\theta_i}$ and $\phi_n^{\theta_i}$ are vectors of n elements ($i = 1, ..., N$) and where we omitted the dependence on temporal frequency. It is worth noting that Eq. (3.5) has the same form of Eq. (1.53) that holds for the SCAO case, but it includes a dependence on the tomographic reconstruction through RTF and NTF. If taking the SCAO limit of Eq. (3.6) and Eq. (3.7), $P_{DM}^{\boldsymbol{\theta}}$ and W become equal to one and the classical definitions of RTF (given in Eq. (1.54)) and NTF (given in Eq. (1.55)) are retrieved.

In Fig. 3.2, we show the diagonal terms of the RTF matrix for three different asterisms of three NGSs, where each NGS is used to measure tip and tilt. In this case, $\phi_{res}^{\theta_i}$, $\phi_{turb}^{\theta_i}$ and $\phi_n^{\theta_i}$ are vectors of two elements (i.e. $\phi_{res}^{\boldsymbol{\theta}}$, $\phi_{turb}^{\boldsymbol{\theta}}$ and ϕ_n are vectors of six elements) and the coefficients $(H_r)_{ij}$ and $(H_n)_{ij}$ are vectors of two elements. The diagonal term $(H_r)_{ii}$ represents the rejection function of tip and tilt modes acting on the turbulent wavefront from the ith NGS. The plots show a different rejection of tip and tilt on each NGS depending on the geometry of the asterism. Our understanding is that the signal from the better sensed mode is more rejected, where the better measurement depends on the amount of overlap between NGSs footprints. For instance, the first row of the plot shows a better rejection of tip for the NGS at 0° and of tilt for the NGSs at 120° and 240°: at the first direction, the major overlap occurs along the x axis, thus tip is better sensed and more rejected; at the other two directions, the major overlap occurs along the y axis, thus the rejection is better on tilt.

In Fig. 3.3, we show the diagonal terms of the NTF matrix for the same configuration of Fig. 3.2 and we observe the opposite behavior with respect to the RTF case. This is compatible with the trade-off between RTF and NTF characterizing AO loops: the better the disturbance is rejected, the more the noise is propagated within the loop.

Finally, we can replace Eq. (3.5) in Eq. (3.2) and we get

$$
\begin{aligned}
\phi_{DM}(v) &= H_{ol}(v) W \left(H_r(v) \phi_{turb}^{\boldsymbol{\theta}}(v) - H_n(v) \phi_n(v) + \phi_n(v) \right) \\
&= H_{ol}(v) W H_r(v) \left(\phi_{turb}^{\boldsymbol{\theta}}(v) + \phi_n(v) \right) \\
&= H_{n,tomo}(v) \left(\phi_{turb}^{\boldsymbol{\theta}}(v) + \phi_n(v) \right),
\end{aligned}
\tag{3.9}
$$

where we used the relation $H_r(v) + H_n(v) = Id$, as derived from the sum of Eq. (3.6) and Eq. (3.7), and where we defined the matrix

$$
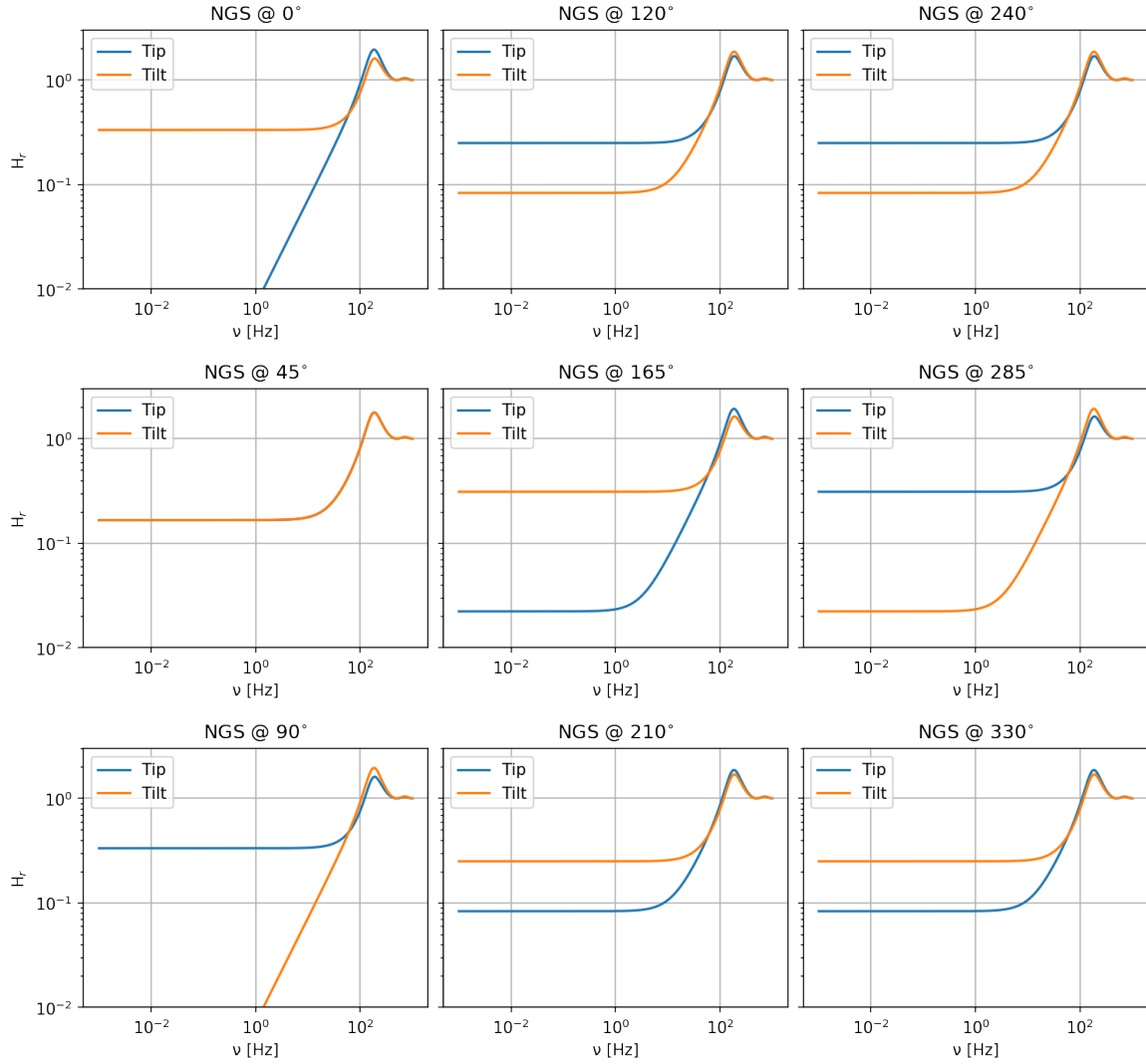H_{n,tomo}(v) = H_{ol}(v) W H_r(v)
\tag{3.10}
$$

Fig. 3.2 RTF for an MCAO loop as a function of temporal frequencies, as obtained from Eq. (3.6). The three rows represent three equilateral asterisms, all with radius of 40" but with a different orientation. In particular, the first asterism has positions (40", 0°), (40", 120°), (40", 240°); the second asterism (40", 45°), (40", 165°), (40", 285°); the third asterism (40", 90°), (40", 210°), (40", 330°). Each plot of the row represents a different NGS of the asterism. A telescope aperture diameter of 39 m has been considered, as well as one DM at 600 m compensating for tip-tilt and one DM at 17 km compensating for focus-astigmatisms. The loop frequency frame rate is 500 Hz.

as a tomographic NTF. Equation (3.9) takes the same form as Eq. (2.53) and becomes equal to it if considering the SCAO limit. Indeed, in this case the reconstructor would become equal to one and $H_{n,tomo} = H_{ol}(\nu)H_r(\nu) = H_n(\nu)$.
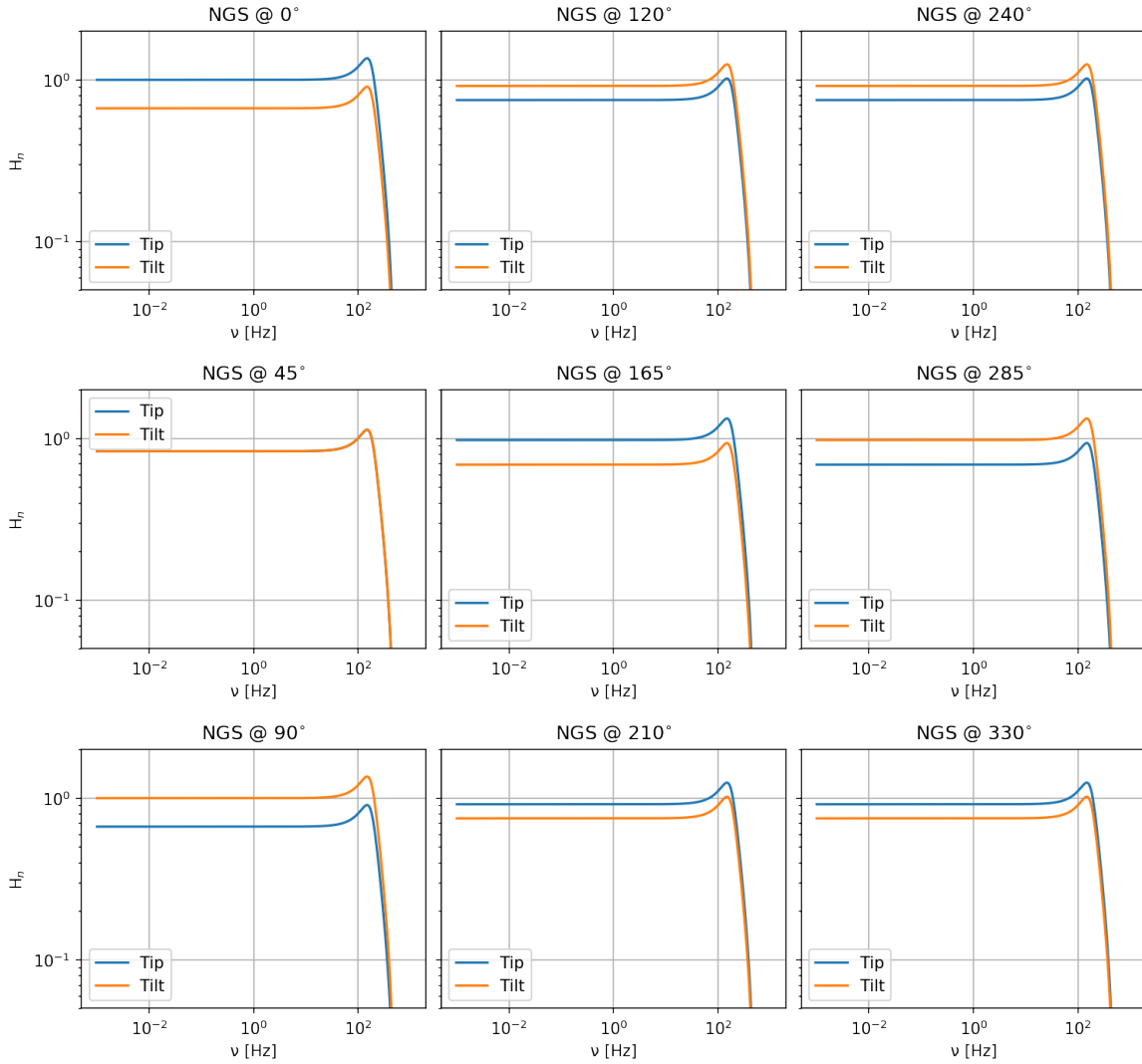
Fig. 3.3 NTF for an MCAO loop as a function of temporal frequencies, as obtained from Eq. (3.7). The three rows represent three equilateral asterisms, all with radius of 40" but with a different orientation. In particular, the first asterism has positions (40", 0°), (40", 120°), (40", 240°); the second asterism (40", 45°), (40", 165°), (40", 285°); the third asterism (40", 90°), (40", 210°), (40", 330°). Each plot of the row represents a different NGS of the asterism. A telescope aperture diameter of 39 m has been considered, as well as one DM at 600 m compensating for tip-tilt and one DM at 17 km compensating for focus-astigmatisms. The loop frequency frame rate is 500 Hz.

3.2   Temporal spectrum of MCAO residual wavefront

We intend to derive the residual phase produced by an MCAO loop in the direction of the target α. From this quantity, the temporal PSD of the residuals can be derived as

$$S_{res}^{\alpha}(v) = \left\langle \phi_{res}^{\alpha}(v)\phi_{res}^{\alpha\dagger}(v) \right\rangle, \tag{3.11}$$

where $\langle\cdot\rangle$ is the ensemble average, † denotes the conjugate-transpose and ϕ represents the $\mathscr{L}$- or Z-transform of the phase, depending on whether a continuous or discrete-time domain is considered. From the integration of S_{res}^{α}, the variance of the residual phase can be computed as well:

$$\left(\sigma_{res}^{\alpha}\right)^2 = \int \mathrm{d}v\, S_{res}^{\alpha}(v). \tag{3.12}$$

We write the residual phase along α as

$$\begin{aligned}
\phi_{res}^{\alpha}(v) &= \phi_{turb}^{\alpha}(v) - \phi_{corr}^{\alpha}(v) \\
&= \phi_{turb}^{\alpha}(v) - P_{DM}^{\alpha}\phi_{DM}(v),
\end{aligned} \tag{3.13}$$

where ϕ_{res}^{α} and ϕ_{turb}^{α} are, respectively, the residual and turbulent phases in the direction of the target, ϕ_{corr}^{α} is the correction phase in the direction of the target and P_{DM}^{α} is a matrix of size $n \times m$ that projects onto the pupil the modes on the DMs as seen in the direction α. We substitute Eq. (3.9) in Eq. (3.13) and we derive the expression of the residual phase along α:

$$\begin{aligned}
\phi_{res}^{\alpha}(v) &= \phi_{turb}^{\alpha}(v) - P_{DM}^{\alpha}\left[H_{n,tomo}(v)\left(\phi_{turb}^{\boldsymbol{\theta}}(v) + \phi_n(v)\right)\right] \\
&= \phi_{turb}^{\alpha}(v) - H_{n,tomo}^{\alpha}(v)\left(\phi_{turb}^{\boldsymbol{\theta}}(v) + \phi_n(v)\right),
\end{aligned} \tag{3.14}$$

where

$$H_{n,tomo}^{\alpha}(v) = P_{DM}^{\alpha}H_{n,tomo}(v) \tag{3.15}$$

is the tomographic NTF projected along α. The diagram of the control loop that we have analytically described is shown in Fig. 3.4.
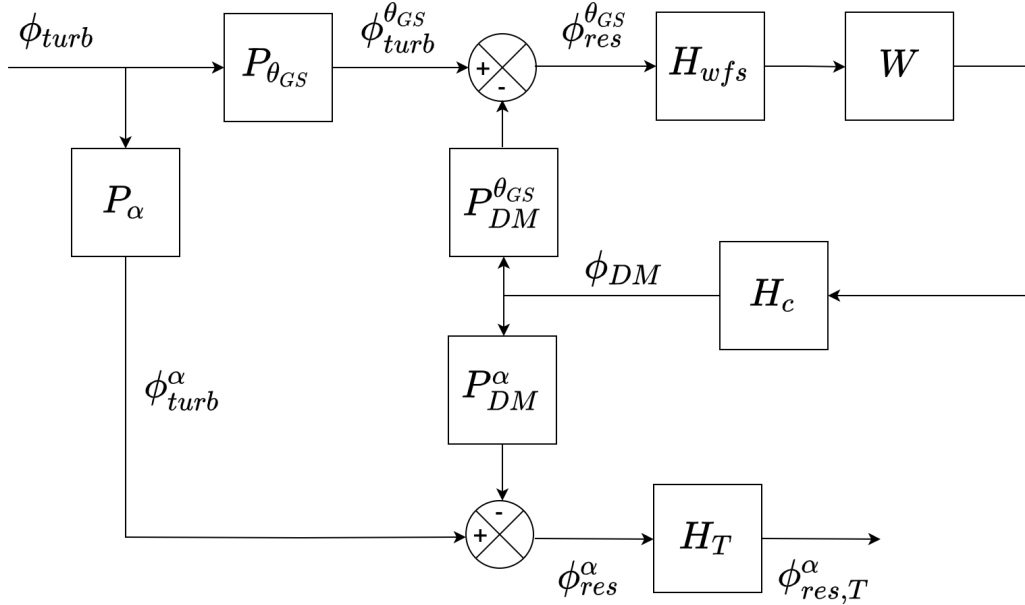
Fig. 3.4 Diagram of the control loop. The phase on the DMs is controlled in closed loop from the measurements on the guide stars and its projection along α determines the residual phase on the target in α. The $P_{\boldsymbol{\theta}}$ and P_α blocks have been introduced as projections of the turbulent phase onto $\boldsymbol{\theta}$ ($\phi_{turb}^{\boldsymbol{\theta}} = P_{\boldsymbol{\theta}}\phi_{turb}$) and α ($\phi_{turb}^\alpha = P_\alpha \phi_{turb}$) respectively. The H_T block represents the temporal filtering by the scientific instrument, as it will be shown in Section 4.4

.

From Eq. (3.11) and Eq. (3.14), we can compute the temporal power spectral density of the residual phase along the direction of the target:

$$
\begin{aligned}
S_{res}^\alpha(v) &= \left\langle \phi_{res}^\alpha(v)\, \phi_{res}^{\alpha\dagger}(v) \right\rangle \\
&= \left\langle \left[\phi_{turb}^\alpha(v) - H_{n,tomo}^\alpha(v)\left(\phi_{turb}^{\boldsymbol{\theta}}(v) + \phi_n(v) \right) \right] \right. \\
&\qquad \left. \cdot \left[\phi_{turb}^\alpha(v) - H_{n,tomo}^\alpha(v)\left(\phi_{turb}^{\boldsymbol{\theta}}(v) + \phi_n(v) \right) \right]^\dagger \right\rangle \\
&= \left\langle \phi_{turb}^\alpha(v)\, \phi_{turb}^{\alpha\dagger}(v) \right\rangle - \left\langle \phi_{turb}^\alpha(v)\left[H_{n,tomo}^\alpha(v)\left(\phi_{turb}^{\boldsymbol{\theta}}(v) + \phi_n(v) \right) \right]^\dagger \right\rangle \\
&\quad - \left\langle H_{n,tomo}^\alpha(v)\left(\phi_{turb}^{\boldsymbol{\theta}}(v) + \phi_n(v) \right) \phi_{turb}^{\alpha\dagger}(v) \right\rangle \\
&\quad + \left\langle H_{n,tomo}^\alpha(v)\left(\phi_{turb}^{\boldsymbol{\theta}}(v) + \phi_n(v) \right) \left[H_{n,tomo}^\alpha(v)\left(\phi_{turb}^{\boldsymbol{\theta}}(v) + \phi_n(v) \right) \right]^\dagger \right\rangle \\
&= S_{turb}^\alpha(v) + H_{n,tomo}^\alpha(v)\left(S_{turb}^{\boldsymbol{\theta}}(v) + S_n(v) \right) H_{n,tomo}^{\alpha\dagger}(v) - 2\,\mathrm{Re}\left(H_{n,tomo}^\alpha(v) S_{turb}^{\boldsymbol{\theta},\alpha}(v) \right),
\end{aligned}
$$

$$(3.16)$$

where we assumed turbulence and noise to be uncorrelated and where S_{turb}^{α} is the temporal PSD of the turbulence, $S_{turb}^{\boldsymbol{\theta}}$ is the temporal PSD of the turbulence on the guide stars directions, S_n is the temporal PSD of the noise and $S_{turb}^{\boldsymbol{\theta},\alpha}$ is the CPSD of the turbulence between the guide stars and the target.

The derived expression can provide a fast evaluation of the MCAO residuals in the field of view, given a statistics of turbulence and noise and the temporal filtering operated by the MCAO loop. It is worth noting that the SCAO limit of Eq. (3.16) gives the same expression as Eq. (2.55). Indeed, in this case $H_{n,tomo}^{\alpha} = H_n$ and $\boldsymbol{\theta} = \theta$, and the equation becomes

$$
\begin{aligned}
S_{res}^{\alpha}(v) &= S_{turb}^{\alpha}(v) + |H_n(v)|^2 \left(S_{turb}^{\theta}(v) + S_n(v) \right) - 2\operatorname{Re}\left(H_n(v) S_{turb}^{\theta,\alpha}(v) \right) \\
&= \left(1 + |H_n(v)|^2 \right) S_{turb}(v) + |H_n(v)|^2 S_n(v) - 2\operatorname{Re}\left(H_n(v) S_{turb}^{\theta,\alpha}(v) \right) \\
&= \left[(1 - H_n(v))^2 + 2\operatorname{Re}(H_n(v)) \right] S_{turb}(v) + |H_n(v)|^2 S_n(v) - 2\operatorname{Re}\left(H_n(v) S_{turb}^{\theta,\alpha}(v) \right) \\
&= \left[|H_r(v)|^2 + 2\operatorname{Re}(H_n(v)) \right] S_{turb}(v) + |H_n(v)|^2 S_n(v) - 2\operatorname{Re}\left(H_n(v) S_{turb}^{\theta,\alpha}(v) \right) \\
&= |H_r(v)|^2 S_{turb}(v) + |H_n(v)|^2 S_n(v) + 2\operatorname{Re}\left[H_n(v) \left(S_{turb}(v) - S_{turb}^{\theta,\alpha}(v) \right) \right],
\end{aligned}
$$

$$(3.17)$$

where we assumed homogeneous and isotropic turbulence, then $S_{turb}^{\alpha} = S_{turb}^{\theta} = S_{turb}$ and where we used the property of AO transfer functions in Eq. (1.56).

Another version of Eq. (3.14) and Eq. (3.16) can be obtained if not only one target, but a set of targets equaling the number of guide stars is considered ($\boldsymbol{\alpha} = [\alpha_1, \alpha_2, ..., \alpha_N]$). In this case, we can modify Eq. (3.14) as

$$
\begin{aligned}
\phi_{res}^{\boldsymbol{\alpha}}(v) &= \phi_{turb}^{\boldsymbol{\alpha}}(v) - H_{n,tomo}^{\boldsymbol{\alpha}}(v) \left(\phi_{turb}^{\boldsymbol{\theta}}(v) + \phi_n(v) \right) \\
&= Id\, \phi_{turb}^{\boldsymbol{\alpha}}(v) - H_{n,tomo}^{\boldsymbol{\alpha}}(v) \left(\phi_{turb}^{\boldsymbol{\theta}}(v) + \phi_n(v) \right) \\
&= H_{r,tomo}^{\boldsymbol{\alpha}}(v) \phi_{turb}^{\boldsymbol{\alpha}}(v) - H_{n,tomo}^{\boldsymbol{\alpha}}(v) \left(\phi_{turb}^{\boldsymbol{\theta}}(v) - \phi_{turb}^{\boldsymbol{\alpha}}(v) + \phi_n(v) \right),
\end{aligned}
$$

$$(3.18)$$

where $H_{r,tomo}^{\boldsymbol{\alpha}}$ is the tomographic RTF projected along $\boldsymbol{\alpha}$, defined so that the relation $H_{r,tomo}^{\boldsymbol{\alpha}}(v) + H_{n,tomo}^{\boldsymbol{\alpha}}(v) = Id$ holds. This expression allows to differentiate the various contributions due to the rejection of turbulence (first term), to generalized anisoplanatism that is filtered as a noise by the AO loop (second plus third term) and to noise (last term).

This is also shown by deriving the related temporal power spectrum:

$$
\begin{aligned}
S_{res}^{\boldsymbol{\alpha}}(\nu) = \ & H_{r,tomo}^{\boldsymbol{\alpha}}(\nu) S_{turb}^{\boldsymbol{\alpha}}(\nu) H_{r,tomo}^{\boldsymbol{\alpha}\,\dagger}(\nu) \\
& + H_{n,tomo}^{\boldsymbol{\alpha}}(\nu) S_n(\nu) H_{n,tomo}^{\boldsymbol{\alpha}\,\dagger}(\nu) \\
& + H_{n,tomo}^{\boldsymbol{\alpha}}(\nu) \left(S_{turb}^{\boldsymbol{\theta}}(\nu) - S_{turb}^{\boldsymbol{\alpha}}(\nu) \right) H_{n,tomo}^{\boldsymbol{\alpha}\,\dagger}(\nu) \\
& + 2\,\mathrm{Re} \left[H_{n,tomo}^{\boldsymbol{\alpha}}(\nu) \left(S_{turb}^{\boldsymbol{\alpha}} - S_{turb}^{\boldsymbol{\theta},\boldsymbol{\alpha}} \right) \right],
\end{aligned}
\tag{3.19}
$$

where the first and second term leads, respectively, to the temporal and noise error, while the remaining terms quantify the tomographic error as well as its temporal filtering by the MCAO loop.

In Appendix A.3, we show a comparison of our analytical results with end-to-end simulations.

3.2.1 Pseudo-Open Loop Control and MMSE reconstruction

In the previous calculations, we considered a closed-loop control, that is, the reconstruction is performed on the residual measurements as shown in Eq. (3.2). The reconstruction matrix W is then intended as the pseudo-inverse of the projection matrix $P_{DM}^{\boldsymbol{\theta}}$, as derived in the Least Square Estimator (LSE) approach (Section 1.2.4). However, as shown in Section 1.3.1, it has been demonstrated not to be the optimal approach to deal with the problem of badly and unseen modes [33, 34, 90, 91] characterizing MCAO correction and that the Minimum Mean Square Error (MMSE) approach can lead to better performance, even if compared to the Truncated LSE (TLSE) [92]. As the MMSE reconstructor operates on the pseudo-open loop measurements of the turbulent phase, it has to be included in a Pseudo-Open Loop control (POLC) [35]. In this context, we provide the expressions to derive the performance of MCAO systems also in the case of POLC and MMSE.

We modify Eq. (3.2) in order to consider a reconstruction acting on the pseudo-open loop measurements [93]:

$$
\phi_{DM}(\nu) = H_{ol}(\nu) \left(W_{MMSE}\,\phi_{OL}^{\boldsymbol{\theta}}(\nu) - \phi_{DM}(\nu) \right),
\tag{3.20}
$$

where W_{MMSE} is the MMSE reconstructor and $\phi_{OL}^{\boldsymbol{\theta}}$ are the open-loop measurements that we write as

$$
\phi_{OL}^{\boldsymbol{\theta}}(\nu) = \phi_{res}^{\boldsymbol{\theta}}(\nu) + \phi_n(\nu) + P_{DM}^{\boldsymbol{\theta}}\phi_{DM}(\nu).
\tag{3.21}
$$

We replace this expression in Eq. (3.20):

$$
\begin{aligned}
\phi_{DM}(\nu) &= H_{ol}(\nu)\left[W_{MMSE}\left(\phi^{\boldsymbol{\theta}}_{res}(\nu)+\phi_n(\nu)+P^{\boldsymbol{\theta}}_{DM}\phi_{DM}(\nu)\right)-\phi_{DM}(\nu)\right] \\
&= H_{ol}(\nu)W_{MMSE}\left(\phi^{\boldsymbol{\theta}}_{res}(\nu)+\phi_n(\nu)\right)+H_{ol}(\nu)\left(W_{MMSE}P^{\boldsymbol{\theta}}_{DM}-Id\right)\phi_{DM}(\nu).
\end{aligned}
\tag{3.22}
$$

We group the terms related to ϕ_{DM}:

$$
\left[Id-H_{ol}(\nu)\left(W_{MMSE}\,P^{\boldsymbol{\theta}}_{DM}-Id\right)\right]\phi_{DM}(\nu)=H_{ol}(\nu)W_{MMSE}\left(\phi^{\boldsymbol{\theta}}_{res}(\nu)+\phi_n(\nu)\right),
\tag{3.23}
$$

and we obtain a final expression of the DMs phase:

$$
\begin{aligned}
\phi_{DM}(\nu) &= \left[Id-H_{ol}(\nu)\left(W_{MMSE}\,P^{\boldsymbol{\theta}}_{DM}-Id\right)\right]^{-1}H_{ol}(\nu)\,W_{MMSE}\left(\phi^{\boldsymbol{\theta}}_{res}(\nu)+\phi_n(\nu)\right) \\
&= \left(Id+H_{ol}(\nu)K\right)^{-1}H_{ol}(\nu)\,W_{MMSE}\left(\phi^{\boldsymbol{\theta}}_{res}(\nu)+\phi_n(\nu)\right) \\
&= H_{polc}(\nu)\,W_{MMSE}\left(\phi^{\boldsymbol{\theta}}_{res}(\nu)+\phi_n(\nu)\right),
\end{aligned}
\tag{3.24}
$$

where we defined the matrices $K=Id-W_{MMSE}P^{\boldsymbol{\theta}}_{DM}$ and $H_{polc}=\left(Id+H_{ol}(\nu)K\right)^{-1}H_{ol}(\nu)$. It follows that the results in Eqs. (3.14) and (3.16) can still be used to compute the residual phase and PSD on target, but considering $H_{ol}=H_{polc}$ and $W=W_{MMSE}$ when taking into account POLC+MMSE.

Chapter 4

Tip-tilt anisoplanatism in MCAO systems

The challenging requirements of astrometric precision that have been set for the future MCAO modules ask for an accurate analysis of the astrometric error budget. Among the classical sources of astrometric error introduced in Section 1.4.1, we are interested in investigating the effect of tip-tilt atmospheric residuals in MCAO-assisted observations. In this context, we first need to have an understanding of the spatial and temporal dependence of tip-tilt residuals in order to characterize the behavior of the related astrometric errors. As shown in Section 1.4.2, tip-tilt anisoplanatism is well known and has been thoroughly modeled for SCAO systems. However, the characterization is more elaborate for the MCAO case, since the geometry with multiple guide stars and multiple DMs can lead to complex behaviors. As pointed out in Trippe *et al.* [51], tip-tilt anisoplanatism is not well understood for this flavour of adaptive optics and, to our knowledge, an analysis does not exist yet. In this context, in Carlà *et al.* [53, 54], we presented a study of MCAO tip-tilt anisoplanatism. The analysis has been carried out by means of the analytical formulation derived in Chapter 3. Indeed, since the presented approach assumes the phase as decomposed on to wavefront modes, we can derive the temporal PSD and the variance of tip-tilt residuals from Eq. (3.16) and Eq. (3.12) respectively, by applying both equations to tip and tilt modes.

In Section 4.1, we present the framework that we use to analyze MCAO tip-tilt residuals (i.e. choice of GSs, DMs, atmospheric profile, etc.); in Section 4.2, we analyze MCAO tip-tilt residuals PSDs; in Section 4.3, we characterize the behavior of MCAO on-axis tip-tilt residuals; in Section 4.4, we model the effect of the scientific integration time on tip-tilt residuals; finally, in Section 4.5, we derive an expression to estimate differential tilt jitter in MCAO systems.

4.1 Framework

All the analysis is carried out within a MORFEO-like configuration, that is, we consider a 39-m telescope, with the DM0 conjugated at 600 m and the DM1 at 17 km. We assume the ELT median turbulence profile reported in Sarazin *et al.* [89], with a seeing of 0.644" and an average wind speed of 9.2 m/s. We consider the contribution of all the modes to the turbulence-induced wavefront distortions and a reconstruction of tip-tilt with the DM0 and focus-astigmatisms with the DM1, based on the tip-tilt measurements from three NGSs in equilateral asterisms. Such NGS loop can be used for the control of *null modes* [94] in MCAO systems using a split tomography approach [95]. We assume the equilateral asterism of NGSs centered at the origin of the field of view and the diameter of the NGSs technical FoV of 160".

It is worth pointing out that this configuration does not include the compensation for focus-astigmatisms at the pupil plane, thus it would provide an out of focus and astigmatic PSF; indeed, from the results in Appendix B.1 can be deduced that a focus (or astigmatisms) applied on a meta-pupil in altitude introduces (thus, helps compensate for) tip and tilt on the telescope pupil, but also a focus scaled by the squared ratio between the pupil and meta-pupil radii that should be corrected. However, since we are interested in tip-tilt variations in the field, not considering the compensation for focus and astigmatisms at the telescope pupil plane does not represent a limitation for our analysis.

Among the contributors to the temporal PSD of the residuals shown in Chapter 3, for this analysis we are mainly interested in the tomographic error. Thus, we neglect the noise assuming NGSs with infinite flux, as well as we minimize the temporal error considering a loop with a frequency frame rate of 1 kHz and where the control is a pure integrator with a delay given by the WFSs exposure time only. Finally, we use the LSE-closed loop approach. Indeed, using MMSE-POLC would not bring any advantage in this case: as shown in Section 1.3.1, the MMSE reconstructor takes the same form as the LSE reconstructor if the measurements are characterized by high SNR (that is infinite under our assumptions). This is verified in Fig. 4.1, where tip-tilt maps and related tip-tilt errors are shown in the two cases.

4.2 Characterization of tip-tilt residual PSDs

In this section, we use the analytical results of the previous chapter to analyze the behavior of temporal PSDs of tip-tilt residuals from an MCAO correction. In Section 2.6.1, we showed that, for SCAO configurations, anisoplanatism leads to a flat behavior of the
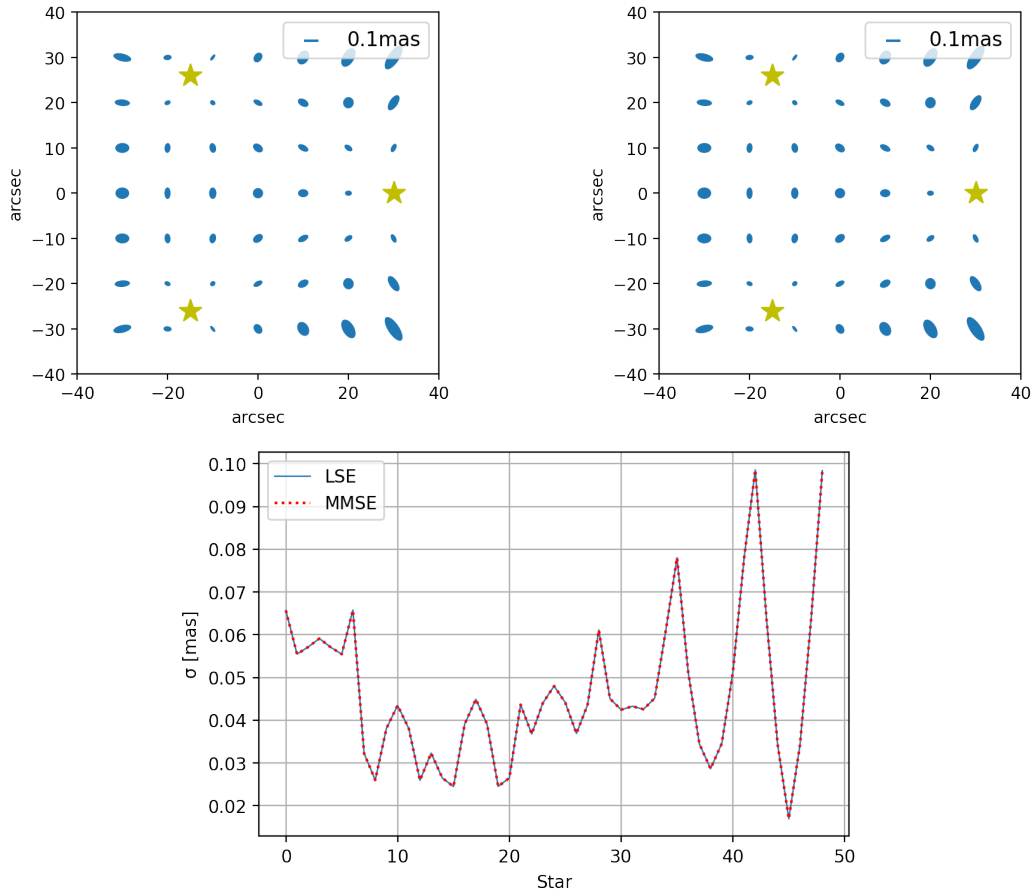
Fig. 4.1 Tip-tilt maps in case of equilateral asterism of NGSs with radius of 30 arcsec and for LSE (top left) and MMSE (top right) reconstruction. The NGSs are assumed to have infinite flux, that is, the noise is not considered in the computation. The values of tip-tilt residuals at each position are also plotted (bottom). It is shown that, in this configuration, the residuals from an LSE reconstruction are the same as the residuals from an MMSE reconstruction.

residual tip-tilt PSD at low temporal frequencies and that the PSD cutoff frequency has a linear dependence on the ratio between the mean wind speed of the turbulence profile and the diameter of the telescope. In Fig. 4.2, we show temporal PSDs of MCAO tip-tilt residuals computed at the barycenter of the correction (i.e. for a target at polar coordinates $(0", 0°)$) and for different values of the radius of the NGSs asterism. Since we are limiting the contribution of temporal error and we are neglecting noise, the results are mostly related to the contribution from MCAO anisoplanatism. The PSDs still show a flat behavior at low temporal frequencies. Moreover, the amount of energy at low temporal frequencies increases with increasing asterism radius. Indeed, larger asterisms determine smaller cross-correlations between the GSs and the on-axis target, then a worse correction. This

aspect is also evident from Eq. (3.16), that shows that the cross-correlation term $S_{turb}^{\boldsymbol{\theta},\alpha}$ might help reduce the residual power on the target.

In Fig. 4.3, we plot MCAO tip-tilt residuals PSD for three different values of the telescope diameter, then of the ratio between the mean wind speed of the atmospheric profile and the diameter. The curves show that the cutoff frequency of the MCAO residual PSDs still has an approximately linear dependence on the ratio v_m/D.
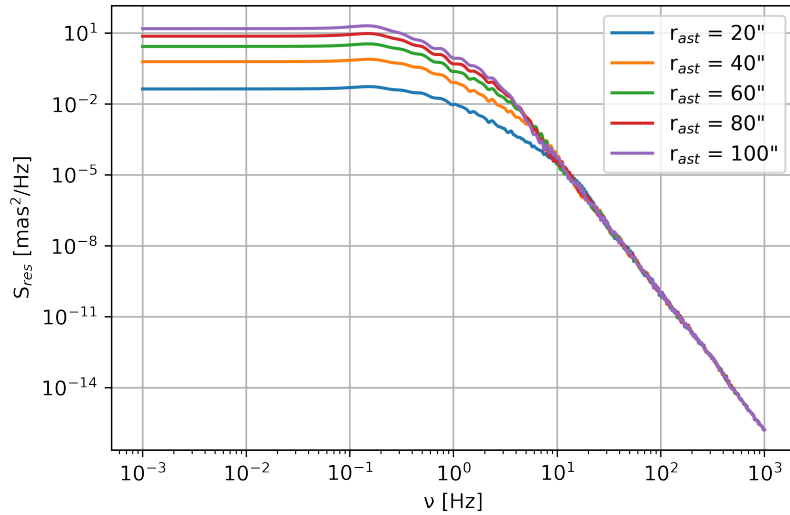

Fig. 4.2 Temporal PSDs of MCAO tip-tilt residuals for an on-axis target. The sum of tip and tilt PSDs is shown. The different colors represent different values of the radius of the NGSs asterism.
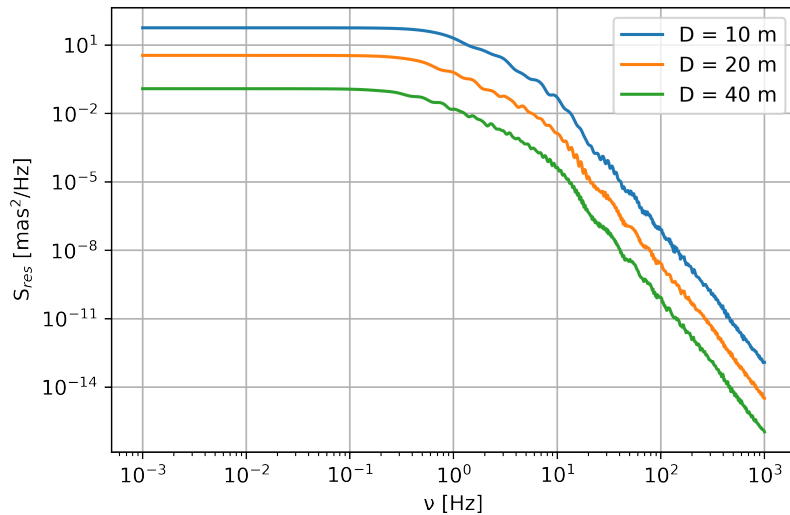

Fig. 4.3 Temporal PSDs of MCAO tip-tilt residuals for an on-axis target. The sum of tip and tilt PSDs is shown. The different colors represent different values of the telescope aperture diameter.

4.3 On-axis tip-tilt residuals

We want now to analyze the dependence of MCAO tip-tilt residuals on parameters like the radius of the NGS asterism and the distance from the barycenter of the correction, and also compare the results with the SCAO case.

In Fig. 4.4, we show the dependence on the asterism radius of tip-tilt residuals for a target on axis. The errors are computed from the square root of Eq. (3.12), where the residual PSD is obtained from Eq. (3.16) as applied to tip-tilt. The MCAO residuals are shown in comparison to the errors derived from the SCAO case, where the radius of the asterism becomes the angular separation between the target and the off-axis NGS. As
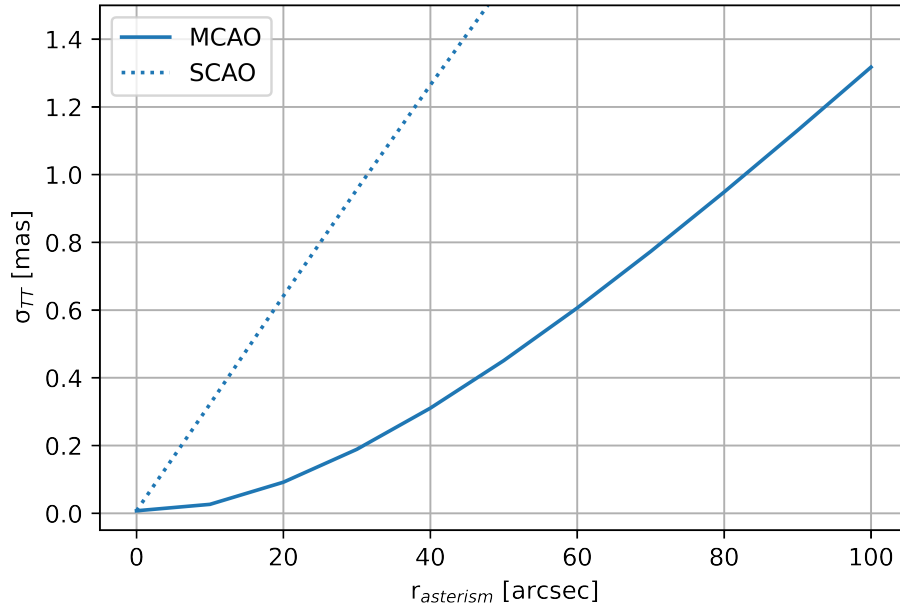

Fig. 4.4 Tip-tilt residuals for a target at the origin of the field of view, as functions of the radius of the NGS asterism. The SCAO limit is also shown for comparison (dotted line); in this case, the values on the x axis represent the angular separation between the target and the NGS.

expected from the larger isoplanatic patch provided by the MCAO correction, MCAO residuals are reduced with respect to the SCAO ones. Moreover, differently from the SCAO case, whose errors linearly depend on the off-axis separation, MCAO residuals show a quadratic dependence on the NGSs separation. We can explain the different behaviors as follows: the turbulence-induced distortions that are observed on the pupil plane can be described by a combination of polynomials with increasing degree:

$$\Delta x = a_1 + a_2 x + a_3 y + a_4 x^2 + a_5 x y + a_6 y^2 + ...$$
$$\Delta y = b_1 + b_2 y + b_3 x + b_4 y^2 + b_5 y x + b_6 x^2 + ...,$$

(4.1)

where the zeroth order coefficients (a_1, b_1) represent a global tip-tilt, that is a shift in x and y common to all directions of the field of view, the first order coefficients (a_2, a_3, b_2, b_3) represent the plate-scale distortions produced by the projection of focus and astigmatisms in altitude onto the tip-tilt in pupil (see Appendix B.2), and so on for the higher orders. The covariance matrix of the distortions is $\langle \Delta r \Delta r^T \rangle$, with $\Delta r = (\Delta x, \Delta y)$. The SCAO, correcting with only a DM at the ground and using a single WFS, is able to compensate for the zeroth order of the distortions (i.e. overall pointing), leaving residual distortions that are then dominated by the first order (i.e. plate-scale variations). The MCAO, in our NGS-based configuration, removes a global tip-tilt with the DM0 and, in addition, is able to control the first order distortions by compensating for focus and astigmatisms with the DM1 conjugated in altitude. The residual distortions are, in this case, dominated by the second order. The sum of the diagonal terms of the residual distortions covariance matrix leads, for the SCAO case, to the following expression:

$$\sum_{i=1,2} \langle \Delta r \Delta r^T \rangle_{ii} = (a_2 x + a_3 y + ...)^2 + (b_2 y + b_3 x + ...)^2$$
$$= u(x^2 + y^2) + ..., \tag{4.2}$$

and, for the MCAO case, to:

$$\sum_{i=1,2} \langle \Delta r \Delta r^T \rangle_{ii} = (a_4 x^2 + a_5 xy + a_6 y^2 + ...)^2$$
$$+ (b_4 y^2 + b_5 yx + b_6 x^2 + ...)^2$$
$$= v(x^2 + y^2)^2 + ..., \tag{4.3}$$

where the simplification in the coefficient u for the former and v for the latter is obtained by replacing the coefficients of the polynomial series with the proper coefficients that relate tip-tilt on the pupil plane with the higher orders on a meta-pupil in altitude. If we consider (x, y) as the position of the target with respect to the NGS, we find a dependence of the variance on the second power of the separation for the SCAO case and on the fourth power for the MCAO case. In Appendix C, we provide detailed calculations.

In Fig. 4.5, we show the spatial distribution of tip-tilt residuals in the field of view. The errors are computed for targets at different radial separations from the origin (that also represents the barycenter of the asterism) and the final values are obtained from the average over several polar angles in order not to be affected by the geometry of the asterism. The errors show similar values for targets within the NGS asterism and increase outside of the asterism, where tip-tilt is indeed not controlled. The minimum of the curves is not exactly at a distance equal to the asterism radius value, depending on the fact that

the targets at an angular separation equal to the asterism radius fall outside of the NGSs triangle (except the ones with the same exact polar angles as the NGSs ones), where tip-tilt is worse controlled.
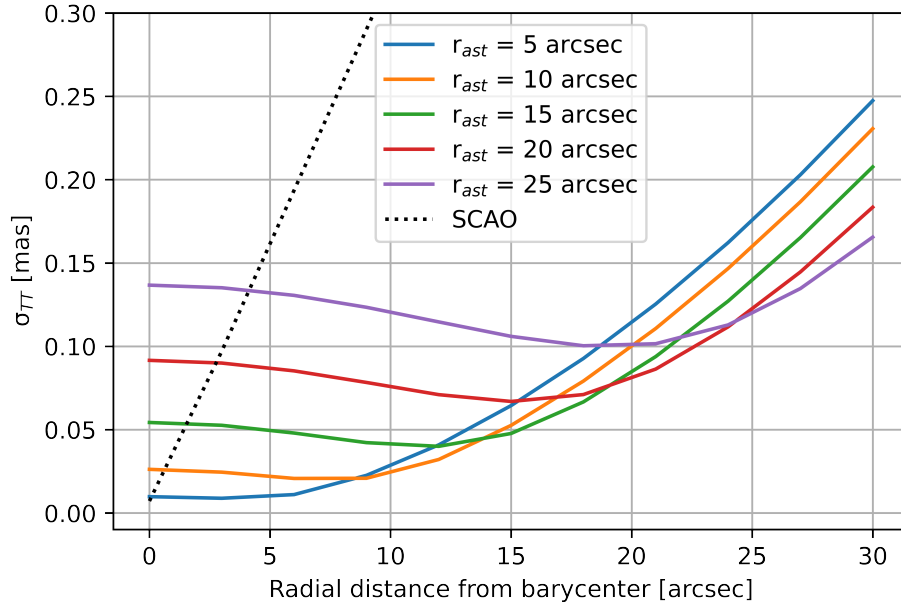

Fig. 4.5 Tip-tilt residuals as functions of the radial distance of the target with respect to the origin. The curves are shown for different values of the NGS asterism radius (r_{ast}) and the SCAO limit is also shown (dotted line).

4.4 Effect of the scientific integration time on tip-tilt residuals

As mentioned in Section 1.4.2, tip-tilt residuals can introduce uncertainties in the astrometric measurements, either with a PSF elongation effect due to the residuals that are integrated during a single exposure, either with a jitter of the position of the target observed between successive frames due to the amount of fluctuations that is not integrated within the exposure. The results shown in Section 4.3, obtained from a pure integration of Eq. (3.16), represent the case where the fluctuations in position are fully integrated within the exposure and thus impact entirely on the PSF elongation effect. In this section, we introduce the effect of the scientific integration time in order to be able to estimate both the PSF elongation and the residual jitter effects.

We identify the residuals leading to the PSF elongation effect as *intra-exposure* and the residuals leading to the position jitter between successive frames as *inter-exposure*.

The sum of intra- and inter-exposure residuals spectra gives the total residual spectrum of residual tip-tilt:

$$S_{res}^{\alpha}(\nu) = S_{intra}^{\alpha}(\nu) + S_{inter}^{\alpha}(\nu), \tag{4.4}$$

where S denotes the temporal PSD of tip-tilt and α indicates a specific direction of the field of view.

4.4.1 Inter-exposure residuals

We start with the computation of inter-exposure residuals by still following an approach that makes use of temporal transfer functions, as in Chapter 3. We write the expression of the phase residuals that are left after a scientific integration of length T as

$$\phi_{inter}^{\alpha}(\nu) = H_T(\nu)\phi_{res}^{\alpha}(\nu), \tag{4.5}$$

where ϕ_{res}^{α} is given by Eq. (3.14) for the MCAO case and H_T is the temporal transfer function of the scientific camera, that is, the $\mathscr{L}$- or Z-transform of the time-average operation. In the Laplace case, the expression is given by

$$\begin{aligned} H_T(\nu) &= \frac{1}{T}\widetilde{\Pi}_T(\nu) \\ &= \mathrm{sinc}(\pi\nu T)e^{-i\pi\nu T}, \end{aligned} \tag{4.6}$$

where $\widetilde{\Pi}_T$ denotes the transform of the rectangular function Π_T.

From Eq. (4.5), we can get the expression of the residual PSD for scientific frames of length T:

$$\begin{aligned} S_{inter}^{\alpha}(\nu) &= \left\langle \phi_{inter}^{\alpha}(\nu)\phi_{inter}^{\alpha\dagger}(\nu) \right\rangle \\ &= |H_T(\nu)|^2 S_{res}^{\alpha}(\nu) \\ &= H_{T,inter}(\nu)S_{res}^{\alpha}(\nu), \end{aligned} \tag{4.7}$$

where we have identified $H_{T,inter}$ as the temporal transfer function of inter-exposure residuals.

In Fig. 4.6, we plot inter-exposure temporal transfer functions for different values of the exposure time. The curves show that low temporal frequencies are passed and high temporal frequencies are filtered, starting from the cutoff frequency of the transfer function, $\nu_H = 1/T$.
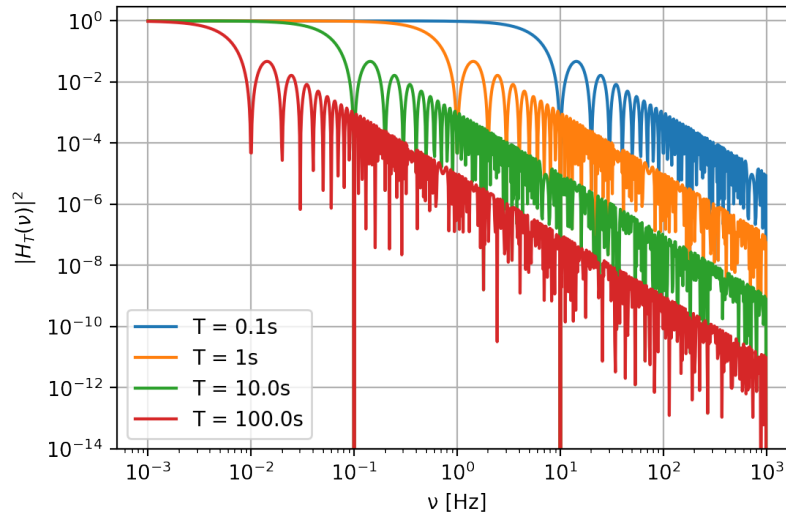
Fig. 4.6 Temporal transfer function of inter-exposure tip-tilt residuals as a function of the temporal frequencies. The colors represent different exposure times in a range from 0.1 to 100 s. The cutoff frequency $\nu_H = 1/T$ determines when the inter-exposure transfer function starts filtering the temporal PSD of tip-tilt residuals.

In Fig. 4.7, we plot the temporal PSD of both total and inter-exposure tip-tilt residuals, for values of the exposure time ranging from 0.001 to 100 s. It is evident the effect of low-pass filtering from the inter-exposure transfer function, that depends on the exposure time.

In Fig. 4.8, we show inter-exposure residuals (from the square root of the integral of Eq. (4.7)) as a function of the exposure time. The curves show a flat behavior at small integration times ($T \lesssim 0.1$ s) and a $T^{-1/2}$ law for larger times. The impact of the scientific exposure depends on the relation between the cutoff frequency of the camera transfer function and the one of the residual PSD ($\nu_S \approx \nu/D$, as shown in Section 4.2): if ν_H is either larger or about the same as ν_S, the scientific integration is not long enough to average the residuals and the position jitter observed between different exposures is at its maximum. Indeed, in this case, the camera is either unable to filter any frequency of the PSD, or it filters only the frequencies that are larger than ν_S, where the energy falls rapidly to zero. At these frequencies, inter-exposure residuals do not depend on the integration time (the curve follows a power law T^0). As the integration time increases, ν_H becomes smaller than ν_S and the inter-exposure transfer function passes the frequencies where the PSD is flat, leaving then a residual power spectrum that is proportional to $1/T$. Thus, the RMS is proportional to $T^{-1/2}$. It is worth noting that this dependence holds for SCAO tip-tilt residuals as well since, as shown in Section 2.6, also SCAO tip-tilt residuals PSDs are characterized by a flat behavior at low temporal frequencies.
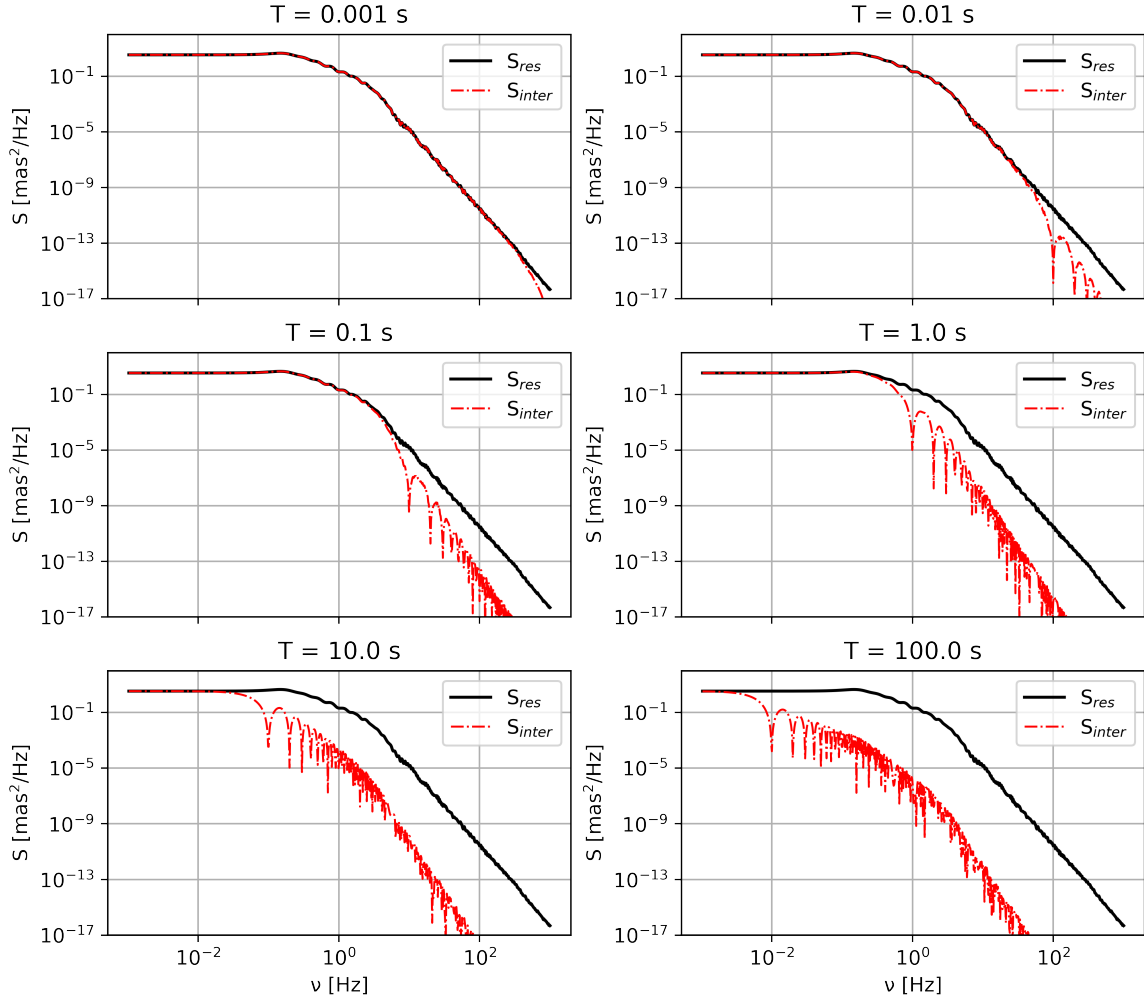
Fig. 4.7 Temporal PSD of total (black line) and inter-exposure (red line) tip-tilt residuals as a function of the temporal frequencies. The exposure time ranges from 0.001 (top left) to 100 s (bottom right). The PSDs are computed for a source on axis.

4.4.2 Intra-exposure residuals

From Eq. (4.4) and Eq. (4.7), we derive an expression to estimate the temporal PSD of the intra-exposure residuals temporal spectrum as well:

$$
\begin{aligned}
S^\alpha_{intra}(\nu) &= \left(1 - |H_T(\nu)|^2\right) S^\alpha_{res}(\nu) \\
&= H_{T,intra}(\nu) S^\alpha_{res}(\nu),
\end{aligned}
\tag{4.8}
$$

where we have introduced $H_{T,intra}$ as the temporal transfer function of the intra-exposure residuals.
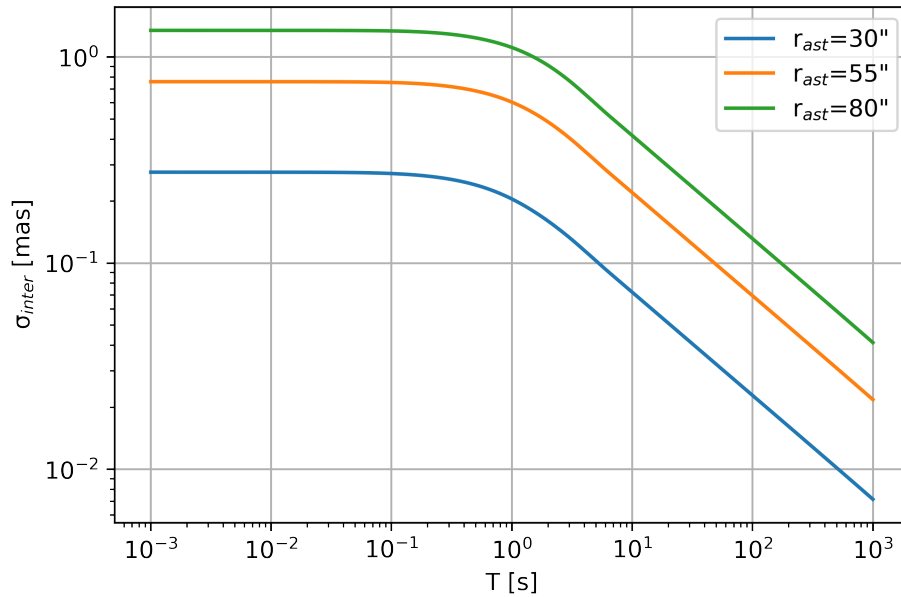
Fig. 4.8 Inter-exposure tip-tilt error as a function of the exposure time, for an on-axis target. Three different values of the asterism radius are considered.

In Fig. 4.9, we plot the intra-exposure temporal transfer functions for different values of the exposure time. The curves show that the intra-exposure transfer function acts as a high-pass filter with cutoff frequency $\nu_H = 1/T$.
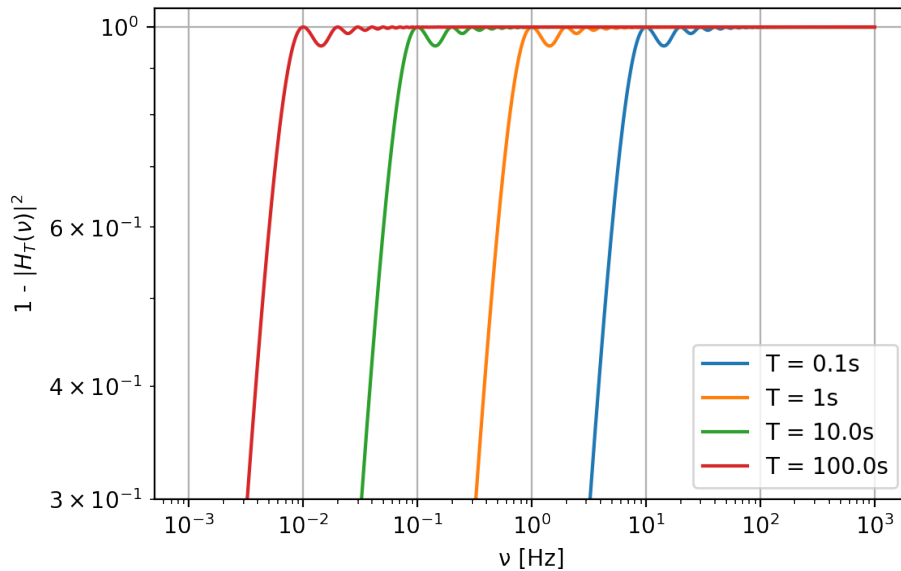

Fig. 4.9 Temporal transfer function of intra-exposure tip-tilt residuals as a function of the temporal frequencies. The colors represent different exposure times in a range from 0.1 to 100 s. The cutoff frequency $\nu_H = 1/T$ determines when either the intra-exposure transfer function stops filtering.

In Fig. 4.10, we plot the temporal PSD of both total and intra-exposure tip-tilt residuals, for values of the exposure time ranging from 0.001 to 100 s. It is evident the effect of high-pass filtering of the tip-tilt residuals PSD from the intra-exposure transfer function.
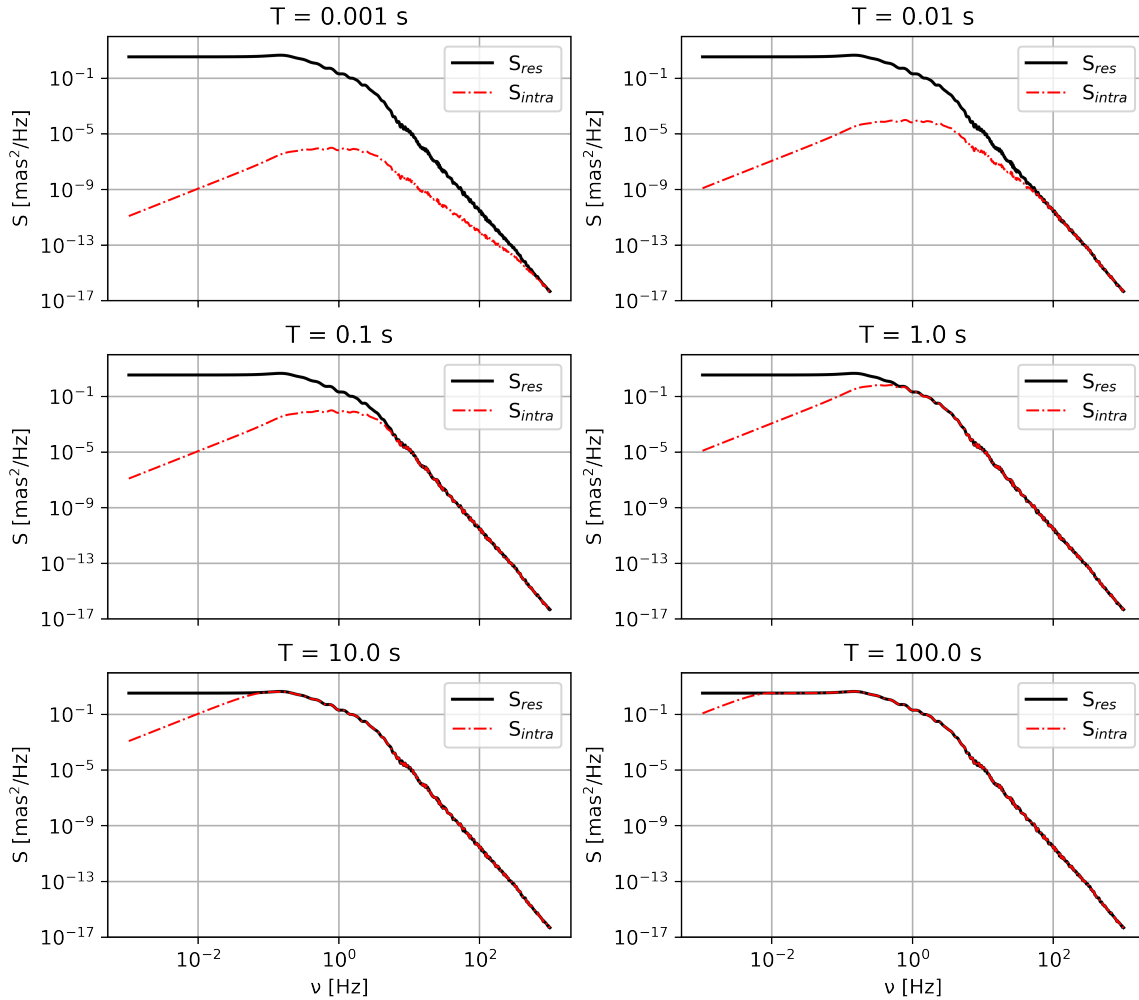

Fig. 4.10 Temporal PSD of total (black line) and intra-exposure (red line) tip-tilt residuals as a function of the temporal frequencies. The exposure time ranges from 0.001 (top left) to 100 s (bottom right). The PSDs are computed for an on-axis source.

In Fig. 4.11, we show intra-exposure residuals (square root of the integral of Eq. (4.8)) as a function of the exposure time. In this case, we observe a dependence of the errors on the exposure time through a T^1 law for small times ($T \lesssim 0.1$ s) and a flat behavior for larger times. The flat behavior is motivated by the fact that, for large integration times, most frequencies are passed and almost all the energy is integrated. For smaller times, all frequencies where the PSD is flat are filtered, and a residual PSD whose maximum value depends on T^2 is left. Thus, the variance is proportional to T^2 and the RMS to T^1. As seen
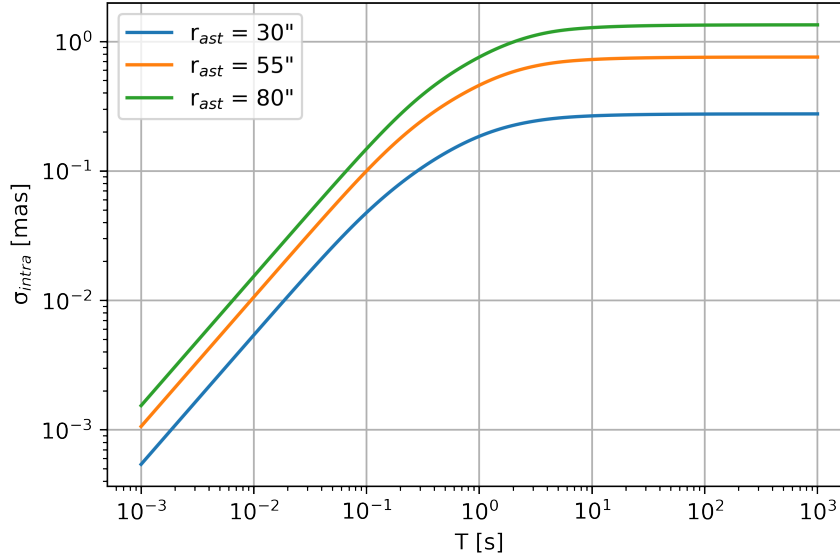
Fig. 4.11 Intra-exposure tip-tilt error as a function of the exposure time, for an on-axis target. Three values of the asterism radius are considered.

for inter-exposure residuals, switching from one power law to the other one depends on the relationship between the camera transfer function and the AO residual PSD cutoff frequencies.

4.5 Differential tip-tilt residuals

The results in Section 4.3 give information about the repeatability of the position measurement of a single source. However, the science cases of future instruments show a major interest in differential astrometry, that is, in measuring the distance between sources. To be able to estimate the precision in the distance measurements, we extend the analysis to differential tilt jitter. This effect is well known for the SCAO case but, to our knowledge, is less well understood and no expression has been presented in the literature to compute this error for the MCAO case. In this section, we derive an analytical expression that allows to estimate differential tilt jitter for this flavor of adaptive optics as well and that takes into account both spatial and temporal aspects. The derivation makes use of the results in Chapter 3.

We define the differential tilt jitter phase as the difference between the residual phases in the directions α and β of the two astrometric targets:

$$\phi_{DTJ}^{\alpha,\beta}(\nu) = \phi_{res}^{\alpha}(\nu) - \phi_{res}^{\beta}(\nu),$$

(4.9)

where $\phi_{DTJ}^{\alpha,\beta}$ is the phase describing the differential tilt jitter between the two sources, ϕ_{res}^{α} is the residual phase along α and ϕ_{res}^{β} is the residual phase along β. The temporal PSD of differential tilt jitter is

$$
\begin{aligned}
S_{DTJ}^{\alpha,\beta}(v) &= \left\langle \phi_{DTJ}^{\alpha,\beta}(v)\, \phi_{DTJ}^{\alpha,\beta\,\dagger}(v) \right\rangle \\
&= \left\langle \left(\phi_{res}^{\alpha}(v) - \phi_{res}^{\beta}(v) \right) \left(\phi_{res}^{\alpha}(v) - \phi_{res}^{\beta}(v) \right)^{\dagger} \right\rangle .
\end{aligned}
\tag{4.10}
$$

In Section 2.6.2, we showed that this equation leads, for the SCAO case, to the following expression of differential tilt jitter PSD:

$$
S_{DTJ}^{\alpha,\beta}(v) = 2 \left(S_{turb}(v) - S_{turb}^{\alpha,\beta}(v) \right),
\tag{4.11}
$$

and of differential tilt jitter variance:

$$
\left(\sigma_{DTJ}^{\alpha,\beta} \right)^2 = 2 \int dv \left(S_{turb}(v) - S_{turb}^{\alpha,\beta}(v) \right).
\tag{4.12}
$$

For MCAO systems, we derive an expression of the differential tilt jitter PSD by replacing ϕ_{res}^{α} and ϕ_{res}^{β} with the expression in Eq. (3.14) applied to α and β respectively:

$$
\begin{aligned}
S_{DTJ}^{\alpha,\beta}(v) &= \left\langle \phi_{DTJ}^{\alpha,\beta}(v)\, \phi_{DTJ}^{\alpha,\beta\,\dagger}(v) \right\rangle \\
&= \left\langle \left(\phi_{res}^{\alpha}(v) - \phi_{res}^{\beta}(v) \right) \left(\phi_{res}^{\alpha}(v) - \phi_{res}^{\beta}(v) \right)^{\dagger} \right\rangle \\
&= \left\langle \left(\phi_{turb}^{\alpha}(v) - \phi_{turb}^{\beta}(v) \right) \left(\phi_{turb}^{\alpha}(v) - \phi_{turb}^{\beta}(v) \right)^{\dagger} \right\rangle \\
&\quad - 2\,\mathrm{Re} \left\langle \Delta H_{n,tomo}^{\alpha,\beta}(v) \left(\phi_{turb}^{\boldsymbol{\theta}}(v) + \phi_n(v) \right) \left(\phi_{turb}^{\alpha}(v) - \phi_{turb}^{\beta} \right)^{\dagger} \right\rangle \\
&\quad + \Delta H_{n,tomo}^{\alpha,\beta}(v) \left\langle \left(\phi_{turb}^{\boldsymbol{\theta}}(v) + \phi_n(v) \right) \left(\phi_{turb}^{\boldsymbol{\theta}}(v) + \phi_n(v) \right)^{\dagger} \right\rangle \Delta H_{n,tomo}^{\alpha,\beta}(v)^{\dagger} \\
&= 2 \left(S_{turb}(v) - S_{turb}^{\alpha,\beta}(v) \right) + \Delta H_{n,tomo}^{\alpha,\beta}(v) \left(S_{turb}^{\boldsymbol{\theta}}(v) + S_n(v) \right) \Delta H_{n,tomo}^{\alpha,\beta}(v)^{\dagger} \\
&\quad - 2\,\mathrm{Re} \left[\Delta H_{n,tomo}^{\alpha,\beta}(v) \left(S_{turb}^{\boldsymbol{\theta},\alpha}(v) - S_{turb}^{\boldsymbol{\theta},\beta}(v) \right) \right],
\end{aligned}
\tag{4.13}
$$

where we defined $\Delta H_{n,tomo}^{\alpha,\beta}(v) = H_{n,tomo}^{\alpha}(v) - H_{n,tomo}^{\beta}(v)$, we assumed noise and turbulence to be uncorrelated and where we considered $S_{turb}^{\alpha} = S_{turb}^{\beta} = S_{turb}$. The variance of

MCAO differential tilt jitter is then

$$\left(\sigma_{DTJ}^{\alpha,\beta}\right)^2 = \int d\nu \left\{ 2\left(S_{turb}(\nu) - S_{turb}^{\alpha,\beta}(\nu)\right) \right.$$
$$+ \Delta H_{n,tomo}^{\alpha,\beta}(\nu)\left(S_{turb}^{\boldsymbol{\theta}}(\nu) + S_n(\nu)\right)\Delta H_{n,tomo}^{\alpha,\beta}(\nu)^{\dagger} \qquad (4.14)$$
$$\left. - 2\,\mathrm{Re}\left[\Delta H_{n,tomo}^{\alpha,\beta}(\nu)\left(S_{turb}^{\boldsymbol{\theta},\alpha}(\nu) - S_{turb}^{\boldsymbol{\theta},\beta}(\nu)\right)\right]\right\}.$$

If we take the SCAO limit of Eq. (4.13), we get $H_{n,tomo}^{\alpha} = H_{n,tomo}^{\beta}$ (i.e. $\Delta H_{n,tomo}^{\alpha,\beta} = 0$) and we retrieve the results for the SCAO case in Eq. (4.11). Equation (4.13) shows that the differential tilt jitter PSD in MCAO systems is given by the SCAO case PSD (first two terms) and additional terms that depend on the correction (asterism/targets geometry, temporal filtering of the AO loop, noise) and on spatiotemporal cross-correlations of turbulence. These additional terms might reduce the error with respect to the SCAO case. In Fig. 4.12, we analyze this aspect from the RMS of the difference between the variances obtained from Eq. (4.12) and Eq. (4.14) (denoted as $\Delta\sigma_{DTJ}$ in the plot) as a function of the outer scale. It is shown that the discrepancy between the SCAO and the MCAO values increases
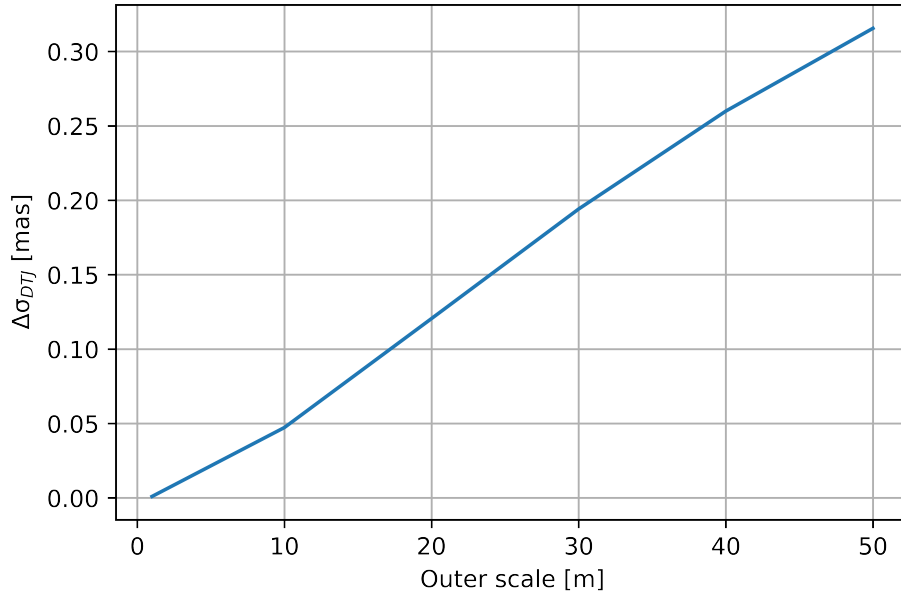

Fig. 4.12 RMS of the difference between SCAO and MCAO differential tilt jitter variances (Eq. (4.12) and Eq. (4.14), respectively) as a function of the outer scale. The angular separation of the targets is 5" and the asterism radius is 40".

with the outer scale, as a larger outer scale leads to larger cross-correlations that help reduce the differential tilt jitter error in the MCAO correction.

In Fig. 4.13, we plot the MCAO differential tilt jitter error as a function of the radius of the NGS asterism. The smaller cross-correlations given by larger asterisms determine an increasing of the differential tilt jitter error with the asterism radius. This is evident when the distance is small and both targets are included within the asterism (d = 1", 5"); for larger distances, the errors are about constant up to an asterism radius comparable to the targets' separation and then show the increasing behavior.

In Fig. 4.14, we show the differential tilt jitter error as a function of the distance between the two astrometric sources. In the MCAO case, the dependence of the differential tilt jitter error on the distance is influenced by the position of the sources with respect to the asterism of guide stars and it becomes approximately linear when the asterism radius is significantly larger than the scientific field.
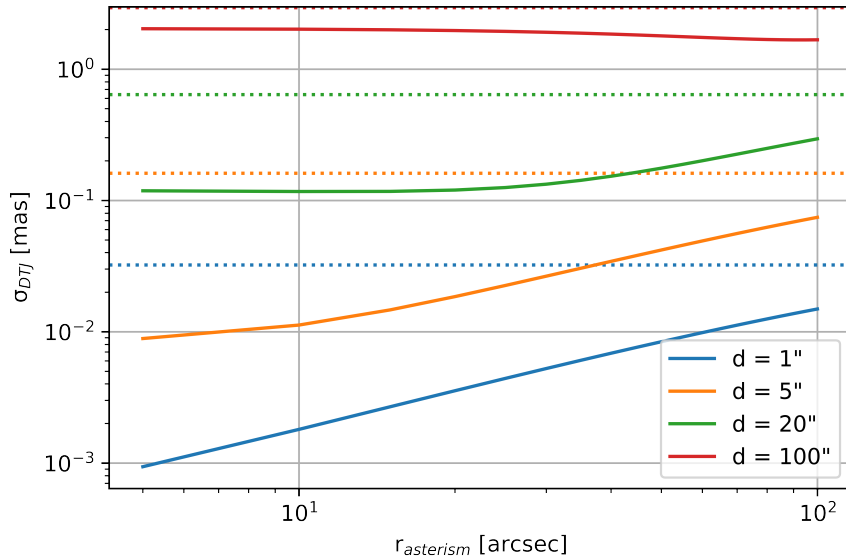

Fig. 4.13 MCAO differential tilt jitter error as a function of the NGS asterism radius. The colors show different values of the distance between the astrometric targets. For each curve, the SCAO case is shown as comparison (dotted lines).

Finally, we can take into account the effect of the scientific integration time as well. Since differential tilt jitter is caused by the residual (differential) tip-tilt that is left between successive frames, it can be modeled as inter-exposure residuals. The time-averaged differential tilt jitter phase can then be written as

$$\phi_{DTJ,T}^{\alpha,\beta}(\nu) = H_T(\nu) \left(\phi_{res}^{\alpha}(\nu) - \phi_{res}^{\beta}(\nu) \right). \tag{4.15}$$
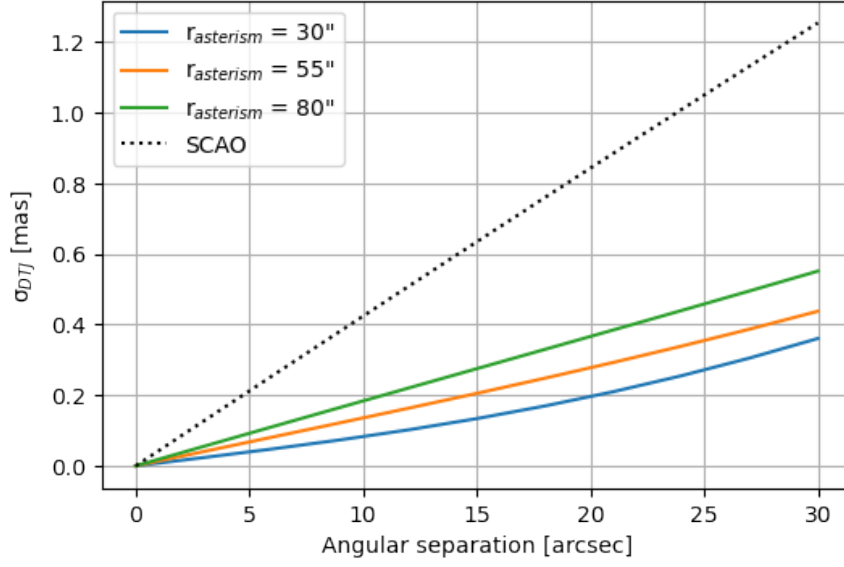
Fig. 4.14 Differential tilt jitter error as a function of the angular separation of the sources. The colored solid lines represent different values of the asterism radius. The errors for the SCAO case are shown in comparison (black dotted line).

Thus the PSD of time-averaged differential tilt jitter becomes

$$S^{\alpha,\beta}_{DTJ,T}(\nu) = |H_T(\nu)|^2 S^{\alpha,\beta}_{DTJ}(\nu), \qquad (4.16)$$

and the variance

$$\left(\sigma^{\alpha,\beta}_{DTJ,T}\right)^2 = \int d\nu |H_T(\nu)|^2 S^{\alpha,\beta}_{DTJ}(\nu), \qquad (4.17)$$

where $S^{\alpha,\beta}_{DTJ}$ is given by Eq. (4.13) for MCAO and by Eq. (4.11) for SCAO. It follows that differential tilt jitter can be reduced with proper integration times, thanks to the $T^{-1/2}$ law of inter-exposure residuals.

Chapter 5

Impact of MCAO tip-tilt residuals on future astrometric observations

In this chapter we study the contribution of tip-tilt atmospheric residuals to the astrometric error budget of future MCAO-assisted astrometric observations. In particular, we give results on MORFEO at the ELT and on MAVIS at the VLT.

In Section 5.1, we show how tip-tilt residuals contribute to the astrometric error budget through differential tilt jitter and centroiding error terms; in Section 5.2 and in Section 5.3, we estimate the errors for future observations of differential astrometry with, respectively, MORFEO and MAVIS.

5.1 Tip-tilt residuals within the astrometric error budget

As introduced in Section 1.4.2, tip-tilt residuals can affect the precision on the differential astrometric measurements through both differential tilt jitter and centroiding error. If considering the measurement of the distance between two objects at positions α and β, the uncertainty on the differential astrometric measurements due to tip-tilt residuals can be estimated as [49]:

$$\left(\sigma_d^{\alpha,\beta}\right)^2 = \left(\sigma_{DTJ}^{\alpha,\beta}\right)^2 + \left(\sigma_{cent}^{\alpha}\right)^2 + \left(\sigma_{cent}^{\beta}\right)^2, \tag{5.1}$$

where $\left(\sigma_d^{\alpha,\beta}\right)^2$ is the variance of the distance measurements between α and β, $\left(\sigma_{DTJ}^{\alpha,\beta}\right)^2$ is the variance of differential tilt jitter and $\left(\sigma_{cent}^{x}\right)^2$ indicates the variance due to the centroiding error in a direction x ($x = \alpha$, β) of the field of view.

The variance of differential tilt jitter can be estimated through Eq. (4.17), where the differential tilt jitter PSD can be computed by means of Eq. (4.13) for MCAO.

The centroiding error, i.e. the theoretical limit to the astrometric precision that is due to the photon noise, can be estimated from [52]

$$\sigma_{cent} \approx \frac{1}{\pi} \frac{FWHM}{SNR}. \tag{5.2}$$

thus, depends on both the dimension of the PSF, through its FWHM, and the SNR. The FWHM can be affected by intra-exposure tip-tilt residuals as they can lead to PSF elongation effects and then have an impact on the PSF shape and size. In this case, the effect has to be taken into account within the computation of the centroiding error.

Assuming tip-tilt residuals approximated through Gaussian statistics [96], we can estimate the elongated PSF from the convolution between the diffraction-limited PSF and the gaussian kernel due to tip-tilt residuals (Fig. 5.1). In this case, the FWHM can be
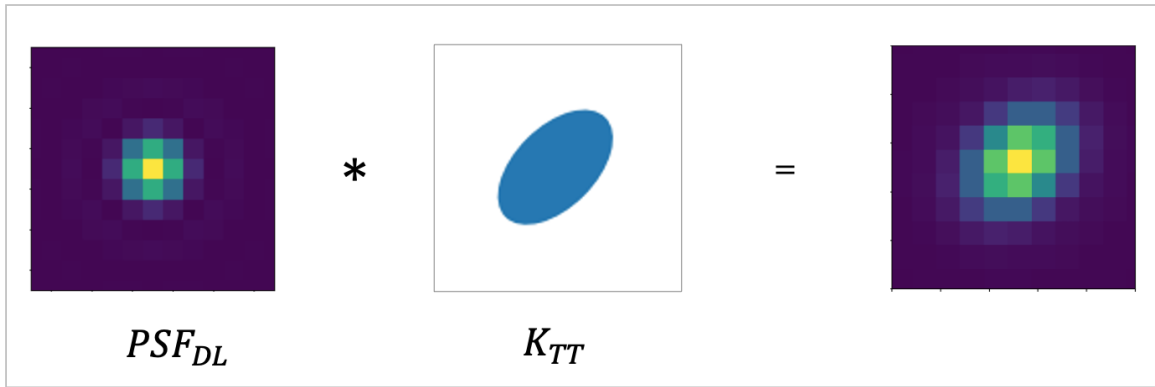

Fig. 5.1 Scheme of the convolution operation between the diffraction-limited PSF (left) and the tip-tilt kernel (center), derived from tip-tilt covariance matrices, to obtain the elongated PSF (right) due to the effect of tip-tilt residuals.

derived as

$$FWHM = \sqrt{f_{conv,x}^2 + f_{conv,y}^2}, \tag{5.3}$$

where

$$\begin{aligned} f_{conv,x} &= \sqrt{f_{DL}^2 + f_{tip}^2} \\ f_{conv,y} &= \sqrt{f_{DL}^2 + f_{tilt}^2}. \end{aligned} \tag{5.4}$$

We defined f_{conv} as the FWHM of the convolved PSF (x and y indicate the two axes), f_{DL} as the FWHM of the diffraction-limited PSF and $f_{tip(tilt)}$ as the FWHM computed from

the standard deviation related to the intra-exposure tip(tilt) residuals. Thus, Eq. (5.2) can be written as

$$\sigma_{cent} = \frac{1}{\pi}\sqrt{\frac{2f_{DL}^2}{SNR^2} + \frac{f_{tip}^2 + f_{tilt}^2}{SNR^2}}. \qquad (5.5)$$

In photon-noise limited case, SNR $\propto T^{-1/2}$. Thus, the centroiding error has still a $T^{-1/2}$ dependence if the diffraction-limited contribution is dominant; if intra-exposure tip-tilt residuals contribute more, the dependence on the exposure time will follow a $T^{1/2}$ law for small times where intra-exposure residuals show a T^1 behavior, and still a $T^{-1/2}$ law for larger times where intra-exposure residuals are not time-dependent.

Putting altogether the results on differential tilt jitter and centroiding error, we can estimate Eq. (5.1) as

$$\left(\sigma_d^{\alpha,\beta}\right)^2 = \int d\nu |H_T(\nu)|^2 S_{DTJ}^{\alpha,\beta}(\nu) + \frac{1}{\pi^2}\frac{2f_{DL}^2 + f_{tip_\alpha}^2 + f_{tilt_\alpha}^2}{SNR_\alpha^2} + \frac{1}{\pi^2}\frac{2f_{DL}^2 + f_{tip_\beta}^2 + f_{tilt_\beta}^2}{SNR_\beta^2}. \quad (5.6)$$

5.2   Tip-tilt residuals in MORFEO-assisted observations

MORFEO will provide an MCAO correction to the first light near-infrared camera MICADO at the ELT. One of the main science drivers of MORFEO-MICADO is high precision differential astrometry and MORFEO must guarantee that MICADO astrometric observations fulfill the requirement of 50 μas of precision (the goal is 10 μas).

In this context, we exploit the formulation and the reasoning of the previous chapters to have an estimate of the impact of tip-tilt atmospheric residuals on MORFEO-MICADO astrometric error budget. The results are obtained within the framework of analysis presented in Section 4.1. Thus, we consider a 39-m telescope, with the DM0 conjugated at 600 m and the DM1 at 17 km. We assume the ELT median turbulence profile reported in Sarazin *et al.* [89], with a seeing of 0.644" and an average wind speed of 9.2 m/s. We consider the contribution of all the modes to the turbulence-induced wavefront distortions and a reconstruction of tip-tilt with the DM0 and focus-astigmatisms with the DM1, based on the tip-tilt measurements from three NGSs in equilateral asterisms. We assume the equilateral asterism of NGSs centered at the origin of the field of view and the diameter of the NGSs technical FoV of 160". We neglect the noise assuming NGSs with infinite flux, as well as we minimize the temporal error considering a loop with a

frequency frame rate of 1 kHz and where the control is a pure integrator with a delay given by the WFSs exposure time only.

5.2.1 Differential tilt jitter error

We start estimating the astrometric error due to differential tilt jitter when measuring the distance between two astrometric targets in the MICADO FoV. We always consider one target at the center of the FoV and the other one at a specific angular separation; in order not to be affected by the geometry of the asterism of NGSs, for each separation we make an azimuthal average of the errors obtained at different polar coordinates.

In Fig. 5.2, we plot the differential tilt jitter as a function of the angular separation between the astrometric sources, for different values of the NGSs asterism radius up to the radius of the technical FoV. The errors are computed for exposures with integration time of 120 s, that is the one that has been identified for a typical single exposure with MICADO. We explore three different values of the zenith angle, $\zeta = 30°$, $45°$ and $60°$, that correspond to a seeing of 0.70", 0.79" and 0.98", respectively. The first value ($\zeta = 30°$) represents the "reference zenith angle" for MORFEO performance analysis, that is, it is the angle at which MORFEO shall deliver the required performance; the last value ($\zeta = 60°$) represents the maximum zenith angle for MORFEO, as it is the maximum angle at which the lasers can operate. The curves show that the astrometric error due to differential tilt jitter is within the requirement in the whole FoV, with values up to 30-40 μas at the edge of the FoV, for $\zeta = 30°$; the goal of 10 μas is met at only few arcseconds angular separations when considering the maximum value of the asterism radius. The requirement of 50 μas is not fulfilled in the whole FoV for both $\zeta = 45°$ and $60°$. In particular, at $\zeta = 60°$ differential tilt jitter might represent a relevant contributor to the astrometric error budget for targets at $\approx 10"$ separation considering the whole technical FoV. At this zenith angle, few arcseconds separations are still within the requirement, but the errors are at the limit of the goal value. Longer integration times could help reduce differential tilt jitter error at these zenith angle, considering the $T^{-1/2}$ dependence.

However, current specifications suggest a major interest in high-precision differential astrometry for targets at small angular separations (d $\approx 1"$) and, in this case, differential tilt jitter should not be the dominant limiting factor to astrometric precision.
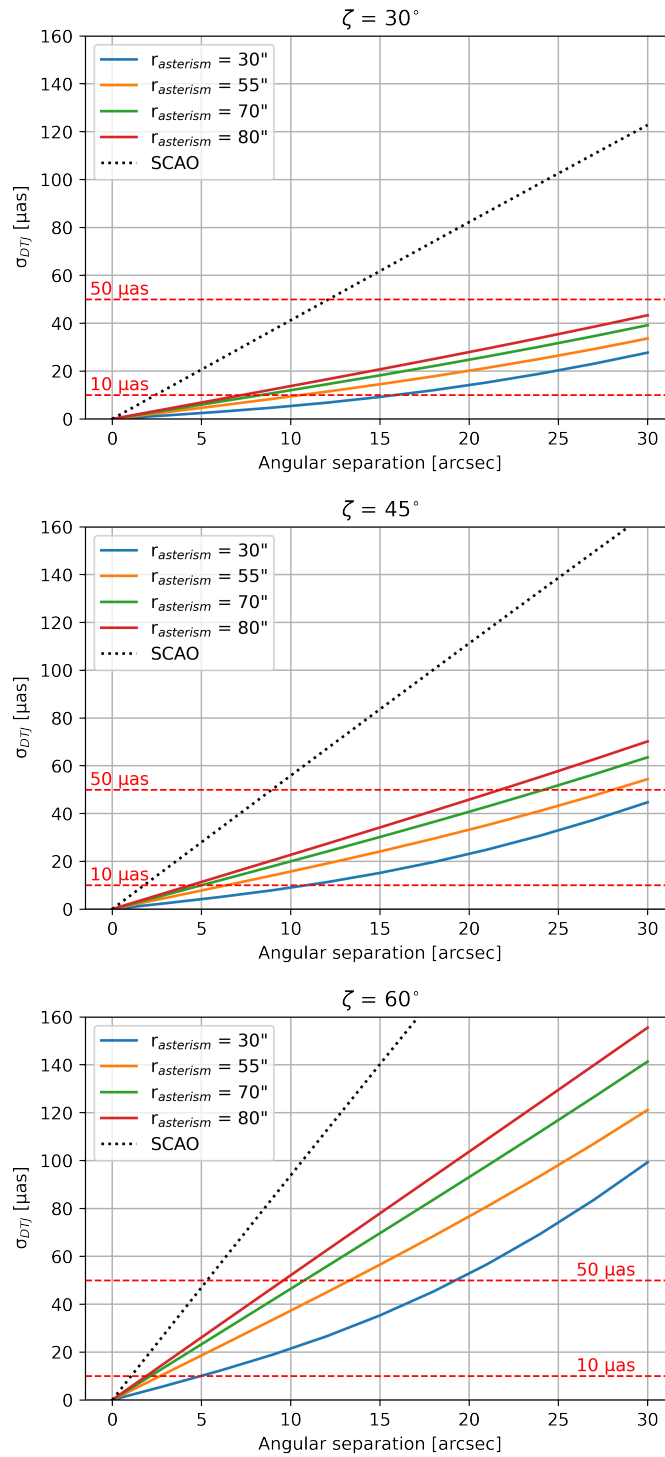
Fig. 5.2 Differential tilt jitter error as a function of the angular separation for MORFEO-assisted observations with exposure time T = 120 s and zenith angle ζ = 30° (top), 45° (center) and 60° (bottom). Solid colored lines represent the MCAO errors for different values of the NGSs asterism radius. The SCAO case (dotted black line) is shown for comparison, as well as the astrometric precision requirement and goal (dashed red lines).

5.2.2   Centroiding error

We analyze the contribution of MORFEO atmospheric tip-tilt residuals to centroiding error. We restrict the analysis to an angular separation between astrometric sources of 1" and to the worst case of asterism radius, i.e. 80". One of the two sources is at the center of the FoV.

In Fig. 5.3, we first show the FWHM of the gaussian kernel due to intra-exposure tip-tilt residuals on the source at the origin of the FoV, as a function of the integration time. The diffraction-limited FWHM for infrared observations in H band ($\lambda = 1.6$ μm; FWHM $\approx$ 8.5 mas) is shown in comparison. Again, we consider three zenith angle values, $\zeta = 30°$, 45° and 60°. Since the PSF elongation effect is caused by intra-exposure residuals, we retrieve the dependence on the exposure time that has been shown in Fig. 4.11 and we see that larger integration times lead to larger elongation of the PSF. However, for $\zeta = 30°$ and 45°, the contribution of tip-tilt residuals to the FWHM is smaller than the value of the diffraction-limited FWHM, which therefore dominates the contribution to the centroiding error. On the other hand, for $\zeta = 60°$ the errors are more important and, for exposures larger than ≈ 1 s, they exceed the diffraction-limited FWHM.

These results must be combined with the SNR to estimate the centroiding error, as shown in Eq. (5.5). Thus, we consider different values of magnitude in H band ($\text{mag}_H = 10$, 15, 20, 25), spanning in an observable range with MICADO-MORFEO, and we estimate the SNR considering a total transmission of 65%. In Fig. 5.4, we show the related centroiding error for the source at the origin of the FoV, computed from Eq. (5.5) and where the FWHM is estimated from Eqs. (5.3) and (5.4). The curves behavior is still dominated by the $T^{-1/2}$ law. However, it is interesting to note, for $\zeta = 60°$, the small bumps occurring at few seconds of integration time where intra-exposure tip-tilt residuals start dominating the contribution to the FWHM, as shown in Fig. 5.3. For larger times, tip-tilt residuals are not time-dependent and the $T^{-1/2}$ law of the centroiding error is maintained.

In general, for all zenith angles, centroiding error on brighter objects shows to be within MORFEO astrometric requirement for typical exposures of 120 s and should not represent a dominant limiting factor.
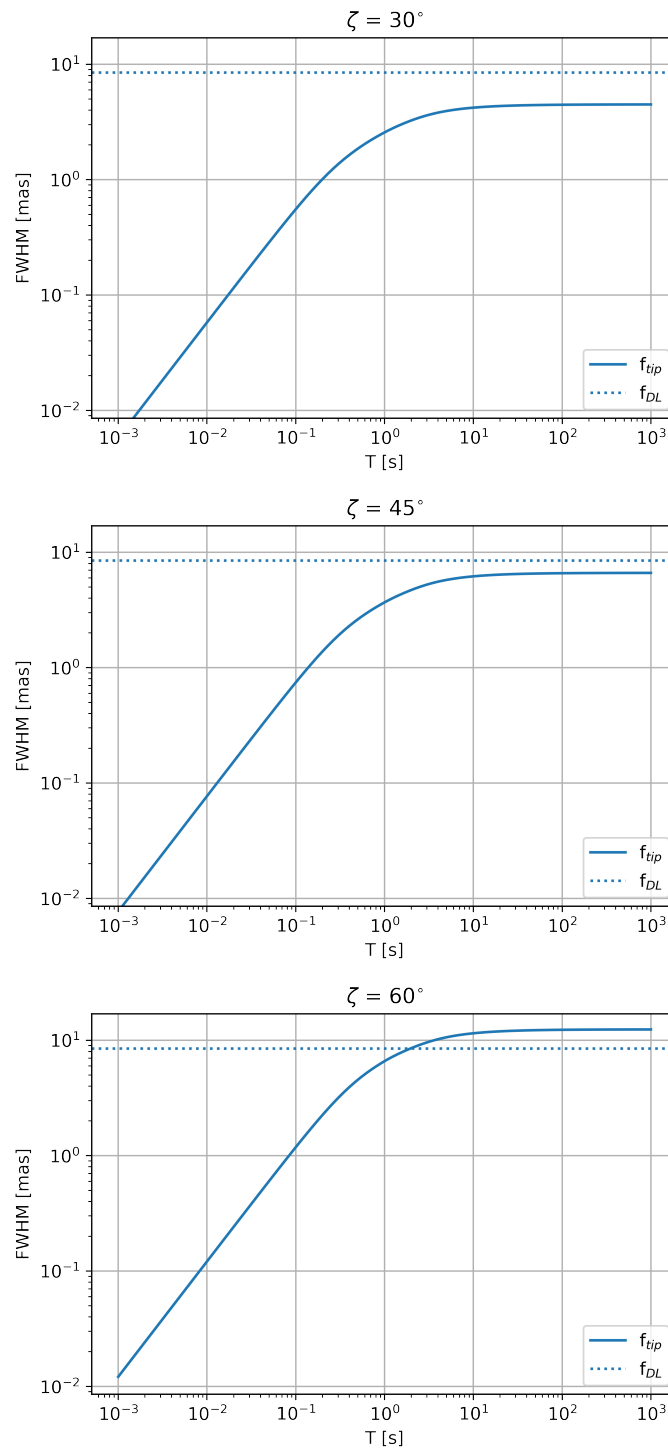
Fig. 5.3 FWHM of the gaussian kernel related to intra-exposure residuals of tip (solid line), for a source on axis, as a function of the exposure time and for zenith angle $\zeta = 30°$ (top), 45° (center) and 60° (bottom). The value of the diffraction-limited FWHM in the H band is shown in comparison (dotted line). The asterism radius is 80".

Fig. 5.4 Centroiding error as a function of the exposure time, for two targets at 1" separation. The colors show different values of the magnitude of the source in the H band. Both the requirement (50 μas) and the goal (10 μas) of MORFEO astrometric precision are shown in comparison (dotted black lines).

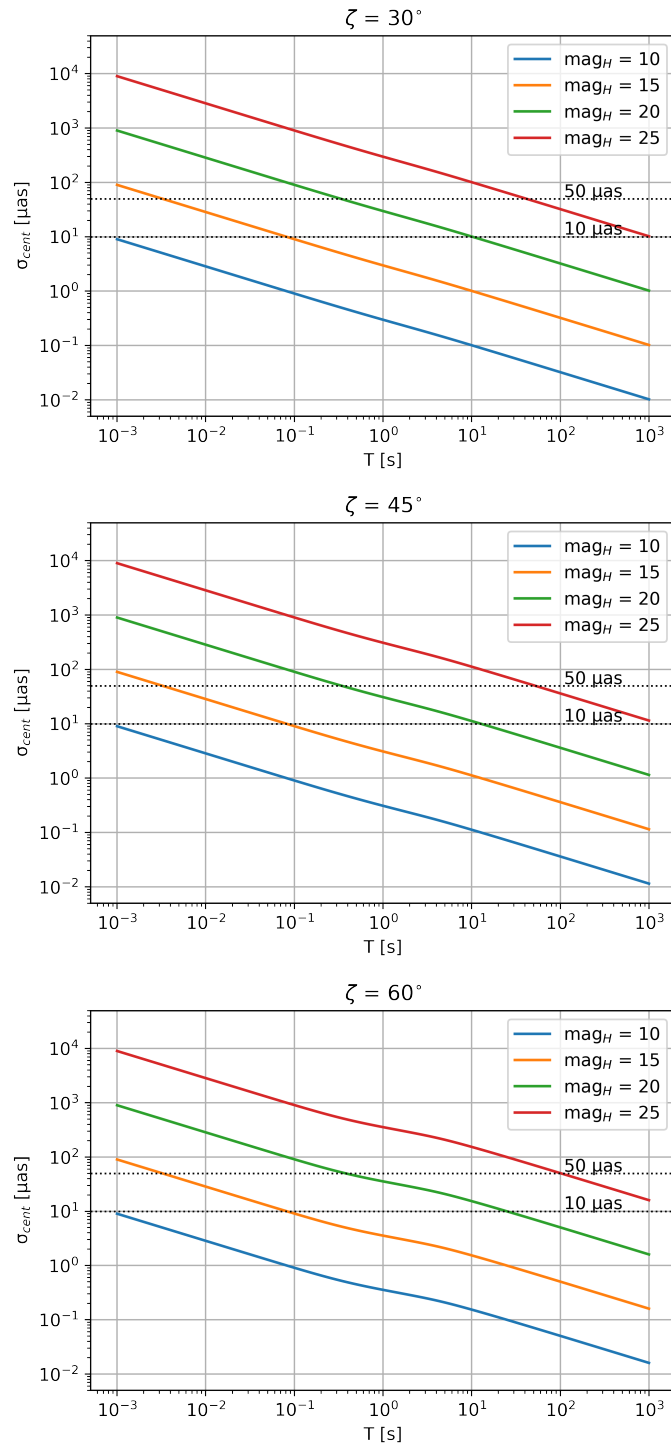### 5.2.3   Error budget at 1" separation

In this section, we estimate the total contribution of tip-tilt atmospheric residuals to MORFEO astrometric error budget for targets at 1" separation. We put together the results on differential tilt jitter and centroiding error obtained in the two previous paragraphs and we use Eq. (5.6) for a global estimation. We consider an NGS asterism radius of 80" and we still vary the zenith angle from $\zeta = 30°$ to $\zeta = 60°$.

In Fig. 5.5, we show the total error budget from tip-tilt atmospheric residuals for two sources at 1" angular separation, with one of the two targets at the center of the FoV. The sources are assumed to have same magnitude, which varies from $\text{mag}_H = 10$ to $\text{mag}_H = 25$. The plots show that the centroiding error dominates the contribution to the astrometric error for the fainter sources. On the other hand, the high SNR of the brighter objects ($\text{mag}_H = 10, 15$) makes the centroiding error negligible with respect to differential tilt jitter effect.

For typical exposure times, tip-tilt atmospheric residuals should not impact on MORFEO astrometric requirements at 1" separations for sources with mag_H up to 20. Fainter objects are at the limit of MORFEO requirements for 2 min exposures but, in general, these errors can be reduced with longer integration times. Of course, in this case, other sources of astrometric error becomes relevant (e.g plate-scale distortions from the telescope) and a trade-off in the choice of the exposure time must be found.

It is worth pointing out that these results show the contribution of atmospheric residuals only: the contribution of temporal errors of the AO loop is minimized, noise terms are neglected and other contributors such as aliasing and high-order residuals are also not considered. On the other hand, we did not consider the correction of higher orders than astigmatisms from the LGS loop, thus, in this context, our results should represent an upper limit.
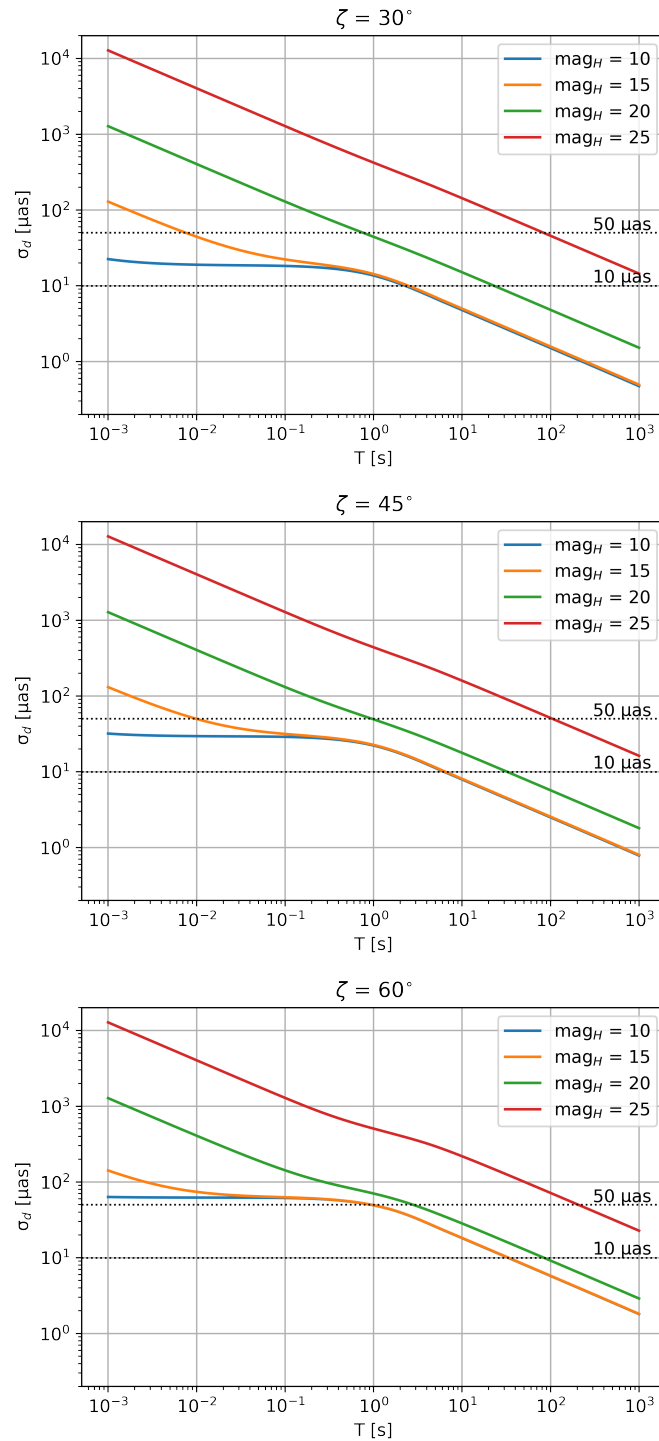
Fig. 5.5 Astrometric error due to MORFEO atmospheric tip-tilt residuals as a function of the scientific integration time, for two targets at 1″ separation. The errors are shown for three zenith angles, $\zeta = 30°$ (top), 45° (center) and 60° (bottom). The colors represent different magnitudes of the astrometric sources in H band. Both the requirement (50 μas) and the goal (10 μas) of MORFEO astrometric precision are shown in comparison (dotted black lines).

5.3   Tip-tilt residuals in MAVIS-assisted observations

We apply the analysis of the previous section to MAVIS. MAVIS is an instrument being built for the VLT Adaptive Optics Facility (AOF) [29] and will be the first MCAO system to perform AO correction in the visible, with performance optimized at 550 nm. It will feed both an imager and a spectrograph and one of the main science targets is high-precision astrometry in crowded stellar fields, which is shared in common with MORFEO-MICADO. In this case, it is required an astrometric precision of 150 μas and the goal is 50 μas.

For the analysis of MAVIS astrometric error due to atmospheric tip-tilt residuals, we considered the 8-m aperture of the VLT, the MAVIS technical FoV of 120" diameter for the NGSs, the scientific FoV of 30"×30", one DM at the ground compensating for tip and tilt and one DM at 13.5 km compensating for focus and astigmatisms. We still assumed the turbulence profile in Sarazin *et al.* [89], with seeing of 0.644".

5.3.1   Differential tilt jitter error

As for MORFEO analysis, we consider one target at the center of the FoV and we vary the angular separation of the second astrometric target; the errors computed at different polar coordinates are then averaged for each separation.

In Fig. 5.6, we plot the astrometric error due to differential tilt jitter as a function of the angular separation between the astrometric targets, for different values of the radius of the NGSs asterism up to the radius of the technical FoV. The errors are averaged over exposures of T = 120 s. We compute the errors for zenith angles ζ = 30°, 45° and 60°, corresponding to seeing values of 0.70", 0.79" and 0.98" respectively. Differential tilt jitter shows to have a major impact with respect to the requirements, compared to the MORFEO case, as expected from the small telescope aperture diameter. At ζ = 30°, only few arcseconds separations are affected by errors within the requirement of 150 μas and, at ζ = 60°, only 1" separations are at the limit of the requirement; besides, in this case it is interesting to note that differential tilt jitter for the maximum asterism radius (r_{ast} = 60") is approximately the same as the one obtained with a SCAO correction. The plots show that averaging over longer times is required: with $\approx$ 20 min of exposures, the error due to differential tilt jitter can be reduced by a factor $\approx$ 10 and be within the requirement value over the whole FoV, even for the worst case at ζ = 60°.

However, as for MORFEO, current specifications suggest a major interest in high-precision differential astrometry at $\approx$ 1" separations where differential tilt jitter is controlled.
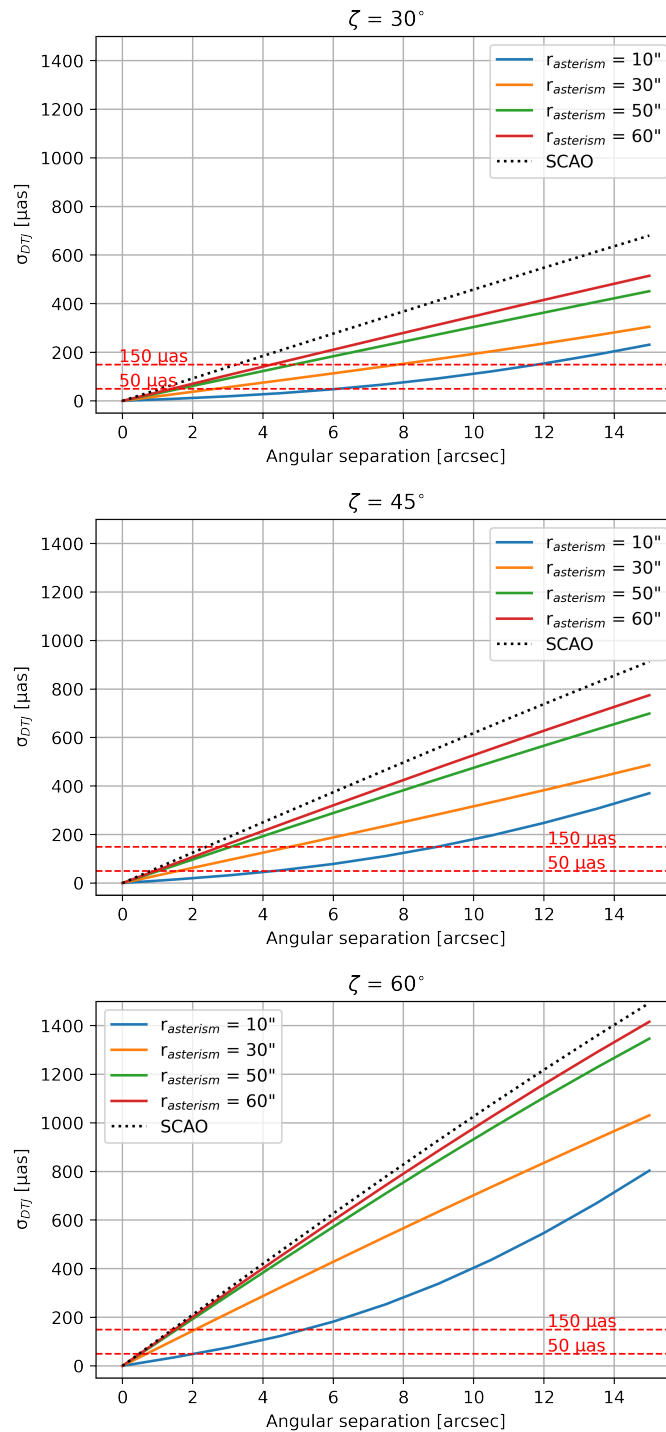
Fig. 5.6 Differential tilt jitter error as a function of the angular separation for MAVIS-assisted observations with exposure time T = 120 s and zenith angle $\zeta = 30°$ (top), 45° (center) and 60° (bottom). Solid colored lines represent the MCAO errors for different values of the NGSs asterism radius. The SCAO case (dotted black line) is shown for comparison, as well as the astrometric precision requirement and goal (dashed red lines).

5.3.2   Centroiding error

We analyze the impact of atmospheric tip-tilt residuals from MAVIS on centroiding error. We consider two targets at 1" separation, one of which at the center of the FoV, and the maximum asterism radius (r_{ast} = 60").

In Fig. 5.7, we show the FWHM of the gaussian kernel due to intra-exposure tip-tilt residuals on the source at the origin of the FoV, as a function of the integration time. We consider ζ = 30°, 45° and 60° and we compare the results to the diffraction-limited FWHM in V band (λ=550 nm; FWHM≈14 mas). Unlike MORFEO case, MAVIS intra-exposure tip-tilt residuals show to be dominant than the diffraction-limited FWHM, even at ζ = 30° and starting from small exposure times. This effect is evident in the centroiding error.

In Fig. 5.8, we show the centroiding error computed from Eq. (5.5), considering values of magnitude in V band from 10 to 25 and having estimated the SNR in case of 80% total transmission. The sources are assumed to have the same magnitude. The plots show a bump at exposure times smaller than 1 s, where intra-exposure tip-tilt residuals start dominating the contribution to the FWHM with respect to its diffraction-limited value, and then a dependence on time as $T^{-1/2}$, where the FWHM due to tip-tilt residuals is not time-dependent. For typical exposure times ($T \gtrsim$ 120 s), tip-tilt residuals do not have a major impact on astrometric precision and are within the requirement for the brighter objects; on the other hand, for fainter objects (mag_V = 25), they lead to centroiding errors that never meet the requirement of 150 μas.

5.3.3   Error budget at 1" separation

We estimate the total contribution of tip-tilt atmospheric residuals from MAVIS to astrometric precision for targets at 1" separations. We consider an asterism radius of 60" and ζ = 30°, 45° and 60°.

In Fig. 5.9, we plot the astrometric error, as computed from Eq. (5.6), on the measurement of the distance between the two sources. The astrometric objects are assumed to have the same magnitude in V band, that varies from 10 to 25. As for MORFEO case, the astrometric error on the brighter objects is dominated by differential tilt jitter error, whose value is within the requirement of 150 μas for exposure times larger than 120 s, but not within the goal of 50 μas for ζ = 60°; on the other hand, fainter objects are dominated by the centroiding error that never fullfills the requirements on astrometric precision. Ideally, one could reduce the error by integrating more than the maximum value of exposure time shown in the plots (T = 1000 s ≈ 17 min), but other sources of astrometric error would become relevant over such time intervals.
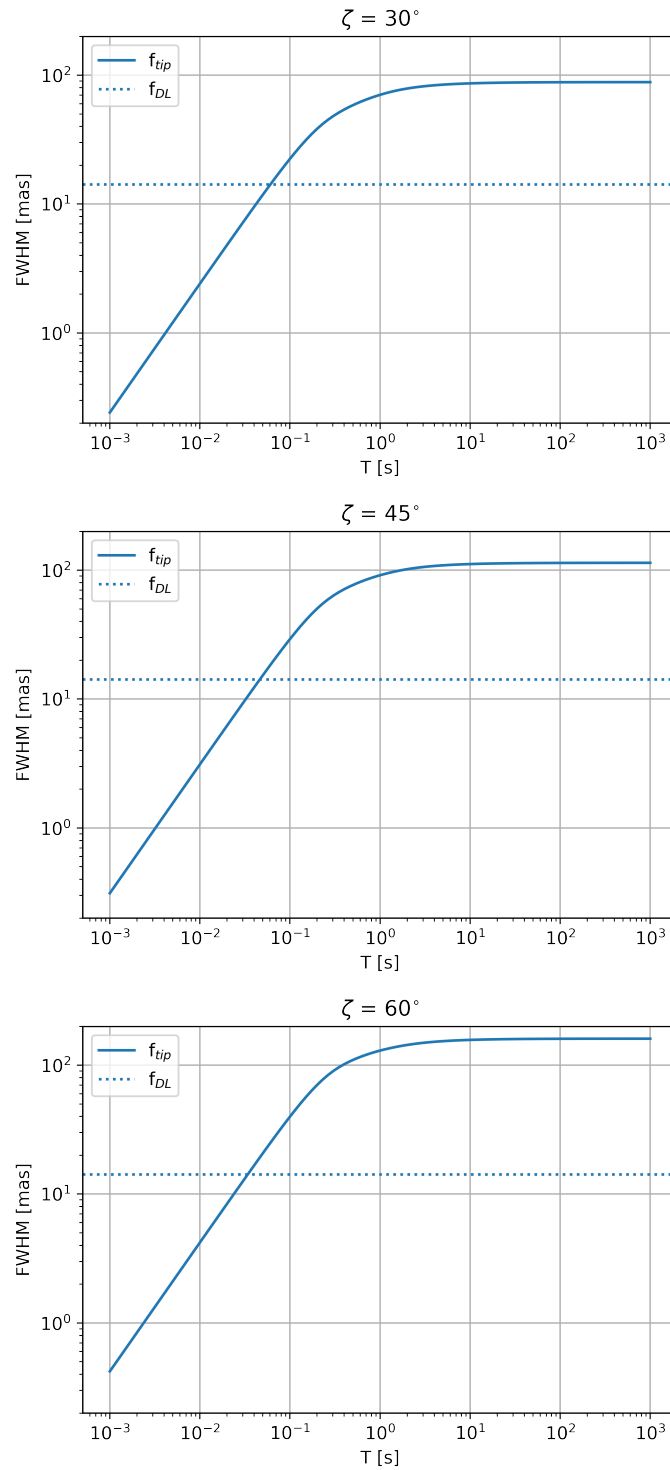
Fig. 5.7 FWHM of the gaussian kernel related to intra-exposure residuals of tip (solid line) from MAVIS, for a source on axis, as a function of the exposure time and for zenith angle $\zeta = 30°$ (top), $45°$ (center) and $60°$ (bottom). The value of the diffraction-limited FWHM in the V band is shown in comparison (dotted line). The asterism radius is 60".
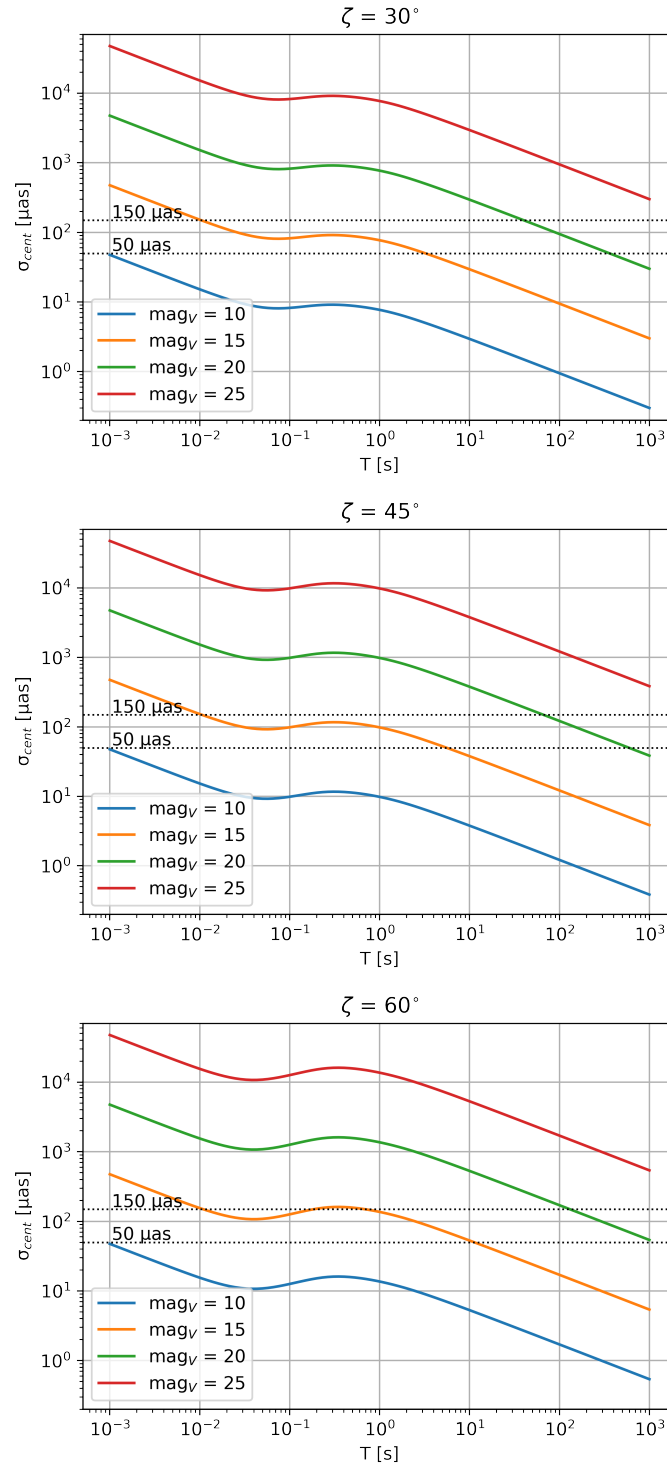
Fig. 5.8 Centroiding error as a function of the exposure time, for two targets at 1" separation. The colors show different values of the magnitude of the source in the V band. Both the requirement (150 μas) and the goal (50 μas) of MAVIS astrometric precision are shown in comparison (dotted black lines).
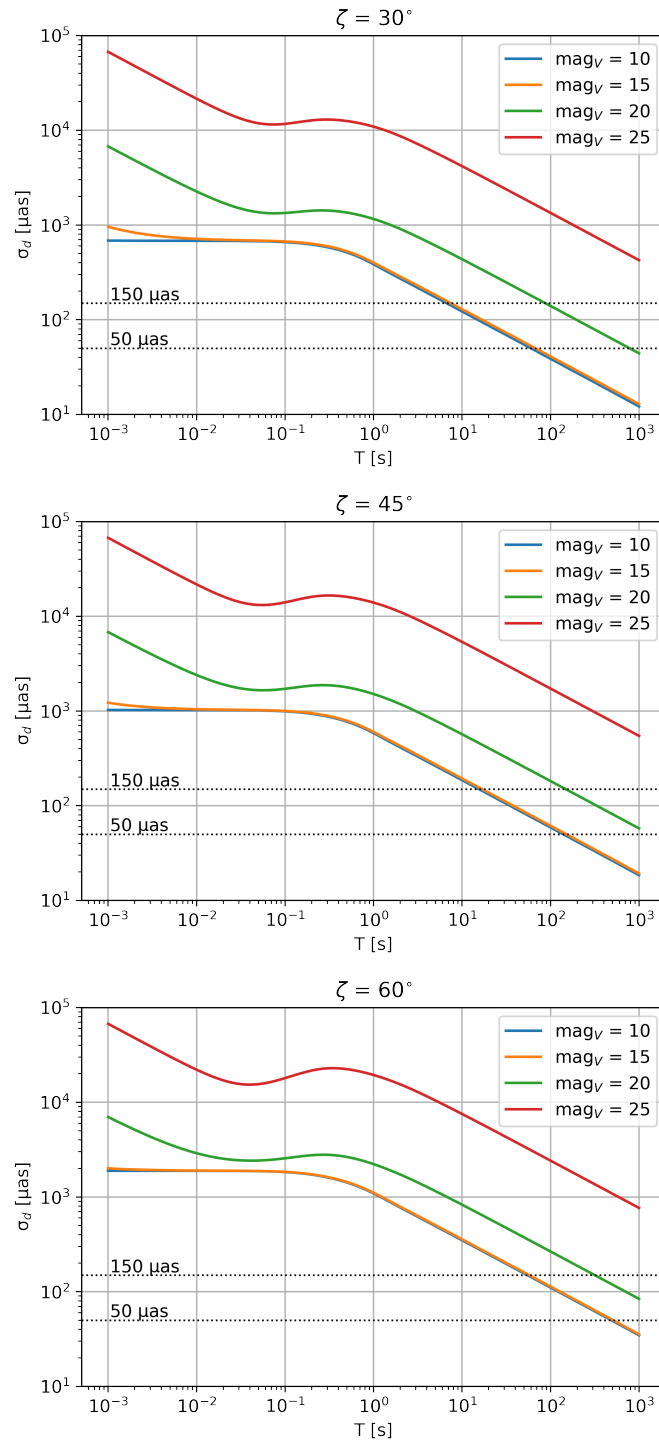
Fig. 5.9 Astrometric error due to MAVIS atmospheric tip-tilt residuals as a function of the scientific integration time, for two targets at 1" separation. The errors are shown for three zenith angles, $\zeta = 30°$ (top), 45° (center) and 60° (bottom). The colors represent different magnitudes of the astrometric sources in V band. Both the requirement (150 μas) and the goal (50 μas) of MAVIS astrometric precision are shown in comparison (dotted black lines).

Chapter 6

Testing astrometric capabilities of actual AO systems for future MCAO observations

In parallel to the study presented in the previous chapters, we worked on a proposal to observe the gravitational light bending from Jupiter by means of differential astrometry with SOUL-LUCI [67] at the LBT. We submitted our proposal of observations, "Bend it like Jupiter", on the occasion of the "Call for Proposal for the LBT Observing period 2021-2022". The aim is to test the astrometric capabilities of actual AO systems, SOUL in this case, to have an understanding of potential issues that can occur during the observations or the data reduction process, in order to have a better comprehension of the strategies to be adopted in astrometric observations with MORFEO at the ELT. Despite the acceptance of the proposal, unfortunately the observations could not be made at the LBT; thus, we are working on new analyses to perform the observations with the upcoming ERIS, the AO system that is going to equip the near-infrared imager NIX at the VLT [97].

6.1   Scientific framework

Gravitational light bending was the first new prediction of general relativity to be successfully tested during the solar eclipse of 1919, when Eddington and Dyson announced that the results of their expeditions were consistent with Einstein's general relativistic prediction of a deflection of 1.75" at the solar limb [98]. Since then, light bending due to the Sun during eclipses has been measured many times until 1973, without big improvements in the uncertainties with respect to Eddington's one (around 6%). Uncertainties were reduced to below 1% using radio emission from quasars in the 1970's [99] and further improved by means of optical measurements from space, when astrometric satellites

became operational (Hipparcos reached 0.2%) [100]; the best available measurements to date, obtained by VLBI techniques, have relative uncertainties around $10^{-4} \div 10^{-5}$, and the Gaia satellite is expected to reach 10^{-6} at optical wavelengths.

The Sun is not special at all, however, and any massive body gravitationally bends the light that passes close to it. Indeed, astrometric catalogs take light bending due to many solar system bodies into account when calculating the apparent positions of stars. Besides the Sun, the largest effect is due to the planet Jupiter, and roughly amounts to 1/100 of the solar one: 16 mas of deflection for a star at Jupiter's limb. Such a deflection has been measured from the ground with VLBI at the radio wavelengths emitted by a quasar [101] and a measurement in the visible band from space with HST was recently planned [102]; the observations have been executed, but results have not been published yet. One of the goals of the Gaia mission is to measure Jupiter's light bending with sufficiently high accuracy to extract and quantify the quadrupole contribution [103]; first results have been published in this direction [104], but without being able to disentagle quadrupole from monopole contribution. To the best of our knowledge, no measurements of Jupiter's gravitational light bending using ground-based telescopes at visible or infrared wavelengths have been performed yet.

In this context, the aim of our proposal is to measure Jupiter's gravitational light bending by measuring the relative positions of as many stars as possible in a field close to Jupiter, using SOUL in the near infrared (K band). It is a challenging measurement and it would be impossible from the ground without an AO system, because we need to perform astrometry with precision of the order of the mas or better. This would be the first ground-based measurement of Jupiter's light bending at near-infrared wavelengths and the first using an AO system. Uncertainties will not allow to measure any contribution to light bending due to Jupiter beyond the monopole (the quadrupole would require a μas precision). However, such an observation would be a test of the performance of SOUL in non-ideal conditions (e.g. at rather large zenith angles). Moreover, carrying out measurements that are close to the limits of currently available instruments is useful to clarify potential issues in data acquisition and data analysis strategies, also paving the way to similar astrometric measurements with future facilities, especially MCAO systems like MORFEO.

6.2 Observational strategy

In principle this measurement could be performed through the measurements of the shift in the positions of many stars with respect to the known undeflected positions: assuming

the shift s is along the radial direction from the center of Jupiter and that it follows the law $s = C(r/R_J)$, where r is the distance of the star from Jupiter's center and R_J is Jupiter's radius, the constant C is obtained by means of a best fit of the measured shifts. Such an absolute astrometry approach is not expected to yield the required accuracy in our case, though.

Our proposal is then to perform differential astrometric measurements, i.e., to measure the distance between pairs of stars (although in the typical case the relative shift is smaller than the absolute one) and compare it with the theoretical prediction, again treating C as the free parameter of a best fit procedure. In the Jupiter case one has an advantage over solar eclipse experiments, that is, one can perform a time-resolved observation taking m measurements over a given timespan where Jupiter moves appreciably so that the relative deflection changes. Of course, a random choice of an observing date with Jupiter above the horizon would not work: one has to select observing windows where there is at least one AO reference star and a sufficient number of other stars, with a suitable geometrical arrangement, in a 30"×30" (i.e. the FoV of LUCI's N30 camera) field close to Jupiter.

Thus, we performed the following analysis to identify good observing windows: we extracted the apparent coordinates of Jupiter within the SOUL-LUCI observing period (September 2021-July 2022) and we identified the dates when Jupiter's elevation is larger than 30° in order to limit airmass. We then made a query from the NOMAD [105] catalog to find stars near Jupiter within the selected windows. We chose as good cases the windows with more than three stars within the 30" FoV and at least one good star as reference for the AO correction (i.e. $\mathrm{mag}_R < 15$).

In Fig. 6.1, we show, as an example, one of the good configurations that we selected: Jupiter transits through a field of 7 stars (i.e. 21 distances to be measured) within the time interval of the observation. This is a particularly convenient framework, as there are 4 potential GSs for the AO, that means stars with a high SNR and then with a low astrometric error due to photon noise.

For the selected cases, we performed an analysis of the astrometric error budget and we identified differential tilt jitter as the major contributor, considering to compensate differential atmospheric refraction and instrumental distortions in post-processing analysis and having selected high-flux sources to reduce centroiding error. This is expected due to the SCAO configuration, as well as to the large zenith angles characterizing the observing windows.

To estimate differential tilt jitter and centroiding error, we used the Python codes in the Arcetri AO group's libraries that we wrote to implement the analytical formulation presented in the previous chapters.
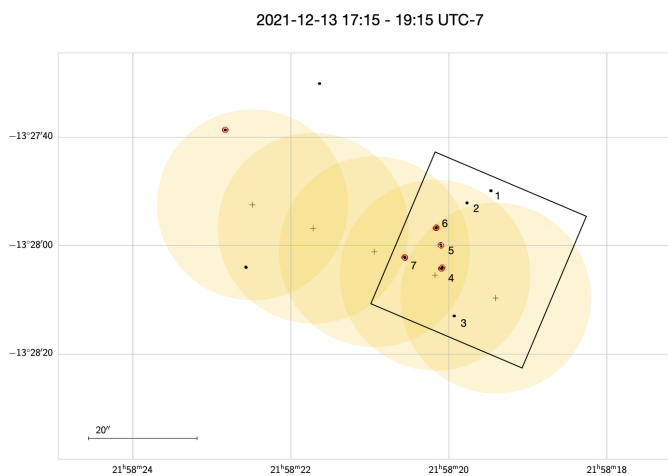
Fig. 6.1 Apparent motion of Jupiter with respect to the field stars on December 13, 2021. The box is the N30 camera FoV and the red circles highlight possible NGSs.

In Fig. 6.2, we show the expected observed variation of distance between "star 5" and "star 6" of Fig. 6.1 as a function of observing time and with the estimated error.
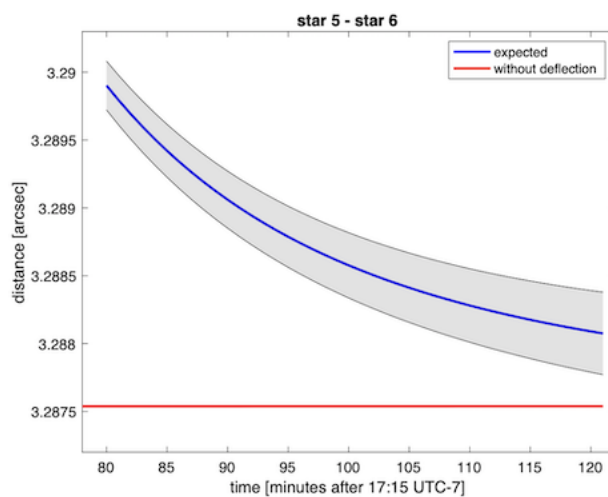
Fig. 6.2 Distance between stars 5 and 6 of Fig. 6.1 as a function of time (blue curve). The error bar is represented by the shaded region. The red line is the distance without the gravitational effect.

Conclusions and perspectives

The goal of this PhD work, as part of the MORFEO project, is the estimation of the impact of tip-tilt residuals from MCAO systems on ground-based astrometric observations. Differential astrometry is, indeed, one of the main science drivers of the future instruments equipped with MCAO systems and challenging requirements have been set on the astrometric precision. Several contributors to astrometric error on MCAO-assisted observations are currently being analyzed, but an accurate study of the errors caused by MCAO tip-tilt residuals has not been carried out. The modeling of such source of error is, indeed, not straightforward for this flavour of AO since the geometry with multiple GSs and multiple DMs must be considered and can lead to complex behaviors.

In this context, we proposed an analytical derivation that allows to model and estimate the astrometric errors due to MCAO atmospheric tip-tilt residuals, specifically differential tilt jitter and centroiding errors. The derivation involves the computation of the temporal PSD of the residual wavefront from an MCAO correction that is based on spatiotemporal statistics of turbulence-induced wavefront distortions and on its temporal filtering by the MCAO loop. We implemented all the analytical derivations into Python codes that are now included in the libraries of the AO group of INAF - Arcetri Astrophysical Observatory (https://github.com/ArcetriAdaptiveOptics/arte) and that are going to be available for the MORFEO project.

As a first step, we derived analytical expressions to estimate spatiotemporal CPSDs of the turbulent phase, considering either the whole piston-removed phase or its modal decomposition into Zernike modes. The formulas are provided in a general framework: CPSDs can be computed between two wavefronts observed with two different apertures and, from this, all the limiting cases can be extracted (one aperture looking at two sources, two apertures looking at one source, one aperture looking at one source). The expressions have been validated through comparisons with results that are present in the literature for the limiting cases, as well as with simulations. The general configuration can help study different aspects of actual and future AO systems, providing faster results than simulations. For our case study, we needed to model spatiotemporal statistics between the multiple

beams involved in MCAO-assisted observations, thus, we restricted the analysis to the configuration with one aperture and two sources.

Then, we derived an analytical formulation to compute the residual wavefront phase from an MCAO loop. First, we performed the calculations for the simpler SCAO case: we derived expressions to estimate the residual PSD in the direction of an on-axis target when using an off-axis guide star. The formulation allows to take into account noise, temporal errors and anisoplanatism, as well as its temporal filtering from the AO loop. We validated the results with simulations and we compared them with expressions present in the literature. Since our formulas take into account the temporal filtering of anisoplanatism from the AO loop, we demonstrated that they can lead to more accurate analyses of anisoplanatic error.

Next, we extended the results on SCAO to the MCAO case and we derived analytical expressions to compute the temporal PSD of the residual wavefront phase from an MCAO correction in any direction of the scientific field of view. The formulas are general and allow to analyze specific frameworks through the definition of the telescope aperture, the turbulence profile, the NGS and/or LGS asterism, the number and conjugation heights of the DMs, and the sensed and corrected modes of distortion. The derivation within the temporal domain allowed to include the MCAO control within the formulation: in particular, we provided expressions in the case of either a closed-loop or a pseudo-open loop control. The temporal domain allowed us also to model the dependence of tip-tilt residuals on the scientific integration time: we identified inter-exposure residuals, that are responsible for the relative jitter of the position of a target between successive frames, and intra-exposure residuals, that are responsible for typical PSF elongation effects. We found a dependence of the former on T^0 for small integration times and on $T^{-1/2}$ for large integration times, and of the latter on T^1 for small integration times and on T^0 for large integration times. In both cases, switching from one power law to the other one depends on the relationship between the camera transfer function and the residual PSD cutoff frequencies. We used the derivation to also analyze the spatial behavior of on-axis MCAO tip-tilt residuals and we found a quadratic dependence on the angular separation of the asterism, that we demonstrated to be consistent with the control of plate-scale distortions operated by the MCAO correction. We provided analytical expressions for differential tilt jitter as well and we showed that the cross-correlations between the guide stars with each other and between the guide stars and the target can play a role in reducing this source of error with respect to the SCAO case.

Finally, we used our results to estimate the contribution of both differential tilt jitter and centroiding error to the astrometric error budget of future MCAO instruments, in

particular MORFEO at the ELT and MAVIS at the VLT. Atmospheric tip-tilt residuals should not be the dominant limiting factor to the astrometric precision of these systems for targets at ≈ 1 separation and with magnitude < 20. However, for larger separations and fainter magnitudes mitigation strategies may be foreseen, especially if considering zenith angles larger than $30°$.

This PhD work has taken part in the MORFEO project and we are going to include the results within the AO system analysis in the next phase of the project starting in the next months. We also plan to extend the analysis to high-order residuals from the LGS loop and their impact on the PSF. In this context, we aim at including spatial frequencies in our analytical derivation, exploring the possibility to join our approach with existing methods on the study of spatial frequencies (e.g. Fourier approach). Moreover, in the framework of high-orders correction, we aim at verifying and validating POLC-MMSE algorithm within the MORFEO framework through the development of an optical setup for test procedures in the laboratories of the Arcetri Astrophysical Observatory.

Appendix A

Numerical verifications

We performed simple simulation cases in order to verify and validate our analytical derivations on CPSDs and on residual PSDs from both SCAO and MCAO corrections.

A.1 CPSDs of piston-removed phase and Zernike modes

The CPSDs and PSDs have been averaged on 2000 turbulence occurrences and computed using a Hanning window to improve the dynamical range. A single simulation (i.e. one turbulence occurrence) has 10,000 iterations with a time step of 0.002 s. The propagation of the phase is performed through end-to-end simulations as follows: the pupil phase is the sum of the phases within the footprints of the beam on each layer. For a source at finite distance, a linear interpolation is used to scale all the footprint phases to the pupil size.

In Figs. A.1 and A.2, we show the comparison of Eqs. (2.34) and (2.44) respectively with simulations. We considered a single turbulent layer at 10 km, with r_0 = 16 cm in V band, L_0 = 25 m, wind speed of 10 m/s and wind direction of -20° with respect to the x axis. We considered one source on axis at infinity and one source at polar coordinates (50", 30°) and altitude of 100 km. We assumed a single aperture of 10 m diameter.

A.2 Residual PSD from SCAO correction

The CPSDs and PSDs have been averaged on 100 turbulence occurrences and computed using a Hanning window to improve the dynamical range. A single simulation (i.e. one turbulence occurrence) has 5,000 iterations with a time step of 0.002 s. The propagation

Fig. A.1 Real (left) and imaginary (right) part of piston-removed phase CPSD.
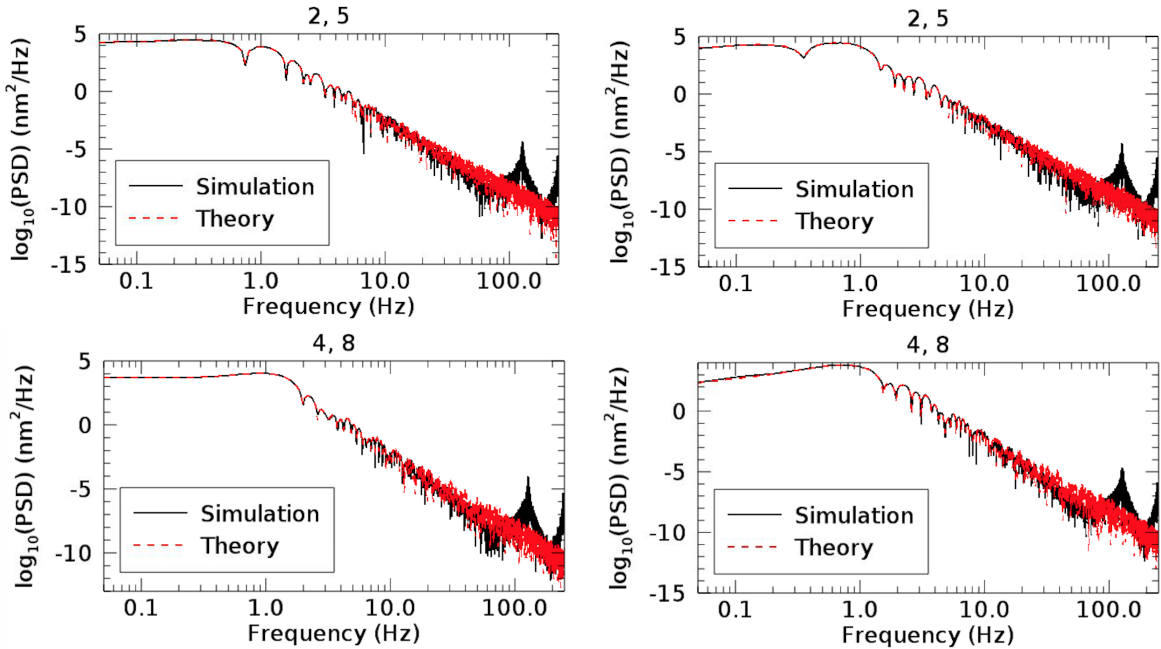
Fig. A.2 Real (left) and imaginary (right) part of CPSD of Zernike modes 2 and 5 (top) and 4 and 8 (bottom).

of the phase is performed through end-to-end simulations as described in the previous section, but also considering the sum of the correction phase.

In Fig. A.3, we show the residual PSDs of tip and tilt on an on-axis target obtained from Eq. (2.55) and a comparison of the results with simulations. We considered the NGS at polar coordinates (5", 30°) and the target in (0", 0°). We assumed a turbulence profile following Kolmogorov model and given by three layers with $r_{0,V}$ = 16 cm in V band, heights of [0, 5, 15] km, wind speed of [10, 5, 15] m/s, wind direction of [90°, 0°, -90°]. We

considered a control given by a simple integrator with loop frequency frame rate of 500 Hz, gain $g = 0.5$ and delay in frames $d = 2$. We chose a telescope entrance aperture with diameter D = 8 m.

Fig. A.3 SCAO residual PSD of tip (left) and tilt (right) for a target in (0", 0°). The results from Eq. (2.55) are represented by the solid line, while the results from the simulation are shown with the dotted line. The peaks at high frequencies characterizing the "Simulation" curves are caused by the filtering of the data with a Hanning window to improve the CPSD dynamical range.

A.3   Residual PSD from MCAO correction

The CPSDs and PSDs have been averaged on 100 turbulence occurrences and computed using a Hanning window to improve the dynamical range. A single simulation (i.e. one turbulence occurrence) has 5,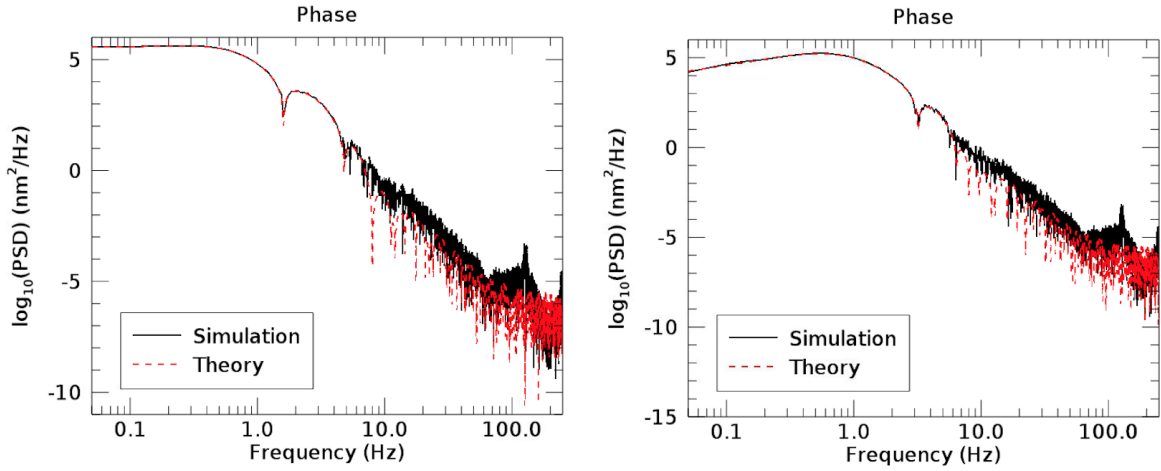000 iterations with a time step of 0.002 s. The propagation of the phase is performed through end-to-end simulations as described in Section A.1, but also considering the sum of the correction phases.

In Fig. A.4, we show the residual PSDs of tip and tilt on an on-axis target obtained from Eq. (3.16) and a comparison of the results with simulations. We assumed an asterism of three NGSs in (30", 30°), (50", 120°) and (40", 270°) to sense tip and tilt, one DM at the ground to compensate for tip and tilt and another DM at 10 km to compensate for focus and astigmatisms. We assumed a turbulence profile following the Kolmogorov model, characterized by three layers with $r_{0,V} = 16$ cm in V band, heights of [0, 5, 15] km, wind speed of [10, 5, 15] m/s, wind direction of [90°, 0°, -90°]. We considered a control given by a simple integrator with loop frequency frame rate of 500 Hz, gain $g = 0.5$ and delay in frames $d = 2$. The telescope entrance aperture has a diameter D = 8 m. We neglected noise on the WFSs measurements.
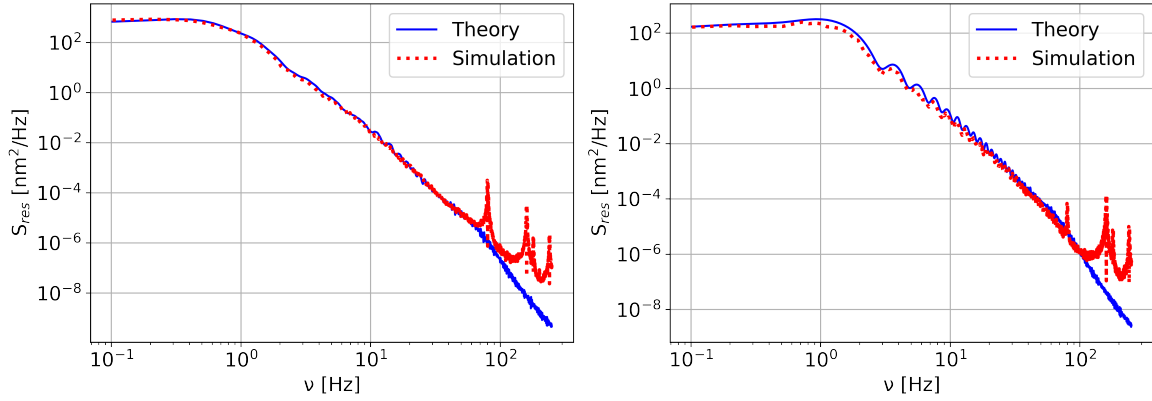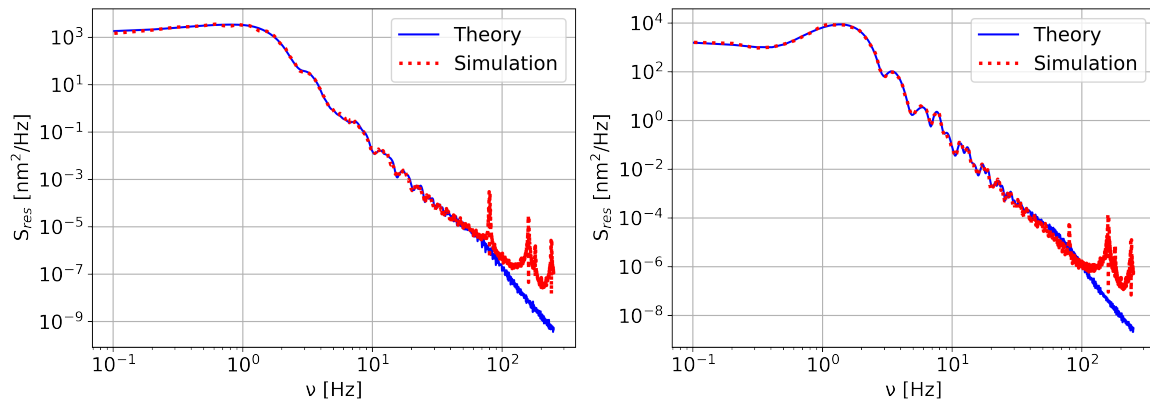
Fig. A.4 MCAO residual PSD of tip (left) and tilt (right) for a target in (0", 0°). The results from Eq. (3.16) are represented by the solid line, while the results from the simulation are shown with the dotted line. The peaks at high frequencies characterizing the "Simulation" curves are caused by the filtering of the data with a Hanning window to improve the CPSD dynamical range.

Appendix B

Relating the wavefront on a metapupil in altitude and on the telescope pupil plane

The computation of projection matrices, to relate for instance the wavefront on a metapupil in altitude to the wavefront on the telescope pupil plane, is often required in MCAO systems. In this context, if the wavefront is considered as decomposed onto Zernike modes, the knowledge of coefficients to transform Zernike polynomials defined on a full aperture to Zernike polynomials on a subaperture is needed. Analytical derivations have been presented in the literature, and here we report the results from Negro [32].

B.1 Transformation coefficients from full aperture to subaperture Zernike modes

The geometry is shown in Fig. B.1: the subaperture, with radius r, is at polar coordinates (h, α) in the reference system of the full aperture of radius R. The derivation of transformation coefficients is based on the geometric relationships between the variables (ρ', θ') and (ρ, θ) of, respectively, the subaperture and the full aperture. These relationships are

$$R\rho\cos\theta = h\cos\alpha + r\rho'\cos\theta' \tag{B.1}$$

$$R\rho\sin\theta = h\sin\alpha + r\rho'\sin\theta'. \tag{B.2}$$
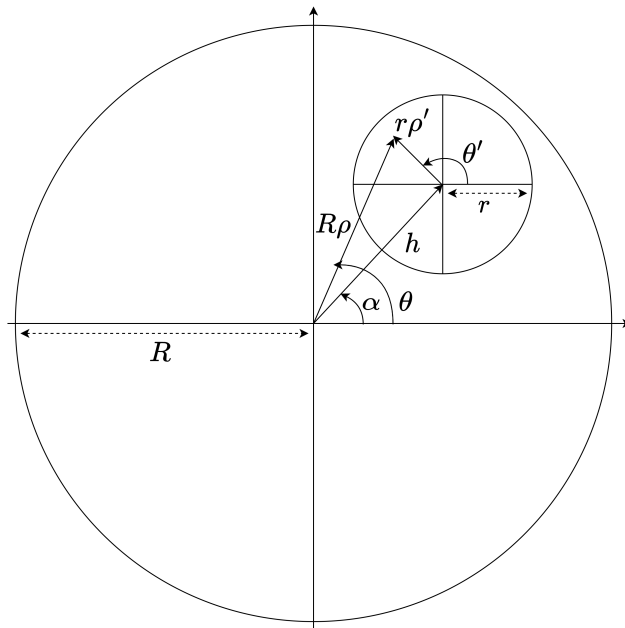
Fig. B.1 Geometry of the subaperture within the full aperture.

We start estimating the coefficients relating full aperture and subaperture tip. The full aperture tip is given by

$$
\begin{aligned}
Z_2 = 2\rho \cos\theta &= \frac{2}{R} R\rho \cos\theta \\
&= \frac{2}{R}\left(h\cos\alpha + r\rho'\cos\theta'\right) = \frac{2}{R}h\cos\alpha + \frac{r}{R}2\rho'\cos\theta' \\
&= \frac{2}{R}h\cos\alpha + \frac{r}{R}Z_2',
\end{aligned}
\tag{B.3}
$$

where we followed Noll's Zernike indexing [12] and where we used Eq. (B.1). The first term is a piston term, while the second term represents the subaperture tip scaled by the ratio between subaperture and full aperture radii r/R. Ignoring the piston term, Eq. (B.3) shows that one wave of full aperture tip corresponds to r/R waves of subaperture tip.

The same can be demonstrated for tilt:

$$
\begin{aligned}
Z_3 = 2\rho \sin\theta &= \frac{2}{R} R\rho \sin\theta \\
&= \frac{2}{R}\left(h\sin\alpha + r\rho'\sin\theta'\right) = \frac{2}{R}h\sin\alpha + \frac{r}{R}2\rho'\sin\theta' \\
&= \frac{2}{R}h\sin\alpha + \frac{r}{R}Z_3'.
\end{aligned}
\tag{B.4}
$$

For what concerns focus, it is useful the following relationship

$$\left(R\rho\right)^2 = \left(R\rho\right)^2 \left(\cos^2\theta + \sin^2\theta\right)$$
$$= h^2 + r^2\rho'^2 + 2hr\rho'\cos(\theta' - \alpha),$$

(B.5)

derived from squaring and adding Eqs. (B.1) and (B.2). Dividing both sides by R^2 and making $\cos(\theta' - \alpha)$ explicit gives

$$\rho^2 = \left(\frac{h}{R}\right)^2 + \left(\frac{r}{R}\right)^2 \rho'^2 + \frac{h}{R}\frac{r}{R}\left(\cos\alpha\, 2\rho'\cos\theta' + \sin\alpha\, 2\rho'\sin\theta'\right).$$

(B.6)

Through this expression, the full aperture focus can be written in terms of subaperture modes:

$$
\begin{aligned}
Z_4 &= \sqrt{3}\left(2\rho^2 - 1\right) \\
&= \sqrt{3}\left[2\left(\frac{h}{R}\right) - 1 + \left(\frac{r}{R}\right)^2\right] + \left(\frac{r}{R}\right)^2\sqrt{3}\left(2\rho'^2 - 1\right) \\
&\quad + 2\sqrt{3}\left(\frac{h}{R}\right)\left(\frac{r}{R}\right)\left(\cos\alpha\, 2\rho'\cos\theta' + \sin\alpha\, 2\rho'\sin\theta'\right) \\
&= \sqrt{3}\left[2\left(\frac{h}{R}\right) - 1 + \left(\frac{r}{R}\right)^2\right] + \left(\frac{r}{R}\right)^2 Z_4' \\
&\quad + 2\sqrt{3}\left(\frac{h}{R}\right)\left(\frac{r}{R}\right)\left(\cos\alpha\, Z_2' + \sin\alpha\, Z_3'\right).
\end{aligned}
$$

(B.7)

The equation shows that full aperture focus can be seen on a subaperture as piston, tip, tilt and focus itself. In particular, the subaperture focus is $(r/R)^2$ times the full aperture focus and both subaperture tip and tilt scales with a coefficient proportional to $(h/R)\,(r/R)$. Same reasoning leads to the coefficients in Fig. B.2 for Zernike modes up to j=11. In general, it is worth noting that each full aperture mode couples into only lower-order radial subaperture modes.

$s(\alpha,h) =$

Full Aperture Mode

A_1	A_2	A_3	A_4	A_5	A_6	A_7	A_8	A_9	A_{10}
$\frac{r}{R}$	0	$2\sqrt{3}\,\frac{h}{R}\frac{r}{R}\cos\alpha$	$\sqrt{6}\,\frac{h}{R}\frac{r}{R}\cos\alpha$	$\sqrt{6}\,\frac{h}{R}\frac{r}{R}\sin\alpha$	$3\sqrt{2}\,\frac{r}{R}\!\left[\left(\frac{h}{R}\right)^2(1+2\cos^2\alpha)+\frac{2}{3}\left(\frac{r}{R}\right)^2-\frac{2}{3}\right]$	$3\sqrt{2}\,\frac{h}{R}\frac{2r}{R}\sin2\alpha$	$3\sqrt{2}\,\frac{h}{R}\frac{2r}{R}\cos2\alpha$	$3\sqrt{2}\,\frac{h}{R}\frac{2r}{R}\sin2\alpha$	$\frac{12}{5}\frac{h}{R}\frac{r}{R}\!\left[\left(\frac{h}{R}\right)^2+\frac{2}{3}\left(\frac{r}{R}\right)^2-\frac{1}{2}\right]\cos\alpha$
0	$\frac{r}{R}$	$2\sqrt{3}\,\frac{h}{R}\frac{r}{R}\sin\alpha$	$-\sqrt{6}\,\frac{h}{R}\frac{r}{R}\sin\alpha$	$\sqrt{6}\,\frac{h}{R}\frac{r}{R}\cos\alpha$	$3\sqrt{2}\,\frac{h}{R}\frac{2r}{R}\sin2\alpha$	$3\sqrt{2}\,\frac{r}{R}\!\left[\left(\frac{h}{R}\right)^2(1+2\sin^2\alpha)+\frac{2}{3}\left(\frac{r}{R}\right)^2-\frac{2}{3}\right]$	$-3\sqrt{2}\,\frac{h}{R}\frac{2r}{R}\sin2\alpha$	$3\sqrt{2}\,\frac{h}{R}\frac{2r}{R}\cos2\alpha$	$\frac{12}{5}\frac{h}{R}\frac{r}{R}\!\left[\left(\frac{h}{R}\right)^2+\frac{2}{3}\left(\frac{r}{R}\right)^2-\frac{1}{2}\right]\sin\alpha$
0	0	$\left(\frac{r}{R}\right)^2$	0	0	$2\sqrt{6}\,\frac{h}{R}\left(\frac{r}{R}\right)^2\cos\alpha$	$2\sqrt{6}\,\frac{h}{R}\left(\frac{r}{R}\right)^2\sin\alpha$	0	0	$\sqrt{15}\left(\frac{r}{R}\right)^2\!\left[4\left(\frac{h}{R}\right)^2+\left(\frac{r}{R}\right)^2-1\right]$
0	0	0	$\left(\frac{r}{R}\right)^2$	0	$2\sqrt{3}\,\frac{h}{R}\left(\frac{r}{R}\right)^2\cos\alpha$	$-2\sqrt{3}\,\frac{h}{R}\left(\frac{r}{R}\right)^2\sin\alpha$	$2\sqrt{3}\,\frac{h}{R}\left(\frac{r}{R}\right)^2\cos\alpha$	$2\sqrt{3}\,\frac{h}{R}\left(\frac{r}{R}\right)^2\sin\alpha$	$2\sqrt{30}\,\frac{h}{R}\left(\frac{r}{R}\right)^2\cos2\alpha$
0	0	0	0	$\left(\frac{r}{R}\right)^2$	$2\sqrt{3}\,\frac{h}{R}\left(\frac{r}{R}\right)^2\sin\alpha$	$2\sqrt{3}\,\frac{h}{R}\left(\frac{r}{R}\right)^2\cos\alpha$	$2\sqrt{3}\,\frac{h}{R}\left(\frac{r}{R}\right)^2\sin\alpha$	$-2\sqrt{3}\,\frac{h}{R}\left(\frac{r}{R}\right)^2\cos\alpha$	$2\sqrt{30}\,\frac{h}{R}\left(\frac{r}{R}\right)^2\sin2\alpha$
0	0	0	0	0	$\left(\frac{r}{R}\right)^3$	0	0	0	$2\sqrt{10}\,\frac{h}{R}\left(\frac{r}{R}\right)^3\cos\alpha$
0	0	0	0	0	0	$\left(\frac{r}{R}\right)^3$	0	0	$2\sqrt{10}\,\frac{h}{R}\left(\frac{r}{R}\right)^3\sin\alpha$
0	0	0	0	0	0	0	$\left(\frac{r}{R}\right)^3$	0	0
0	0	0	0	0	0	0	0	$\left(\frac{r}{R}\right)^3$	0
0	0	0	0	0	0	0	0	0	$\left(\frac{r}{R}\right)^4$

Fig. B.2 Table of transformation coefficients from full aperture to subaperture Zernike modes from Negro [32]. The coefficients do not follow Noll's indexing: in particular, the column A_i with $i = 1,...,10$ in the figure corresponds to $i = 2,...,11$ in Noll's ordering and also the pairs of columns (A_4, A_5), (A_6, A_7) and (A_8, A_9) must be inverted between them in order to follow Noll's indexing.

B.2   Plate-scale distortions

Plate-scale distortions are first-order distortions, thus, they can be described by the following combination of polynomials

$$\Delta x = a_1 + a_2 x + a_3 y$$
$$\Delta y = b_1 + b_2 y + b_3 x. \tag{B.8}$$

In particular, they are caused by focus and astigmatisms in altitude projected on to tip-tilt in pupil. The effect is the displacement of the position of an object in the pupil plane, that linearly depends on the off-axis distance of the object. If we consider, for example, a focus applied on a meta-pupil in altitude, the wavefront phase from an off-axis object is seen on to the pupil as

$$\varphi(h, \alpha) = c_4 \left[\left(\frac{r}{R} \right)^2 Z_4 + 2\sqrt{3} \left(\frac{h}{R} \right) \left(\frac{r}{R} \right) \cos \alpha \, Z_2 + 2\sqrt{3} \left(\frac{h}{R} \right) \left(\frac{r}{R} \right) \sin \alpha \, Z_3 \right], \tag{B.9}$$

where c_4 is the focus coefficient applied on the meta-pupil and where we used the transformation coefficients in Fig. B.2. Thus, a focus on a meta-pupil in altitude is seen as only a focus scaled by $(r/R)^2$ in case of an object on axis; for an off-axis object, it is seen as a focus scaled by $(r/R)^2$, a tip linearly increasing in the field (dependence of tip coefficient on $h\cos\alpha$) and a tilt also linearly increasing in the field (dependence of tilt coefficient on $h\sin\alpha$). Therefore, focus in altitude generates a displacement proportional to x along x and proportional to y along y (considering the compensation for the focus term applied in the pupil). Similarly, from Fig. B.2 derives that astigmatism Z_5 in altitude generates

$$\varphi(h, \alpha) = c_5 \left[\left(\frac{r}{R} \right)^2 Z_5 + \sqrt{6} \left(\frac{h}{R} \right) \left(\frac{r}{R} \right) \sin \alpha \, Z_2 + \sqrt{6} \left(\frac{h}{R} \right) \left(\frac{r}{R} \right) \cos \alpha \, Z_3 \right], \tag{B.10}$$

that is, a displacement proportional to y along x and proportional to y along x (considering the compensation for the astigmatism term applied in the pupil), and astigmatism Z_6

$$\varphi(h, \alpha) = c_6 \left[\left(\frac{r}{R} \right)^2 Z_6 + \sqrt{6} \left(\frac{h}{R} \right) \left(\frac{r}{R} \right) \cos \alpha \, Z_2 - \sqrt{6} \left(\frac{h}{R} \right) \left(\frac{r}{R} \right) \sin \alpha \, Z_3 \right], \tag{B.11}$$

that is, a displacement proportional to x along x and proportional to $-y$ along y (considering the compensation for the astigmatism term applied in the pupil). The combination of these first-order distortions leads to plate-scale distortions. The effect is sketched in Fig. B.3.

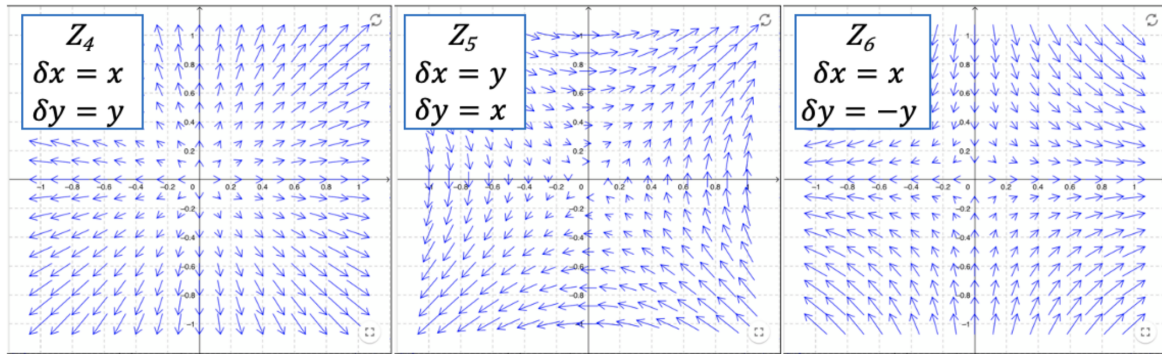**Fig. B.3** Maps of field offset, converted from polar (h, α) to Cartesian coordinates, due to focus (left) and astigmatisms Z_5 (center) and Z_6 (right) applied in altitude. The compensation for, respectively, focus and astigmatisms in pupil is included.

Appendix C

Residual distortions on a pupil plane

We want to relate tip-tilt on the telescope pupil plane with the distortions on a layer of turbulence at altitude h_l. The phase observed at the pupil plane can be seen as a linear combination of tip and tilt

$$\varphi(\boldsymbol{x}, \boldsymbol{\theta}, t) = \sum_{k=2}^{3} \gamma_k(\boldsymbol{\theta}, t) Z_k(\boldsymbol{x}/R),$$ (C.1)

where we used the same notation as the one presented in Flicker *et al.* [106], where φ is the phase observed at coordinates $\boldsymbol{x}$ on the pupil plane for a source at position $\boldsymbol{\theta}$, R is the telescope pupil radius, Z_k is the kth Zernike mode and $\gamma_k(\boldsymbol{\theta}, t)$ are time and field dependent coefficients relating tip-tilt on the pupil plane with all the modes of distortion on a meta-pupil in altitude

$$\gamma_k(\boldsymbol{\theta}, t) = \sum_{i=2}^{N} c_{ik}(\boldsymbol{\theta}) A_i(t).$$ (C.2)

The coefficients $c_{ik}(\boldsymbol{\theta})$ and A_i can be defined from the first two rows of the table in Fig. B.2 as

$$\begin{aligned}
\boldsymbol{c_2}(\boldsymbol{\theta}) &= [1, 0, 2\sqrt{3}\theta_x, \sqrt{6}\theta_y, \sqrt{6}\theta_x, 6\sqrt{2}\theta_x\theta_y, \\
&\quad 3\sqrt{2}(3\theta_x^2 + \theta_y^2), 6\sqrt{2}\theta_x\theta_y, 3\sqrt{2}(\theta_x^2 - \theta_y^2), \cdots] \\
\boldsymbol{c_3}(\boldsymbol{\theta}) &= [0, 1, 2\sqrt{3}\theta_y, \sqrt{6}\theta_x, -\sqrt{6}\theta_y, 3\sqrt{2}(\theta_x^2 + 3\theta_y^2), \\
&\quad 6\sqrt{2}\theta_x\theta_y, 3\sqrt{2}(\theta_x^2 - \theta_y^2), -6\sqrt{2}\theta_x\theta_y, \cdots],
\end{aligned}$$ (C.3)

and as

$$A_{[2,3]}(t) = a_{[2,3]l}(t)R/R_l; \ A_{[4:10]}(t) = a_{[4:10]l}(t)h_l R/R_l^2; \ \cdots$$ (C.4)

Due to the orthogonality of the Zernike, the phase variance can be computed as:

$$
\sigma_\varphi^2 = \mathrm{Tr}\left(C_\gamma\right) = \sum_{k=2}^{3} C_\gamma^{kk}
$$
$$
= \sum_{k=2}^{3} \left\langle \left(\sum_{i=2}^{N} c_{ik}(\boldsymbol{\theta}) A_i(t) \right) \left(\sum_{i=2}^{N} c_{ik}(\boldsymbol{\theta}) A_i(t) \right)^\dagger \right\rangle ,
$$

(C.5)

where the notation C_γ denotes the covariance matrix of the coefficients $\gamma_k(\boldsymbol{\theta}, t)$.

C.1 SCAO

The SCAO systems compensate for the zeroth order of the distortions, thus the contribution of modes higher than the tilt has to be considered. By exploiting the covariance properties of the Zernike and through straightforward algebra, it can be demonstrated that the phase variance becomes:

$$
\sigma_\varphi^2 = \sum_{k=2}^{3} \left\langle \left(\sum_{i=4}^{N} c_{ik}(\boldsymbol{\theta}) A_i(t) \right) \left(\sum_{i=4}^{N} c_{ik}(\boldsymbol{\theta}) A_i(t) \right)^\dagger \right\rangle
$$
$$
= \left[\left(2\sqrt{3}\theta_x\right)^2 + \left(2\sqrt{3}\theta_y\right)^2 \right] \left\langle A_4(t) A_4^\dagger(t) \right\rangle
$$
$$
+ \left[\left(\sqrt{6}\theta_y\right)^2 + \left(\sqrt{6}\theta_x\right)^2 \right] \left\langle A_5(t) A_5^\dagger(t) \right\rangle
$$
$$
+ \left[\left(\sqrt{6}\theta_x\right)^2 + \left(-\sqrt{6}\theta_y\right)^2 \right] \left\langle A_6(t) A_6^\dagger(t) \right\rangle + \cdots
$$
$$
= 6 \left(2 \left\langle A_4(t) A_4^\dagger(t) \right\rangle + \left\langle A_5(t) A_5^\dagger(t) \right\rangle + \left\langle A_6(t) A_6^\dagger(t) \right\rangle \right) \left(\theta_x^2 + \theta_y^2 \right) + \cdots ,
$$

(C.6)

where we showed the results from the first order distortions. In this case the variance shows to be, at the first order, proportional to the second power of the off-axis separation (i.e. the RMS has a linear dependence).

C.2 MCAO

The NGS-based MCAO configuration that we considered in our analysis is able to compensate for the first order distortions. The contribution of the uncorrected modes, in this case the ones higher than the astigmatisms, leads to a phase variance that is, at the first order, proportional to the fourth power of the off-axis separation (i.e. RMS proportional to

the second power):

$$
\begin{aligned}
\sigma_\varphi^2 &= \sum_{k=2}^{3} \left\langle \left(\sum_{i=7}^{N} c_{ik}(\boldsymbol{\theta}) A_i(t) \right) \left(\sum_{i=7}^{N} c_{ik}(\boldsymbol{\theta}) A_i(t) \right)^\dagger \right\rangle \\
&= 18 \left(10 \left\langle A_8(t) A_8^\dagger(t) \right\rangle + \left\langle A_9(t) A_9^\dagger(t) \right\rangle + \left\langle A_{10}(t) A_{10}^\dagger(t) \right\rangle \right) \left(\theta_x^2 + \theta_y^2 \right)^2 + \cdots .
\end{aligned}
\tag{C.7}
$$

Bibliography

[1] H. W. Babcock, "The Possibility of Compensating Astronomical Seeing," *Publications of the Astronomical Society of the Pacific*, vol. 65, p. 229, Oct. 1953.

[2] F. Merkle, P. Kern, P. Léna, F. Rigaut, J. C. Fontanella, G. Rousset, C. Boyer, J. P. Gaffard, and P. Jagourel, "Successful tests of adaptive optics.," *The Messenger*, vol. 58, pp. 1–4, Dec. 1989.

[3] R. Davies, V. Hörmann, S. Rabien, E. Sturm, J. Alves, Y. Clénet, J. Kotilainen, F. Lang-Bardl, H. Nicklas, J.-U. Pott, E. Tolstoy, B. Vulcani, and T. M. Consortium, "MICADO: The Multi-Adaptive Optics Camera for Deep Observations," *Published in The Messenger vol. 182*, vol. pp. 17-21, p. March 2021., 2021.

[4] R. Tamai, B. Koehler, M. Cirasuolo, F. Biancat-Marchet, M. Tuti, and J.-C. González-Herrera, "The ESO's ELT construction progress," in *Society of Photo-Optical Instrumentation Engineers (SPIE) Conference Series*, vol. 11445 of *Society of Photo-Optical Instrumentation Engineers (SPIE) Conference Series*, p. 114451E, Dec. 2020.

[5] P. Ciliegi, G. Agapito, M. Aliverti, F. Annibali, C. Arcidiacono, N. Azzaroli, A. Balestra, I. Baronchelli, A. Baruffolo, M. Bergomi, A. Bianco, M. Bonaglia, R. Briguglio, L. Busoni, M. Cantiello, G. Capasso, G. Carlà, E. Carolo, E. Cascone, S. Chinellato, V. Cianniello, M. Colapietro, J.-J. Correia, G. Cosentino, D. D'Auria, V. D. Caprio, N. Devaney, I. D. Antonio, A. D. Cianno, A. D. Dato, U. D. Giammatteo, G. D. Rico, M. Dolci, C. Eredia, S. Esposito, D. Fantinel, J. Farinato, P. Feautrier, I. Foppiani, M. Genoni, E. Giro, L. Gluck, A. Goncharov, P. Grani, D. Greggio, S. Guieu, M. Gullieuszik, P. Haguenauer, Z. Hubert, T. Lapucci, F. Laudisio, M. L. Louarn, D. Magrin, D. Malone, L. Marafatto, M. Munari, S. Oberti, G. Pariani, L. Pettazzi, C. Plantet, E. Portaluri, A. Puglisi, P. Rabou, R. Ragazzoni, E. Redaelli, M. Riva, S. Rochat, G. Rodeghiero, B. Salasnich, S. Savarese, M. Scalera, P. Schipani, R. Sordo, M.-H. Sztefek, A. Valentini, and M. Xompero, "MAORY/MORFEO@ELT: general overview up to the preliminary design and a look towards the final design," in *Adaptive Optics Systems VIII* (L. Schreiber, D. Schmidt, and E. Vernet, eds.), vol. 12185, p. 1218514, International Society for Optics and Photonics, SPIE, 2022.

[6] V. I. Tatarski, *Wave Propagation in Turbulent Medium.* Dover Publications Inc., 1961.

[7] J. W. Hardy, *Adaptive Optics for Astronomical Telescopes.* Oxford University Press, 1998.

[8] F. Roddier, *Adaptive optics in astronomy.* Cambridge University Press, 1999.

[9] E. Masciadri, J. Stoesz, S. Hagelin, and F. Lascaux, "Optical turbulence vertical distribution with standard and high resolution at Mt Graham," *Monthly Notices of the Royal Astronomical Society*, vol. 404, pp. 144–158, 04 2010.

[10] A. N. Kolmogorov, "Dissipation of Energy in Locally Isotropic Turbulence," *Akademiia Nauk SSSR Doklady*, vol. 32, p. 16, Apr. 1941.

[11] J. W. Goodman, *Statistical Optics.* Wiley, 2000.

[12] R. J. Noll, "Zernike polynomials and atmospheric turbulence.," *Journal of the Optical Society of America (1917-1983)*, vol. 66, pp. 207–211, Mar. 1976.

[13] J. M. Conan, G. Rousset, and P. Y. Madec, "Wave-front temporal spectra in high-resolution imaging through turbulence.," *Journal of the Optical Society of America A*, vol. 12, pp. 1559–1570, July 1995.

[14] F. Roddier, M. Northcott, J. Graves, D. McKenna, and D. Roddier, "One-dimensional spectra of turbulence-induced Zernike aberrations: time-delay and isoplanicity error in partial adaptive compensation," *J. Opt. Soc. Am. A*, vol. 10, no. 5, pp. 957–965, 1993.

[15] F. Rigaut and E. Gendron, "Laser guide star in adaptive optics: the tilt determination problem.," *Astronomy & Astrophysics*, vol. 261, pp. 677–684, Aug. 1992.

[16] R. V. Shack, "Production and use of a lecticular hartmann screen," *J. Opt. Soc. Am.*, vol. 61, pp. 656–661, 1971.

[17] R. Ragazzoni, "Pupil plane wavefront sensing with an oscillating prism," *Journal of Modern Optics*, vol. 43, no. 2, pp. 289–293, 1996.

[18] S. Esposito, O. Feeney, and A. Riccardi, "Laboratory test of a pyramid wavefront sensor," in *Adaptive Optical Systems Technology* (P. L. Wizinowich, ed.), vol. 4007 of *Society of Photo-Optical Instrumentation Engineers (SPIE) Conference Series*, pp. 416–422, July 2000.

[19] P.-Y. Madec, "Overview of deformable mirror technologies for adaptive optics and astronomy," in *Adaptive Optics Systems III* (B. L. Ellerbroek, E. Marchetti, and J.-P. Véran, eds.), vol. 8447, p. 844705, International Society for Optics and Photonics, SPIE, 2012. https://doi.org/10.1117/12.924892.

[20] P. Y. Madec, "Control techniques," in *Adaptive Optics in Astronomy* (F. Roddier, ed.), p. 131, Cambridge University Press, 1999.

[21] D. Sandler, S. Stahl, R. Angel, M. Lloyd-Hart, and D. McCarthy, "Adaptive Optics for Diffraction-Limited Imaging with 8m Telescopes," in *European Southern Observatory Conference and Workshop Proceedings*, vol. 48 of *European Southern Observatory Conference and Workshop Proceedings*, p. 509, Jan. 1994.

[22] J. M. Beckers, "Increasing the Size of the Isoplanatic Patch with Multiconjugate Adaptive Optics," in *Very Large Telescopes and their Instrumentation, Vol. 2*, vol. 30 of *European Southern Observatory Conference and Workshop Proceedings*, p. 693, Oct. 1988.

[23] F. Rigaut and B. Neichel, "Multiconjugate Adaptive Optics for Astronomy," *Annual Review of Astronomy and Astrophysics*, vol. 56, pp. 277–314, Sept. 2018.

[24] S. Esposito, "Introduction to Multi-Conjugate Adaptive Optics systems," *Comptes Rendus Physique*, vol. 6, pp. 1039–1048, Dec. 2005.

[25] M. Tallon and R. Foy, "Adaptive telescope with laser probe: isoplanatism and cone effect.," *Astronomy & Astrophysics*, vol. 235, pp. 549–557, Aug. 1990.

[26] R. Ragazzoni, E. Marchetti, and F. Rigaut, "Modal tomography for adaptive optics," *Astronomy & Astrophysics*, vol. 342, pp. L53–L56, Feb. 1999.

[27] B. Neichel, F. Rigaut, M. Bec, M. Boccas, F. Daruich, C. D'Orgeville, V. Fesquet, R. Galvez, A. Garcia-Rissmann, G. Gausachs, M. Lombini, G. Perez, G. Trancho, V. Upadhya, and T. Vucina, "The Gemini MCAO System GeMS: nearing the end of a lab-story," in *Adaptive Optics Systems II* (B. L. Ellerbroek, M. Hart, N. Hubin, and P. L. Wizinowich, eds.), vol. 7736 of *Society of Photo-Optical Instrumentation Engineers (SPIE) Conference Series*, p. 773606, July 2010.

[28] F. Rigaut, B. Neichel, M. Boccas, C. D'Orgeville, G. Arriagada, V. Fesquet, S. J. Diggs, C. Marchant, G. Gausach, W. N. Rambold, J. Luhrs, S. Walker, E. R. Carrasco-Damele, M. L. Edwards, P. Pessev, R. L. Galvez, T. B. Vucina, C. Araya, A. Gutierrez, A. W. Ebbers, A. Serio, C. Moreno, C. Urrutia, R. Rogers, R. Rojas, C. Trujillo, B. Miller, D. A. Simons, A. Lopez, V. Montes, H. Diaz, F. Daruich, F. Colazo, M. Bec, G. Trancho, M. Sheehan, P. McGregor, P. J. Young, M. C. Doolan, J. van Harmelen, B. L. Ellerbroek, D. Gratadour, and A. Garcia-Rissmann, "GeMS: first on-sky results," in *Adaptive Optics Systems III* (B. L. Ellerbroek, E. Marchetti, and J.-P. Véran, eds.), vol. 8447 of *Society of Photo-Optical Instrumentation Engineers (SPIE) Conference Series*, p. 84470I, July 2012.

[29] F. Rigaut, R. McDermid, G. Cresci, V. Viotto, S. Ellis, D. Brodrick, G. Agapito, T. Fusco, B. Neichel, P. Haguenauer, C. Plantet, B. Salasnich, M. Aliverti, S. Antoniucci, A. Balestra, A. Baruffolo, O. Beltramo-Martin, M. Bergomi, A. Blanco, M. Bonaglia, G. Bono, L. Busoni, E. Carolo, S. Chinellato, R. Content, J. Cranney, G. de Silva, S. Esposito, D. Fantinel, J. Farinato, D. Haynes, A. Horton, G. Gausachs, J. Gilbert, D. Gratadour, D. Greggio, M. Gullieuszik, V. Korkiakoski, D. Magrin, L. Magrini, L. Marafatto, H. McGregor, T. Mendel, S. Monty, F. Pedichini, E. Pinna, E. Portaluri, K. Radhakrishnan, R. Ragazzoni, D. Robertson, C. Schwab, S. Ströbele, E. Thorn, A. Vaccarella, D. Vassallo, L. Waller, F. Zamkotsian, A. Zanutta, and H. Zhang, "MAVIS conceptual design," in *Society of Photo-Optical Instrumentation Engineers (SPIE) Conference Series*, vol. 11447 of *Society of Photo-Optical Instrumentation Engineers (SPIE) Conference Series*, p. 114471R, Dec. 2020.

[30] J. Crane, G. Herriot, D. Andersen, J. Atwood, P. Byrnes, A. Densmore, J. Dunn, J. Fitzsimmons, T. Hardy, B. Hoff, K. Jackson, D. Kerley, O. Lardière, M. Smith, J. Stocks, J.-P. Véran, C. Boyer, L. Wang, G. Trancho, and M. Trubey, "NFIRAOS adaptive optics for the Thirty Meter Telescope," in *Adaptive Optics Systems VI* (L. M. Close, L. Schreiber, and D. Schmidt, eds.), vol. 10703 of *Society of Photo-Optical Instrumentation Engineers (SPIE) Conference Series*, p. 107033V, Jul. 2018.

[31] P. Ciliegi, G. Agapito, M. Aliverti, F. Annibali, C. Arcidiacono, A. Balestra, A. Baruffolo, M. Bergomi, A. Bianco, M. Bonaglia, L. Busoni, M. Cantiello, E. Cascone, G. Chauvin, S. Chinellato, V. Cianniello, J. J. Correia, G. Cosentino, M. Dall'Ora, V. De Caprio, N. Devaney, I. Di Antonio, A. Di Cianno, U. Di Giammatteo, V. D'Orazi, G. Di Rico, M. Dolci, S. Doutè, C. Eredia, J. Farinato, S. Esposito, D. Fantinel, P. Feautrier, I. Foppiani, E. Giro, L. Gluck, A. Golden, A. Goncharov, P. Grani, M. Gullieuszik, P. Haguenauer, F. Hénault, Z. Hubert, M. Le Louran, D. Magrin, E. Maiorano, F. Mannucci, D. Malone, L. Marafatto, E. Moraux, M. Munari, S. Oberti, G. Pariani, L. Pettazzi, C. Plantet, L. Podio, E. Portaluri, A. Puglisi, R. Ragazzoni, A. Rakich, P. Rabou, E. Redaelli, M. Redman, M. Riva, S. Rochat, G. Rodeghiero, B. Salasnich, P. Saracco, R. Sordo, M. Spavone, M. H. Sztefek, A. Valentini, E. Vanzella, C. Verinaud, M. Xompero, and S. Zaggia, "MAORY: A Multi-conjugate Adaptive Optics RelaY for ELT," *The Messenger*, vol. 182, pp. 13–16, Mar. 2021.

[32] J. E. Negro, "Subaperature optical system testing," *Applied Optics*, vol. 23, pp. 1921–1930, June 1984.

[33] T. Fusco, J.-M. Conan, V. Michau, G. Rousset, and F. Assemat, "Multiconjugate adaptive optics: comparison of phase reconstruction approaches for large field of view," in *Atmospheric Propagation, Adaptive Systems, and Laser Radar Technology for Remote Sensing* (J. D. Gonglewski, G. W. Kamerman, A. Kohnle, U. Schreiber, and C. H. Werner, eds.), vol. 4167 of *Society of Photo-Optical Instrumentation Engineers (SPIE) Conference Series*, pp. 168–179, Jan. 2001.

[34] B. Neichel, T. Fusco, and J.-M. Conan, "Tomographic reconstruction for wide-field adaptive optics systems: Fourier domain analysis and fundamental limitations," *Journal of the Optical Society of America A*, vol. 26, p. 219, Dec. 2008.

[35] B. L. Ellerbroek and C. R. Vogel, "Simulations of closed-loop wavefront reconstruction for multiconjugate adaptive optics on giant telescopes," in *Astronomical Adaptive Optics Systems and Applications* (R. K. Tyson and M. Lloyd-Hart, eds.), vol. 5169 of *Society of Photo-Optical Instrumentation Engineers (SPIE) Conference Series*, pp. 206–217, Dec. 2003.

[36] "MORFEO." https://elt.eso.org/instrument/MORFEO/.

[37] L. Busoni, G. Agapito, C. Plantet, G. Carlà, S. Oberti, M. Bonaglia, T. Lapucci, M. Xompero, C. Arcidiacono, Z. Hubert, P. Rabou, B. Salasnich, A. Baruffolo, I. Foppiani, G. Pariani, M. Munari, D. Magrin, M. Riva, and P. Ciliegi, "MAORY/MORFEO @ ELT: preliminary design of the adaptive optics subsystem," in *Adaptive Optics Systems VIII* (L. Schreiber, D. Schmidt, and E. Vernet, eds.), vol. 12185, p. 121854R, International Society for Optics and Photonics, SPIE, 2022.

[38] "ELT." https://elt.eso.org/.

[39] R. Tamai, B. Koehler, M. Cirasuolo, F. Biancat-Marchet, M. Tuti, and J.-C. González-Herrera, "The ESO's ELT construction progress," in *Society of Photo-Optical Instrumentation Engineers (SPIE) Conference Series*, vol. 11445 of *Society of Photo-Optical Instrumentation Engineers (SPIE) Conference Series*, p. 114451E, Dec. 2020.

[40] "MICADO." https://elt.eso.org/instrument/MICADO/.

[41] E. Vernet, M. Cirasuolo, M. Cayrel, R. Tamai, A. Kellerer, L. Pettazzi, P. Lilley, P. Zu-
      luaga, C. Diaz Cano, B. Koehler, F. Biancat Marchet, J. C. Gonzalez, M. Tuti, and
      The ELT Team, "ELT M4 — The Largest Adaptive Mirror Ever Built," *The Messenger*,
      vol. 178, pp. 3–4, Dec. 2019.

[42] Gaia Collaboration, A. Brown, A. Vallenari, T. Prusti, J. H. J. de Bruijne, C. Babu-
      siaux, M. Biermann, O. L. Creevey, D. W. Evans, L. Eyer, A. Hutton, F. Jansen,
      C. Jordi, S. A. Klioner, U. Lammers, L. Lindegren, X. Luri, F. Mignard, C. Panem,
      D. Pourbaix, S. Randich, P. Sartoretti, C. Soubiran, N. A. Walton, F. Arenou, C. A. L.
      Bailer-Jones, U. Bastian, M. Cropper, R. Drimmel, D. Katz, M. G. Lattanzi, F. van
      Leeuwen, J. Bakker, C. Cacciari, J. Casta neda, F. De Angeli, C. Ducourant, C. Fabri-
      cius, M. Fouesneau, Y. Frémat, R. Guerra, A. Guerrier, J. Guiraud, A. Jean-Antoine
      Piccolo, E. Masana, R. Messineo, N. Mowlavi, C. Nicolas, K. Nienartowicz, F. Pailler,
      P. Panuzzo, F. Riclet, W. Roux, G. M. Seabroke, R. Sordo, P. Tanga, F. Thévenin,
      G. Gracia-Abril, J. Portell, D. Teyssier, M. Altmann, R. Andrae, I. Bellas-Velidis,
      K. Benson, J. Berthier, R. Blomme, E. Brugaletta, P. W. Burgess, G. Busso, B. Carry,
      A. Cellino, N. Cheek, G. Clementini, Y. Damerdji, M. Davidson, L. Delchambre,
      A. Dell'Oro, J. Fernández-Hernández, L. Galluccio, P. García-Lario, M. Garcia-
      Reinaldos, J. González-Núñez, E. Gosset, R. Haigron, J. L. Halbwachs, N. C. Ham-
      bly, D. L. Harrison, D. Hatzidimitriou, U. Heiter, J. Hernández, D. Hestroffer, S. T.
      Hodgkin, B. Holl, K. Janßen, G. Jevardat de Fombelle, S. Jordan, A. Krone-Martins,
      A. C. Lanzafame, W. Löffler, A. Lorca, M. Manteiga, O. Marchal, P. M. Marrese,
      A. Moitinho, A. Mora, K. Muinonen, P. Osborne, E. Pancino, T. Pauwels, J. M. Petit,
      A. Recio-Blanco, P. J. Richards, M. Riello, L. Rimoldini, A. C. Robin, T. Roegiers, J. Ry-
      bizki, L. M. Sarro, C. Siopis, M. Smith, A. Sozzetti, A. Ulla, E. Utrilla, M. van Leeuwen,
      W. van Reeven, U. Abbas, A. Abreu Aramburu, S. Accart, C. Aerts, J. J. Aguado, M. Ajaj,
      G. Altavilla, M. A. Álvarez, J. Álvarez Cid-Fuentes, J. Alves, R. I. Anderson, E. Anglada
      Varela, T. Antoja, M. Audard, D. Baines, S. G. Baker, L. Balaguer-Núñez, E. Bal-
      binot, Z. Balog, C. Barache, D. Barbato, M. Barros, M. A. Barstow, S. Bartolomé,
      J. L. Bassilana, N. Bauchet, A. Baudesson-Stella, U. Becciani, M. Bellazzini, M. Ber-
      net, S. Bertone, L. Bianchi, S. Blanco-Cuaresma, T. Boch, A. Bombrun, D. Bossini,
      S. Bouquillon, A. Bragaglia, L. Bramante, E. Breedt, A. Bressan, N. Brouillet, B. Buc-
      ciarelli, A. Burlacu, D. Busonero, A. G. Butkevich, R. Buzzi, E. Caffau, R. Cancelliere,
      H. Cánovas, T. Cantat-Gaudin, R. Carballo, T. Carlucci, M. I. Carnerero, J. M. Car-
      rasco, L. Casamiquela, M. Castellani, A. Castro-Ginard, P. Castro Sampol, L. Chaoul,
      P. Charlot, L. Chemin, A. Chiavassa, M. R. L. Cioni, G. Comoretto, W. J. Cooper,
      T. Cornez, S. Cowell, F. Crifo, M. Crosta, C. Crowley, C. Dafonte, A. Dapergolas,
      M. David, P. David, P. de Laverny, F. De Luise, R. De March, J. De Ridder, R. de Souza,
      P. de Teodoro, A. de Torres, E. F. del Peloso, E. del Pozo, M. Delbo, A. Delgado, H. E.
      Delgado, J. B. Delisle, P. Di Matteo, S. Diakite, C. Diener, E. Distefano, C. Dolding,
      D. Eappachen, B. Edvardsson, H. Enke, P. Esquej, C. Fabre, M. Fabrizio, S. Faigler,
      G. Fedorets, P. Fernique, A. Fienga, F. Figueras, C. Fouron, F. Fragkoudi, E. Fraile,
      F. Franke, M. Gai, D. Garabato, A. Garcia-Gutierrez, M. García-Torres, A. Garofalo,
      P. Gavras, E. Gerlach, R. Geyer, P. Giacobbe, G. Gilmore, S. Girona, G. Giuffrida,
      R. Gomel, A. Gomez, I. Gonzalez-Santamaria, J. J. González-Vidal, M. Granvik,
      R. Gutiérrez-Sánchez, L. P. Guy, M. Hauser, M. Haywood, A. Helmi, S. L. Hidalgo,
      T. Hilger, N. Hładczuk, D. Hobbs, G. Holland, H. E. Huckle, G. Jasniewicz, P. G. Jonker,
      J. Juaristi Campillo, F. Julbe, L. Karbevska, P. Kervella, S. Khanna, A. Kochoska,
      M. Kontizas, G. Kordopatis, A. J. Korn, Z. Kostrzewa-Rutkowska, K. Kruszyńska,

S. Lambert, A. F. Lanza, Y. Lasne, J. F. Le Campion, Y. Le Fustec, Y. Lebreton, T. Lebzelter, S. Leccia, N. Leclerc, I. Lecoeur-Taibi, S. Liao, E. Licata, E. P. Lindstrøm, T. A. Lister, E. Livanou, A. Lobel, P. Madrero Pardo, S. Managau, R. G. Mann, J. M. Marchant, M. Marconi, M. M. S. Marcos Santos, S. Marinoni, F. Marocco, D. J. Marshall, L. Martin Polo, J. M. Martín-Fleitas, A. Masip, D. Massari, A. Mastrobuono-Battisti, T. Mazeh, P. J. McMillan, S. Messina, D. Michalik, N. R. Millar, A. Mints, D. Molina, R. Molinaro, L. Molnár, P. Montegriffo, R. Mor, R. Morbidelli, T. Morel, D. Morris, A. F. Mulone, D. Munoz, T. Muraveva, C. P. Murphy, I. Musella, L. Noval, C. Ordénovic, G. Orrù, J. Osinde, C. Pagani, I. Pagano, L. Palaversa, P. A. Palicio, A. Panahi, M. Pawlak, X. Peñalosa Esteller, A. Penttilä, A. M. Piersimoni, F. X. Pineau, E. Plachy, G. Plum, E. Poggio, E. Poretti, E. Poujoulet, A. Prša, L. Pulone, E. Racero, S. Ragaini, M. Rainer, C. M. Raiteri, N. Rambaux, P. Ramos, M. Ramos-Lerate, P. Re Fiorentin, S. Regibo, C. Reylé, V. Ripepi, A. Riva, G. Rixon, N. Robichon, C. Robin, M. Roelens, L. Rohrbasser, M. Romero-Gómez, N. Rowell, F. Royer, K. A. Rybicki, G. Sadowski, A. Sagristà Sellés, J. Sahlmann, J. Salgado, E. Salguero, N. Samaras, V. Sanchez Gimenez, N. Sanna, R. Santoveña, M. Sarasso, M. Schultheis, E. Sciacca, M. Segol, J. C. Segovia, D. Ségransan, D. Semeux, S. Shahaf, H. I. Siddiqui, A. Siebert, L. Siltala, E. Slezak, R. L. Smart, E. Solano, F. Solitro, D. Souami, J. Souchay, A. Spagna, F. Spoto, I. A. Steele, H. Steidelmüller, C. A. Stephenson, M. Süveges, L. Szabados, E. Szegedi-Elek, F. Taris, G. Tauran, M. B. Taylor, R. Teixeira, W. Thuillot, N. Tonello, F. Torra, J. Torra, C. Turon, N. Unger, M. Vaillant, E. van Dillen, O. Vanel, A. Vecchiato, Y. Viala, D. Vicente, S. Voutsinas, M. Weiler, T. Wevers, Ł. Wyrzykowski, A. Yoldas, P. Yvard, H. Zhao, J. Zorec, S. Zucker, C. Zurbach, and T. Zwitter, "Gaia early data release 3 - summary of the contents and survey properties," *A&A*, vol. 649, p. A1, 2021.

[43] E. Marchetti, R. Brast, B. Delabre, R. Donaldson, E. Fedrigo, C. Frank, N. Hubin, J. Kolb, J.-L. Lizon, M. Marchesi, S. Oberti, R. Reiss, J. Santos, C. Soenke, S. Tordo, A. Baruffolo, P. Bagnara, and CAMCAO Consortium, "On-sky Testing of the Multi-Conjugate Adaptive Optics Demonstrator," *The Messenger*, vol. 129, pp. 8–13, Sept. 2007.

[44] B. Neichel, J. R. Lu, F. Rigaut, S. M. Ammons, E. R. Carrasco, and E. Lassalle, "Astrometric performance of the Gemini multiconjugate adaptive optics system in crowded fields," *Monthly Notices of the Royal Astronomical Society*, vol. 445, pp. 500–514, Nov. 2014.

[45] E. Meyer, M. Kürster, C. Arcidiacono, R. Ragazzoni, and H. W. Rix, "Astrometry with the MCAO instrument MAD. An analysis of single-epoch data obtained in the layer-oriented mode," *Astronomy & Astrophysics*, vol. 532, p. A16, Aug. 2011.

[46] G. Rodeghiero, J. U. Pott, D. Massari, M. Fabricius, V. Garrel, H. Riechert, R. Davies, C. Arcidiacono, M. Patti, F. Cortecchia, G. Fiorentino, and M. Lombini, "Towards an overall astrometric error budget with MICADO-MCAO," *arXiv e-prints*, p. arXiv:1902.00933, Feb. 2019.

[47] S. Monty, F. Rigaut, R. McDermid, H. Baumgardt, J. Cranney, G. Agapito, J. T. Mendel, C. Plantet, D. Greggio, P. B. Stetson, G. Fiorentino, and D. Haynes, "Towards realistic modelling of the astrometric capabilities of MCAO systems: detecting an

intermediate-mass black hole with MAVIS," *Monthly Notices of the Royal Astronomical Society*, vol. 507, pp. 2192–2207, Oct. 2021.

[48] M. Schöck, T. Do, B. L. Ellerbroek, L. Gilles, G. Herriot, L. Meyer, R. Suzuki, L. Wang, and S. Yelda, "Thirty Meter Telescope astrometry error budget," in *Adaptive Optics Systems IV* (E. Marchetti, L. M. Close, and J.-P. Vran, eds.), vol. 9148 of *Society of Photo-Optical Instrumentation Engineers (SPIE) Conference Series*, p. 91482L, July 2014.

[49] P. B. Cameron, M. C. Britton, and S. R. Kulkarni, "Precision Astrometry With Adaptive Optics," *The Astronomical Journal*, vol. 137, pp. 83–93, Jan. 2009.

[50] T. Fritz, S. Gillessen, S. Trippe, T. Ott, H. Bartko, O. Pfuhl, K. Dodds-Eden, R. Davies, F. Eisenhauer, and R. Genzel, "What is limiting near-infrared astrometry in the Galactic Centre?," *Monthly Notices of the Royal Astronomical Society*, vol. 401, pp. 1177–1188, Jan. 2010.

[51] S. Trippe, R. Davies, F. Eisenhauer, N. M. Förster Schreiber, T. K. Fritz, and R. Genzel, "High-precision astrometry with MICADO at the European Extremely Large Telescope," *Monthly Notices of the Royal Astronomical Society*, vol. 402, pp. 1126–1140, Feb. 2010.

[52] L. Lindegren, "Photoelectric Astrometry - a Comparison of Methods for Precise Image Location," in *IAU Colloq. 48: Modern Astrometry*, p. 197, Jan. 1978.

[53] G. Carlà, C. Plantet, L. Busoni, and G. Agapito, "Temporal spectrum of multi-conjugate adaptive optics residuals and impact of tip-tilt anisoplanatism on astrometric observations," *Monthly Notices of the Royal Astronomical Society*, vol. 516, pp. 3837–3846, Aug. 2022. stac2377.

[54] G. Carlà, L. Busoni, C. Plantet, G. Agapito, C. Arcidiacono, and P. Ciliegi, "Tip-tilt anisoplanatism in MCAO-assisted astrometric observations," in *Adaptive Optics Systems VIII* (L. Schreiber, D. Schmidt, and E. Vernet, eds.), vol. 12185, p. 121850O, International Society for Optics and Photonics, SPIE, 2022.

[55] C. Plantet, G. Carlà, G. Agapito, and L. Busoni, "Spatiotemporal statistics of the turbulent piston-removed phase and Zernike coefficients for two distinct beams," *Journal of the Optical Society of America A*, vol. 39, p. 17, Jan. 2022.

[56] S. Esposito, A. Riccardi, F. Quirós-Pacheco, E. Pinna, A. Puglisi, M. Xompero, R. Briguglio, L. Busoni, L. Fini, P. Stefanini, G. Brusa, A. Tozzi, P. Ranfagni, F. Pieralli, J. C. Guerra, C. Arcidiacono, and P. Salinari, "Laboratory characterization and performance of the high-order adaptive optics system for the large binocular telescope," *Appl. Opt.*, vol. 49, pp. G174–G189, Nov 2010.

[57] R. J. Sasiela, "Wave-front correction by one or more synthetic beacons," *J. Opt. Soc. Am. A*, vol. 11, no. 1, pp. 379–393, 1994.

[58] R. Conan, "Mean-square residual error of a wavefront after propagation through atmospheric turbulence and after correction with Zernike polynomials," *J. Opt. Soc. Am. A*, vol. 25, no. 2, pp. 526–536, 2008.

[59] R. Navarro, J. Arines, and R. Rivera, "Direct and inverse discrete Zernike transform," *Opt. Express*, vol. 17, no. 26, pp. 24269–24281, 2009.

[60] N. A. Roddier, "Atmospheric wavefront simulation using Zernike polynomials," *Opt. Eng.*, vol. 29, no. 10, pp. 1174–1181, 1990.

[61] E. Gendron and G. Rousset, "Temporal analysis of aliasing in Shack-Hartmann wave-front sensing," *Proc. SPIE*, 2012.

[62] G. Molodij and G. Rousset, "Angular correlation of Zernike polynomials for a laser guide star in adaptive optics," *J. Opt. Soc. Am. A*, vol. 14, no. 8, pp. 1949–1966, 1997.

[63] P. Hu, J. Stone, and T. Stanley, "Application of Zernike polynomials to atmospheric propagation problems," *J. Opt. Soc. Am. A*, vol. 6, no. 10, pp. 1595–1608, 1989.

[64] N. Takato and I. Yamaguchi, "Spatial correlation of Zernike phase-expansion coefficients for atmospheric turbulence with finite outer scale," *J. Opt. Soc. Am. A*, vol. 12, no. 5, pp. 958–963, 1995.

[65] M. R. Whiteley, M. C. Roggemann, and B. M. Welsh, "Temporal properties of the Zernike expansion coefficients of turbulence-induced phase aberrations for aperture and source motion," *J. Opt. Soc. Am. A*, vol. 15, pp. 993–1005, Apr 1998.

[66] C. B. Hogge and R. R. Butts, "Frequency spectra for the geometric representation of wavefront distortions due to atmospheric turbulence," *IEEE Transactions on Antennas and Propagation*, vol. 24, pp. 144–154, 1976.

[67] E. Pinna, S. Esposito, P. Hinz, G. Agapito, M. Bonaglia, A. Puglisi, M. Xompero, A. Riccardi, R. Briguglio, C. Arcidiacono, L. Carbonaro, L. Fini, M. Montoya, and O. Durney, "SOUL: the single conjugated adaptive optics upgrade for LBT," in *Adaptive Optics Systems V*, vol. 9909, p. 99093V, International Society for Optics and Photonics, 2016.

[68] C. Petit, J.-F. Sauvage, A. Costille, T. Fusco, D. Mouillet, J.-L. Beuzit, K. Dohlen, M. E. Kasper, M. S. Valles, C. Soenke, A. Baruffolo, B. Salasnich, S. Rochat, E. Fedrigo, P. Baudoz, E. Hugot, A. Sevin, D. Perret, F. Wildi, M. Downing, P. Feautrier, P. Puget, A. Vigan, J. O'Neal, J. H. V. Girard, D. Mawet, H. M. Schmid, and R. Roelfsema, "SAXO: the extreme adaptive optics system of SPHERE (I) system overview and global laboratory performance," *Journal of Astronomical Telescopes, Instruments, and Systems*, vol. 2, no. 2, p. 025003, 2016.

[69] B. Neichel, F. Rigaut, M. Bec, M. Boccas, F. Daruich, C. D'Orgeville, V. Fesquet, R. Galvez, A. Garcia-Rissmann, G. Gausachs, M. Lombini, G. Perez, G. Trancho, V. Upadhya, and T. Vucina, "The Gemini MCAO System GeMS: nearing the end of a lab-story," in *Adaptive Optics Systems II*, vol. 7736, p. 773606, International Society for Optics and Photonics, 2010.

[70] R. Stuik, R. Bacon, R. Conzelmann, B. Delabre, E. Fedrigo, N. Hubin, M. Le Louarn, and S. Ströbele, "GALACSI–the ground layer adaptive optics system for MUSE," *New Astronomy Reviews*, vol. 49, no. 10-12, pp. 618–624, 2006.

[71] E. Diolaiti, P. Ciliegi, R. Abicca, G. Agapito, C. Arcidiacono, A. Baruffolo, M. Bellazzini, V. Biliotti, M. Bonaglia, G. Bregoli, R. Briguglio, O. Brissaud, L. Busoni, L. Carbonaro, A. Carlotti, E. Cascone, J.-J. Correia, F. Cortecchia, G. Cosentino, V. D. Caprio, M. de Pascale, A. D. Rosa, C. D. Vecchio, A. Delboulbé, G. D. Rico, S. Esposito, D. Fantinel, P. Feautrier, C. Felini, D. Ferruzzi, L. Fini, G. Fiorentino, I. Foppiani, M. Ghigo, C. Giordano, E. Giro, L. Gluck, F. Hénault, L. Jocou, F. Kerber, P. L. Penna, S. Lafrasse, M. Lauria, E. le Coarer, M. L. Louarn, M. Lombini, Y. Magnard, E. Maiorano, F. Mannucci, M. Mapelli, E. Marchetti, D. Maurel, L. Michaud, G. Morgante, T. Moulin, S. Oberti, G. Pareschi, M. Patti, A. Puglisi, P. Rabou, R. Ragazzoni, S. Ramsay, A. Riccardi, S. Ricciardi, M. Riva, S. Rochat, F. Roussel, A. Roux, B. Salasnich, P. Saracco, L. Schreiber, M. Spavone, E. Stadler, M.-H. Sztefek, N. Ventura, C. Vérinaud, M. Xompero, A. Fontana, and F. M. Zerbi, "MAORY: adaptive optics module for the E-ELT," *Proc. SPIE*, 2016.

[72] B. Neichel, T. Fusco, J.-F. Sauvage, C. Correia, K. Dohlen, K. El-Hadi, L. Blanco, N. Schwartz, F. Clarke, N. A. Thatte, M. Tecza, J. Paufique, J. Vernet, M. L. Louarn, P. Hammersley, J.-L. Gach, S. Pascal, P. Vola, C. Petit, J.-M. Conan, A. Carlotti, C. Vérinaud, H. Schnetler, I. Bryson, T. Morris, R. Myers, E. Hugot, A. M. Gallie, and D. M. Henry, "The adaptive optics modes for HARMONI: from Classical to Laser Assisted Tomographic AO," *Proc. SPIE*, 2016.

[73] G. Herriot, D. Andersen, J. Atwood, C. Boyer, A. Beauvillier, P. Byrnes, R. Conan, B. Ellerbroek, J. Fitzsimmons, L. Gilles, P. Hickson, A. Hill, K. Jackson, O. Lardière, J. Pazder, T. Pfrommer, V. Reshetov, S. Roberts, J.-P. Véran, L. Wang, and I. Wevers, "NFIRAOS: TMT's facility adaptive optics system," *Proc. SPIE*, 2010.

[74] P. M. Hinz, A. Bouchez, M. Johns, S. Shectman, M. Hart, B. McLeod, and P. McGregor, "The GMT adaptive optics system," *Proc. SPIE*, 2010.

[75] R. McDermid, "MAVIS: A new MCAO-Assisted Visible Imager and Spectrograph for the Very Large Telescope," in *Linking Galaxies from the Epoch of Initial Star Formation to Today*, 2019.

[76] R. Conan, F. Bennet, A. H. Bouchez, M. A. van Dam, B. Espeland, W. Gardhouse, C. d'Orgeville, S. Parcell, P. Piatrou, I. Price, F. Rigaut, G. Trancho, and K. Uhlendorf, "The Giant Magellan Telescope laser tomography adaptive optics system," in *Adaptive Optics Systems III*, vol. 8447, p. 84473P, International Society for Optics and Photonics, 2012.

[77] Y. Clénet, E. Gendron, D. Gratadour, G. Rousset, and F. Vidal, "Anisoplanatism effect on the E-ELT SCAO point spread function. A preserved coherent core across the field," *Astronomy & Astrophysics*, vol. 583, p. A102, Nov. 2015.

[78] E. Gendron, A. Charara, A. Abdelfattah, D. Gratadour, D. Keyes, H. Ltaief, C. Morel, F. Vidal, A. Sevin, and G. Rousset, "A novel fast and accurate pseudo-analytical simulation approach for MOAO," in *Adaptive Optics Systems IV*, vol. 9148, p. 91486L, International Society for Optics and Photonics, 2014.

[79] F. J. Rigaut, J.-P. Véran, and O. Lai, "Analytical model for Shack-Hartmann-based adaptive optics systems," in *Adaptive Optical System Technologies*, vol. 3353, pp. 1038–1048, International Society for Optics and Photonics, 1998.

[80] B. L. Ellerbroek, "Linear systems modeling of adaptive optics in the spatial-frequency domain," *JOSA A*, vol. 22, no. 2, pp. 310–322, 2005.

[81] L. Jolissaint, "Synthetic modeling of astronomical closed loop adaptive optics," *Journal of the European Optical Society - Rapid publications*, vol. 5, no. 0, 2010.

[82] R. M. Clare, B. L. Ellerbroek, G. Herriot, and J.-P. Véran, "Adaptive optics sky coverage modeling for extremely large telescopes," *Applied optics*, vol. 45, no. 35, pp. 8964–8978, 2006.

[83] C. M. Correia, C. Z. Bond, J.-F. Sauvage, T. Fusco, R. Conan, and P. L. Wizinowich, "Modeling astronomical adaptive optics performance with temporally filtered Wiener reconstruction of slope data," *JOSA A*, vol. 34, no. 10, pp. 1877–1887, 2017.

[84] P. M. Hinz, D. Defrère, A. Skemer, V. Bailey, J. Stone, E. Spalding, A. Vaz, E. Pinna, A. Puglisi, S. Esposito, M. Montoya, E. Downey, J. Leisenring, O. Durney, W. Hoffmann, J. Hill, R. Millan-Gabet, B. Mennesson, W. Danchi, K. Morzinski, P. Grenz, M. Skrutskie, and S. Ertel, "Overview of LBTI: a multipurpose facility for high spatial resolution observations," *Proc. SPIE*, 2016.

[85] F. Chassat, G. Rousset, and J. Primot, "Theoretical and experimental evaluation of isoplanatic patch size for adaptive optics.," in *Active telescope systems* (F. J. Roddier, ed.), vol. 1114 of *Society of Photo-Optical Instrumentation Engineers (SPIE) Conference Series*, pp. 14–22, Sept. 1989.

[86] J. Hill, R. Green, D. Ashby, J. Brynnel, N. Cushing, J. Little, J. Slagle, and R. Wagner, "The Large Binocular Telescope," *Proc. SPIE*, 2012.

[87] G. Agapito, C. Arcidiacono, F. Quirós-Pacheco, and S. Esposito, "Adaptive optics at short wavelengths," *Experimental Astronomy*, vol. 37, no. 3, pp. 503–523, 2014.

[88] S. Esposito, A. Riccardi, and B. Femenía, "Differential piston angular anisoplanatism for astronomical optical interferometers," *Astronomy and Astrophysics*, 2000.

[89] M. Sarazin, M. Le Louarn, J. Ascenso, G. Lombardi, and J. Navarrete, "Defining reference turbulence profiles for E-ELT AO performance simulations," in *Proceedings of the Third AO4ELT Conference* (S. Esposito and L. Fini, eds.), p. 89, Dec. 2013.

[90] T. Fusco, J.-M. Conan, G. Rousset, L. M. Mugnier, and V. Michau, "Optimal wavefront reconstruction strategies for multiconjugate adaptive optics," *Journal of the Optical Society of America A*, vol. 18, pp. 2527–2538, Oct. 2001.

[91] B. Le Roux, J.-M. Conan, C. Kulcsár, H.-F. Raynaud, L. M. Mugnier, and T. Fusco, "Optimal control law for classical and multiconjugate adaptive optics," *Journal of the Optical Society of America A*, vol. 21, pp. 1261–1276, July 2004.

[92] F. Quiros-Pacheco, C. Petit, J.-M. Conan, T. Fusco, and E. Marchetti, "Control laws for a multiconjugate adaptive optics system," in *Advancements in Adaptive Optics* (D. Bonaccini Calia, B. L. Ellerbroek, and R. Ragazzoni, eds.), vol. 5490 of *Society of Photo-Optical Instrumentation Engineers (SPIE) Conference Series*, pp. 1460–1471, Oct. 2004.

[93] A. G. Basden, D. Jenkins, T. J. Morris, J. Osborn, and M. J. Townson, "Efficient implementation of pseudo open-loop control for adaptive optics on Extremely Large Telescopes," *MNRAS*, vol. 486, pp. 1774–1780, June 2019.

[94] R. Flicker, F. Rigaut, and B. Ellerbroek, "Tilt anisoplanatism in laser-guide-star-based multiconjugate adaptive optics. Reconstruction of the long exposure point spread function from control loop data," *A&A*, vol. 400, pp. 1199–1207, Mar. 2003.

[95] L. Gilles and B. L. Ellerbroek, "Split atmospheric tomography using laser and natural guide stars," *Journal of the Optical Society of America A*, vol. 25, p. 2427, Sept. 2008.

[96] S. S. Olivier, C. E. Max, D. T. Gavel, and J. M. Brase, "Tip-Tilt Compensation: Resolution Limits for Ground-based Telescopes Using Laser Guide Star Adaptive Optics," *The Astrophysical Journal*, vol. 407, p. 428, Apr. 1993.

[97] "ERIS." https://www.eso.org/public/teles-instr/paranal-observatory/vlt/vlt-instr/eris/.

[98] F. W. Dyson, A. S. Eddington, and C. Davidson, "A Determination of the Deflection of Light by the Sun's Gravitational Field, from Observations Made at the Total Eclipse of May 29, 1919," *Philosophical Transactions of the Royal Society of London Series A*, vol. 220, pp. 291–333, Jan. 1920.

[99] E. B. Fomalont and R. A. Sramek, "The deflection of radio waves by the sun," *Comments on Astrophysics*, vol. 7, pp. 19–33, Jan. 1977.

[100] C. M. Will, "The 1919 measurement of the deflection of light," *Classical and Quantum Gravity*, vol. 32, p. 124001, June 2015.

[101] E. B. Fomalont and S. M. Kopeikin, "The Measurement of the Light Deflection from Jupiter: Experimental Results," *The Astrophysical Journal*, vol. 598, pp. 704–711, Nov. 2003.

[102] S. Casertano, U. Abbas, J. Anderson, M. Crosta, M. Kamionkowski, M. G. Lattanzi, J. W. MacKenty, R. Morbidelli, A. Riess, and A. Vecchiato, "Astrometric Light Deflection Test of General Relativity for Non-spherical Bodies: Close Approach to Jupiter." HST Proposal. Cycle 24, ID. #14666, June 2016.

[103] M. T. Crosta and F. Mignard, "Microarcsecond light bending by Jupiter," *Classical and Quantum Gravity*, vol. 23, pp. 4853–4871, Aug. 2006.

[104] U. Abbas, B. Bucciarelli, M. G. Lattanzi, M. Crosta, R. Morbidelli, D. Busonero, L. Bramante, and R. Messineo, "Differential astrometry with Gaia. Investigating relativistic light deflection close to Jupiter," *Astronomy & Astrophysics*, vol. 664, p. A143, Aug. 2022.

[105] N. Zacharias, D. G. Monet, S. E. Levine, S. E. Urban, R. Gaume, and G. L. Wycoff, "The Naval Observatory Merged Astrometric Dataset (NOMAD)," in *American Astronomical Society Meeting Abstracts*, vol. 205 of *American Astronomical Society Meeting Abstracts*, p. 48.15, Dec. 2004.

[106] R. Flicker and F. Rigaut, "Tilt anisoplanatism and PSF retrieval in LGS MCAO using a predictive controller," in *European Southern Observatory Conference and Workshop Proceedings*, vol. 58 of *European Southern Observatory Conference and Workshop Proceedings*, p. 377, Jan. 2002.